

A Realistic Model of the Human Ventricular Myocardium: Application to the Study of Ectopic Activation

Rok Hren

Department of Physiology and Biophysics

Submitted in partial fulfillment of
the requirements for the degree of
Doctor of Philosophy

at

Dalhousie University
Halifax, Nova Scotia, Canada

August 1996

© Rok Hren 1996



National Library
of Canada

Acquisitions and
Bibliographic Services Branch

395 Wellington Street
Ottawa, Ontario
K1A 0N4

Bibliothèque nationale
du Canada

Direction des acquisitions et
des services bibliographiques

395, rue Wellington
Ottawa (Ontario)
K1A 0N4

Your file *Voire référence*

Our file *Notre référence*

The author has granted an irrevocable non-exclusive licence allowing the National Library of Canada to reproduce, loan, distribute or sell copies of his/her thesis by any means and in any form or format, making this thesis available to interested persons.

L'auteur a accordé une licence irrévocable et non exclusive permettant à la Bibliothèque nationale du Canada de reproduire, prêter, distribuer ou vendre des copies de sa thèse de quelque manière et sous quelque forme que ce soit pour mettre des exemplaires de cette thèse à la disposition des personnes intéressées.

The author retains ownership of the copyright in his/her thesis. Neither the thesis nor substantial extracts from it may be printed or otherwise reproduced without his/her permission.

L'auteur conserve la propriété du droit d'auteur qui protège sa thèse. Ni la thèse ni des extraits substantiels de celle-ci ne doivent être imprimés ou autrement reproduits sans son autorisation.

ISBN 0-612-15935-3

Canada

Name _____

Dissertation Abstracts International is arranged by broad, general subject categories. Please select the one subject which most nearly describes the content of your dissertation. Enter the corresponding four-digit code in the spaces provided.

MEDICAL BIOPHYSICS

SUBJECT TERM

0760 U.M.I.

SUBJECT CODE

Subject Categories

THE HUMANITIES AND SOCIAL SCIENCES

COMMUNICATIONS AND THE ARTS

Architecture 0729
 Art History 0377
 Cinema 0900
 Dance 0378
 Fine Arts 0357
 Information Science 0723
 Journalism 0391
 Library Science 0399
 Mass Communications 0708
 Music 0413
 Speech Communication 0459
 Theater 0465

EDUCATION

General 0515
 Administration 0514
 Adult and Continuing 0516
 Agricultural 0517
 Art 0273
 Bilingual and Multicultural 0282
 Business 0688
 Community College 0275
 Curriculum and Instruction 0727
 Early Childhood 0518
 Elementary 0524
 Finance 0277
 Guidance and Counseling 0519
 Health 0680
 Higher 0745
 History of 0520
 Home Economics 0278
 Industrial 0521
 Language and Literature 0279
 Mathematics 0280
 Music 0522
 Philosophy of 0998
 Physical 0523

Psychology 0525
 Reading 0535
 Religious 0527
 Sciences 0714
 Secondary 0533
 Social Sciences 0534
 Sociology of 0340
 Special 0529
 Teacher Training 0530
 Technology 0710
 Tests and Measurements 0288
 Vocational 0747

LANGUAGE, LITERATURE AND LINGUISTICS

Language
 General 0679
 Ancient 0289
 Linguistics 0290
 Modern 0291
 Literature
 General 0401
 Classical 0294
 Comparative 0295
 Medieval 0297
 Modern 0298
 African 0316
 American 0591
 Asian 0305
 Canadian (English) 0352
 Canadian (French) 0355
 English 0593
 Germanic 0311
 Latin American 0312
 Middle Eastern 0315
 Romance 0313
 Slavic and East European 0314

PHILOSOPHY, RELIGION AND THEOLOGY

Philosophy 0422
 Religion
 General 0318
 Biblical Studies 0321
 Clergy 0319
 History of 0320
 Philosophy of 0322
 Theology 0469

SOCIAL SCIENCES

American Studies 0323
 Anthropology
 Archaeology 0324
 Cultural 0326
 Physical 0327
 Business Administration
 General 0310
 Accounting 0272
 Banking 0770
 Management 0454
 Marketing 0338
 Canadian Studies 0385
 Economics
 General 0501
 Agricultural 0503
 Commerce-Business 0505
 Finance 0508
 History 0509
 Labor 0510
 Theory 0511
 Folklore 0358
 Geography 0366
 Gerontology 0351
 History
 General 0578

Ancient 0579
 Medieval 0581
 Modern 0582
 Black 0328
 African 0331
 Asia, Australia and Oceania 0332
 Canadian 0334
 European 0335
 Latin American 0336
 Middle Eastern 0333
 United States 0337
 History of Science 0585
 Law 0398
 Political Science
 General 0615
 International Law and Relations 0616
 Public Administration 0617
 Recreation 0614
 Social Work 0452
 Sociology
 General 0626
 Criminology and Penology 0627
 Demography 0938
 Ethnic and Racial Studies 0631
 Individual and Family Studies 0628
 Industrial and Labor Relations 0629
 Public and Social Welfare 0630
 Social Structure and Development 0700
 Theory and Methods 0344
 Transportation 0709
 Urban and Regional Planning 0999
 Women's Studies 0453

THE SCIENCES AND ENGINEERING

BIOLOGICAL SCIENCES

Agriculture
 General 0473
 Agronomy 0285
 Animal Culture and Nutrition 0475
 Animal Pathology 0476
 Food Science and Technology 0359
 Forestry and Wildlife 0478
 Plant Culture 0479
 Plant Pathology 0480
 Plant Physiology 0817
 Range Management 0777
 Wood Technology 0746
 Biology
 General 0306
 Anatomy 0287
 Biostatistics 0308
 Botany 0309
 Cell 0379
 Ecology 0329
 Entomology 0353
 Genetics 0369
 Limnology 0793
 Microbiology 0410
 Molecular 0307
 Neuroscience 0317
 Oceanography 0416
 Physiology 0433
 Radiation 0821
 Veterinary Science 0778
 Zoology 0472
 Biophysics
 General 0786
 Medical 0760

Geodesy 0370
 Geology 0372
 Geophysics 0373
 Hydrology 0388
 Mineralogy 0411
 Paleobotany 0345
 Paleontology 0426
 Paleogeology 0418
 Paleozoology 0985
 Polynology 0427
 Physical Geography 0368
 Physical Oceanography 0415

HEALTH AND ENVIRONMENTAL SCIENCES

Environmental Sciences 0768
 Health Sciences
 General 0566
 Audiology 0300
 Chemotherapy 0992
 Dentistry 0567
 Education 0350
 Hospital Management 0769
 Human Development 0758
 Immunology 0982
 Medicine and Surgery 0564
 Mental Health 0347
 Nursing 0569
 Nutrition 0570
 Obstetrics and Gynecology 0380
 Occupational Health and Therapy 0354
 Ophthalmology 0381
 Psychology 0571
 Pharmacology 0419
 Pharmacy 0572
 Physical Therapy 0382
 Public Health 0573
 Radiology 0574
 Recreation 0575

Speech Pathology 0460
 Toxicology 0383
 Home Economics 0386

PHYSICAL SCIENCES

Pure Sciences
 Chemistry
 General 0485
 Agricultural 0749
 Analytical 0486
 Biochemistry 0487
 Inorganic 0488
 Nuclear 0738
 Organic 0490
 Pharmaceutical 0491
 Physical 0494
 Polymer 0495
 Radiation 0754
 Mathematics 0405
 Physics
 General 0605
 Acoustics 0986
 Astronomy and Astrophysics 0606
 Atmospheric Science 0608
 Atomic 0748
 Electronics and Electricity 0607
 Elementary Particles and High Energy 0798
 Fluid and Plasma 0759
 Molecular 0609
 Nuclear 0610
 Optics 0752
 Radiation 0756
 Solid State 0611
 Statistics 0463
 Applied Sciences
 Applied Mechanics 0346
 Computer Science 0984

Engineering
 General 0537
 Aerospace 0538
 Agricultural 0539
 Automotive 0540
 Biomedical 0541
 Chemical 0542
 Civil 0543
 Electronics and Electrical 0544
 Heat and Thermodynamics 0348
 Hydraulic 0545
 Industrial 0546
 Marine 0547
 Materials Science 0794
 Mechanical 0548
 Metallurgy 0743
 Mining 0551
 Nuclear 0552
 Packaging 0549
 Petroleum 0765
 Sanitary and Municipal 0554
 System Science 0790
 Geotechnology 0428
 Operations Research 0796
 Plastics Technology 0795
 Textile Technology 0994

PSYCHOLOGY

General 0621
 Behavioral 0384
 Fluid and Plasma 0622
 Clinical 0620
 Developmental 0620
 Experimental 0623
 Industrial 0624
 Personality 0625
 Physiological 0989
 Psychobiology 0349
 Psychometrics 0632
 Social 0451

EARTH SCIENCES

Biogeochemistry 0425
 Geochemistry 0996



DALHOUSIE UNIVERSITY
FACULTY OF GRADUATE STUDIES


The undersigned hereby certify that they have read and recommend to the Faculty of Graduate Studies for acceptance a thesis entitled "A Realistic Model of the Human Ventricular Myocardium: Application to the Study of Ectopic Activation"

by Rok Hren

in partial fulfillment of the requirements for the degree of Doctor of Philosophy.

Dated August 26, 1996

External Examiner
Research Supervisor
Research Supervisor
Examining Committee



DALHOUSIE UNIVERSITY

Date: *September 6, 1996*

Author: Rok Hren

Title: "A Realistic Model of the Human Ventricular Myocardium: Application to the Study of Ectopic Activation"

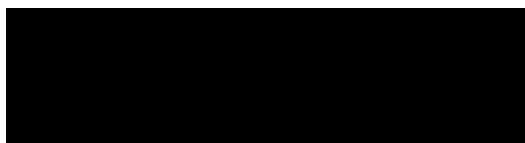
Department: Physiology and Biophysics

Degree: Ph.D.

Convocation: Fall

Year: 1996

Permission is herewith granted to Dalhousie University to circulate and to have copied for non-commercial purposes, at its discretion, the above title upon the request of individuals or institutions.



Signature of Author

The author reserves other publication rights, and neither the thesis nor extensive extracts from it may be printed or otherwise reproduced without the author's written permission.

The author attests that permission has been obtained for the use of any copyrighted material appearing in this thesis (other than brief excerpts requiring only proper acknowledgement in scholarly writing) and that all such use is clearly acknowledged.

Contents

List of Figures	vi
List of Tables	xi
Abstract	xii
Symbols and Abbreviations	xiii
Acknowledgements	xvi
1 Introduction	1
2 Model of the ventricular geometry and fibrous structure	6
2.1 Introduction	6
2.1.1 Fiber architecture of ventricular myocardium	7
2.1.2 Approach to constructing a ventricular model	10
2.2 Surface harmonic expansion	12
2.3 Construction of a ventricular model	15
2.3.1 Modeling strategy	15
2.3.2 Model generation	17
2.4 Implementation of the ventricular model	24
2.5 Discussion	37
3 Simulation of propagated excitation in the anisotropic myocardium	44
3.1 Introduction	44
3.1.1 Cardiac source modeling	45
3.1.2 Volume conductor modeling	50
3.2 Macroscopic description of cardiac sources by the bidomain model . .	53
3.2.1 Conductivity tensor as a descriptor of anisotropy	53

3.2.2	Derivation of the bidomain equations	55
3.2.3	Boundary conditions	58
3.2.4	Assumption of an equal anisotropy ratio	59
3.2.5	Cellular automata approach	62
3.3	Model for evaluating the extracardiac electric potentials and magnetic field	63
3.3.1	Extracardiac electric potentials	68
3.3.2	Extracardiac magnetic field	72
3.4	Summary	74
4	Epicardial potentials during the initial phase of ventricular activation	76
4.1	Introduction	76
4.2	Slab model of myocardial tissue	79
4.2.1	Model description	79
4.2.2	Parameter calibration	81
4.2.3	Activation wavefronts for epicardial, intramural, and endocardial pacing	83
4.2.4	Maps of the electric potentials and magnetic field for epicardial, intramural, and endocardial pacing	88
4.2.5	Effect of tipping fibers from the tangential plane on the electric potentials and magnetic field	97
4.2.6	Effect of subepicardial necrosis on the electric potentials and magnetic field	99
4.3	Realistic ventricular myocardium	102
4.3.1	Methodology	102
4.3.2	Epicardial potential distributions for epicardial, intramural, and endocardial pacing	104
4.3.3	Nontransmural necrosis and epicardial potentials	114
4.3.4	Comparison of simulations with experimental studies	116
5	Epicardial potentials during later phases of ventricular activation	118
5.1	Model of the ventricular conduction system	119
5.1.1	Implementation of the conduction system	122
5.2	Realistic ventricular myocardium	127
5.2.1	Epicardial potential distributions for epicardial, intramural, and endocardial pacing	127

5.2.2	Effect of intramural and subendocardial necrosis on epicardial potentials	137
5.3	Discussion	139
6	Localization of sites of ectopic activation using simulated BSPMs as templates	144
6.1	Introduction	144
6.2	Methodology	145
6.3	BSPM localization of septal preexcitation sites in WPW syndrome . .	147
6.3.1	Results	148
6.4	BSPM localization of the site of origin of idiopathic VT	154
6.4.1	Results	155
6.5	BSPM reference data base for paced activation sequences in human ventricles	162
6.5.1	Simulated activation sequences	165
6.5.2	Data base of QRS-integral maps	180
6.5.3	Correspondence with clinical data	197
6.5.4	Protocol for localizing the site of origin of ectopic LV activation using the data base of QRS-integral maps	200
6.6	Discussion	205
7	Conclusions	213
A	Functions used in simulating propagated excitation	215
B	Effect of volume conductor boundaries on epicardial and body surface potentials	217
C	Localization of the site of origin of idiopathic VT by magnetic field mapping	229
	Bibliography	235

List of Figures

2.1	Coordinate system for surface harmonic expansion	13
2.2	The vector of the local principal fiber direction	18
2.3	Epicardial surface reconstructed by surface harmonic expansion	26
2.4	LV endocardial surface reconstructed by surface harmonic expansion	27
2.5	Slices through the principal surfaces of the human ventricular model	29
2.6	Anterior view of the human ventricular model	31
2.7	Posterior view of the human ventricular model	32
2.8	Apical view of the human ventricular model	33
2.9	Basal view of the geometry of the human ventricular model	34
2.10	Basal view of the human ventricular model	35
2.11	Coronal cross section through the human ventricular model	38
2.12	Apical transaxial cross sections through the human ventricular model	39
2.13	Medial transaxial cross sections through the human ventricular model	40
2.14	Basal transaxial cross sections through the human ventricular model	41
4.1	The slab model of myocardial tissue	79
4.2	Isochrones during epicardial pacing	84
4.3	Isochrones during intramural pacing I	85
4.4	Isochrones during intramural pacing II	87
4.5	Maps of the electric potentials during epicardial pacing	89
4.6	Maps of the magnetic field during epicardial pacing	89
4.7	Maps of the electric potentials and magnetic field due to pair of dipoles	90
4.8	Epicardial electrograms for epicardial pacing	92
4.9	Maps of the electric potentials and magnetic field for intramural pacing	94
4.10	Maps of the electric potentials and magnetic field for endocardial pacing	95
4.11	Maps of the electric potentials and magnetic field for intramural pacing in a slab with tipping of fibers	98
4.12	Maps of the electric potentials and magnetic field for epicardial pacing in a slab with simulated subepicardial necrosis	100

4.13	Isochrones during epicardial pacing with subepicardial necrosis	101
4.14	Position of epicardial electrode arrays	103
4.15	EPDs for epicardial pacing	105
4.16	EPDs for pacing in the RV free wall	106
4.17	EPDs for pacing in the LV free wall	107
4.18	EPDs for LV intramural pacing	108
4.19	EPDs for RV endocardial pacing	110
4.20	EPDs for LV endocardial pacing	111
4.21	EPD for pacing in the LV trabeculata	112
4.22	EPDs for epicardial pacing in the ventricular model with subepicardial necrosis	114
4.23	EPDs for intramural pacing in the ventricular model with intramural necrosis	115
4.24	EPDs for endocardial pacing in the ventricular model with subendo- cardial necrosis	116
5.1	Isochronal maps on the LV endocardial surface for the RBBB activa- tion sequence	125
5.2	Isochronal maps on the epicardial surface for the RBBB activation sequence	125
5.3	Isochronal maps on the RV endocardial surface for the LBBB activa- tion sequence	126
5.4	Isochronal maps on the epicardial surface for the LBBB activation sequence	126
5.5	EPDs for RV epicardial pacing during the later phases of ventricular activation	128
5.6	EPDs for LV epicardial pacing during the later phases of ventricular activation	129
5.7	EPDs for RV intramural pacing during the later phases of ventricular activation	131
5.8	EPDs for LV intramural pacing during the later phases of ventricular activation	132
5.9	Isochronal map for LV intramural pacing	133
5.10	EPDs for LV subendocardial pacing during the later phases of ventric- ular activation I	134
5.11	EPDs for LV subendocardial pacing during the later phases of ventric- ular activation II	135

5.12	EPDs for RV endocardial pacing during the later phases of ventricular activation	136
5.13	EPDs for RV epicardial pacing in the ventricular model with subendocardial necrosis	138
5.14	EPDs for LV epicardial pacing in the ventricular model with intramural necrosis	138
6.1	Anterior and posterior views of the standard homogeneous torso . . .	146
6.2	BSPMs corresponding to the septal preexcitation sites in WPW syndrome	149
6.3	BSPMs corresponding to the anteroseptal and posteroseptal preexcitation sites in WPW syndrome	150
6.4	BSPMs corresponding to the left posteroseptal preexcitation	153
6.5	BSPM and EPM for an activation sequence initiated at the RVOT . .	156
6.6	BSPMs for an activation sequence initiated at the RVOT	157
6.7	BSPM and EPM for an activation sequence initiated at the posteroseptal apical region of the LV endocardium	158
6.8	BSPMs for an activation sequence initiated at the posteroseptal apical region of the LV endocardium	159
6.9	QRS-integral maps for activation sequences initiated at the RVOT and at the posteroseptal apical area of the LV endocardium	161
6.10	QRS-integral maps for activation sequences initiated at two sites of the RVOT	162
6.11	Isochronal map for an activation sequence initiated at the anterior endocardial pacing site in the middle level of the LV	166
6.12	BSPMs and EPMs for an activation sequence initiated at the anterior endocardial pacing site in the middle level of the LV	167
6.13	BSPMs for an activation sequence initiated at the anterior endocardial pacing site in the middle level of the LV	168
6.14	Isochronal map for an activation sequence initiated at the anterolateral endocardial pacing site in the middle level of the LV	169
6.15	BSPM and EPM for an activation sequence initiated at the anterolateral endocardial pacing site in the middle level of the LV	170
6.16	BSPMs for an activation sequence initiated at the anterolateral endocardial pacing site in the middle level of the LV	171
6.17	Isochronal maps for an activation sequence initiated near the apex of the RV endocardium	173

6.18	BSPMs and EPMs for an activation sequence initiated near the apex of the RV endocardium	174
6.19	BSPMs for an activation sequence initiated near the apex of the RV endocardium	175
6.20	Isochronal map for an activation sequence initiated at the posterolateral endocardial pacing site in the basal level of the LV	176
6.21	BSPMs and EPMs for an activation sequence initiated at the posterolateral endocardial pacing site in the basal level of the LV	177
6.22	Isochronal map for an activation sequence initiated at the anterior epicardial pacing site in the middle level of the LV	178
6.23	BSPMs for an activation sequence initiated at the anterior epicardial pacing site in the middle level of the LV	179
6.24	QRS-integral maps for activation sequences initiated at 12 endocardial sites in the basal level of the LV	181
6.25	QRS-integral maps for activation sequences initiated at 12 endocardial sites in the basal/midbasal level of the LV	182
6.26	QRS-integral maps for activation sequences initiated at 12 endocardial sites in the midbasal level of the LV	183
6.27	QRS-integral maps for activation sequences initiated at 12 endocardial sites in the middle level of the LV	184
6.28	QRS-integral maps for activation sequences initiated at 12 endocardial sites in the midapical level of the LV	185
6.29	QRS-integral maps for activation sequences initiated at 6 endocardial sites in the apical level of the LV	186
6.30	QRS-integral maps for activation sequences initiated at 8 levels in the anterior aspect of the LV endocardium	189
6.31	QRS-integral maps for activation sequences initiated at 8 levels in the posteroseptal aspect of the LV endocardium	190
6.32	QRS-integral maps for activation sequences initiated at 8 levels in the anterior aspect of the LV endocardium	191
6.33	QRS-integral maps for activation sequences initiated at 8 endocardial sites in the basal/midbasal level of the RV	193
6.34	QRS-integral maps for activation sequences initiated at 8 endocardial sites in the middle level of the RV	194
6.35	QRS-integral maps for activation sequences initiated at 8 endocardial sites in the midapical level of the RV	195

6.36	QRS-integral maps for activation sequences initiated at endocardial sites near the LV and RV apex	196
6.37	QRS-integral maps for activation sequences initiated at LV endocardial sites	202
6.38	QRS-integral map and correlation maps for an activation sequence initiated at the lateral/anterolateral endocardial pacing site in mid-basal/basal level of the LV	203
6.39	QRS-integral map and correlation maps for an activation sequence initiated at the posteroseptal/posterior endocardial pacing site in middle/midapical level of the LV	203
6.40	QRS-integral maps and correlation maps for activation sequences initiated at 12 endocardial sites in the LV	204
B.1	Anterior and posterior views of the standard torso model	218
B.2	Individualized male and female torso models	218
B.3	Effect of epicardial boundary on the epicardial potential distribution .	221
B.4	Effect of torso boundaries on BSPMs	224
B.5	Effect of individualized torso boundaries on BSPMs	225
C.1	The measurement grid for magnetic field mapping	230
C.2	MFMs for an activation sequence initiated at the RVOT	231
C.3	MFMs for an activation sequence initiated at the posteroseptal apical area of the LV endocardium	232
C.4	QRS-integral magnetic field maps for activation sequences initiated at the RVOT and the posteroseptal apical area of the LV endocardium .	233

List of Tables

2.1	Fit of Principal Surfaces by Surface Harmonic Expansion	25
4.1	Values of Propagation Velocity	82
4.2	Selected Propagation Parameters	83
6.1	Correlation Coefficients between QRS-integral Maps	187
B.1	Effect of Epicardial Boundary on Epicardial Potentials	222
B.2	Effect of Torso Boundaries on BSPMs	223
B.3	Effect of Individulized Torso Boundaries on BSPMs	226

Abstract

Body surface potential maps recorded during catheter pace mapping can facilitate the localization of the site of origin of ventricular tachycardia. This study investigated the value of a realistic computer model of the human ventricular myocardium in identifying sites of ectopic activation using simulated body surface potential maps as templates. Our model of the human ventricular myocardium features an anatomically accurate geometry and an intramural anisotropic structure that were reconstructed with a spatial resolution of 0.5 mm. It simulates the electrotonic interactions of cardiac cells by solving a nonlinear parabolic partial differential equation, but it behaves as a cellular automaton when the transmembrane potential exceeds the threshold value.

We successfully validated our model by comparing the simulated activation sequences of isochronal maps, epicardial potential maps, and body surface potential maps with the measured sequences of maps reported in the literature. Based on our simulations, we have developed clinical protocols for differentiating among septal accessory pathways in Wolff-Parkinson-White syndrome and for localizing the origin of idiopathic ventricular tachycardia. By systematically pacing the left ventricular and right ventricular endocardial surfaces in our ventricular model, we generated a data base of isointegral maps, which provides a high-resolution reference frame for localizing distinct endocardial pacing sites. This data base promises to be a useful tool in improving the performance of catheter pace mapping used in combination with body surface potential mapping. Overall, the results demonstrate that our computer model of the human ventricular myocardium is well suited for complementing a data base of isointegral maps obtained during clinical pace mapping and can help enhance the efficacy of the ablative treatment of ventricular arrhythmias.

Symbols and Abbreviations

a - The scalar a

\mathbf{a} - The vector \mathbf{a}

\mathbf{A} - The matrix \mathbf{A}

\mathbf{A}^{-1} - Inverse of the matrix \mathbf{A}

\mathbf{A}^T - Transpose of the matrix \mathbf{A}

B - Bounded monodomain region (thoracic tissues)

\mathbf{B} - Magnetic flux density [$\text{T} = \text{Vs}/\text{m}^2$]

\mathbf{B}_n - Vector of normal components of the magnetic flux density

C_m - Membrane capacitance per unit area [F/m^2]

\mathbf{D} - Conductivity tensor

δ - Dirac delta function

ϕ - Electric potential [V]

Φ - Vector of potential values

ϕ_i - Intracellular potential [V]

ϕ_e - Interstitial potential [V]

H - Anisotropic bidomain region (ventricular myocardium)

χ - Membrane surface area per unit volume [$1/\text{m}$]

\mathbf{I} - Identity matrix

I - Transmembrane current density [A/m^2]

i - Transmembrane current per unit volume [A/m^3]

\mathbf{j} - Current density [A/m^2]

\mathbf{n} - Outward unit normal to a surface

∇ - Gradient operator - nabla

∇^2 – Laplacian operator
 \mathbf{p} – Dipole moment [Am]
 P_n – Legendre polynomial of degree n of the first kind
 P_n^m – Associated Legendre polynomial of degree n and order m of the first kind
 \mathbf{r} – Source point [m]
 \mathbf{r}' – Observation point [m]
 R – Distance between source and observation points [m]
 S – Surface area [m²]
 dS – Differential surface area
 σ – Conductivity [S/m]
 V – Volume [m³]
 dV – Differential volume
 v_m – Transmembrane potential [V]
 2-D – Two-dimensional
 3-D – Three-dimensional
 AP – Action potential
 A-V – Atrioventricular
 BEM – Boundary element method
 BSPM – Body surface potential map(ping)
 CA – Cellular automata, Cellular automaton
 CAT – Computer assisted tomography
 CCW – Counterclockwise
 CW – Clockwise
 CPU – Central processing unit

ECG – Electrocardiogram
EPD – Epicardial potential distribution
EPM – Epicardial potential map
FEM – Finite element method
LV – Left ventricle, Left ventricular
MFM – Magnetic field map(ping)
MRI – Magnetic resonance imaging
P, Q, R, S, T – Nomenclature of the waves of the electrocardiogram
rms – Root-mean-square (error)
RF – Radiofrequency
RV – Right ventricle, Right ventricular
SD – Standard deviation
 $V_1 - V_6$ – Standard precordial ECG leads (electrode sites)
VT – Ventricular tachycardia
WPW – Wolff-Parkinson-White (syndrome)

Acknowledgements

I wish to extend my gratitude to Dr. B. Milan Horáček for his invaluable support and to Dr. Gerhard Stroink for helpful suggestions. I would like to thank Peter King for careful reading of the manuscript. I also gratefully appreciate the cooperation of Brian Hoyt, Cindy Penney, Helen Cook, and Paul MacInnis. Financial support for my studies was provided by the Izaak Walton Killam Memorial Foundation.

I wish to thank my family, Ida and Franc, Eli and Franci, grandmother Francka, and, most of all, Daniela for loving me, understanding me and encouraging me. Finally, I would like to thank my friends Jure, Sandi, and Tomaz. This dissertation is dedicated to Jure Uran (1967–1985).

Chapter 1

Introduction

Under normal conditions, the human heart undergoes highly synchronized mechanical contraction, which is preceded by propagated electrical activation. Although electron micrographs reveal that the heart consists of cells that are connected by tight junctions [158, 275, 346], on the macroscopic scale the heart acts as a syncytium. The individual myocardial cells maintain the potential difference between intracellular and extracellular media, which are separated by a semipermeable membrane. The characteristic property of myocardial cells is that they are excitable; upon receiving an appropriate electrical stimulus, their membrane changes its selective ionic conductance for Na^+ , K^+ , Ca^{2+} and other ions in a time- and voltage-dependent manner and, as a consequence, after each stimulus the transmembrane potential follows the sequence of depolarization and repolarization, which is referred to as the cardiac action potential (AP) [101]. The fundamental property of cardiac AP is the prolonged repolarization phase (observed as a characteristic 200- to 300-ms plateau) during which the cells are refractory, i.e., unable to respond to an additional stimulus. Accordingly, during every normal cardiac excitation cycle, the wave of propagated activation is unidirectional (progressing, in general, from the endocardium to the epicardium and

from the apex to the base), and each myocardial cell is activated only once [101]. The membrane currents accompanying the depolarization and repolarization of individual myocardial cells generate a current flow in the heart and in the surrounding thoracic tissues. These currents give rise to the potential differences that can be recorded as electrograms on the surface of the heart and as electrocardiograms (ECGs) on the chest surface.

The advent of body surface potential mapping [68, 98]—in which electrocardiographic recordings are collected simultaneously from multiple thoracic electrodes (ranging in number from 30 to 240)—made it possible to produce greatly enhanced images of the electrical manifestations of cardiac sources on the body surface. In addition, the development of multilead cardiac mapping techniques enabled researchers to achieve an unprecedented insight into the underlying intracardiac activity by allowing the registration of cardiac electrograms near the primary sources [376, 399]. Now, there is a growing interest in integrating the extensive body of experimental work into a quantitative model and in making use of such a model in clinical cardiology.

One of the most challenging tasks on the way towards understanding cardiac electrograms and body surface ECGs is to establish a dynamic model of cardiac primary sources in conjunction with an anatomically faithful representation of the complex ventricular architecture (including the ventricular conduction system) and to relate such a model to measurable phenomena. However, the road to accomplishing this task is fraught with difficulties for several reasons. First, the ventricular myocardium is strongly anisotropic, with conductivity being higher along than across the fibers; the spatial organization of anisotropy is complex and dependent on the irregular ge-

ometry of the ventricles. Second, because the heart is a large organ, with about 50 billion ventricular cells being depolarized and repolarized during each cardiac cycle, defining the cardiac primary sources in a mathematically rigorous way is very difficult. Third, given the inhomogeneous electrical properties and irregular shape of the human chest, one can only calculate the extracardiac electric potentials and magnetic field produced by cardiac primary sources if one uses numerical models that take into account Neumann boundary conditions. Reconciling all these requirements for a physiologically accurate modeling of the genesis of electrograms/ECGs with the necessity of computational feasibility is not easy.

The aim of the simulations presented here was to approximate the process of propagated activation in human ventricles and to generate an extracardiac field in a manner that would incorporate as much of the current knowledge about ventricular anatomy and electrophysiology as could possibly be incorporated given the bounds enforced by our present computing resources. The specific area of interest is the relationship between the structure of the ventricular myocardium and the distribution of epicardial or body surface potentials. Such spatial distributions of potentials at selected time instants, or integrated over a time interval, best reveal the underlying cardiac activity when presented as isocontour maps. In addition, it is often possible to assess the main morphological features of maps by simple measures extracted from them, such as the location of extrema, the distance between extrema, and the configuration of the region of near-zero potentials. The entire isocontour maps, as well as their features, provide an effective means to rigorously validate the models of cardiac primary sources.

This study is geared to the simulation of human ECGs because they constitute the first-hand experimental data in this laboratory (body surface potential distributions have been recorded in about 4,000 subjects during the past 20 years). However, the knowledge of ventricular architecture is at present based on measurements performed in canine hearts, and a large body of experimental evidence in cardiac mapping also comes from studies performed in canine hearts. To use this wealth of information for the purposes of constructing and validating the human ventricular model, we had to assume that there are—apart from the size—no qualitative anatomical and functional differences between the human and canine ventricular myocardium. This assumption is in accord with the general premise underlying animal studies.

The scope of the study presented in this dissertation is defined by four objectives:

- to develop a computer model of the human ventricular myocardium that features an anatomically accurate geometry and an intramural anisotropic structure and a physiologically accurate description of the excitation process
- to validate the ventricular model by simulating ectopic activation sequences initiated at endocardial, intramural, and epicardial sites and by comparing their isochronal maps and potential distributions on the epicardial surface with the recorded maps in the literature
- to simulate body surface potential distributions that can be used as templates for discriminating between septal preexcitation sites in patients suffering from Wolff-Parkinson-White (WPW) syndrome and for localizing the site of origin of idiopathic ventricular tachycardia (VT)

- to simulate a data base of body surface potential distributions for ectopic activation sequences initiated at endocardial sites on a regular reference grid and compare those that have such a counterpart to the body surface potential distributions actually recorded during paced activation sequences in patients

The construction of an anatomically accurate model of the human ventricular myocardium is described in Chapter 2. Chapter 3 outlines the simulation of propagated excitation in the anisotropic myocardium. Epicardial potential distributions of simulated ectopic ventricular activation are presented in Chapters 4 and 5. Chapter 6 presents simulated body surface potential distributions corresponding to pathological conditions of ventricular preexcitation in WPW syndrome and of ectopic activation in VT in the structurally normal heart. Chapter 7 contains a general discussion and conclusions. Appendix A summarizes functions used in simulating propagated excitation in the anisotropic myocardium. Appendix B presents the results of an auxiliary study on the effect of volume conductor boundaries on epicardial and body surface potential distributions. The simulated magnetic field distributions for initial activation sites in idiopathic VT are shown in Appendix C.

Chapter 2

Model of the ventricular geometry and fibrous structure

2.1 Introduction

The human ventricular myocardium is a complex structure that consists of interconnected cardiac muscle cells (myocytes), which resemble cylinders with a diameter of 10 to 20 μm and a length of 80 to 100 μm . Hoyt et al. [158], among others, observed that the individual cardiac cells form more end-to-end (longitudinal) connections than side-to-side (transverse) connections. As a result, the orientation of cardiac muscle cells at any point within the myocardium can be macroscopically described in terms of a local principal fiber direction. (*Principal fiber direction* is an abstraction, referring to an average direction of a number of cardiac muscle cells, rather than to an anatomical entity.)

The global distribution of fibers over the ventricular myocardium has a typical spiral arrangement from the apex to the base, with a transmural counterclockwise (CCW) rotation of fibers from the epicardial to the endocardial surface. It is well established that the myocardium is electrically anisotropic; that is, it has higher

conductivity along than across the principal fiber direction [44, 59, 79, 322]. Consequently, the ventricles' fibrous architecture profoundly affects their function because it determines the primary course of electrical excitation. Anatomically accurate reconstruction of both the ventricles' geometry and their fibrous structure is therefore a prerequisite for an adequate quantitative modeling of ventricular function.

Early ventricular models generally did not take into account the anisotropic fibrous structure and included only the left ventricle; they were based on simplified, axisymmetrical geometric shapes, such as spheres, spheroids, ellipsoids, truncated spheroids, and axisymmetric finite element models [73, 125, 173, 202, 240, 243, 366, 417]. In more recent models, however, much effort has been devoted to the nonaxisymmetric representation of the left ventricle [110, 236, 428] or to the realistic reconstruction of both the left ventricle (LV) and the right ventricle (RV) using different imaging modalities [62, 113] or more conventional anatomical techniques [171, 429]. Some of the realistic models also included stylized fiber architecture [218, 257, 401]. However, the simplifying assumptions used in the reconstruction of ventricular geometry and/or fibrous structure severely restrict the usefulness of such models.

2.1.1 Fiber architecture of ventricular myocardium

Although the general features of the fiber architecture of human ventricles have been recognized for over three centuries [220, 222], it was not until the late 1950s that the effort was made to assess ventricular fiber orientation quantitatively [157, 381]. A review of early studies of fiber architecture in the human heart is in Greenbaum et al. [127] and Streeter [364].

Streeter and Bassett [365] and Streeter et al. [368] measured the fiber orientation

within the LV wall in porcine and canine hearts. They observed the smooth CCW rotation by approximately 100° or more of fibers through the wall. They also reported that while the transmural rotation was linear near the apical and middle levels of the ventricles, near the base, it was more rapid in subepicardial and subendocardial layers than in the midwall. Based on these measurements, Streeter [364] proposed a quantitative model of the fiber architecture in which the fibers run uniformly at -58° on the epicardial surface, clockwise (CW) relative to the basal plane when the epicardium is viewed from the outside, and at 42° on the endocardial surface. This model was only the first approximation of Streeter's own measurements that have shown significant local variation in the fiber orientation over, for example, epicardial or endocardial surfaces.

Armour and Randall [11] studied the fiber architecture in 9 mammalian species and found little variability among them. The important conclusion of their study was the observation that although fiber direction changed smoothly through the myocardial wall (compacta), it changed abruptly at the border between the compacta and the endocardial layer consisting of trabecular tissue and papillary muscle (trabeculata). These authors noted that the fibers in trabeculata were running predominantly in the apico-basal direction. Similar observations were made by Ross and Streeter [309] in macaque left ventricles. However, at variance with the earlier work of Streeter et al. [368], Ross and Streeter observed a linear variation of fiber angle through the compacta.

Greenbaum et al. [127] examined 25 *post mortem* human hearts. Their study confirmed previous reports of local variation in the fiber direction over epicardial and

endocardial surfaces. In addition, they also measured the fiber angles in the RV free wall. The major limitation of their study is that the transmural fiber orientation was sampled only at five LV sites, two RV sites, and a single septal site. McLean et al. [235] provided a more complete 3-D description of the ventricular myocardium of prenatal and neonatal mice by performing measurements of fiber orientation in serial transverse and longitudinal cross sections; however, no 3-D model of the ventricles based on their measurements was constructed.

Recently, Nielsen [261] and Nielsen et al. [262] developed a compact mathematical model of the entire canine ventricular myocardium that is based on the finite element method [432]. The model consists of 60 bicubic Hermite elements defined by 117 nodes, each of which is specified in the prolate-spheroidal coordinate system. A combination of linear and cubic Hermite polynomials subjected to parameterized boundary conditions at the nodes are used as the basis interpolation functions to determine the local fiber direction inside each of the 60 elements. The nodal parameters of the model are based on accurate and systematic measurements of the fiber orientation (at over 12,000 points) throughout the biventricular myocardium of the canine heart. Their study thus provides the most comprehensive and accurate description of the canine fibrous ventricular architecture to date. However, since this model was primarily developed for studies of the mechanical function of the ventricles (e.g., the estimation of stress distribution within the ventricular wall), the emphasis was on reducing the number of parameters describing the model. As a result, the geometry of the model is idealized—lacking sufficient detail in certain parts of the ventricles that are important for high-resolution modeling of ventricular electrical activation (such

as the LV endocardium, the right ventricle, and the apical part of both ventricles).

2.1.2 Approach to constructing a ventricular model

Due to the absence of accurate measurements of local fiber orientation in *human* ventricular myocardium, we have adopted for our purposes the *canine* model of ventricular myocardium constructed by Nielsen et al. [262]. This task proved to be very difficult because the human and canine ventricles both are topologically highly complex objects, and because an appropriate one-to-one mapping of fiber orientation, which forms a three-dimensional vector field, requires the matching of two complex volumetric structures encoded in the canine and human ventricular models.

One possible approach to solving this problem is to reconstruct “principal” surfaces that enclose the volume occupied by the ventricular myocardium (i.e., the basal plane, the epicardial surface, and the surfaces of the LV and RV cavities) from digitized anatomical data and then—by an appropriate matching of the corresponding principal surfaces in both models—to assign fiber orientations on these surfaces. The intramural fibrous structure can then be specified as a function of the fiber direction on the principal surfaces. Implementing this approach depends on an efficient reconstruction of the principal surfaces.

There are two general approaches to the mathematical reconstruction of a 3-D surface: 1) an interpolation, which describes the surface locally [43, 422] and 2) a comprehensive representation, which describes the surface globally with a relatively small number of parameters [343, 358]. The former approach, having many degrees of freedom, can reconstruct local deformations with high accuracy, while the latter causes smoothing of local deformations but imposes more organization on the

data. The specific application usually dictates the choice of the particular reconstruction technique. As the observations reviewed above have indicated, the ventricular myocardium is composed of two distinct substructures: compacta, whose fibrous structure is highly organized and characterized by pronounced local changes in fiber direction and trabeculata, whose fibrous structure is organized in a more uniform manner and is independent of the organization in the compacta. In addition, the compacta is enclosed by irregular but relatively smooth surfaces, while the surfaces of trabeculata are considerably more complex.

We wanted to reconstruct the fibrous architecture within the compacta very accurately; therefore, we represented the relatively smooth surfaces enclosing the compacta by means of the global parameterized model. In this way, we created the suitable reference frame for mapping between the canine and human models and for determining the intramural fibrous structure from the known distributions of fiber direction on the principal surfaces. Since in the trabeculata the fiber organization is significantly simpler but the surfaces are more complex, we decided to use local representation of endocardial surfaces based on the interpolation of digitized data. Both types of representation—the global and local—were hierarchically organized.

The surface harmonic expansion offers a complete description of irregularly shaped surfaces in a mathematically compact and continuous form (see, e.g., [162]). Accordingly, we used it as the basis for the representation of the fiber architecture in the compacta, with the aim of reconstructing the ventricular structure at the submillimeter (0.5-mm) level—thereby achieving the maximal spatial resolution that is practical with our computational resources.

2.2 Surface harmonic expansion

A given ventricular surface can be described by a vector function $\mathbf{X}(\theta, \phi)$

$$\mathbf{X}(\theta, \phi) = \mathbf{X}_0 + r(\theta, \phi) \begin{pmatrix} \cos \phi \sin \theta \\ \sin \phi \sin \theta \\ \cos \theta \end{pmatrix}, \quad (2.1)$$

where \mathbf{X}_0 is the origin of the expansion and the angles θ and ϕ are defined relative to this origin as shown in Fig. 2.1. (Our global right-handed Cartesian coordinate system has its origin at the LV apex, with x axis pointing from the RV to the LV, y axis from anterior to posterior, and z axis from the apex to the base. The z axis coincides with the anatomical axis of the human ventricles as defined by Durrer et al. [84], i.e., connecting the LV apex and the root of aorta.) An arbitrary single-valued function, which satisfies Laplace's equation, can be expanded in an absolutely convergent series of surface harmonics on the surface of a sphere (for applications in potential theory, see [186, 231, 362]). Hence, the radial coordinate $r(\theta, \phi)$ of a point on a nonspherical surface (e.g., the epicardium or endocardium), being a single-valued function of θ and ϕ , can be represented by the surface harmonic expansion

$$r(\theta, \phi) = \sum_{n=0}^{\infty} \left\{ a_n P_n(\cos \theta) + \sum_{m=1}^n (a_{nm} \cos m\phi + b_{nm} \sin m\phi) P_n^m(\cos \theta) \right\}, \quad (2.2)$$

for $0 \leq \theta \leq \pi$ and $0 \leq \phi \leq 2\pi$. P_n is the Legendre function of degree n of the first kind, and P_n^m is the associated Legendre function, of degree n and order m , of the first kind [231].

For the purposes of numerical calculation, the series is truncated at N terms. The chosen ventricular surface is thus uniquely determined by the origin of the expansion $\mathbf{X}_0 = (x_0, y_0, z_0)$ and the vector of the expansion coefficients $\mathbf{a} = \{\mathbf{a}_n, \mathbf{a}_{nm}, \mathbf{b}_{nm}\}$. The total number of parameters, including the origin of the expansion, is $(N+1)^2+3$. Once

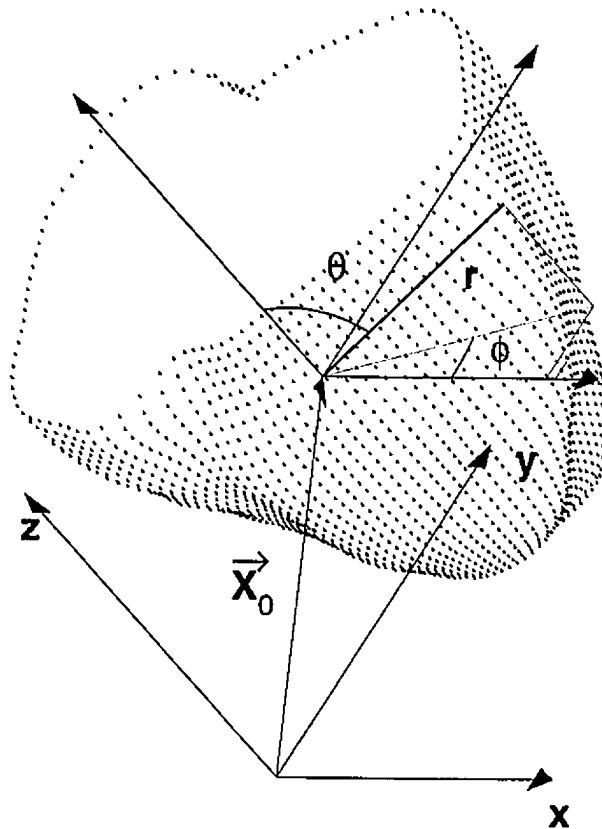


Figure 2.1: Coordinate system for surface harmonic expansion. The surface is uniquely determined by the origin of the expansion $\mathbf{X}_0 = (x_0, y_0, z_0)$ and the expansion coefficients $\mathbf{a} = \{\mathbf{a}_n, \mathbf{a}_{nm}, \mathbf{b}_{nm}\}$.

the given ventricular surface is sampled at specific points, which can be obtained by the standard tomographic modalities (MRI or X-ray CAT) or conventional anatomical techniques (examination of the excised hearts), the coefficients of the series can be determined by means of a least-squares fitting procedure [293].

For a given set of measured surface coordinates $\mathbf{X}_i = (x_i, y_i, z_i)$, $i = 1, 2, \dots, N_p$, where N_p is the number of measurements, the desired parameters (i.e., the origin and

the coefficients in Eq. 2.1) can be obtained by minimizing the quantity

$$\sigma^2(\mathbf{X}_0, \mathbf{a}) = \sum_{i=1}^{N_p} |\mathbf{X}_i - \mathbf{X}(\theta_i, \phi_i)|^2. \quad (2.3)$$

The spherical polar angles θ_i and ϕ_i (Fig. 2.1) are given by

$$\theta_i = \arctan \frac{\sqrt{(x_i - x_0)^2 + (y_i - y_0)^2}}{z_i - z_0}, \quad (2.4)$$

$$\phi_i = \arctan \frac{y_i - y_0}{x_i - x_0}. \quad (2.5)$$

It follows from the definitions of θ_i and ϕ_i that the model function given in Eq. 2.1 depends nonlinearly on the origin of the expansion \mathbf{X}_0 and linearly on the expansion coefficients \mathbf{a}_n , \mathbf{a}_{nm} and \mathbf{b}_{nm} . The nonlinear fitting of the parameters in the model function (Eq. 2.1) was performed using a Levenberg-Marquardt algorithm [233], which requires derivatives of σ^2 with respect to the parameters \mathbf{X}_0 and \mathbf{a} to guide the minimization of the squared residual between sampled and computed data. The derivatives have been presented in full elsewhere [159].

Once the parameters \mathbf{X}_0 and \mathbf{a} are evaluated, the ventricular surface can be readily reconstructed by predetermining a grid of θ and ϕ values and then calculating the x, y, z coordinates of points on the ventricular surface. If the transaxial cross section through the reconstructed surface is required at a given level above the LV apex, the z coordinate corresponding to this level and a set of ϕ values are preassigned; the minimization methods (e.g., a golden-section search or Brent's method) [293] are then used to minimize the absolute value of the difference with respect to the spherical angle θ between the preassigned value of the z coordinate and the value of the z coordinate calculated using the surface harmonic expansion. (Sagittal or

any oblique cross section can be reconstructed in an analogous manner.) An important feature of the surface harmonic expansion method is that it can reconstruct the x, y, z coordinates with any required resolution. This is particularly advantageous when constructing the finite difference or cellular automaton models of the ventricular structure. In addition, the surface harmonic expansion model describes the overall shape of the particular ventricular surface even if some areas of the ventricles are inadequately digitized. The lack of local information affects a continuously defined and robust global representation only to a very minor degree. Furthermore, truncating a series of surface harmonics at a specific order of approximation controls the degree of smoothing of the digitized data. Using this method, one can, therefore, smoothly fit the given surface features to any required degree of accuracy by choosing the number of parameters that characterize them. Finally, both the tangential ($\partial\mathbf{X}/\partial\theta$ and $\partial\mathbf{X}/\partial\phi$) and normal ($\partial\mathbf{X}/\partial\theta \times \partial\mathbf{X}/\partial\phi$) vectors can be derived directly from Eq. 2.1, which is convenient for defining the tangential plane at a point on the ventricular surface.

2.3 Construction of a ventricular model

2.3.1 Modeling strategy

The basic premise of our approach was that the myocardium can be subdivided into two distinct anatomical regions: compacta and trabeculata. The volume occupied by compacta is bounded by four relatively smooth principal surfaces: 1) an epicardial surface separating the excitable ventricular myocardium from the surrounding volume conductor; 2) a surface separating the compacta from trabeculata or intracavitary

blood masses in the LV; 3) a surface separating the compacta from trabeculata or intracavitary blood masses in the RV; 4) a basal plane oriented perpendicularly to the long axis of the ventricles at the level of the mitral valve.

In representing the ventricular surfaces by means of the surface harmonic expansion method, it is essential that one separates the features of the fibrous structure that are defined by the geometry of the principal surfaces from those that are specified only by the fibers' local characteristics. This separation presented the underlying basis for mapping the fibrous structure between irregularly shaped principal surfaces of the canine and human models; namely, the deformation of principal surfaces was allowed when transforming one model into the other, but the fibers' local characteristics of the canine ventricular model were retained.

In practice, such a separation can be readily accomplished since the fiber direction at any point in the myocardium is completely determined by three parameters: two spherical angles ζ and η which specify the local plane that is tangential to the surface in the global coordinate system, and an additional local angle α which defines the fiber rotation within the tangential plane in the local coordinate system (Fig. 2.2). (Note that spherical angles ζ and η specify the normal to the tangential plane and that angles θ and ϕ determine the location of the surface point; only in the special case of a spherically symmetric body do $\zeta = \theta$ and $\eta = \phi$.) The normal and tangential vectors to the surface were evaluated by the surface harmonic expansion, and these vectors then formed the local basis for the assignment of fiber orientation at any point in the ventricular myocardium. The implicit assumption of such an approach—that the fibers are constrained to lie tangentially to the ventricular surfaces—is supported

by the experimental evidence that within small “imbrication” angles ($< 3^\circ$), the fibers actually follow the ventricular surfaces [367].

The separation of global fibrous architecture into the geometry of its local bases (characterized by angles ζ and η) and the local fiber characteristics (angle α) within these local bases provided an efficient vehicle for our purposes. However, to establish the point-to-point correspondence between the canine and human models, we required additional global anatomical constraints, or reference points. We used as such anatomical landmarks of the ventricles (the apex, papillary muscles, and ventricular sulci), points that are easy to identify yet comprehensively describe the irregularly shaped principal surfaces and thus anchor the transformation without significant distortions of the fibrous structure.

2.3.2 Model generation

Our reconstruction of the human ventricular architecture can be described in several steps which were organized in such a fashion that every subsequent step incorporated more detail into the model without affecting the results of the preceding steps. The first step was to accurately define and reconstruct the principal surfaces in which the fibers were constrained to lie. The second step—which concluded the construction of the geometrical frame for the assignment of local fiber rotation—was to identify the tangential planes in the volume bounded by these surfaces. The third step was to assign the angle of fiber rotation α over the reconstructed principal ventricular surfaces in the model of the human ventricular myocardium accordingly to the corresponding angle α on the principal surfaces in the canine ventricular model. The fourth step was to define the angle α as the function of depth (wall thickness) in consecutive

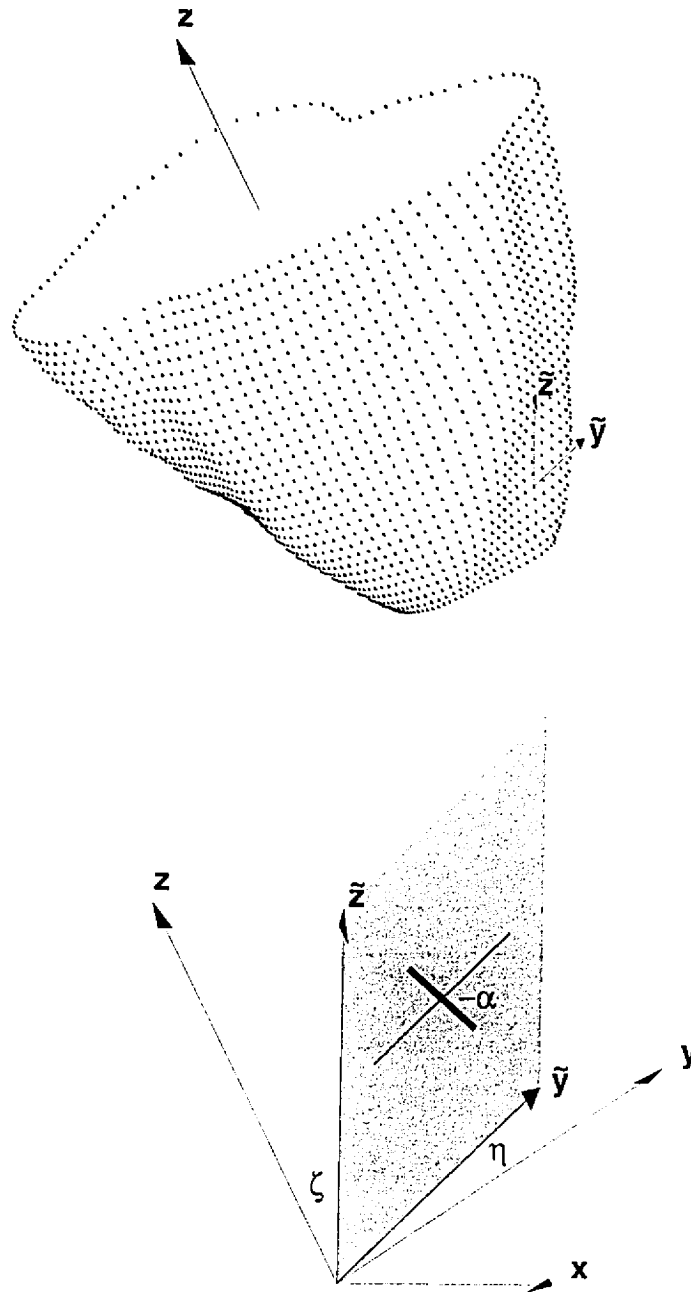


Figure 2.2: The vector of the local principal fiber direction. This vector lies in the tangential plane defined by the spherical polar angles ζ and η in the global coordinate system (x, y, z) ; the angle α determines the fiber rotation within the tangential plane in the local coordinate system $(\tilde{x}, \tilde{y}, \tilde{z})$.

layers between the principal surfaces. (The purpose of the latter two steps was to assign the local fiber direction to the local bases of geometrical frame.) The final step was to add the trabeculata to the model. Each of these steps will be now discussed in more detail.

Step 1: Assignment of principal surfaces. After the geometry of the principal ventricular surfaces had been digitized with an adequate number of data points, the sets of surface harmonic expansion parameters \mathbf{X}_0 and \mathbf{a} were evaluated (as described in Section 2.2) separately for each principal ventricular surface. Next, the reconstruction of the surfaces was performed on a $d \times d \times d$ grid, where d designated the dimension of each volume element (voxel). The grid position of each voxel was identified by three integer indices (i, j, k) , with the range of the indices being determined by the size of the epicardial surface and the required resolution (range $>$ size/resolution). In this representation, the 3-D principal surfaces were considered as shells in the voxel representation; each voxel was allocated a byte in the memory storage, and it was assigned a flag to identify which principal surface it was on.

To create the myocardial volume—defined completely by the basal plane and the principal surfaces—the latter were reconstructed up to the basal plane level. This enhanced the control and compact representation of the volume, but it required some additional “ghost” voxels near the base of the ventricles that did not correspond to the actual myocardium and that had to be removed from the final model.

The normals to the principal surfaces were analytically calculated at the center of each voxel, thereby locally defining the tangential plane to the surface. To save memory, the normal to this plane at each voxel was identified by the spherical angles

ζ and η and stored in a byte format, with the angle ζ mapped into a byte as 0 to 127 and the angle η as -127 to 127 .

Step 2: Assignment of tangential planes for intramural voxels. First, to establish the solid structure that represents the ventricular myocardium, we had to identify the intramural voxels between principal surfaces by means of a raster-filling algorithm. A potential ambiguity in defining the tangential planes for the intramural voxels arises because the bounding surfaces are irregularly shaped. Instead of reconstructing the tangential sheets (i.e., “onion layers”) by the surface harmonic expansion—which would have been the ultimate, but not quite feasible, method—we chose to assign the spherical angles ζ and η of each voxel on the principal surface to the myocardial voxels intersected by the local normal to that surface. The drawback of this relatively simple approach was that the reconstructed epicardial and endocardial surfaces, though relatively smooth in general, change locally from a convex to a concave shape and *vice versa*. This may cause local variation in the principal surface shape to propagate into deeper layers of the myocardium, and the algorithm may not necessarily reconstruct the tangential planes within the myocardium realistically. Thus we calculated—specifically for this task—normals on the principal surfaces by using lower-order harmonics to attain globally smoother principal surfaces. Then we proceeded iteratively—with every subsequent iteration propagating deeper into the wall simultaneously from the endocardial and epicardial surfaces—along the normal direction derived from the progressively lower-order fit by the surface harmonic expansion to the principal surface. Since the change of the normal direction specifying the given “normal” path depended on the initial voxel of the given principal surface,

all voxels processed along the given path were coded so that every myocardial voxel corresponded to only a single voxel on the principal surface. The described algorithm is analogous to a solution—known from graph theory [136]—to the problem of finding the shortest path between the given voxel on the endocardial surface and the epicardial surface.

Step 3: Assignment of fiber direction on the principal surfaces. The key procedure in this step was to map the distribution of the fiber angles α over the principal surfaces of the canine ventricular model onto the principal surfaces of the human model. To make such a transformation between the irregularly shaped surfaces tractable, we selected seven anatomical reference points: 1) the LV epicardial apex, 2) the LV endocardial apex, 3) the RV epicardial apex, 4) the LV anterior papillary muscle, 5) the pulmonary outflow tract, 6) the anterior ventricular sulcus, and 7) the posterior ventricular sulcus.

The transformation between the principal surfaces of the two ventricular models was approximated by successively scaling the canine model, first along the long axis of the ventricles and then in each of the short-axis slices. Scaling along the long axis was performed piecewise: the two ventricular models were subdivided into four vertical sectors by the first five of the anatomical landmarks listed above, then the height of each sector in the canine model was scaled to match the height of the corresponding sector of the human model. Scaling in the short-axis slices was carried out by matching the axial (angular) positions in the two models of the ventricular sulci relative to the geometric center of each slice of the given principal surface. (Scaling in the short-axis slices by matching the length of the contours formed by the

two sulci gave similar results.)

It should be noted that since the canine model was defined by only 60 elements and 117 nodes, the transformation generating the voxel-based model of the ventricles required interpolation between the nodes. The resolution d' of the canine model necessary for there to be a one-to-one correspondence between the voxels of the principal surfaces in both models was a function of scaling factors along the long axis. Finally, the angle α for each voxel was mapped into a byte as -127 to 127 in the same manner as spherical angles.

Step 4: Assignment of intramural fiber direction. Once the fiber orientation had been completely specified (by ζ , η , and α) in the voxels on the principal surfaces, the angle α could be assigned to intramural voxels. To accomplish that, we assumed that the transmural fiber rotation between the principal ventricular surfaces could be described by the mathematically smooth analytical function $\alpha = f_{ijk}(\mu, e)$, where e corresponds to the wall thickness. The parameter e was evaluated as follows. The endocardial voxel identified by the indices (i, j, k) represented the origin of a piecewise-linear path μ that was defined along the vectors normal to the local tangential planes lying between the endocardial and epicardial voxels; the distance e between these two voxels and measured along the path μ represented the local wall thickness. Since the epicardium and endocardium are irregularly shaped, the distance e varied through the ventricles and was a function of the starting endocardial voxel determined by the grid coordinates i, j, k . The function f of transmural rotation can vary for different regions of the ventricles, if required.

Once the function f had been chosen and the distances e had been evaluated

for each intramural voxel, the angles α were assigned to intramural voxels along the path μ . However, since there were fewer voxels on the endocardial surface than on the epicardial surface, some intramural voxels were not processed by the algorithm. To determine the angle α in these voxels, the algorithm was applied in the reverse direction, starting from the epicardium.

Step 5: Incorporation of trabeculata. The main problem caused by the inclusion of trabeculata into the model is that considerable subject-to-subject variability is known to exist in this part of the ventricular myocardium. For this reason, we used a more heuristic approach in assigning fiber direction to voxels of the trabeculata than we did to those of the compacta.

The bounding surfaces of the trabeculata on the interface with the intracavitary blood masses can have very complex shapes and, because points on such surfaces may not be uniquely determined by the spherical angles θ and ϕ , the surface harmonic expansion method is not applicable. To describe the geometry of trabeculata in detail, but still using a reasonably simple procedure, we reconstructed these surfaces using the bilinear interpolation of data obtained by digitizing anatomical sections.

The tangential planes in the trabecular voxels were assigned by the algorithm propagating into the trabeculata along the directions determined by normals on the principal (LV endocardial, RV endocardial, and RV septal) surfaces. The tangential planes thus defined may differ from the actual tangential planes of the voxels lining the RV and LV cavities. However, since the fibers in the trabeculata are oriented primarily in the apico-basal direction, the resulting imbrication angle should be small.

The fiber rotation angle α of the trabecular voxels of the LV cavity was assigned,

as in Step 3, by the axial matching of canine and human ventricular models. All trabecular voxels with the same axial coordinate were given the same value of α . Since such an assignment of the fiber rotation angles creates discontinuity at the junction between the compacta and trabeculata, the nearest-neighbor interpolation along the local normals was performed for the trabecular voxels positioned adjacent to the junction. This matching of the canine and human ventricular models was a loose one, however, because the trabecular surface was much more detailed in the human than in the canine model. Since the trabecular structures (e.g., the *trabecula septomarginalis*) were largely excluded from the reconstruction of the RV in the canine model, the fiber rotation angle α was assumed to be 90° throughout the RV trabeculata. Again, to ensure the continuous rotation of α at the interface between compacta and trabeculata, the nearest-neighbor interpolation along the local normals was carried out.

2.4 Implementation of the ventricular model

The techniques for assigning fiber direction to the ventricular model's voxels, described in Section 2.3, were applied to anatomical data obtained from an excised structurally normal human heart. The procedures involved in preparing an anatomical specimen of the human heart have been described in detail elsewhere [86]. Briefly, the heart was positioned as in the thorax and sectioned transaxially at 1-mm slices; next, the boundary lines of the ventricular myocardium were carefully identified. In addition, the border between the compacta and trabeculata was determined by visual inspection. The digitized data were then rotated into the coordinate system,

Table 2.1: Fit of Principal Surfaces by Surface Harmonic Expansion

N	rms Error [mm]				Maximum Error [mm]			
	EP	LE	SP	RE	EP	LE	SP	RE
0	4.46	4.27	3.89	4.35	12.28	12.49	10.78	11.97
4	1.63	1.16	0.93	1.79	6.43	6.54	5.65	6.72
8	0.87	0.69	0.68	1.02	4.30	3.90	3.88	4.90
12	0.63	0.52	0.50	0.69	3.33	3.48	2.99	3.34
16	0.54	0.47	0.43	0.55	3.01	3.04	2.59	3.02
20	0.47	0.41	0.38	0.48	2.86	2.64	2.45	2.94

N , order of approximation

EP, epicardial surface

LE, LV endocardial surface

SP, RV septal surface

RE, RV free-wall endocardial surface

with the z axis coinciding with the ventricular long axis—defined as in Durrer et al. [84], i.e., passing through the LV apex and the root of aorta—and origin at the LV apex. The epicardial, LV endocardial, RV septal, and RV free-wall endocardial surfaces were represented by, respectively, 16872, 7310, 4348, and 3926 nonequidistantly distributed data points (x_i, y_i, z_i) .

The surface harmonic expansion method was then used to reconstruct the principal surfaces from these anatomical data. A separate set of parameters, including the origin of the expansion and the expansion coefficients, was evaluated for each principal surface. The accuracy of the approximation of the principal surfaces was quantitatively assessed by the root-mean-square (rms) error. Table 2.1 shows the change of the rms error and maximum error with the order of approximation N for the epicardial, LV endocardial, RV septal, and RV free-wall endocardial surfaces. The rms error decreased rapidly with the increasing number of lower-order harmonics, but

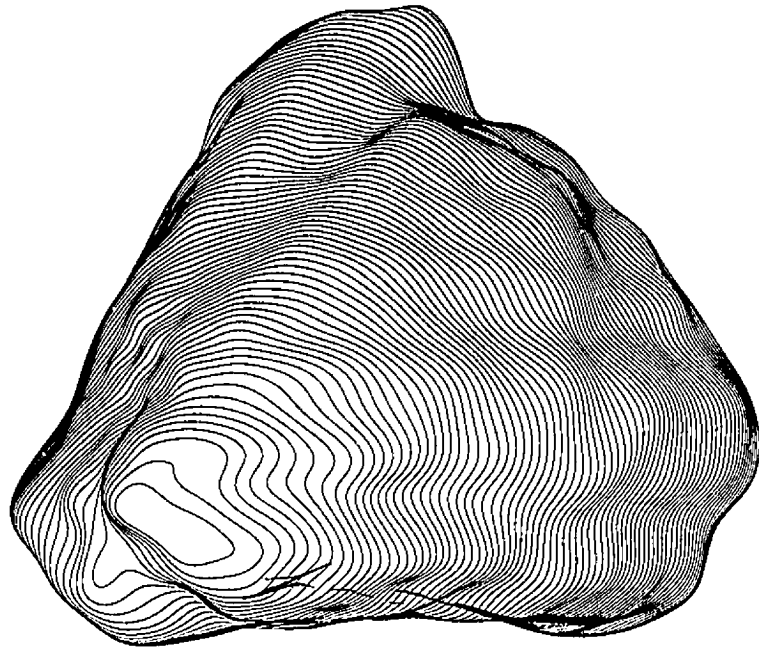
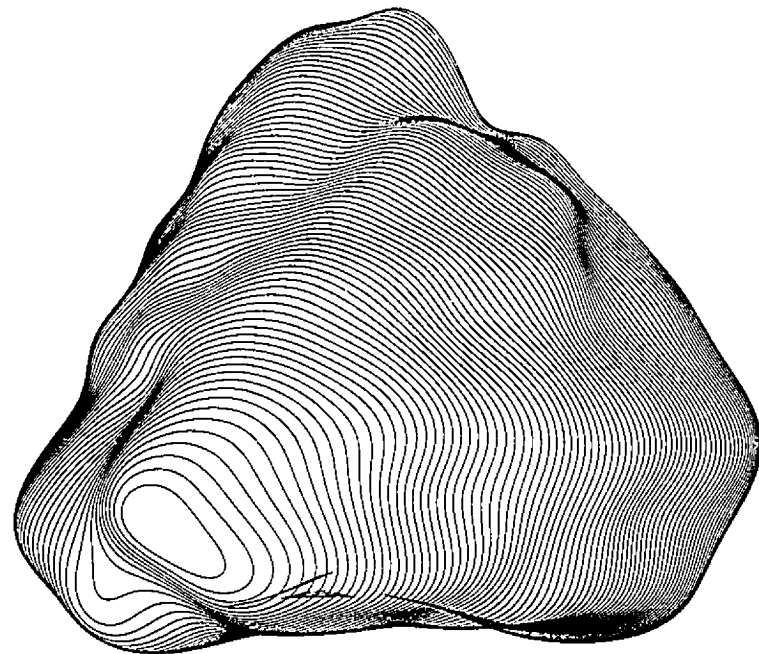
A**B**

Figure 2.3: The epicardial surface described by means of surface harmonic expansion for orders of expansion $N = 20$ (A) and $N = 12$ (B). Note that despite the smoothness of the solutions, the epicardial surface is reconstructed in considerable detail, with more local information included when higher-order harmonics are employed.

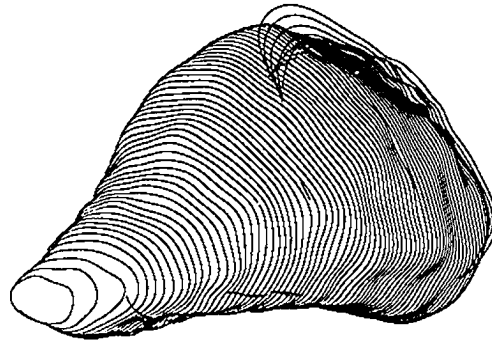


Figure 2.4: The LV endocardial surface described by means of surface harmonic expansion. The order of expansion $N = 16$.

this decrease eventually slowed down for higher-order harmonics ($N > 16$). There was almost no improvement in the solution (improvement in the rms error < 0.1 mm) beyond $N = 24$. With $N = 16$ or $N = 20$ (292 or 423 parameters, respectively), each surface could be described with an rms error < 0.5 mm; this error was acceptable for a model with a spatial resolution of 0.5 mm. The fidelity of the surface reconstruction was visually verified when a large number of nodes were generated to represent the surface. Examples of the reconstructed epicardial and LV endocardial surfaces are shown in Figs. 2.3 and 2.4. The maximum error (ranging in all ventricular surfaces between 2.4 mm and 2.9 mm) occurred near the base of the ventricles. The maximum errors in the apical to midbasal part of the principal surfaces were < 1 mm in all cases.

The representation of the principal surfaces by voxels and the construction of local tangential planes at each voxel was performed as outlined in Step 1 above. The resolution of the model was 0.5 mm, so the volume of each voxel was 0.125 mm^3 . During

the construction of the model, the voxels were stored in a $220 \times 220 \times 220$ cube to accommodate the entire ventricular structure with the LV apex positioned at the voxel with integer coordinates (110,110,1). The reconstruction of the principal surfaces was performed for z coordinates ranging between 0 mm and 85 mm above the LV apex. The most basal part of the ventricles was represented separately using an approach that is to be described below. The reconstructed epicardial, LV endocardial, RV septal, and RV free-wall endocardial surfaces consisted of, respectively, 106971, 46340, 23883, and 23903 voxels. The voxels on the epicardium were distinguished as RV and LV according to their location relative to the anterior and posterior ventricular sulci; 60088 voxels represented the LV epicardium and 46883 voxels represented the RV epicardium. The boundaries of the principal surfaces taken in short-axis sections are shown in Fig. 2.5.

As described in Step 2 above, the tangential planes were defined separately for the voxels enclosed by the RV septal, LV epicardial, and LV endocardial surfaces and for the voxels enclosed by the RV epicardial and RV free-wall endocardial surfaces. Consequently—and in agreement with the qualitative observations of Fox et al. [99] and quantitative measurements performed by Nielsen et al. [262]—a discontinuous change in the tangential plane normals occurred at the junction between the deeper myocardial layers of the RV and the septum.

The transformation between the principal surfaces of the canine and human ventricular models was accomplished according to an algorithm detailed as Step 3 in Section 2.3. Figs. 2.6 through 2.8 show the anterior, posterior, and apical views of the human ventricular model, and reveal a pronounced local variation in the fiber

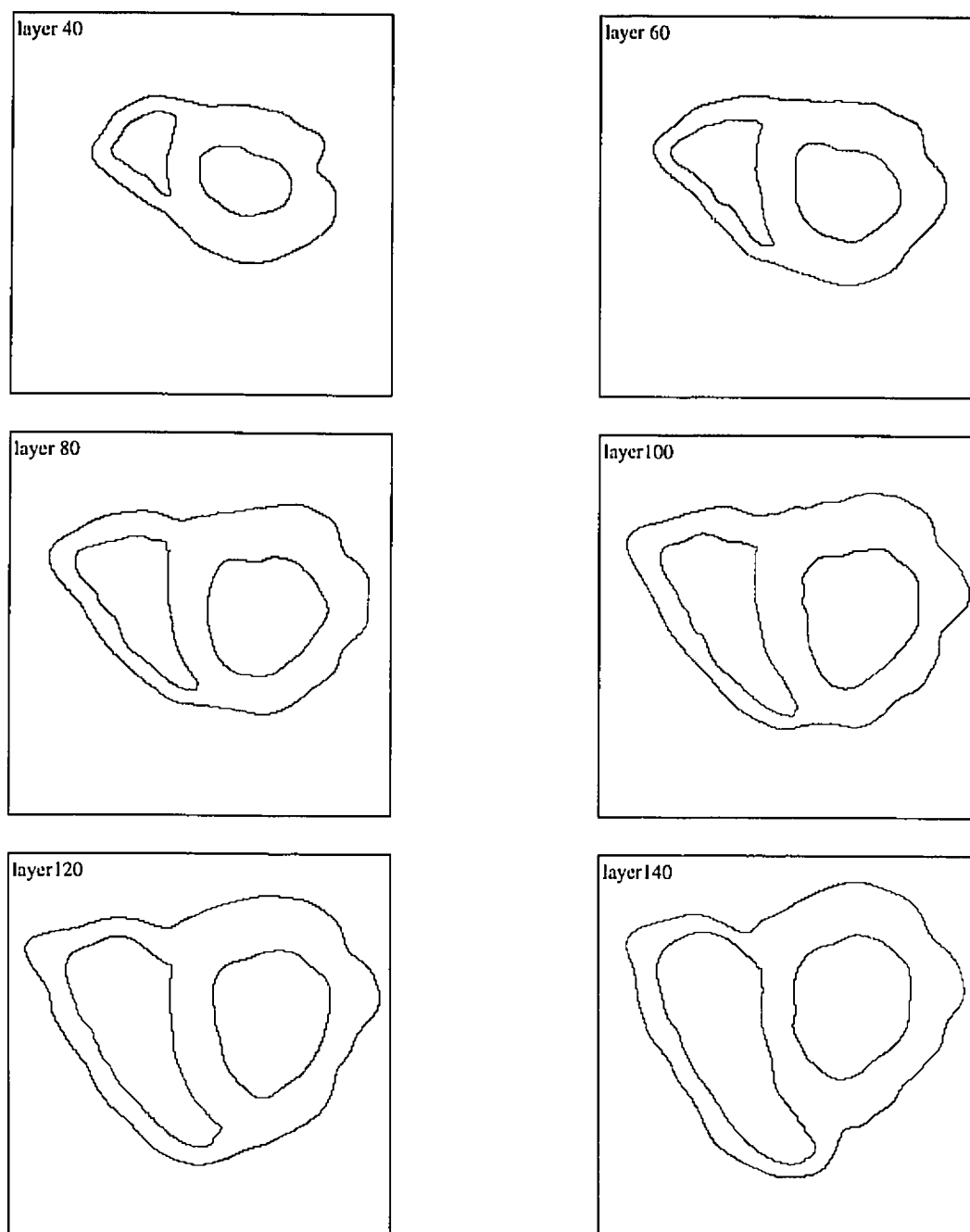


Figure 2.5: Slices through the principal surfaces of the human ventricular model. Each slice shows the borders of voxels that represent principal surfaces at $z = \text{const.}$; the six layers shown are at 20, 30, 40, 50, 60, and 70 mm above the LV apex.

orientation over the epicardial surface.

The key factor in Step 4 was making an appropriate choice for the fiber rotation function f . Unfortunately, there is no consensus regarding the course of intramural fiber rotation in human ventricles. Ross and Streeter [309] and Nielsen [261] found that the transmural change in the fiber angle was linear throughout the ventricles in macaque and dog hearts, respectively. This conclusion is in variance with those in studies performed by Streeter et al. [368], Armour and Randall [11], and Nielsen et al. [262], who observed that in the midbasal to basal region, the change in the fiber rotation of intramural fibers was smaller than that of those near the epicardium and endocardium but that for the rest of ventricular myocardium, the fiber rotation from the epicardium to endocardium was linear. No quantitative study of the intramural fiber rotation in the ventricles of human hearts has as yet been reported. For these reasons, in the construction of the present model, the linear function f was assigned for changes of the angle α in all intramural voxels.

The incorporation of trabeculata was carried out as specified in Step 5. We had to make additional refinements of the model, particularly when reconstructing the ridge-like structure of the basal part of the ventricles, which consists of the mitral, aortic, and pulmonary conus and has a complex shape. We therefore determined the myocardial elements from 85 mm to 91 mm above the LV apex by interpolating digitized data (Fig. 2.9); the space between the contours was filled with voxels using a similar algorithm to the one used in Step 1. This procedure generated 9833 voxels representing the basal portion of myocardial volume. Defining the angles η , ζ , and α in these voxels required special attention. However, since the number of voxels in this

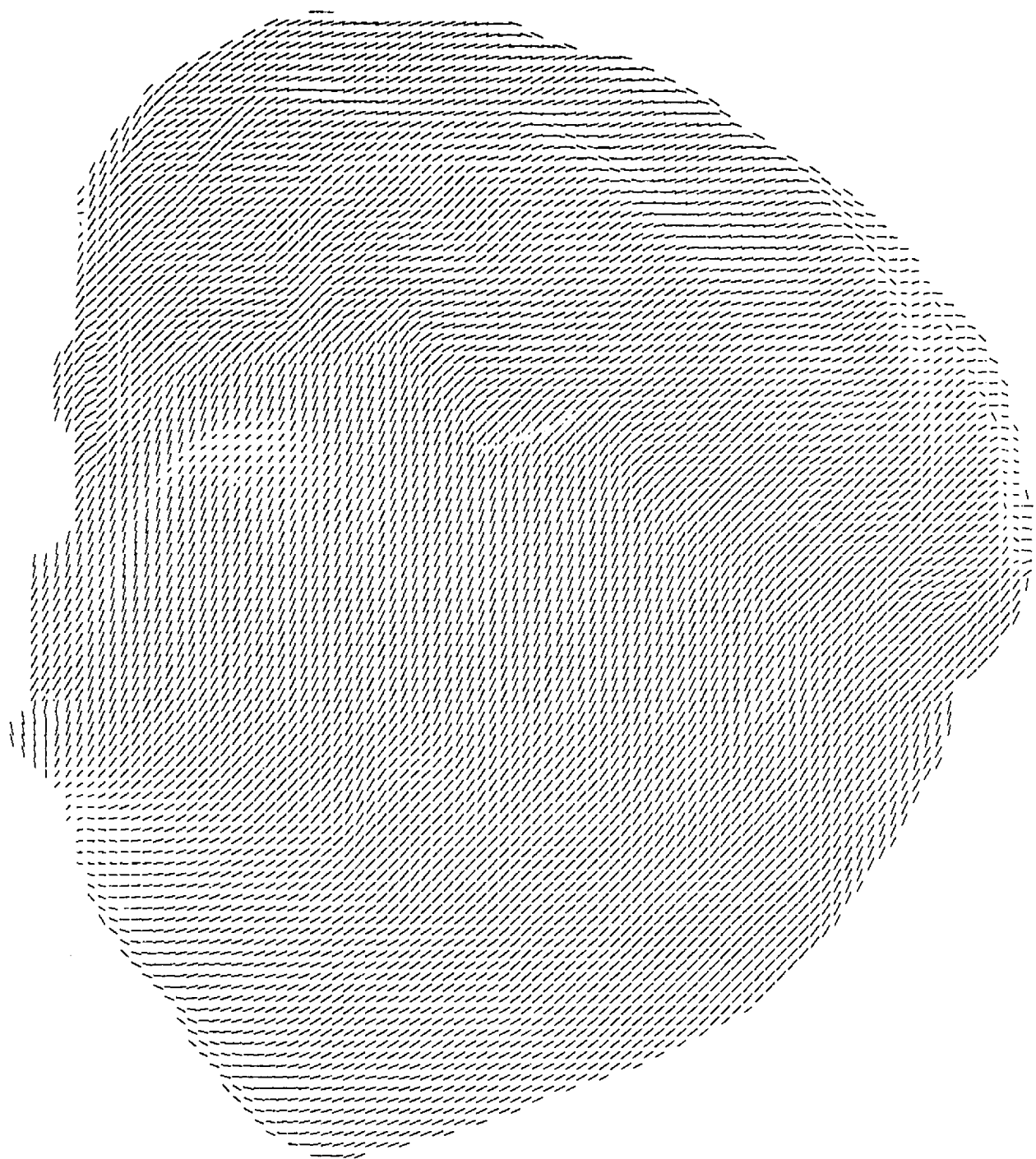


Figure 2.6: Anterior view of the model of the human ventricular myocardium. To make the display clearer, the fiber direction is shown only in every second voxel along each axis.

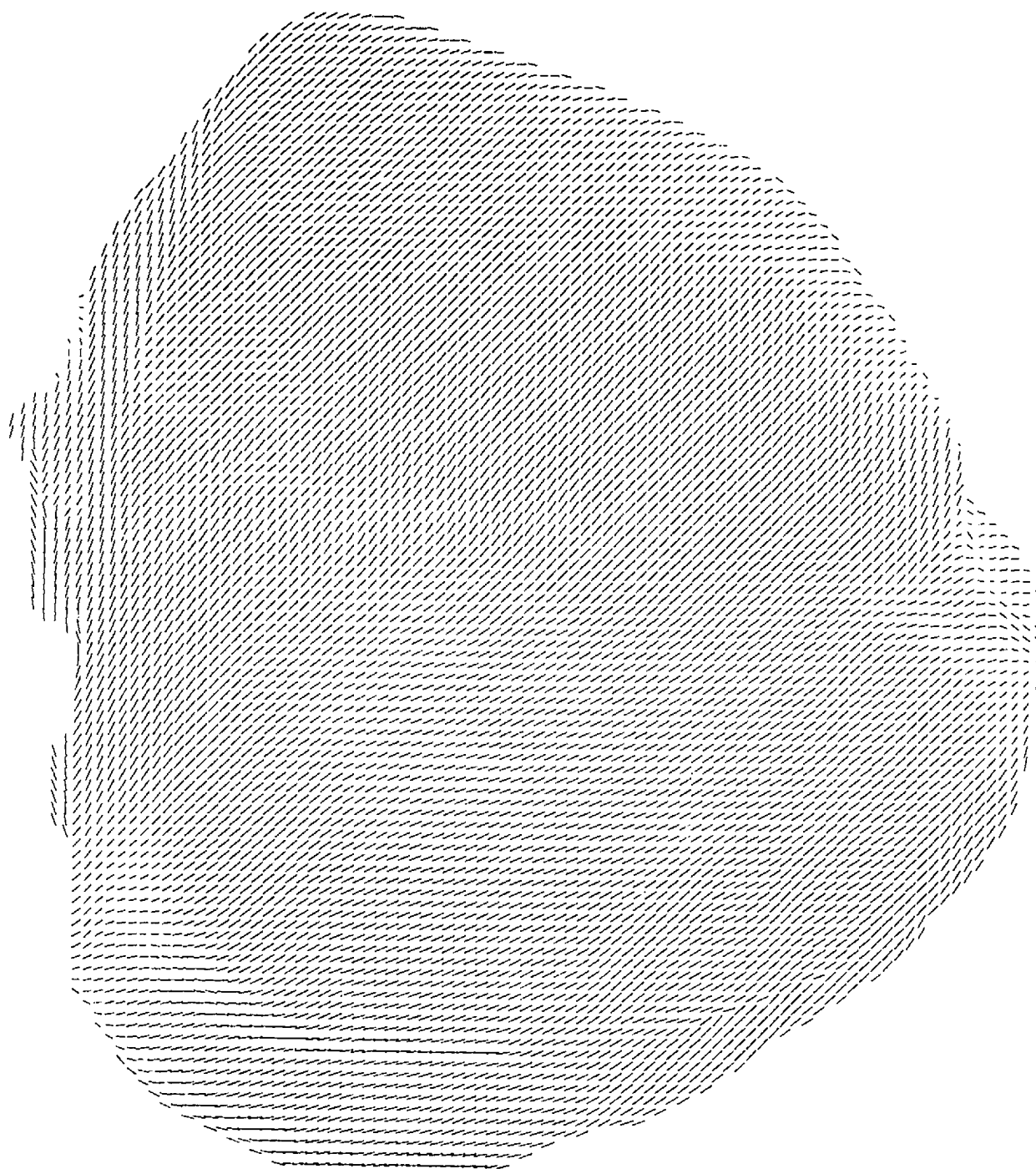


Figure 2.7: Posterior view of the model of the human ventricular myocardium. As in Fig. 2.6, the fiber direction is displayed only in every second voxel along each axis.



Figure 2.8: Apical view of the model of the human ventricular myocardium. As in Fig. 2.6, only every second voxel along each axis is displayed.

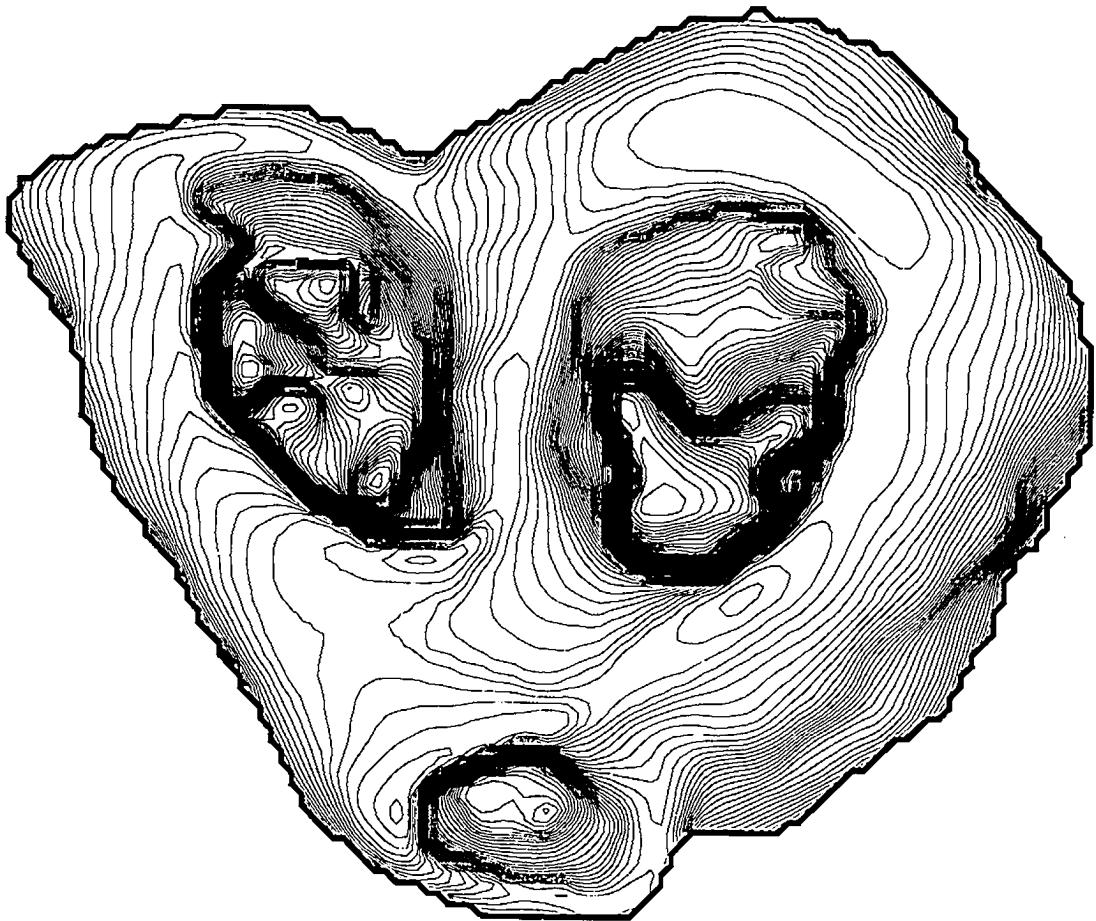


Figure 2.9: Basal view of the geometry of the human ventricular model. Sections are 1 mm apart, and each is represented by smoothed contour lines ($z = \text{const.}$) to achieve better rendering of the shape.



Figure 2.10: Basal view of the model of the human ventricular myocardium. Only the top basal layers (70 mm above the LV apex and up) are shown; as in Fig. 2.6, only every second voxel along each axis is displayed.

region was relatively small (about 0.5 per cent of the total number of voxels in the entire human ventricular model), the following *ad hoc* approach was adopted. Since on the top of the ventricles, the angle ζ approaches zero and thus determines the curvature of the surfaces, the angles η and α determine the same rotational angle. For this reason, the value of η in all voxels (i,j,k) positioned above the 85-mm layer was simply copied from the voxel at 85 mm above the LV apex with the same planar coordinates (i,j) . In the voxels that defined the top of the basal ridges, ζ was set at 0° and angle α was assigned in accordance with anatomical atlases [342]. In the remaining voxels, ζ and α were determined by linear interpolation between the ridge voxels and voxels located 85 mm above the apex, which had been reconstructed by surface harmonic expansion. The basal view of the model of the human ventricular myocardium is shown in Fig. 2.10.

The entire human ventricular model constructed in the manner described consists of 1690448 voxels. Associated with each voxel are three bytes defining the fiber orientation and one byte designating the voxel type (e.g., RV vs. LV, endocardial vs. epicardial). To minimize the required memory allocation, the model data were further compressed. First, only myocardial voxels (not the “void” inside the cavities or the extracardiac space) were stored in the final version. Next, the fiber orientation was, with the proper transformation, represented only by two spherical angles Θ and Φ defined in the global coordinate system. Hence, the anatomical characteristics of each myocardial cell were specified by six bytes: three to determine the indices (i,j,k) , one to assign the cell type, and two to define the spherical polar angles. The model was stored in this configuration and used as the input for simulating the propagated

activation described in Chapters 4–6.

To visualize the model of the human ventricular myocardium, we developed software which allows the viewing of individual slices. In addition, each slice can be rotated and the fiber orientation displayed three-dimensionally. Figs. 2.11–2.14 show plots of the global distribution of fibers in the model.

The reconstruction of the human ventricular model was implemented on an IBM RS/6000 model 590 computer. The CPU time required to perform the surface harmonic expansion fitting of the surface depended on the number of input data points and the order of expansion; when using approximately 15000 data points and $N = 20$, the CPU time was on the order of 25 minutes. The surface reconstruction, including the calculation of the tangential and normal vectors, took about 11 minutes of CPU time. Steps 1 through 5 were completed in about 19 minutes of CPU time.

2.5 Discussion

We have designed a model of the human ventricular myocardium that features a very accurate description of the ventricular anatomy and fibrous architecture. In the absence of quantitative data on the human heart, we used as the source for our rotation angle information a highly reliable model of the canine ventricular myocardium. The principal ventricular surfaces were accurately and efficiently parameterized by the surface harmonic expansion method, which provided a robust and compact basis for constructing the tangential sheets throughout the ventricles. The transformation between the principal surfaces of the canine and human models was guided by a set of anatomical landmarks.



Figure 2.11: Coronal cross section through the model of the human ventricular myocardium. The section is 5 mm posterior to the LV apex; the resolution of the display is the same as that of the model (0.5 mm).

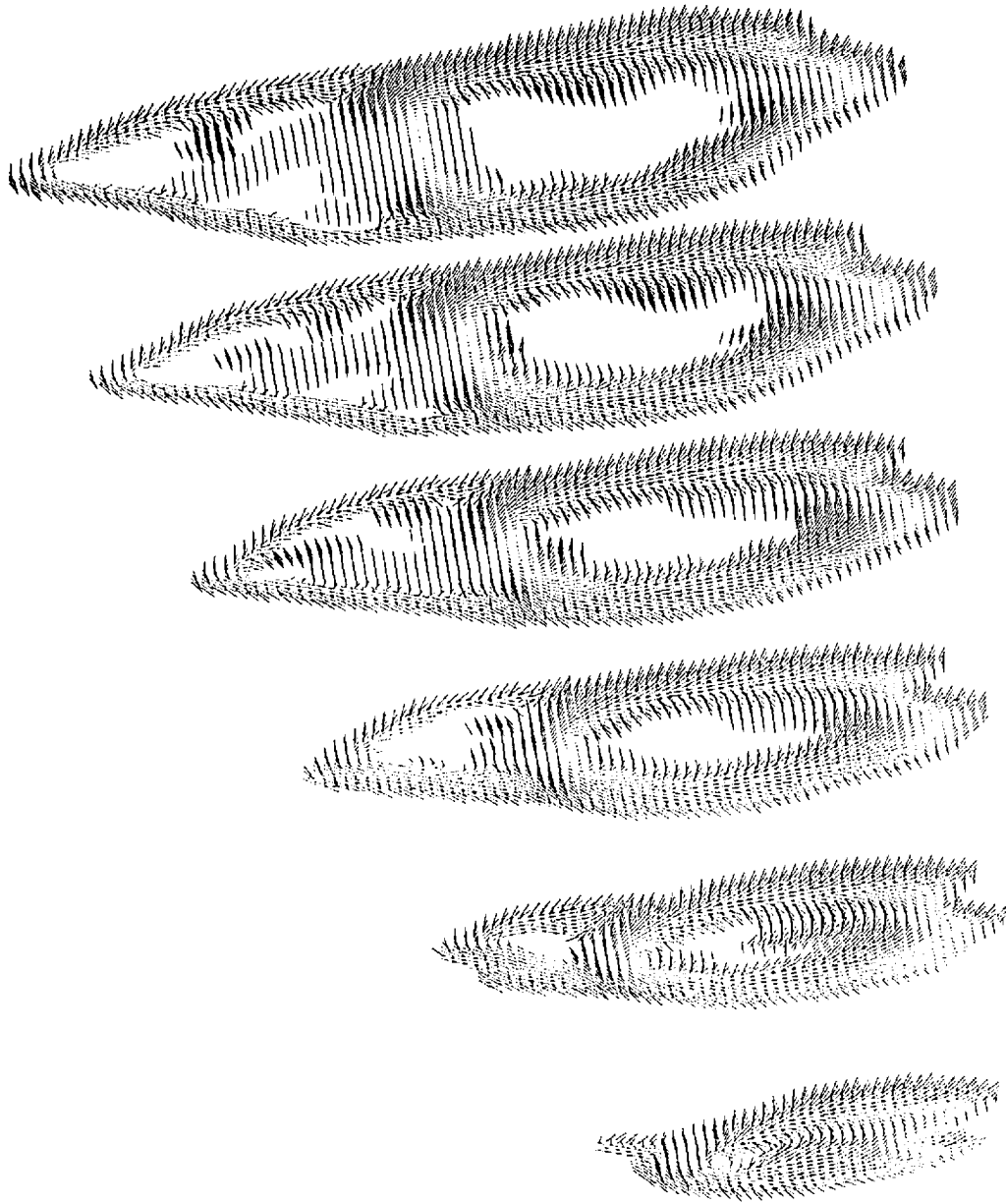


Figure 2.12: Apical transaxial cross sections through the model of the human ventricular myocardium. Sections are, from top to bottom, at 32.5, 27.5, 22.5, 17.5, 12.5, and 7.5 mm above the LV apex; fibers are displayed with a resolution of 1.0 mm to make the display clearer.

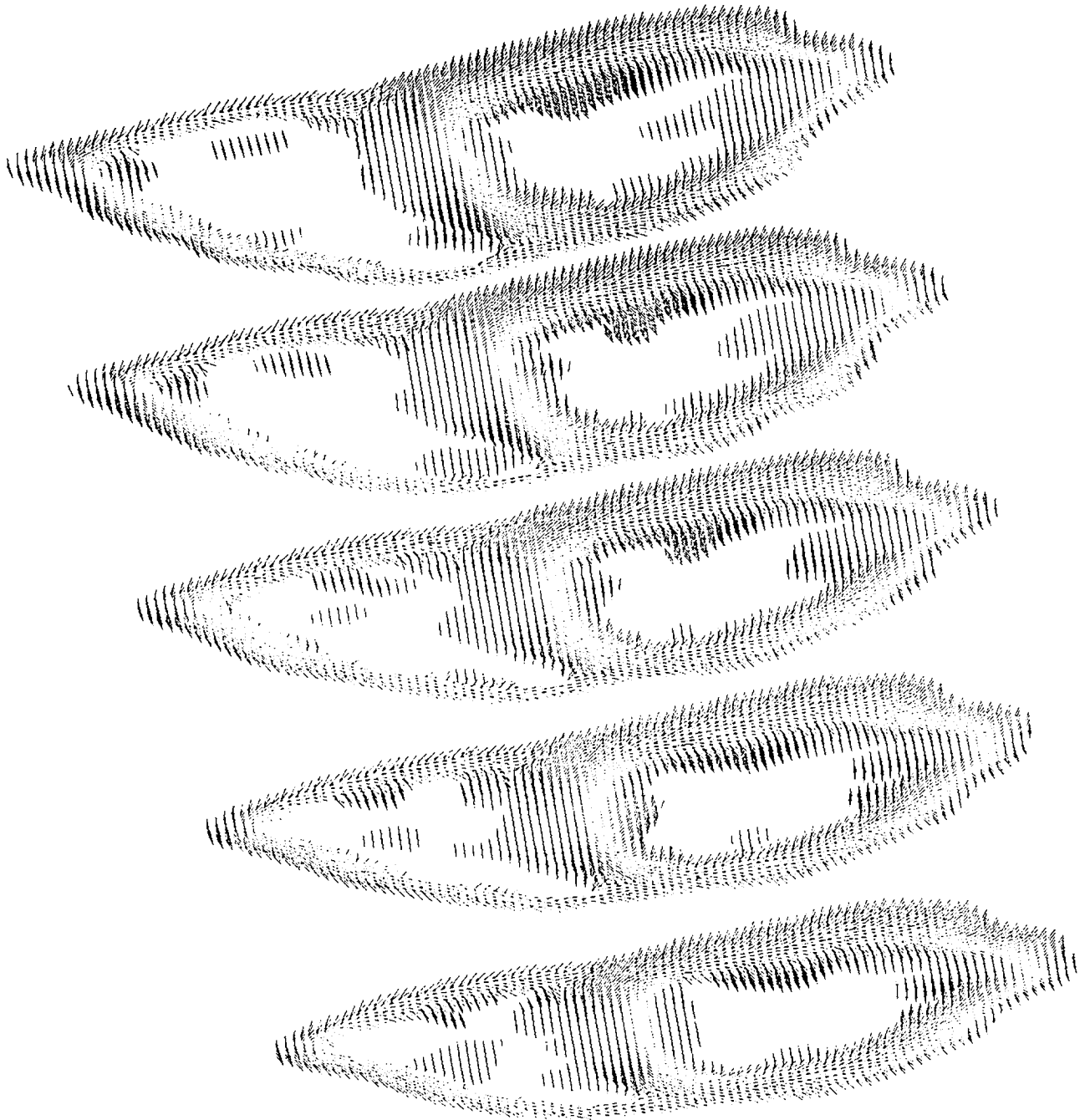


Figure 2.13: Medial transaxial cross sections through the model of the human ventricular myocardium. Sections are, from top to bottom, at 57.5, 52.5, 47.5, 42.5, and 37.5 mm above the LV apex; fibers are displayed with a resolution of 1.0 mm to make the display clearer.



Figure 2.14: Basal transaxial cross sections through the model of the human ventricular myocardium. Sections are, from top to bottom, at 82.5, 77.5, 72.5, 67.5, and 62.5 mm above the LV apex; fibers are displayed with a resolution of 1.0 mm to make the display clearer.

Landmark selection is a significant factor in one's ability to adequately approximate the transformation between two models. We have chosen a set of landmarks that is simple to identify when using both noninvasive imaging techniques and an anatomical examination of excised hearts. This is an important consideration for eventual clinical applications. (Reese et al. [303] have demonstrated that magnetic resonance imaging allows noninvasive *in vivo* reconstruction of the fibrous architecture.) The accuracy of the transformation between the canine and human models could be enhanced, and flexibility in the matching of two surfaces could be increased by using more degrees of freedom (such as the local surface normal) at the landmark locations.

Since the tangential planes were defined in our model of the human ventricular myocardium for any point between the epicardial and endocardial surfaces, the electrical and mechanical properties of the ventricular myocardium can also be assigned to vary with respect to the direction perpendicular to the tangential plane of fibers (i.e., the anisotropy can be defined as not axially symmetric). LeGrice et al. [205] suggested that the ventricular myocardium is a discrete laminar structure with distinct anisotropic features in all three directions in space, i.e., in the direction along the fiber, in the direction perpendicular to the fiber in its tangential plane, and in the direction perpendicular to the tangential plane of the fiber.

Another issue in the accurate modeling of a fibrous structure such as the ventricles is the selection for the function f for the transmural rotation of the angle α . Our model incorporates the feature that any smooth function f can be defined between the endocardial and epicardial principal surfaces. However, to actually use such a

feature in the model, we would need quantitative data collected transmurally in the ventricles of human hearts.

Although our method of constructing the fibrous structure of human ventricles is simple, fast, and easy to implement, it has its limitations as well. First, the principal ventricular surfaces in our model are described by more parameters than in the model constructed by Nielsen et al. [262]. Second, the fibrous structure of the trabeculata and the most basal parts of the ventricles were reconstructed by means of rather heuristic *ad hoc* algorithms, and no attempt has been made to include a detailed description of the intramural rotation of fibers within the trabeculata.

In the future, our model can be improved by the development of more advanced and generally applicable methods for reconstructing the geometry of the trabecular surfaces. Also, a small correction to account for the tipping of the fibers in the free wall out of the tangential planes (“imbrication” angle) can be readily incorporated into our ventricular model provided the necessary anatomical data are available. Another area of future development would be to incorporate semiautomatic techniques compatible with the imaging modalities for delineating the principal surfaces [5, 91, 213, 278].

Chapter 3

Simulation of propagated excitation in the anisotropic myocardium

3.1 Introduction

In myocardial tissue, the cell membranes that have been depolarized beyond their threshold potential spontaneously undergo a nonlinear electrical process of *activation* powered by intracellular sources of energy, and this activation process spreads throughout the tissue [170]. The boundary between the region of the myocardium that has been depolarized and the region that is still in the resting state can be viewed macroscopically as a thin (1–2 mm) moving surface [272, 394, 403]—*the activation wavefront*. This activation wavefront is, from the standpoint of mathematical physics, an electrical double layer which represents the bioelectrically active sources in the heart and gives rise to the measurable extracardiac electric potentials and magnetic field.

Determining these potentials for a given set of primary bioelectric sources in the heart when the properties of the surrounding volume conductor are known constitutes

the forward problem of electrocardiography. This problem is generally uniquely solvable for various cardiac primary sources and volume conductors. The computational complexity in solving the forward problem largely depends on the accuracy with which one approximates the primary sources and the volume conductor that represents the human body. The simplest forward solution is based on the assumption that the bioelectric activity of the heart can be described in terms of a fixed single dipole source embedded in an infinite homogeneous conductor [114, 121, 153]. This model originates from the early theory of electrocardiographic leads [87] and, in fact, still dominates present-day diagnostic electrocardiography [124].

This chapter deals with the simulation of propagated excitation in the ventricular myocardium and with the relationship of propagated excitation to the measurable electric potentials on the epicardium and body surface. (In this study, we define *excitation* as a process that includes both depolarization and repolarization; *activation* refers to the depolarization phase only.)

3.1.1 Cardiac source modeling

A variety of approaches that have been used to solve the forward problem were reviewed by Gulrajani [130] and Gulrajani et al. [134], and, more recently, by Colli Franzone and Guerri [48] and Henriquez [143]. In this subsection, we shall concentrate on those methods that are important for the simulation of propagated excitation in the human heart.

The first macroscopic model of propagated activation was developed by Wiener and Rosenblueth [409]. The propagation in their model was rule-based (as in present-day cellular automata models) with an active point exciting its nearest neighbors

isotropically in all directions in a way resembling Huygens' principle of wave propagation. This scheme was retained through many variations in a number of numerical implementations of propagation models, including at early stages of development only 2-D sheets of cardiac cells [41, 96, 97, 100, 241]. Later, with the addition of the third dimension, the models were generalized to allow the inclusion of realistic ventricular geometry. The first isotropic 3-D ventricular models were those developed by Ledley [204], Okajima et al. [265], Ritsema van Eck [305], and Selvester and Solomon [344, 345], and they were later advanced by others [8, 12, 86, 227, 238, 239, 402]. In these models, the extracardiac potentials were calculated from distributed equivalent source generators (current dipoles) oriented in a direction normal to the advancing wavefront at each of its discrete points [118, 238, 425].

More recent work of Corbin and Scher [59], combining experiments and modeling, indicated that the propagation of excitation is markedly affected by myocardium's anisotropic structure. These authors noted that the activation wavefront moved three times faster along the fibers than across them. To evaluate extracardiac potentials, Corbin and Scher proposed a new cardiac source model in which the dipoles are oriented locally parallel to the direction of the myocardial fibers. Further experimental studies of Roberts and Scher [308], Roberts et al. [307], Baruffi et al. [25], and Spach et al. [355] substantiated the finding that the isotropic model of propagated excitation is not adequate. Baruffi et al. [25] stimulated the canine LV at endocardial, intramural, and epicardial sites and showed that recorded electrograms on the ventricular surface had negative deflections where the isotropic model would have predicted positive deflections; by measuring extracardiac currents, they demon-

strated that this phenomenon can only be explained by an anisotropic model of myocardial tissue [57]. An attempt to incorporate anisotropy in propagation models motivated a modification of the Wiener-Rosenblueth approach, with the wavefronts constructed as ellipsoids (rather than spheres) oriented along the principal fiber direction [4, 6, 131, 218, 397, 401]. Although such models are computationally efficient, they cannot adequately reproduce potentials measured near the epicardium. In addition, the velocity of propagated activation is preassigned by inserting a delay in the passing of activation from one point to another. The velocity has, therefore, no direct relation to the underlying physiology of the process.

A more advanced approach to solving the problem of propagated excitation, and one that explicitly describes the structure of the pertinent myocardium, is the bidomain model (see Section 3.2) proposed by Schmitt [331] and first implemented by Tung [389] and Geselowitz and Miller [120]. In the bidomain model, myocardial tissue is represented as a bisyncytium, that is, as a pair of continuous and congruent spaces corresponding to the intracellular and interstitial (i.e., extracellular within the tissue) spaces, which are separated everywhere by a membrane. Plonsey and Rudy [288] used this model in studying how tissue thickness affects extracardiac potentials. They assumed that the ratio of conductivities along and across the axes of anisotropy is the same in the intracellular medium and in the interstitial medium (an equal anisotropy ratio condition). Plonsey and Barr [284] used the bidomain model to analyze current flow during propagated excitation in 2-D network of cells, using several hypothetical arrangements of intracellular and interstitial domains and a range of anisotropy ratios. They concluded that when the anisotropy ratio in two con-

gruent spaces differs, the spatial distributions of ohmic currents can be significantly different in the interstitial space than it is in the intracellular space. Plonsey and Barr also noted that the bidomain model under conditions of equal anisotropy ratio is equivalent to a monodomain representation and that the calculated transmembrane potentials are the same as those predicted by a uniform double layer. Their results were later confirmed by Sepulveda and Wikswo [332], who also computed the magnetic field and found that it becomes zero when anisotropy ratios are equal.

Colli Franzone and coworkers [57, 58] included the third dimension and generalized the model of Corbin and Scher [59] by introducing the oblique dipole layer to explain experimental potential distributions measured from isolated canine hearts. The oblique dipole layer model represents the cardiac sources as the superposition of two layers of dipolar sources constructed on the surface of the activation wavefront: 1) a normal dipole layer, with dipoles oriented in the direction normal to the wavefront surface and 2) an axial dipole layer, with dipoles oriented along the local direction of fibers. It follows from Gauss' law of flux [363] that the extracardiac potential due to the uniform normal layer is absent when the wavefront is closed [57, 58].

More recently, Colli Franzone et al. [55] developed the solution of propagated activation in the bidomain model based on reaction-diffusion equations [95]. The reaction-diffusion model requires considerable amounts of computer time and memory allocation to solve the pertinent partial differential equations and thus can be used only in small blocks of myocardial tissue. For these reasons, Colli Franzone et al. [51, 55] derived from the reaction-diffusion model—using a singular perturbation technique [46, 183]—an approximate eikonal-curvature formulation. A similar

approach was used by Keener [184]. (Colli Franzone and Guerri [49] carefully compared, by means of 3-D simulations, the reaction-diffusion and eikonal models and found excellent agreement.) Both approaches have been used to simulate propagated activation in models of myocardial tissue with the assigned spatial variation of the fiber direction [52, 53, 185]. The limitation of the eikonal-curvature models is that—at the current stage of development—they do not incorporate the kinetics describing the cardiac AP but do determine only the position of the leading edge of the wavefront of propagated activation.

Leon [206] and Leon and Horáček [207, 208, 209] developed a hybrid model of cardiac propagated excitation that combines cellular automata models with those based on bidomain theory. This model is designed for a realistic heart architecture, simulates both activation and recovery, allows for a transmembrane AP of different type for different types of cells, and enables the calculation of extracardiac potentials on both the epicardial and the torso surfaces.

Colli Franzone et al. [52] and Henriquez et al. [144] used the bidomain models to relate epicardial potentials to activation wavefronts. They used the parallelepipedal and curved slabs of ventricular tissue with assigned rotational anisotropy, in which they initiated ectopic sequences from epicardial, intramural and subendocardial sites. Their model provides a thorough insight into intramural distributions of potentials and activation isochrones, which is very valuable when interpreting measured epicardial potentials and unipolar plunge-electrode electrograms [376]. A limitation of their study is the simplified representation of the ventricular myocardium.

The bidomain model has recently been applied to exploring the effect of the

extracardiac volume conductor on the process of propagated activation in cylindrical strands of myocardial fibers [145, 146, 147, 310, 311, 314] and planar slabs of myocardial tissue [122, 148]. Trayanova and Pilkington [387] showed that, in principle, one can expand the bidomain model to approximate the discrete nature of myocardial tissue by introducing junctional resistances into the intracellular domain. During the past 15 years, there also has been progress in incorporating knowledge about the membrane dynamics of cardiac myocytes into single-cell [223, 224] and one-dimensional models that explicitly consider the discontinuous structure of the myocardium [71, 72, 286, 299, 320, 319, 347]. Cellular models provide fundamental insights into the nonlinear properties of the cardiac cell membrane because they can simulate membrane dynamics in an unabridged form. On the other hand, these models cannot simulate phenomena that depend on the topological properties of 3-D ventricles and on their anisotropic structure. Presently, the description of ionic currents in models of the cardiac cell membrane (e.g., [223, 224]) is too computationally costly to be included, without simplifications, in macroscopic ventricular models.

3.1.2 Volume conductor modeling

The simplest volume conductor models representing the human body disregarded boundary effects [114, 121, 153] or considered the human body as a volume with a spherical [37, 63, 102, 318, 413], spheroidal [30, 63, 246, 398], parallelepipedal [92], or cylindrical [149, 201, 264] boundary. The major advantage of such simplifications is that they allow the analytical calculation of extracardiac potentials, e.g., on the body surface or epicardium, or of a magnetic field outside the body surface. However, to obtain the electric potentials and magnetic field in a realistically shaped volume

conductor [20, 111, 117, 151, 152], numerical methods have to be used. Two classes of engineering techniques are used in electrocardiography to model the human body's boundaries and internal structures: the finite element method (FEM) [167, 432] and the boundary element method (BEM) [34]. In both methods, the volume conductor that represents the electrical properties of the human body must first be subdivided into a finite number of basis elements (volume elements in the case of the FEM and area elements in the case of the BEM).

The FEM is based on the minimization of an energy function derived from Poisson's equation within each of the discretized volume elements. An important feature of the FEM is the ability to formulate solutions for individual elements before assembling them to represent the entire problem. Since the electrical properties can vary from element to element, the FEM can model local variations in the electrical properties of the volume conductor, thereby explicitly accommodating conductivity inhomogeneities as well as the tissue's anisotropy. Its disadvantage lies in the large number of nodes that are required to represent the entire volume conductor well enough to obtain a reasonably accurate solution. The FEM has been applied to electrocardiographic modeling by several investigators [54, 56, 216, 333, 334, 360, 426], with the recent Utah model being the most sophisticated model of the human torso to date [174].

The BEM, which has been adopted in this study, is based on Green's theorem. The surfaces, rather than the entire volume, dividing the compartments with different electrical conductivities are tessellated with suitable planar elements [152]. The electric properties of human thoracic tissues can thus be represented as an isotropic, piecewise

homogeneous volume conductor. The major advantage of the BEM is that it involves considerably fewer nodes than the FEM. Because of its simplicity and compactness, the BEM has been widely adopted in electrocardiography and has proved suitable for constructing “tailored” torso models that account for patient-to-patient variability in torso shape and the position of the internal structures [162, 168, 268, 270]. On the other hand, although attempts have been made to account for anisotropy in the boundary element models [132], such procedures are not generally applicable. Consequently, the BEM is largely limited to the modeling of inhomogeneous, but isotropic, structures in the human torso. (Recently, Zhou and van Oosterom [431] demonstrated that by means of a proper coordinate transformation, the BEM can be used for computing electric potentials and a magnetic field generated by bioelectric primary sources in an anisotropic, inhomogeneous volume conductor.)

Pilkington and coworkers [279, 280] directly compared the FEM and BEM and concluded that both techniques generated results of equal accuracy, provided that the sizes of the elements covering the volume and the surfaces were comparable. Thus, fewer elements are required in the BEM than in the FEM to attain the same accuracy of the solution. Stanley and Pilkington [359] and, more recently, Pullan [295] used the FEM to model an anisotropic skeletal muscle layer—which has a higher conductivity in the direction tangential to the outer chest boundary and a lower conductivity in the radial direction—and used the BEM to model other intrathoracic regions. The resulting models required significantly fewer nodes to represent the entire volume conductor than did the standard finite element models.

3.2 Macroscopic description of cardiac sources by the bidomain model

The bidomain model is a macroscopic model; that is, it describes physical quantities averaged over a volume containing many cardiac cells. The basis of the bidomain model is the assumption that one can neglect the microscopic details of myocardial structure and consider myocardial tissue as though it were a continuum [283]. This assumption is reasonable because although it has been shown that at a cellular level the propagation of excitation is discontinuous [347, 349, 350, 351, 353, 354], such discontinuities have not been observed on the macroscopic scale. We shall introduce the mathematical concept of bidomain theory, emphasizing those assumptions and less-known steps that are important for our application.

Bidomain theory treats both the intracellular space and the interstitial space as being continuous and separated by a distributed cell membrane. Both spaces represent interpenetrating (or congruent) domains; i.e., to each point in the bidomain model is attributed both an averaged intracellular potential ϕ_i and an averaged interstitial potential ϕ_e . As a result, the transmembrane potential v_m is defined at any point in the bidomain region. Bidomain theory provides the formal link between ϕ_i , ϕ_e , and v_m , and the electrical properties of the anisotropic conducting medium described in terms of the conductivity tensor.

3.2.1 Conductivity tensor as a descriptor of anisotropy

We consider the ventricular myocardium as the anisotropic bidomain region H whose electric properties are characterized by the conductivity tensors \mathbf{D}_i and \mathbf{D}_e for the

intracellular and interstitial spaces. The tensors \mathbf{D}_i and \mathbf{D}_e are defined in a global Cartesian coordinate system and are symmetrical and positive definite. As a fiber direction varies with its position \mathbf{x} in this volume H , the tensors \mathbf{D}_i and \mathbf{D}_e may generally contain diagonal and off-diagonal elements. However, the tensors \mathbf{D}_i and \mathbf{D}_e are usually measured or defined in their natural basis (that is, in their eigensystem) and then, with the proper transformation, are rotated into a global coordinate system. This procedure will be described in more detail below.

The bidomain region H is assumed to have the local fiber direction (varying with \mathbf{x}) that is defined by an eigenvector $\mathbf{a}_3(\mathbf{x})$ of tensors \mathbf{D}_i and \mathbf{D}_e . If the intracellular and interstitial domains share the same eigenvector $\mathbf{a}_3(\mathbf{x})$, then the eigenvalues $\sigma_3^i = \sigma_i^i$ and $\sigma_3^e = \sigma_i^e$ corresponding to that eigenvector are conductivities along the fiber local direction in the intracellular and interstitial spaces, respectively. Measurements have shown that the electric properties of each fiber can be approximated as axially symmetric with the conductivities σ_i^i and σ_i^e along the fiber and the conductivities σ_t^i and σ_t^e in any direction perpendicular to the fiber. This is algebraically equivalent to stating that the tensors \mathbf{D}_i and \mathbf{D}_e are degenerate, which means that eigenvalues corresponding to the eigenvector $\mathbf{a}_1(\mathbf{x})$ are the same as those corresponding to the eigenvector $\mathbf{a}_2(\mathbf{x})$.

In addition to the above assumptions, we also assume that anisotropy is homogeneous in H , i.e., the eigenvalues σ_t^i , σ_t^e , σ_i^i , and σ_i^e are independent of \mathbf{x} . The diagonal tensors \mathbf{D}_i^* and \mathbf{D}_e^* , defined in the eigensystem, then comprehensively characterize

the intracellular and interstitial anisotropic conductivities,

$$\mathbf{D}_{i,e}^* = \begin{pmatrix} \sigma_t^{i,e} & 0 & 0 \\ 0 & \sigma_t^{i,e} & 0 \\ 0 & 0 & \sigma_t^{i,e} \end{pmatrix}. \quad (3.1)$$

To be represented in a global coordinate system, the tensors \mathbf{D}_i^* and \mathbf{D}_e^* have to be rotated,

$$\mathbf{D}_{i,e} = \mathbf{A} \mathbf{D}_{i,e}^* \mathbf{A}^T, \quad (3.2)$$

where $\mathbf{A} = \{\mathbf{a}_1(\mathbf{x}), \mathbf{a}_2(\mathbf{x}), \mathbf{a}_3(\mathbf{x})\}$ is a matrix of eigenvectors and \mathbf{A}^T is its transpose. In particular, when the local fiber direction is defined by the spherical angles Θ and Φ , the eigenvectors $\mathbf{a}_1(\mathbf{x})$, $\mathbf{a}_2(\mathbf{x})$, and $\mathbf{a}_3(\mathbf{x})$ are the unit vectors \mathbf{e}_Θ , \mathbf{e}_Φ , and \mathbf{e}_r of the spherical coordinate system expressed in the Cartesian coordinate system.

It is convenient to separate the isotropic and anisotropic components of the tensor $\mathbf{D}_{i,e}$ to account for the contribution that is solely due to anisotropy. Using axial symmetry, one can rewrite the conductivity tensor $\mathbf{D}_{i,e}$ as

$$\mathbf{D}_{i,e} = (\sigma_t^{i,e} - \sigma_t^{i,e}) \mathbf{a}_3 \mathbf{a}_3^T + \sigma_t^{i,e} \mathbf{I}, \quad (3.3)$$

where \mathbf{I} is the identity matrix. Thus, the anisotropic interstitial and intracellular media can be thought of as having isotropic conductivities $\sigma_t^{i,e}$ throughout, with an additional increase in conductivity $(\sigma_t^{i,e} - \sigma_t^{i,e})$ along the fiber direction.

3.2.2 Derivation of the bidomain equations

Since the intracellular and interstitial domains in H are continuous and behave as linear conducting media, the current densities [A/m²] in both domains are given by Ohm's law,

$$\mathbf{j}_i = -\mathbf{D}_i \nabla \phi_i, \quad (3.4)$$

$$\mathbf{j}_e = -\mathbf{D}_e \nabla \phi_e . \quad (3.5)$$

In Eqs. 3.4 and 3.5, the quasi-static conditions were assumed; that is, the displacement current was neglected and the electric field was expressed as the gradient of a scalar potential (which is justified for electrocardiographic frequencies < 1000 Hz [287]). The potentials ϕ_i and ϕ_e are approximated by the bidomain model and therefore are local averages of physical quantities based on the spatial discretization of the model. Since the electric charge is conserved at every instant, i.e., $\partial\rho/\partial t = 0$, the total current density $\mathbf{j} = \mathbf{j}_i + \mathbf{j}_e$ is solenoidal,

$$\nabla \cdot \mathbf{j} = -\nabla \cdot \mathbf{D}_i \nabla \phi_i - \nabla \cdot \mathbf{D}_e \nabla \phi_e = 0 . \quad (3.6)$$

Also, in accordance with the conservation law, any change in the intracellular and interstitial current densities has to appear as the transmembrane current [A/m^3]

$$i_m = \nabla \cdot \mathbf{D}_i \nabla \phi_i = -\nabla \cdot \mathbf{D}_e \nabla \phi_e . \quad (3.7)$$

Since it is assumed that the intracellular and interstitial spaces are separated by a distributed membrane, the transmembrane potential v_m can be defined for every point of the region H as the difference between the intracellular and interstitial potentials

$$v_m = \phi_i - \phi_e . \quad (3.8)$$

Using this definition of the transmembrane potential and Eq. 3.6, we can write elliptical partial differential equations for ϕ_i and ϕ_e ,

$$\nabla \cdot (\mathbf{D}_i + \mathbf{D}_e) \nabla \phi_i = \nabla \cdot \mathbf{D}_e \nabla v_m , \quad (3.9)$$

$$\nabla \cdot (\mathbf{D}_i + \mathbf{D}_e) \nabla \phi_e = -\nabla \cdot \mathbf{D}_i \nabla v_m . \quad (3.10)$$

We can see that the distributions of ϕ_i and ϕ_e are generated by the source terms that involve the gradient of the transmembrane potential. Equivalently, we can show—using Eqs. 3.4, 3.5, and 3.8—that the total current density can be formally expressed as the sum of the “impressed” current density $-\mathbf{D}_i \nabla v_m$ driven by the electrochemical generators in the membrane and ohmic volume current $(\mathbf{D}_i + \mathbf{D}_e) \nabla \phi_e$. Eq. 3.10 thus directly relates the interstitial potential distribution ϕ_e to the impressed current sources embedded in a composite medium with the bulk conductivity $\mathbf{D}_i + \mathbf{D}_e$.

In the ventricular muscle, activation propagates due to the spread of electrotonic current between neighboring cardiac cells. Since in the bidomain model intracellular and interstitial spaces are filled with continuous resistive media coupled via a distributed membrane, the inclusion of this fundamental physiological principle into the bidomain model can be accomplished using a nonlinear cable equation [47]. The transmembrane current is then given by

$$i_m = \chi \left(C_m \frac{\partial v_m}{\partial t} + I_{ion} - I_{app} \right), \quad (3.11)$$

where χ is the membrane surface area per unit volume, C_m is the membrane capacitance per unit area, I_{ion} is the ionic current per unit area of the membrane surface, and I_{app} is an applied current stimulus to start the excitation. Including the cable equation (Eq. 3.11) has an important consequence because the ionic current I_{ion} , in principle, can be described as a nonlinear function of v_m . Several semiempirical models have been developed to do so, among them the Beeler-Reuter [28] model and the more recent Ebihara-Johnson [85], Drouhard-Roberge [80, 81, 82], DiFrancesco-Noble [74], or Luo-Rudy [223, 224] models. In this way, the macroscopic current sources $-\mathbf{D}_i \nabla v_m$ can be described in a direct relationship with the physiological parameters

that define the cellular AP.

By combining Eqs. 3.11 and 3.7 and by defining

$$c_m = \chi C_m, \quad i_{ion} = \chi I_{ion}, \quad i_{app} = \chi I_{app},$$

we get an equation that relates the spatial distribution of extracellular potential ϕ_e and the membrane dynamics

$$c_m \frac{\partial v_m}{\partial t} - \nabla \cdot \mathbf{D}_i \nabla v_m + i_{ion}(v_m) = \nabla \cdot \mathbf{D}_i \nabla \phi_e + i_{app}. \quad (3.12)$$

This is a nonlinear parabolic partial differential equation in v_m . When coupled with the elliptic equation in ϕ_e (Eq. 3.10) and corresponding boundary conditions, it completely determines v_m and ϕ_e (and via Eq. 3.8 also ϕ_i) in the region H .

3.2.3 Boundary conditions

The anisotropic bidomain region H is not infinite but is embedded in a bounded monodomain region B . For this reason, the proper boundary conditions at the interface between regions H and B have to be specified.

Let the closed surface S_H bound the bidomain region H , thereby representing an interface between two regions. Assume that the volume conductor B is homogeneous and isotropic with constant conductivity σ_B . At the boundary S_H , the electric potential is continuous in H . Because we assume that the interstitial space in H is contiguous with the volume conductor B , it follows that

$$\phi_B = \phi_e. \quad (3.13)$$

To ensure continuity of the current, the normal component of the current density

must also be continuous

$$\mathbf{n} \cdot \sigma_B \nabla \phi_B = \mathbf{n} \cdot (\mathbf{D}_i \nabla \phi_i + \mathbf{D}_e \nabla \phi_e) , \quad (3.14)$$

where the vector \mathbf{n} is an outward unit normal to the surface S_H .

Additional boundary conditions on the surface S_H follow from the property that the sources in the bidomain region H arise only in the presence of an intracellular medium. Since such sources are confined to H , the quantities $\mathbf{D}_i \nabla v_m$ and $\mathbf{D}_i \nabla \phi_i$ can be assumed to be tangent to S_H , i.e.,

$$\mathbf{n} \cdot \mathbf{D}_i \nabla v_m = 0 , \quad (3.15)$$

$$\mathbf{n} \cdot \mathbf{D}_i \nabla \phi_i = 0 . \quad (3.16)$$

3.2.4 Assumption of an equal anisotropy ratio

In principle, Eqs. 3.10 and 3.12—when subjected to the boundary conditions stated in Eqs. 3.13 through 3.16—completely determine the values of ϕ_i , ϕ_e , and v_m in the bidomain region H . Such a system, comprising an elliptic partial differential equation coupled to the parabolic partial differential equation, can be solved iteratively by first solving the nonlinear parabolic equation (using the explicit finite difference method to update the transmembrane potential) and then finding the solution of the boundary value problem (represented by the elliptic equation and the boundary conditions) [311]. Such an approach, however, requires very fine spatial (< 0.2 mm) and temporal (< 0.001 ms) discretizations to ensure the stability of the solution, and this effectively prevents its application to modeling propagated activation in the entire human ventricular myocardium. A more computationally efficient solution can be obtained under the assumption of an equal anisotropy ratio.

Since the bidomain model is macroscopic, the conductivity tensors \mathbf{D}_i and \mathbf{D}_e refer to the electric properties of tissue in bulk (i.e., a large number of myocardial cells) and it is useful to assume that electrical conductivities in the intracellular and interstitial media are related. For this reason, we assume the equal anisotropy ratio condition, which can be formulated as

$$\mathbf{D}_e = k\mathbf{D}_i . \quad (3.17)$$

Eq. 3.17 implies that the ratio of longitudinal and transverse conductivities is the same in the intracellular and interstitial media, i.e., $\sigma_i^e/\sigma_i^i = \sigma_i^e/\sigma_i^i = k$.

Under the equal anisotropy ratio condition, we obtain from Eq. 3.9 an important relationship

$$\phi_i = \frac{k}{k+1} v_m . \quad (3.18)$$

This means that the potential distributions in the intracellular region—and via Eq. 3.8 in the interstitial region—are solely determined by the transmembrane potential. This result was first obtained for a one-dimensional core conductor model [150]. Plonsey and Barr [284] noted that under the assumption of an equal anisotropy ratio, the intracellular and interstitial potentials depend only on the local change of v_m , in contrast to the condition of arbitrary anisotropy, where the potentials depend on the change of v_m throughout the tissue.

A consequence of this assumption is that the parabolic equation is no longer coupled to the elliptic equation but can be rewritten as

$$c_m \frac{\partial v_m}{\partial t} + i_{ion}(v_m) = \frac{k}{k+1} \nabla \cdot \mathbf{D}_i \nabla v_m + i_{app} . \quad (3.19)$$

Using Eq. 3.3, one can express the term $\mathbf{D}_i \nabla v_m$ as the sum of the anisotropic and

isotropic components, i.e., $\nabla \cdot (\sigma_i^i - \sigma_i^i) \mathbf{a}_3 \mathbf{a}_3^T \nabla v_m + \nabla \cdot \sigma_i^i \nabla v_m$. The boundary condition in Eq. 3.13 is unaffected under an equal anisotropy ratio condition, but the boundary conditions in Eqs. 3.15 and 3.16 become identical and—via the boundary condition in Eq. 3.14—can be satisfied only if the bidomain surface is insulated. Currently, there is some controversy regarding the appropriate boundary conditions for bidomain tissue embedded in an external volume conductor [145, 199, 312, 314]. In a recent experimental study, Green et al. [126] observed that at the macroscopic level, changes in the conductivity of an extracardiac volume conductor have very little effect on the sequence of propagated activation.

Eq. 3.19 is the generalized version of the cable equation [47] and represents, with the boundary conditions in Eqs. 3.13 and 3.15, the governing equation for the transmembrane potential v_m . We can see that when anisotropy ratios are assumed equal, the propagation problem is reduced to solving only a single parabolic partial differential equation. As mentioned earlier, $i_{ion}(v_m)$ depends nonlinearly on the transmembrane potential and can be calculated using the semiempirical ionic models [28, 74, 81, 85, 223, 224]. Indeed, such an approach has been successfully applied to the simulation of propagation in 2-D anisotropic sheets [210, 211, 306] and small 3-D anisotropic volumes [292] of myocardial tissue. The application of the anisotropic bidomain model to simulations of propagated activation and recovery in realistic 3-D models of the ventricles is presently on hold due to the still excessive computational costs. Our current approach to making the propagation problem computationally tractable is to use a cellular automaton to rule the suprathreshold behavior of the AP while applying the anisotropic bidomain model to govern the electrotonic inter-

action between the cells of the automaton. This hybrid approach will be described in more detail in the next subsection.

3.2.5 Cellular automata approach

The discrete and deterministic nature of a cellular automaton (CA) makes it a convenient tool in modeling dynamic systems defined over regions of irregular geometry [386, 416], such as those used to simulate propagated excitation in the ventricular myocardium. As has been shown in Section 3.1.1, CA-type models have been frequently used in electrocardiography [8, 60, 86, 227, 305, 328, 380, 402]. The major advantage of the CA is in the reduction of the complex nonlinear behavior of the ionic channels of the cell membrane into a set of discrete state-transition rules, with the AP function predefined as an analytical function or constructed by means of ionic models (e.g., the modified Beeler-Reuter model). As has been noted elsewhere [327], such a simplified description of the heart's excitable membrane should be adequate in macroscopic models of propagated excitation. We have indicated earlier that while CA algorithms are computationally attractive because they are simple and fast, their major weakness is that the velocity of propagated activation is empirically predetermined. These difficulties can be overcome, as proposed by Leon [206] and Leon and Horáček [207, 208, 209], by allowing a flow of electrotonic current—evaluated by means of the anisotropic bidomain model—between the discrete elements of the CA. On the other hand, their studies [206, 207, 208] and later ones [256] pointed out that to obtain realistic solutions with smooth activation wavefronts and a square-root relationship of conduction velocity to conductivities, the CA model should be spatially discretized at the submillimeter level. We shall concisely define the CA incorporated

into the model of propagated excitation in this study as follows.

The CA model that represents the ventricular myocardium is a network of interconnected and synchronously clocked cells whose size is determined by the resolution of the ventricular model, which for our specific case is 0.5 mm. With each cell of the model is associated a variable called the state. Time in the CA advances in discrete steps; the dynamics of each cell is defined by an explicit rule called the local map, which is applied at every time step t_i to each cell (i,j,k) , to determine the next state of the cell from the current state of that cell and the other cells in its neighborhood. The local map is, in turn, defined by the neighborhood, which specifies which cells affect a given cell, and the state-transition table, which specifies how those cells affect it. We shall describe these features in more detail as they apply to our model.

Each cell in the CA assumes one of four states that are directly linked to the underlying physiological mechanism of the cardiac AP: 1) *quiescent*, 2) *excitatory*, 3) *absolute refractory*, and 4) *relative refractory*. The quiescent state corresponds to an unexcited cell, with the value of its transmembrane potential v_m being equal to the resting potential v_r . The excitatory state corresponds to the presence of the subthreshold activity arising either from an external stimulus or from the electrotonic current (calculated using the bidomain model) from any of the neighboring cells. The absolute and relative refractory states correspond to the absolute and relative refractory periods of the cardiac AP, respectively. The transmembrane potential in the absolute refractory state is approximated by a predetermined AP function that depends only on the elapsed time, the recovery interval t_r , and the cell type τ ,

$$v_m = f(t, t_r, \tau) \quad v_m \geq v_{th} , \quad (3.20)$$

where v_{th} denotes the threshold potential. The recovery time parameter t_r was included to account for the physiological change in the conduction velocity and the refractory period due to previous patterns of local electrical activity (i.e., the electrical restitution curve) [88, 104]. Consequently, the transmembrane potential v_m is not affected by excitatory currents or by any other factor during the absolute refractory period. By contrast, the transmembrane potentials in the excitatory and relative refractory states are calculated from the anisotropic bidomain model by discretizing the governing parabolic partial differential equation (Eq. 3.19) by means of the explicit finite difference method. In this study, the ionic current $i_{ion}(v_m)$ includes only the inward rectifier i_{K1} [28, 223], which, as suggested by the experimental evidence, affects the diastolic depolarization.

The neighborhood of each cell is defined on a cubic lattice and consists of all first-order neighbors sharing at least a common edge with the given cell (in total 18 neighbors). The state-transition table takes the state of the cell, the states of the cell's neighborhood, and the external stimuli at time t_i as arguments and returns the cell's next state at time t_{i+1} . Theoretically, there are 16 possible state transitions (including identity transitions) among the four CA states, but physiological constraints reduce the number of these transitions to 11. In addition, the absolute refractory state requires a clock to control the duration of the predetermined AP function. Similarly, the excitatory and relative refractory states require separate clocks with which to determine the amount of time the cell spends in these states. At every subsequent time step, the given clock is subtracted, and when it runs out, the table specifies the state transition. The state-transition table is defined as follows:

- *quiescent* \rightarrow *quiescent* takes place if a cell in the quiescent state has not received any current from its neighbors or from an external source
- *quiescent* \rightarrow *excitatory* occurs if the transmembrane potential of one of the cell's neighbors exceeds the resting potential, both at time t_i and time t_{i+1} , or when a cell receives an external stimulus at time t_i
- *excitatory* \rightarrow *excitatory* takes place if a cell's transmembrane potential exceeds the resting potential but does not exceed the threshold potential (i.e., $v_r < v_m < v_{th}$); the transmembrane potential is calculated using the bidomain model (Eq. 3.19)
- *excitatory* \rightarrow *absolute refractory* occurs when a cell has received enough current to depolarize above the threshold potential and is about to undergo the predetermined AP function
- *excitatory* \rightarrow *quiescent* occurs when the excitatory clock has run out
- *absolute refractory* \rightarrow *absolute refractory* is maintained until the absolute refractory clock runs out; the transmembrane potential is completely regulated by the CA through the predetermined AP function
- *absolute refractory* \rightarrow *relative refractory* occurs when the absolute refractory clock runs out, that is, the cell has reached the end of its AP
- *relative refractory* \rightarrow *relative refractory* is maintained until the relative refractory clock runs out (i.e., the cell returns to either an excitatory or a quiescent

state) or the cell receives enough current to depolarize above the threshold potential (i.e., its state turns to the absolute refractory state); the transmembrane potential is calculated using the bidomain model (Eq. 3.19)

- *relative refractory* \rightarrow *quiescent* occurs when a cell has gone through the AP and does not have any cells in an excitatory or absolute refractory state within its neighborhood
- *relative refractory* \rightarrow *excitatory* occurs when a cell has gone through the AP but other cells within its neighborhood are in either an excitatory or absolute refractory state
- *relative refractory* \rightarrow *absolute refractory* occurs when a cell that has undergone an AP is receiving enough current from other sources to be depolarized above the threshold potential

In general, the CA models allow a significantly coarser discretization in the time domain than other numerical methods, such as the finite difference method. Since our model is of the hybrid type, two different time steps are used: a smaller time step (microstep) δt , for cells in the excitatory and relative refractory states, and a larger time step (macrostep) $\Delta t = m\delta t$, for cells in the quiescent and absolute refractory states. At each microstep, only those cells that require a solution of the discretized version of Eq. 3.19 are processed; at each macrostep, cells defined solely by the CA are also processed. To keep track of the cells that have to be updated, two masks—one for the microstep and one for the macrostep—are used, representing each cell by one bit.

This hybrid propagation model is laid upon the model of the human ventricular myocardium developed in Chapter 2. A 0.5-mm resolution of the model is crucial for adequately reducing the effects of spatial discretization of the CA model on the propagation velocity and shape of the activation wavefront. Each cell of the model is characterized by one byte that defines a cell type and two bytes that specify the local fiber direction (in terms of the global angles Φ and Θ). These three bytes form the static section of the given cell's storage space. Five bytes (plus two bits in system masks) constitute the cell's dynamic section, specifying (in order) the given state-transition number, its corresponding clock, potentials at the next and current time steps v_{i+1} and v_i , and the activation time. In addition, the propagation parameters designating the equal anisotropy ratio k , the microstep δt , the macrostep multiplier m , the membrane resting potential v_r , the threshold potential v_{th} , the AP function, the membrane capacitance c_m , the surface-to-volume ratio χ , the transverse intracellular conductivity σ_t^i , and the longitudinal intracellular conductivity σ_l^i are chosen before the simulation. The rationale behind the choice of a particular set of parameters will be discussed in Chapter 4. Some of the parameters, such as the membrane resting potential and the AP function, can be assigned individually to a specific region of interest. In that way, it is possible to include different AP types both in the structurally normal myocardium (due to progressive shortening of the AP duration from the endocardium to the epicardium) and in ischemic myocardial tissue (e.g., due to different levels of severity of cardiac ischemia).

The model was implemented on an IBM RS/6000 model 590 computer and was based on algorithms presented in detail elsewhere [258]. In this study, the algo-

rithm has been further improved to allow the inclusion of the conduction system, as described in Chapter 5. Appendix A summarizes functions used in simulating propagated excitation in the anisotropic myocardium.

3.3 Model for evaluating the extracardiac electric potentials and magnetic field

3.3.1 Extracardiac electric potentials

To evaluate the extracardiac electric potential ϕ_∞ , we first assume that the cardiac sources are confined to the membrane and that the membrane is embedded in a linear isotropic and homogeneous volume conductor of infinite extent that is described by its conductivity σ_1 . Consequently, the extracardiac potential can be determined by solving Poisson's equation, i.e.,

$$\phi_\infty = \frac{1}{4\pi\sigma_1} \int_H \mathbf{j}^i \cdot \nabla R^{-1} dV, \quad (3.21)$$

where \mathbf{j}^i is the impressed current density defined by the relation $\mathbf{j}^i = -\mathbf{D}_i \nabla v_m$ and R is the distance from the source point \mathbf{r} to an arbitrary field point. The integration in Eq. 3.21 is performed over the entire bidomain region H containing all cardiac sources. The potential in Eq. 3.21 can be thought of as being generated by isolated current elements—current dipoles [294, 414]. A current dipole \mathbf{p} is constructed as the concentration of a current doublet (i.e., a current source and a current sink) [27] to a single point \mathbf{r}_0 , i.e., $\mathbf{j}^i(\mathbf{r}) = \delta(\mathbf{r} - \mathbf{r}_0) \mathbf{p}$, where $\delta(\mathbf{r})$ is the Dirac delta function. A current dipole is often referred to as the equivalent primary source representing a patch of the border between depolarized and resting myocardium [415]. It is generally a good approximation for a small source viewed from a remote field point.

Next, using Eq. 3.3 in Eq. 3.21, we obtain the expression

$$\phi_\infty = -\frac{1}{4\pi\sigma_1} \left\{ \sigma_i^i \int_H \nabla v_m \cdot \nabla R^{-1} dV + (\sigma_i^i - \sigma_i^i) \int_H \mathbf{a}_3 \mathbf{a}_3^T \nabla v_m \cdot \nabla R^{-1} dV \right\}. \quad (3.22)$$

This is *the oblique dipole model* that is a generalization of the oblique dipole layer model introduced by Colli Franzone et al. [57, 58]. (The oblique dipole model allows the calculation of axial and normal dipoles throughout the cardiac depolarization and repolarization cycle in the region H .) The extracardiac potential ϕ_∞ is calculated in the discretized form of Eq. 3.22 as the superposition of contributions of a large number of dipoles. Their strengths are proportional to spatial gradients of the transmembrane potential between neighboring elements of the CA model. Eq. 3.22 can be interpreted as the linear combination of two distinct dipolar sources. The first term is the contribution of isotropic dipoles (predicted by uniform double layer theory [103, 269]) and the second term is the contribution of axial dipoles that account for the anisotropic properties of myocardial tissue [59]. Colli Franzone et al. [55] and, later, Leon and Horáček [207, 208, 209] observed that the oblique dipole model predicts the salient features of the measured potential distributions on the epicardial surface and on the body surface. However, they noted that agreement between the measurements and model depends on one's choice of the ratio between the isotropic and axial components, and they pointed out that this ratio may differ from that used to simulate propagated activation. The optimal choice of this ratio in conjunction with measured potential distributions will be addressed in Chapter 4.

The assumptions stated above deserve more detailed discussion. Firstly, the equal anisotropy ratio assumption is used in our simulations solely to determine the activation sequence and, hence, the location of the primary sources. Once we obtain

the local direction of fibers from the realistic ventricular model and calculate the local transmembrane potential differences, we can completely specify the extracardiac potentials using the oblique dipole model. Thus, this model does *not* depend on our assumption of an equal anisotropy ratio. Its limitation is that the oblique dipole model assumes that the region H is an isotropic homogeneous monodomain. In our model, anisotropy therefore affects only propagated excitation and evaluation of equivalent cardiac sources; its influence on the spatial distribution of ohmic currents in the intracellular and interstitial media is not accounted for.

The cardiac sources are embedded in the human body, which is a volume conductor and therefore acts as an electrical load for primary current sources. To account accurately for the effects of this conductor, a model of the human body should be inhomogeneous and of a realistic geometrical shape. In electrocardiography, the human body is traditionally represented as a torso, i.e., without extremities or head [20, 64, 152]. This approximation is justified by the fact that the heart-produced potential gradients in those peripheral regions are small. The torso model can also include internal inhomogeneities, such as the lungs and intracavitary blood masses, each with its own constant conductivity; the air surrounding the torso is assumed to have zero conductivity.

We assume that an arbitrarily shaped volume conductor consists of homogeneous and isotropic regions with the conductivity σ_k that are bounded by surfaces S_k ($k = 1, 2, \dots, M$), with the torso surface S_1 enclosing all other regions. It follows from generalized Green's theorem [341] that the electric potential at an arbitrary point on the boundary surface S_r of this volume conductor is given by an inhomogeneous

Fredholm integral equation of the second kind with weak singularity [20, 21, 115, 121], i.e.,

$$\phi = \frac{1}{2\pi(\sigma'_r + \sigma''_r)} \left\{ \int_V \mathbf{j}^i \cdot \nabla R^{-1} dV - \sum_{k=1}^m (\sigma'_k - \sigma''_k) \int_{S_k} \phi \mathbf{n} \cdot \nabla R^{-1} dS \right\}. \quad (3.23)$$

where σ'_k and σ''_k denote conductivities on the inner and outer sides of the surface S_k , with $\sigma''_1 = 0$, and the normal \mathbf{n} is pointing from the single-primed into the double-primed region. The first term in Eq. 3.23 equals twice the infinite medium potential calculated by Eq. 3.22. The second term accounts for the contributions of the conductivity discontinuities, which are equivalent to the contribution of double-layer current sources $-(\sigma'_k - \sigma''_k) \phi \mathbf{n}$ distributed on the interfaces between regions of different conductivity [281, 323]. The electric potential is continuous across the interfaces between regions designated by single prime and double prime [115],

$$\phi'_k = \phi''_k, \quad (3.24)$$

and so is the normal component of the current density [115],

$$(\sigma'_k \nabla \phi'_k) \cdot \mathbf{n} = (\sigma''_k \nabla \phi''_k) \cdot \mathbf{n}. \quad (3.25)$$

Since $\sigma''_1 = 0$, the zero-flux condition at the surface S_1 applies.

In the general case of irregularly shaped boundaries, one must solve Eq. 3.23 numerically to find the potential distributions on, for example, the torso surface or epicardium. Here, we accomplished this using the BEM [164, 330, 430] that required the closed surfaces to be tessellated into triangular elements defined by M nodes. The electric potential Φ at the torso boundary is then calculated from a discretized version of Eq. 3.23 in matrix form [247],

$$\Phi = 2\Phi_\infty + \mathbf{M}\Phi, \quad (3.26)$$

where Φ_∞ is a vector of discrete potentials evaluated at nodes of the tessellated boundaries that would be produced if the given sources were embedded in an infinite homogeneous conductor (Eq. 3.22). The elements of matrix \mathbf{M} ($M \times M$) are geometrical integrands, which can be calculated analytically [247]. Although Eq. 3.26 is singular, it can be deflated [226] and solved by means of the noniterative fast forward method [297]. This formalism has been described in detail elsewhere [159, 296, 297].

3.3.2 Extracardiac magnetic field

The same cardiac primary sources that generate extracardiac electric potentials also generate an associated extracardiac magnetic field. To validate our model of the human ventricular myocardium more thoroughly, we also compared the simulated with the measured magnetic field where such measurements were available (see Chapter 4). In this subsection, we introduce the governing equations for calculating the extracardiac magnetic field as they apply to our model of propagated excitation used in conjunction with the BEM. The derivation of the equations [116, 129, 151] is presented elsewhere in more detail.

Whether the extracardiac magnetic field contains information that is absent in the extracardiac electric potentials is yet to be determined [282, 321, 410, 411]. In their attempt to do so, based on the theoretical reasoning, Sepulveda and Wikswo [332] used the bidomain model of cardiac sources in conjunction with the FEM to simulate the magnetic field of a 2-D anisotropic bisyncytium. They pointed out that under the equal anisotropy ratio assumption, the magnetic field vanishes. Roth et al. [313] investigated qualitatively the magnetic field arising from the spiral arrangement of fibers near the ventricular apex. Based on their earlier hypothetical model of

electrically silent sources [315], they argued that such spiral anisotropy generates sources that are detectable only by measurements of the magnetic field.

Although we use the equal anisotropy ratio condition to predict the wavefronts of propagated activation, we use the oblique dipole model to calculate the extracardiac magnetic field. Within this concept, the sources at any point of the bidomain region H are constructed as two dipoles (isotropic and axial), and, therefore, the theoretical restriction of a nonzero magnetic field does not apply [50]. Assuming that the primary sources $\mathbf{j}^i = -\mathbf{D}_i \nabla v_m$ are embedded in an unbounded homogeneous monodomain, the extracardiac magnetic field \mathbf{B} can be obtained from Biot-Savart's law [116],

$$\mathbf{B}_\infty = -\frac{\mu_0}{4\pi} \left\{ \sigma_t^i \int_H \nabla v_m \times \nabla R^{-1} dV + (\sigma_t^i - \sigma_l^i) \int_H (\nabla v_m \cdot \mathbf{a}_3) \mathbf{a}_3 \times \nabla R^{-1} dV \right\} . \quad (3.27)$$

In an experimental setting, the extracardiac magnetic field is typically measured normal to the surface of the tissue or normal to the anterior chest of a patient at m sensor locations [369]. To account for the influence of the realistic boundaries, we use the BEM. The magnetic field can be then expressed in matrix form as [151],

$$\mathbf{B}_n = \mathbf{B}_{\infty,n} + \mathbf{A} \Phi , \quad (3.28)$$

where Φ is a vector of discrete potentials on tessellated boundary surfaces (Eqs. 3.26) and $\mathbf{B}_{\infty,n}$ is a vector of normal magnetic field values at m sensor locations associated with an infinite homogeneous medium (Eq. 3.27). Matrix \mathbf{A} ($m \times N$) contains geometrical integrands, which can be calculated analytically [94].

3.4 Summary

In this chapter, we have presented the methodology for simulating propagated excitation and calculating the extracardiac electric potentials and magnetic field in a realistic model of the human ventricles that is theoretically tractable and computationally feasible. Our approach rests on a pair of simplifying assumptions.

First, the equal anisotropy ratio condition must be assumed to obtain the governing equation (Eq. 3.19) for calculating the wavefronts of propagated activation. In the light of measurements that have shown that the anisotropy ratio in the intracellular medium differs from that in the interstitial medium [44, 307, 308], such an assumption would appear to be a restriction. However, numerical results by Barach and Wikswo [19] and Colli Franzone et al. [53], both based on models that used an unequal anisotropy ratio, showed that the velocity ratio of propagated activation in the longitudinal and transverse directions is primarily determined by the *intracellular* anisotropy ratio of conductivity. The main difference between equal and unequal anisotropy ratio models is in the different paths of ohmic currents [18, 22, 311]. However, Wikswo et al. [412] noted that this difference may not be as important as first expected for the spread of *electrotonic* currents during the normal process of propagated activation. It may be that our simplifying assumption of an equal anisotropy ratio does *not* significantly affect propagated activation in structurally normal myocardial tissue.

The second assumption on which our approach rests is that the extracardiac electric potentials and magnetic field are calculated via the oblique dipole model, which accounts for the effect of anisotropy in calculating cardiac primary sources.

Although this model relaxes the equal anisotropy ratio condition used by the propagation model, it introduces the assumption that the composite bidomain region H is an isotropic homogeneous monodomain. This assumption is supported by the experimental findings of Geselowitz et al. [119], which showed that the extracardiac potential distribution is not qualitatively altered by neglecting the anisotropic nature of volume currents. Colli Franzone et al. [55] reached a similar conclusion in their modeling study.

Chapter 4

Epicardial potentials during the initial phase of ventricular activation

4.1 Introduction

One relatively new technique for investigating the spread of propagated excitation within the underlying fibrous intramural structure consists in recording a large number of unipolar electrograms on the endocardial surface [32, 138, 187, 228, 372] or, more often, on the epicardial surface [9, 10, 25, 26, 32, 58, 357, 373, 374, 375, 376, 377, 399] of the ventricles during ectopic pacing. The main advantage of measuring such epicardial or endocardial potential distributions over distributions of activation times (isochronal maps) [15, 35, 77, 139, 178] is that potential distributions provide information about the spread of activation even before it reaches the epicardial or endocardial surface. Its main disadvantage—the fact that it is an invasive procedure—has largely limited its use to experimental investigations performed on animals.

Several seminal studies carried out by Taccardi and coworkers [25, 58, 357, 377] have demonstrated that ectopic pacing on the epicardium of canine ventricles gen-

erates epicardial potential distributions on which a distinct pattern—an elongated central area of negative potential and two adjacent areas of positive potential—is readily apparent. The center of the negative area corresponds to the site of the origin of activation, and the positive potentials (the R wave) arise in those areas of the epicardial surface toward which activation is spreading along the direction of fibers [25]. Similar potential distributions, with a negative area flanked by two positive areas, have been observed during ectopic pacing in deeper layers of the ventricular wall even before the arrival of activation at the epicardial surface [32, 357, 374, 375, 377].

It has been hypothesized that such potential distributions reflect the underlying intramural fibrous structure of the ventricular myocardium. In fact, the direction of the axis joining the two maxima recorded on the epicardial surface has correlated well with the direction of fibers near the intramural pacing site. During the propagation of activation through deeper layers of the myocardial wall, the positive areas have been observed to expand and rotate CCW when the activation wavefront propagates from the epicardium to the endocardium, or CW when it propagates in the opposite direction. This expansion-rotation of the epicardial potentials is attributed to the rotation of intramural myocardial fibers—described in Chapter 2—in the ventricular wall through which the activation wavefront is spreading.

To test this hypothesis, Watabe et al. [399] interrupted activation that had been initiated ectopically from the epicardial surface, by creating localized, nontransmural necroses at various depths in the LV wall. They noted that the epicardial potential distributions for activation sequences elicited from certain pacing sites are transiently missing some of the positive areas while those areas undergo CCW rotation-

expansion. They found that the direction of the axis joining the pacing site and the site of missing positive potentials paralleled that of the average fiber direction in the necrotic mass.

Taccardi et al. [376] measured in great detail patterns of potential distributions over the epicardium of the RV and LV that were ectopically paced from a number of sites distributed throughout the ventricular wall. In agreement with the previous findings [25, 357, 377, 399], they concluded that the epicardial potential distributions reflect the ventricular fibrous structure during both the initial and later phases of activation. In addition, they observed a marked asymmetry and fragmentation of the positive areas. Their meticulously executed study provides an invaluable source of information for the validation of our realistic model of the ventricular myocardium.

The primary objective of this and the next chapter is to describe an initial validation of our realistic ventricular model by systematically comparing the epicardial potential distributions produced by the simulation of activation sequences from known initial sites to epicardial potential distributions actually recorded by Taccardi et al. [376] and Watabe et al. [399] during pacing at corresponding sites in canine hearts. The simulated epicardial potentials during the initial phase of ventricular activation (< 18 ms from the time of stimulation) are presented in this chapter; the evolution of epicardial potential distributions during the later phases of activation will be described in the next. The purpose of such an organization is to provide a clearer analysis of the complex activation process. Section 4.2 will describe simulations of the early phase of propagated activation in a 3-D slab of myocardial tissue with rotating anisotropy, and results of simulations in our anatomically accurate model of human

ventricles will be presented in Section 4.3.

4.2 Slab model of myocardial tissue

4.2.1 Model description

Simulations in a slab with rotating anisotropy can provide a valuable insight into the process of propagated activation through the ventricular wall—and into its relationship with the electric potentials and magnetic field—since the parameters that determine the fibrous architecture of the slab can be rigorously controlled and easily manipulated. On the other hand, such a simplified model can simulate only the early phase of propagated activation (< 18 ms or, more conservatively, < 12 ms) when the activation wavefront is small (diameter < 15 mm).

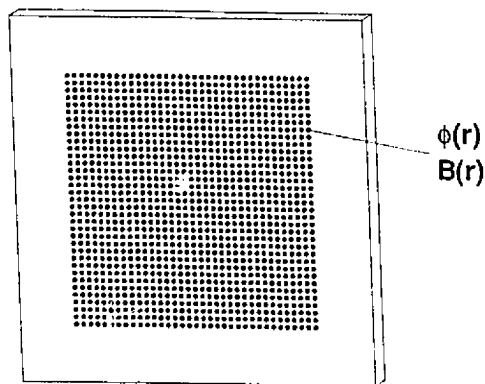


Figure 4.1: The slab model of myocardial tissue measuring $100 \times 100 \times 10$ mm. The distributions of electric potential and magnetic field were calculated 0.5 mm and 2.5 mm above the “epicardial” surface, respectively, on a 35×35 grid with 2-mm spacing.

We used as our idealized myocardial tissue a 100×100 mm, 10-mm-thick parallelepiped (Fig. 4.1). This slab was oriented so that its “epicardial” and “endocardial” surfaces were vertical, with the “epicardium” being represented by the anterior face.

It was reconstructed with a resolution of 0.5 mm per voxel and had an assigned rotating anisotropy. The fiber direction rotated linearly and CCW from -58° on the slab's "epicardial" surface to 42° on its "endocardial" surface, as in Streeter's equations describing the fiber direction in the compacta [364]; anisotropy in each layer of the slab was uniform (i.e., with the fiber direction constant within the layer). We then simulated propagated activation in myocardial tissue from the center of the epicardial surface of the slab at increasing intramural depths (at 0.5-mm increments) along the axis perpendicular to the epicardial plane. The electric potentials and the component of the magnetic field normal to the slab's anterior face were calculated for each activation sequence at 1225 field points (a regular 35×35 grid with 2-mm spacing) located, respectively, 0.5 mm and 2.5 mm above the epicardial surface of the slab. The grid spacing was therefore comparable to the thickness of the activation wavefront (1–2 mm) [272, 394, 403]. We neglected the effect of the boundary surfaces to the extent that we used equations for the semi-infinite homogeneous medium (see Appendix B) and therefore calculated only the first terms in Eqs. 3.26 and 3.28. The electric potentials and magnetic field were calculated every millisecond within 18 ms after the onset of ectopic activation. Results were displayed as instantaneous isopotential and isofield contour maps for each millisecond of the sequence. The entire sequence of propagated activation was shown as isochronal maps of activation (each isochrone connects points that had been activated at the same time) taken at cross sections through the slab that were parallel to the anterior surface.

We also used our model to study the effect of subepicardial necrosis on the electric potentials on, and the magnetic field above, the "epicardial" surface during the initial

phase of an activation sequence initiated on the epicardial surface of the slab. We simulated the necrosis by changing myocardial cells within a hemisphere that had a radius of 2.5 mm and its center on the epicardial surface to nonexcitable (“dead”) cells. Two cases were considered: in the first, the center of the necrotic region was 8.6 mm distal to the initial site of activation along the epicardial fiber direction; in the second, the center of necrosis was 5.7 mm from the initial site in the direction perpendicular to that of the epicardial fibers.

4.2.2 Parameter calibration

The velocity of propagated activation in the bidomain model depends on the conductivity of myocardial tissue along and across the fiber direction ($\sigma_t^{i,e}$ and $\sigma_t^{i,c}$). Unfortunately, the conductivity values reported in the literature vary [44, 307, 308]; they cannot be measured directly but they must be estimated from other measurable quantities under assumptions whose selection amounts to adopting a certain model of myocardial tissue. Therefore, estimates of tissue’s electrical parameters are, as has been pointed out by Plonsey and Barr [285], as accurate as a given model. To derive analytical solutions that relate the conductivity of myocardial tissue to measurable quantities, Plonsey and Barr had to assume the equal anisotropy ratio condition; no similar expression for the case of more complex anisotropy has yet been derived.

Because we agree with Plonsey and Barr’s conclusion that in the absence of a general solution, any conductivity values derived from measurements must be interpreted very cautiously, we decided to use the reported values of electrical parameters only as guidelines. The calibration, i.e., fine tuning, of the model was then performed by comparing the macroscopic observable features in the distributions of isochrones

Table 4.1: Values of Propagation Velocity

Velocity (m/s)	Clerc [44]	Roberts et al. [307]	Roberts and Scher [308]	Frazier et al. [105]	Taccardi et al. [376]
θ_l	0.48 ± 0.04	0.58 ± 0.08	0.57 ± 0.06	0.65 ± 0.10	0.68 ± 0.11
θ_t	0.16 ± 0.01	0.25 ± 0.03	0.24 ± 0.03	0.30 ± 0.08	0.31 ± 0.05

Values are means \pm SD.

and epicardial potentials to the corresponding measured quantities [376].

We take the velocity of propagated activation as the foundation for determining the values of the tissue parameters in our model because unlike the conductivity of myocardial tissue, propagation velocity is related directly to measurements derived from cardiac electrograms [26, 44, 105, 307, 308, 376]. Table 4.1 summarizes the published values for the velocity of propagated activation in the longitudinal and transverse directions with respect to the fiber axis (respectively, θ_l and θ_t). The reported mean values vary considerably; 0.16–0.31 m/s for θ_t and 0.48–0.68 m/s for θ_l . We chose 0.27 m/s for θ_t and 0.77 m/s for θ_l , values that are within the error bounds of the recent measurements by Taccardi et al. [376]. Using $\chi = 225 \text{ cm}^{-1}$ for the surface-to-volume ratio, $C_m = 1.0 \text{ } \mu\text{F}/\text{cm}^2$ for the membrane capacitance, and the square-root relation between the velocity of propagation in the given direction and corresponding conductivity [44, 245], we obtained conductivity values of $\sigma_l^i = 2.75 \text{ mS}/\text{cm}$ and $\sigma_t^i = 0.33 \text{ mS}/\text{cm}$. The values of these chosen parameters are very close to those used by Colli Franzone et al. [55] and similar to those used by other investigators [292, 144]. The propagation parameters chosen for our numerical simulations are summarized in Table 4.2.

Table 4.2: Selected Propagation Parameters

Equal anisotropy ratio k	1
Spatial step d	0.5 mm
Time step δt	0.1 ms
Resting potential v_r	-84 mV
Threshold potential v_{th}	-60 mV
Peak potential v_p	+20 mV
Membrane capacitance C_m	1 $\mu\text{F}/\text{cm}^2$
Surface-to-volume ratio χ	225 cm^{-1}
Transverse intracellular conductivity σ_t^i	0.33 mS/cm
Longitudinal intracellular conductivity σ_l^i	2.75 mS/cm

The second stage in calibrating our model was choosing the factor for combining the normal and axial components of the cardiac primary sources in the oblique dipole model. To determine this empirical value, we carried out the simulations presented below with a combining factor of 0.1–0.9, then compared our simulations with experimental data [376] and simulations using a model with an unequal anisotropy ratio [52, 53]. We found that the optimal value of the combining factor was 0.396.

4.2.3 Activation wavefronts for epicardial, intramural, and endocardial pacing

Epicardial pacing. Fig. 4.2 shows activation isochrones at 2-ms increments, constructed as the intersections of the propagated activation wavefront with the planes parallel to the epicardial surface of the slab. For comparison, the fiber directions in the corresponding planes are also displayed. The isochrones on the epicardial surface are virtually elliptical, with the major axis of the ellipse parallel to the epicardial fiber direction; thus as expected, conduction velocity is greater along the fibers than

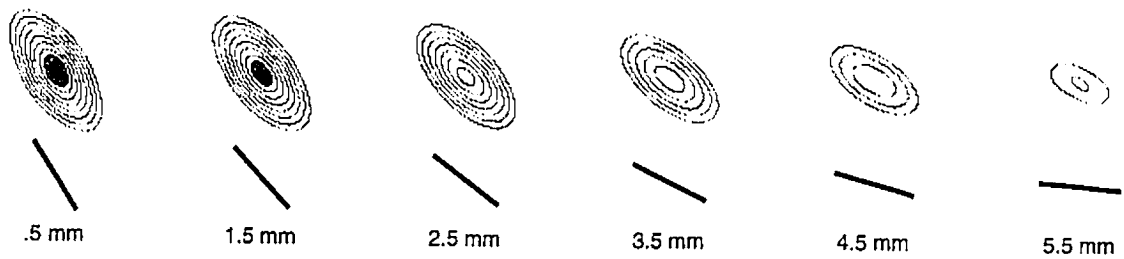


Figure 4.2: Isochronal maps at different intramural depths of the slab model for an activation propagating for 18 ms from the onset of epicardial pacing. Maps are displayed at 2-ms increments; the region activated during the first 6 ms is shaded; the direction of the fibers in each plane is indicated by a thick line below the isochrones.

across them. With increasing intramural depth, the direction of the major axes of the isochrones rotates CCW so that the three-dimensional activation wavefront has the shape of a left-handed helicoid. However, the rotation of the helix lags behind the rotation of the fiber direction, and the amount of lagging increases with intramural depth. The angles between the major axis of the ellipse and the fiber direction in a given plane, as a function of depth from the epicardial surface, agree with the experimental findings [105].

Intramural and endocardial pacing. Near the pacing site (at 5.5 mm from the epicardial surface), the isochrones have an elongated oval shape, departing from that of an ellipse, with the major axis aligned with the fiber direction in that plane (Fig. 4.3). For propagated activation moving from the pacing plane toward the epicardium (top row, from right to left) or endocardium (bottom row, from left to right), the direction of the major axes of these quasielliptical isochrones rotates CW and CCW, respectively. As for the previous case, the rotation of the direction of the major axes of the isochrones in a given plane lags behind that of the fiber direction.

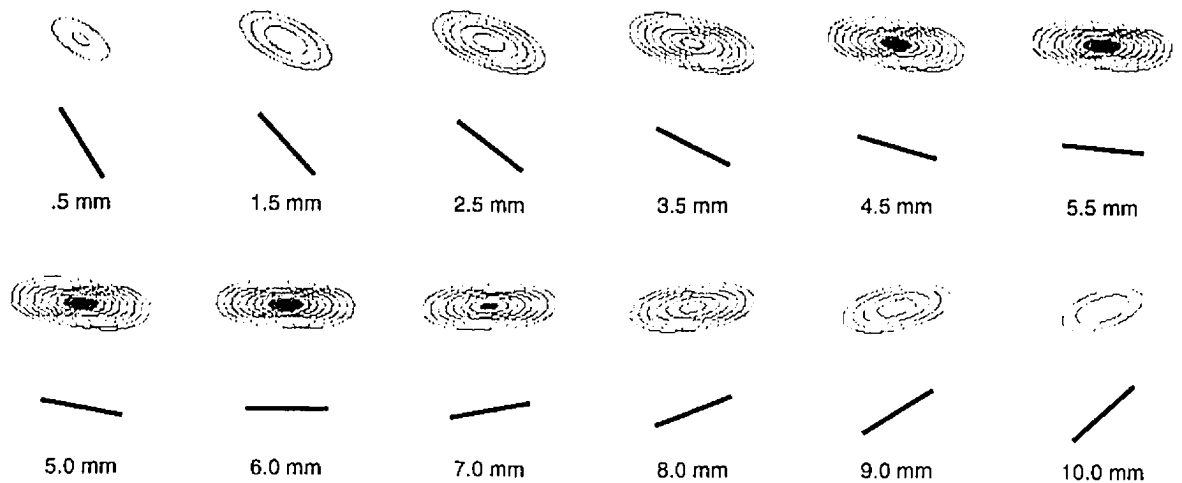


Figure 4.3: Isochronal maps of an activation sequence simulated in the slab model for intramural pacing. The pacing site was 5.5 mm from the epicardial surface; see the legend of Fig. 4.2 for details of the layout.

which agrees with the experimental data [105].

Endocardial pacing generates isochrone patterns similar to those generated by epicardial pacing, with the major axis of endocardial isochrones oriented along the endocardial fiber direction (not shown). As propagated activation moves toward the epicardial surface, the major axes of the isochrones rotate CW and, again, lag behind the fiber rotation.

Correspondence with other simulation studies. Our simulation results are consistent with simulated isochrones during the early phase of activation that were obtained by Colli Franzone et al. [53], who also simulated isochrones during the later phases of the activation sequence. To make this comparison more thorough, we simulated the activation sequence for up to 48 ms after the onset of activation. Fig. 4.4 illustrates the propagation of activation—initiated by pacing at a 5-mm depth—

on the epicardial surface and through the thickness of the wall. The breakthrough occurs at the center of the epicardial face (Fig. 4.4A), and, initially, activation spreads rapidly from the breakthrough site, because the convex-shaped propagation wavefront intersects with the epicardial plane. Isochrones have an oblong shape; the major axis is—as expected—rotated CCW relative to the epicardial fiber direction but is rotated CW relative to the fiber direction in the pacing plane. Figs. 4.4B and 4.4C display the intramural course of propagated activation.

Since the fiber direction halfway from the epicardium to endocardium is nearly parallel to the plane of the cross section in Fig. 4.4B, the wavefront of propagated activation moves fastest in the midwall portion of the slab. When the plane of the cross section is nearly perpendicular to the midwall fiber direction (Fig. 4.4C), the wavefront of propagated activation moves mainly across the fibers in the midwall portion of the slab and becomes progressively more aligned with the fiber direction on the epicardial and endocardial surfaces. After the epicardial and endocardial breakthroughs, the activation wavefront becomes V-shaped, as it propagates faster on the epicardial and endocardial surfaces than in the central layers of the slab. The activation wavefront is thus returning from the epicardial and endocardial planes toward the intramural plane of pacing. This somewhat unexpected feature has been actually observed in experiments [38, 105, 373] and was later reproduced in simulations by Colli Franzone et al. [53] and Keener and Panfilov [185]. Similar features can be observed when the sequence is initiated on the epicardial and endocardial surfaces of the slab (not shown).

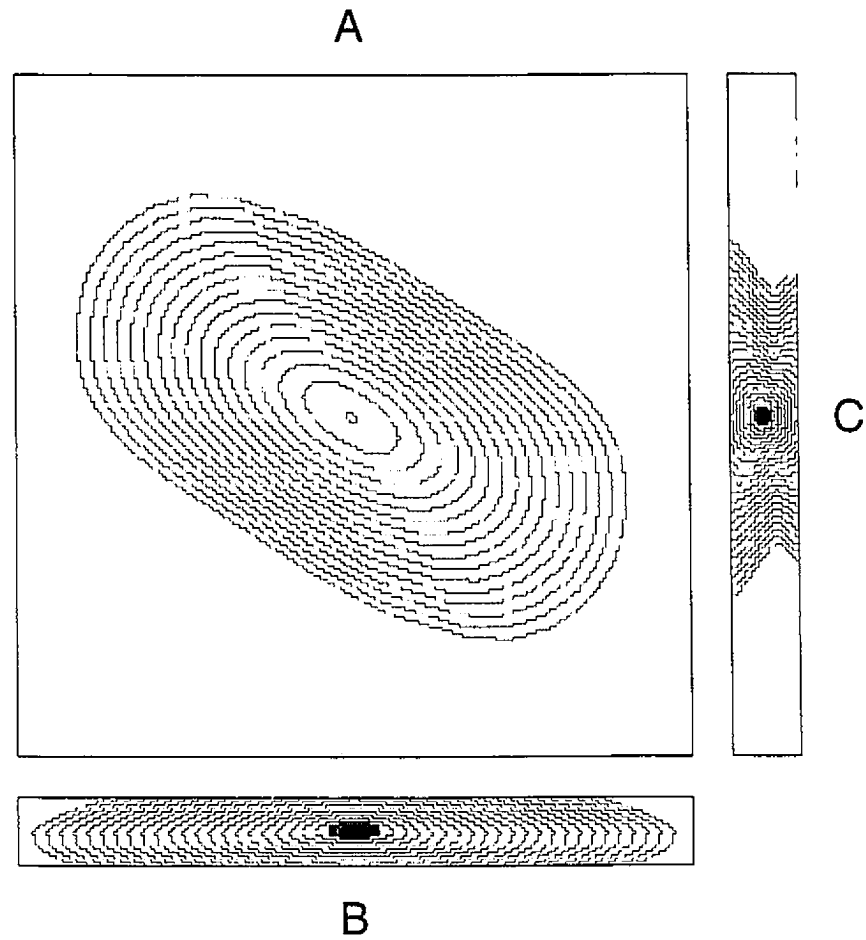


Figure 4.4: Isochronal maps of a 48-ms-long activation sequence initiated at the center of the slab model. The region activated during the first 6 ms is shaded; isochronal maps are shown on the epicardial plane (A) and on two cross sections perpendicular to the epicardial plane taken through the slab at its center and parallel to its rectangular faces (B and C).

4.2.4 Maps of the electric potentials and magnetic field for epicardial, intramural, and endocardial pacing

Epicardial pacing. Fig. 4.5 shows maps of the electric potentials at 9 and 18 ms after the onset of activation initiated on the epicardial surface of the slab. Epicardial pacing generates the potential pattern with an elliptically shaped negative region extending over the area reached by the wavefront of propagated activation shown by the isochronal maps in Fig. 4.2. Densely packed negative isopotential lines reveal the approximate intersection of the wavefront with the epicardial surface. The minimum is at the center above the stimulus site. The negative region is flanked by two positive areas with semioval isopotential lines, and the maxima are of approximately equal amplitude.

The direction of the major axis of elliptical negative isopotential lines coincides with the epicardial fiber direction and the direction of the major axis of the epicardial isochronal map (Fig. 4.2), while the direction of the axis joining the maxima is slightly (8° at 9 ms after the onset of activation) rotated CCW. Also, the pattern of the positive areas is not fully symmetrical with respect to the axis joining their maxima, but its positive areas show a slight CCW expansion. This expansion becomes more pronounced later in the activation sequence, e.g., at 18 ms after the onset of activation (Fig. 4.5B). As shown in the previous subsection, the CCW rotation and expansion occurs because the activation wavefront spreads through deeper layers of the CCW-rotating fibers in the myocardial wall. These observations agree with experimental work [376, 399] and simulation studies [52].

Fig. 4.6 shows maps of the magnetic field at 9 and 18 ms after the onset of

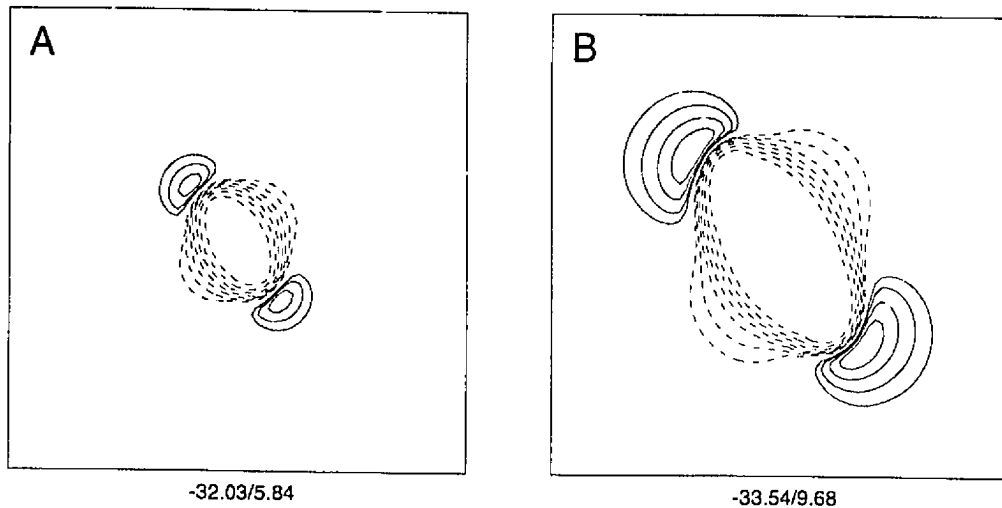


Figure 4.5: Maps of the electric potentials on the epicardial surface of the slab simulated for epicardial pacing at 9 ms (A) and 18 ms (B) after the onset of activation. Isopotential contours are plotted for equal intervals, with solid contours representing the positive and broken contours the negative values of potential; the values of the minimum and maximum are given (in mV) at the bottom of each map.

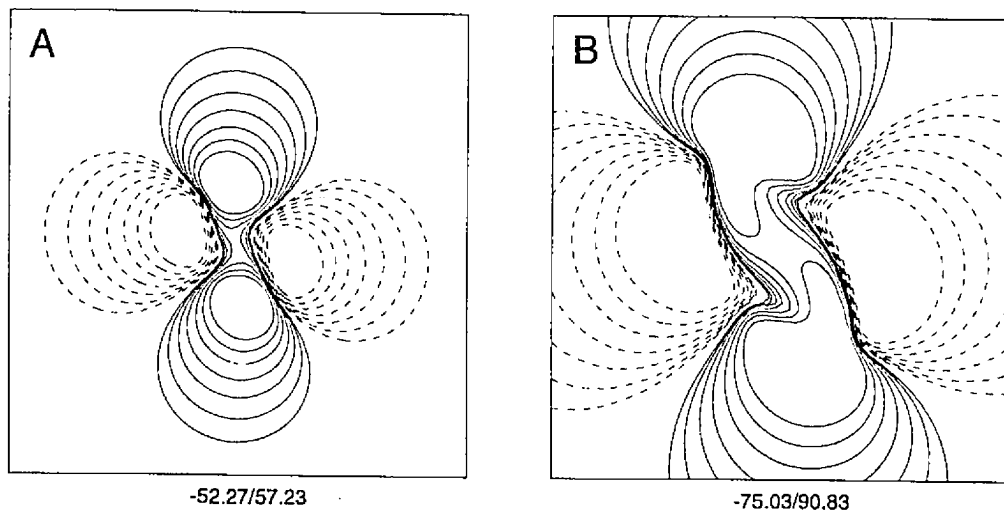


Figure 4.6: Maps of the magnetic field 2.5 mm above the epicardial surface of the slab simulated for epicardial pacing at 9 ms (A) and 18 ms (B) after the onset of activation. Isofield contours are plotted for equal intervals, with solid contours representing the magnetic field directed from the epicardial to the endocardial surface of the slab; the values of the minimum and maximum (in pT) are given at the bottom of each map.

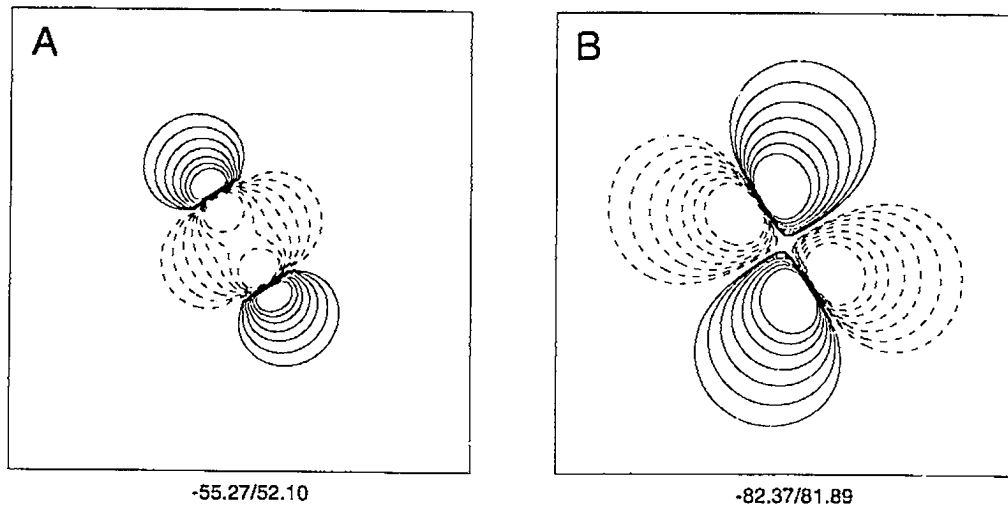


Figure 4.7: Maps of the electric potentials (A) and magnetic field (B) due to the best-fitting pair of colinear dipoles. Compare with corresponding maps in Figs. 4.5A and 4.6A; see the legends of Figs. 4.5 and 4.6 for details of the layout.

activation initiated on the epicardial surface of the slab. Four regions of alternating field direction are located almost symmetrically around the pacing site in a quatrefoil (cloverleaf) pattern; one of the diagonals of the quatrefoil pattern is approximately parallel to the epicardial fiber direction. The values for the positive and negative extrema, which are on the order of 100 pT compare well with measured values [361]. The simulated pattern of the magnetic field also corresponds well with that obtained by Barach and Wikswo [19] in a 2-D anisotropic sheet of myocardial tissue and with the pattern measured experimentally by Staton et al. [361]. At later times of the activation sequence, the central positive area of the quatrefoil deforms into a CCW finger-like twist, which is most likely due to the effect of the rotating fibers.

The patterns of the electric potentials and magnetic field during the initial phase of activation resemble those of two opposing dipoles oriented along the major axis and located near the ends of an elliptical wavefront of propagated activation [228]. For

these maps of the electric potentials and magnetic field that were obtained at each millisecond of the activation sequence via the oblique dipole model, we calculated the pair of colinear dipoles that fitted our simulated data best in a least-squares sense [293]. Fig. 4.7 shows maps of the electric potentials and magnetic field generated by the best-fitting colinear dipole model at 9 ms after the onset of activation. The correlation coefficient between the simulated data and the data obtained via this best-fitting colinear dipole model is 0.6756 (with a normalized rms error of 0.77) for the potential map and 0.8286 (with a normalized rms error of 0.55) for the magnetic field map. The correlation coefficient is considerably lower for the best-fitting distributions at 18 ms after the onset of activation (maps are not shown), being 0.4472 for the potential map and 0.5257 for the magnetic field map. As can be seen from the electric potential maps in Figs. 4.5 and 4.7, the colinear dipole model qualitatively recovers only the leading edge of the wavefront along the fiber direction; the dipolar features of the model causes the potential jump to be overestimated (107 mV in the colinear dipole model compared to 38 mV in the oblique dipole model). On the other hand, the colinear dipole model appears to be reasonably adequate for recapturing the magnetic field patterns in the early phases (< 10 ms) of the activation sequence.

Epicardial electrograms. The results described above for the instantaneous maps of electric potentials showed that the positive regions appear only in those areas toward which the activation wavefront moves along the fibers. To further test whether our model can also accurately simulate recorded epicardial electrograms [355, 376], we simulated the ectopic activation sequence up to 48 ms after the onset of activation.

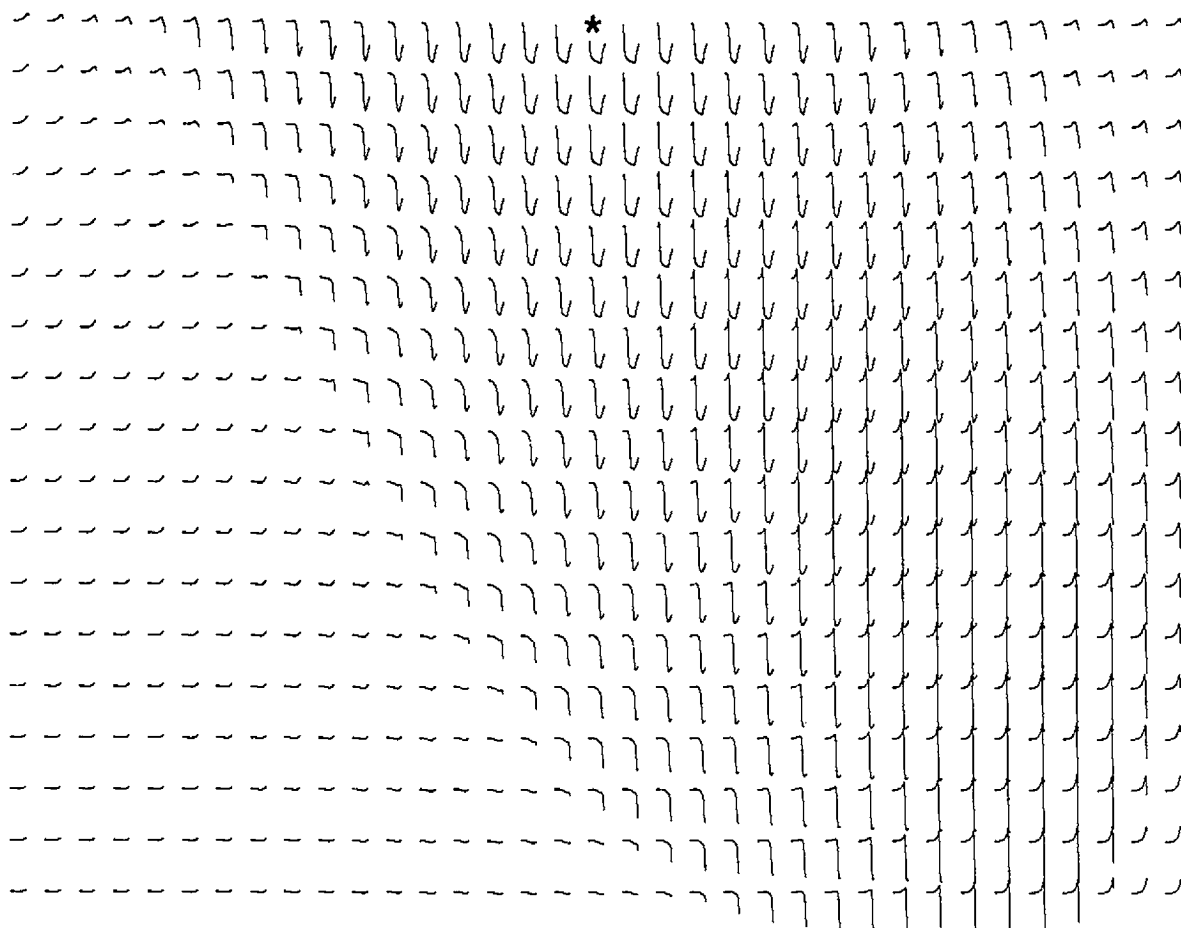


Figure 4.8: Epicardial electrograms for epicardial pacing of the slab model during 48 ms after the onset of activation. Only electrograms from the lower portion of the 1225-point measurement grid are displayed; the upper part can be constructed by symmetrical transformation. The stimulus was delivered at the center of the top line (marked by *). The initial positive deflection (the R wave) occurs only at those sites toward which the activation wavefront is spreading along the fibers.

The initial positive deflection (the R wave) occurs only in those areas toward which the activation wavefront spreads along the fiber direction (Fig. 4.8); its magnitude increases, and the upstroke starts progressively later, as the distance increases from the pacing site. Negative potentials (the Q waves) occur within 15 mm or less from the pacing site in those regions toward which the activation wavefront moves across the fiber direction. Further away along the same direction, the electrograms feature a small R wave, but the initial deflection of those electrograms is negative. This finding shows the inadequacy of the classical theory of electrocardiography [329] based on a uniform double layer, which predicts only positive potentials in those areas toward which the activation wavefront is spreading. The observed features in our simulations agree with data from experimental studies of Spach et al. [355] and Taccardi et al. [376].

Intramural pacing. Fig. 4.9 depicts maps of the electric potentials and magnetic field at 9 ms after the onset of activation initiated intramurally at a depth of 5 mm from the epicardial surface of the slab. Intramural pacing produces potential patterns that have general features similar to those generated by epicardial pacing, namely, the central negative region with surrounding positive areas. However, the negative isopotential lines stretch in the direction perpendicular to the fiber orientation in the given pacing plane, and the positive isopotential lines become more rounded. The position of the maxima or—in maps of the magnetic field—the extrema, rotates CCW with increasing intramural depth. The direction of the axis joining the two maxima is nearly parallel to that of fibers in the pacing plane. With increasing pacing depth, the magnitude of the extrema in maps of both the electric potentials and the magnetic

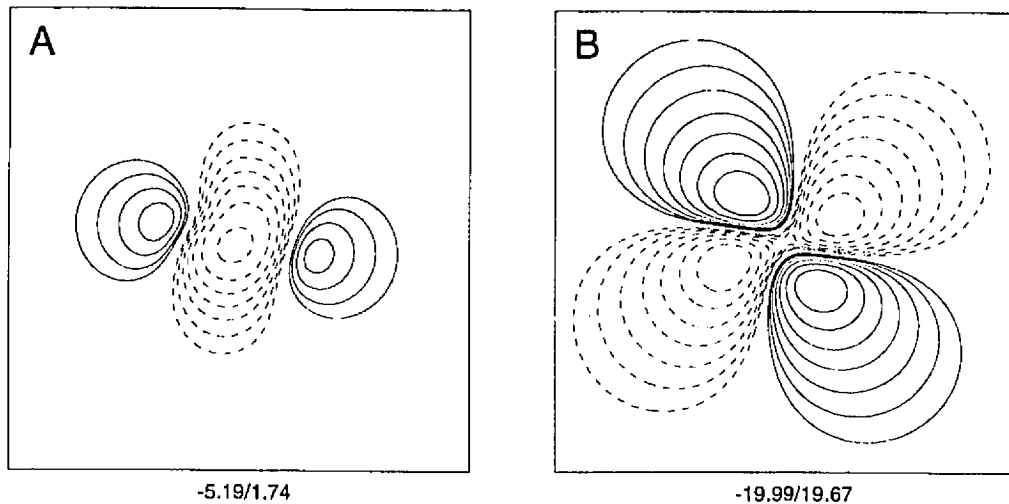


Figure 4.9: Maps of the electric potentials (A) and magnetic field (B) of the slab model simulated for intramural pacing at 9 ms after the onset of activation. Comparison with Figs. 4.5A and 4.6A shows the CCW rotation of the extrema. See the legends of Figs. 4.5 and 4.6 for details of the layout.

field decreases, while the distance between the extrema increases. This is due to the increased distance between the source and field points. Overall, our results agree with simulations performed by Colli Franzone et al. [52].

Endocardial pacing. Fig. 4.10 shows maps of the electric potentials and magnetic field at 9 ms after the onset of activation initiated on the endocardial surface of the slab. Instead of the expected pattern with two maxima and a central minimum (which is characteristic for the epicardial and intramural initial sites), potential maps initially feature an oblong positive area that has a pair of adjacent maxima with amplitudes larger than those of maxima in maps associated with intramural initial sites. The minima have very small amplitudes and are located at the opposite corners of the slab, on the minor axis of the oblong positive area. The direction of the axis

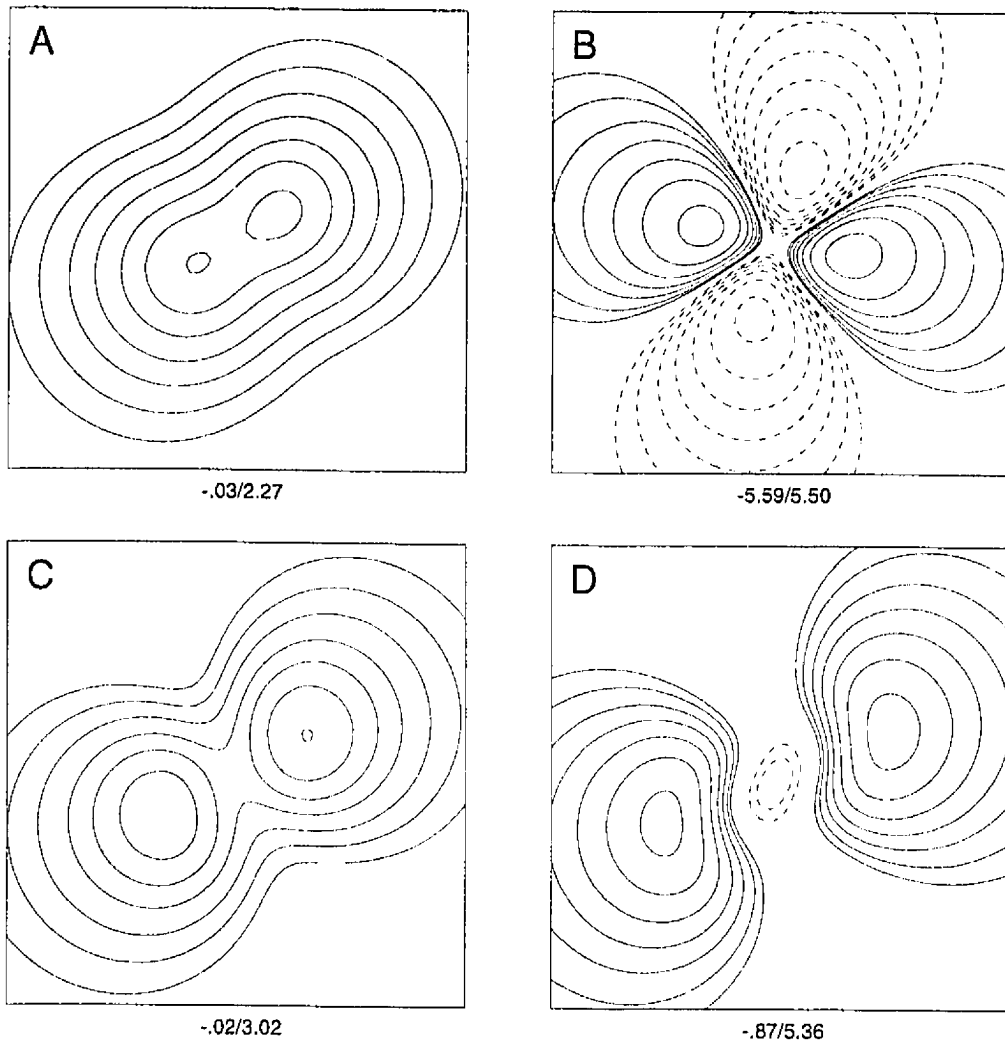


Figure 4.10: Maps of the electric potentials (A) and magnetic field (B) simulated for endocardial pacing at 9 ms after the onset of activation, and maps of the electric potentials simulated for endocardial pacing at 12 ms (C) and 18 ms (D) after the onset of activation. Instead of two peripheral maxima and a central negative area, which are characteristic for intramural stimulation, there is a single elongated mound of positive potential at 9 and 12 ms after the onset of activation (A and C). At 18 ms after the onset of activation (D), the usual pattern is established. See the legends of Figs. 4.5 and 4.6 for details of the layout.

joining the maxima (which is also the major axis of positive mound) is approximately parallel to the vector of endocardial fiber orientation. Later in the sequence, however, the distance between the maxima increases (as seen in the saddle-like mound at 12 ms after the onset of activation in Fig. 4.10C), and at around 18 ms after the onset of activation, the positive areas become separated by the negative area with a central minimum (Fig. 4.10D), thereby establishing the usual pattern familiar from instances of epicardial and intramural stimulation. These results agree with simulations by Colli Franzone et al. [52], who noted that endocardial pacing gives rise to an altered potential pattern on the epicardial surface of a slab model.

The absence of a central minimum in the initial potential pattern for endocardial pacing results from the contribution of a tray-shaped normal dipole layer to the electric potentials on the epicardial surface of the slab. The normal dipole layer is manifested as a projection of positive potentials on the recording plane. As the activation wavefront progresses further through the myocardial wall towards the recording plane, the contribution of the axial dipoles becomes progressively more important and later gives rise to the usual pattern with a central negative region. If the endocardial surface of the slab were exposed to intracavitary blood, with its high conductivity, the contribution of the normal dipole layer would become even more enhanced (increasing the amplitude of the positive mound and decreasing the contribution of the axial component) due to the Brody effect [36]. This effect has been discussed in the simulation study of Colli Franzone et al. [52].

Interestingly, endocardial pacing generates a magnetic field with general features no different than those for epicardial or intramural pacing. Comparison of the mag-

netic field maps at 9 ms after the onset of activation for epicardial (Fig. 4.6A), intramural (Fig. 4.9B), and endocardial (Fig. 4.10B) sites shows that the quatrefoil pattern rotates CCW with increasing pacing depth and that as the distance to the field points increases, the pattern becomes broader, with lower extremal values.

Our study has demonstrated that the potential patterns on the epicardial surface of the slab during the early phase of ventricular activation depend on the direction of fibers near the pacing site and that the direction of the axis joining the extrema in these patterns rotates CCW as the pacing depth increases. In general, we found a good correlation between the fiber orientation at the pacing site and the direction of the axis joining the maxima (or, for subendocardial pacing, the direction of the major axis of the positive mound) in potential maps at 9 ms after the onset of activation (Figs. 4.5A, 4.9A, and 4.10A). However, the total angle of CCW rotation of this axis was smaller than the total angle of rotation of the principal fiber orientation (83° compared with 100°). The rotation of the axis joining the maxima lags behind that of the fibers because the direction of the axis is affected by the intramural propagation of the wavefront and is therefore slightly rotated relative to the local fiber orientation (CCW for epicardial pacing or CW for endocardial pacing).

4.2.5 Effect of tipping fibers from the tangential plane on the electric potentials and magnetic field

To study how tipping fibers out of planes that parallel the epicardial plane affects the patterns of the electric potentials and magnetic field, we introduced a 5° imbrication angle pointing inward from the epicardium to the endocardium and from left to right when one views the epicardial surface of the slab. Fig. 4.11 shows maps of the electric

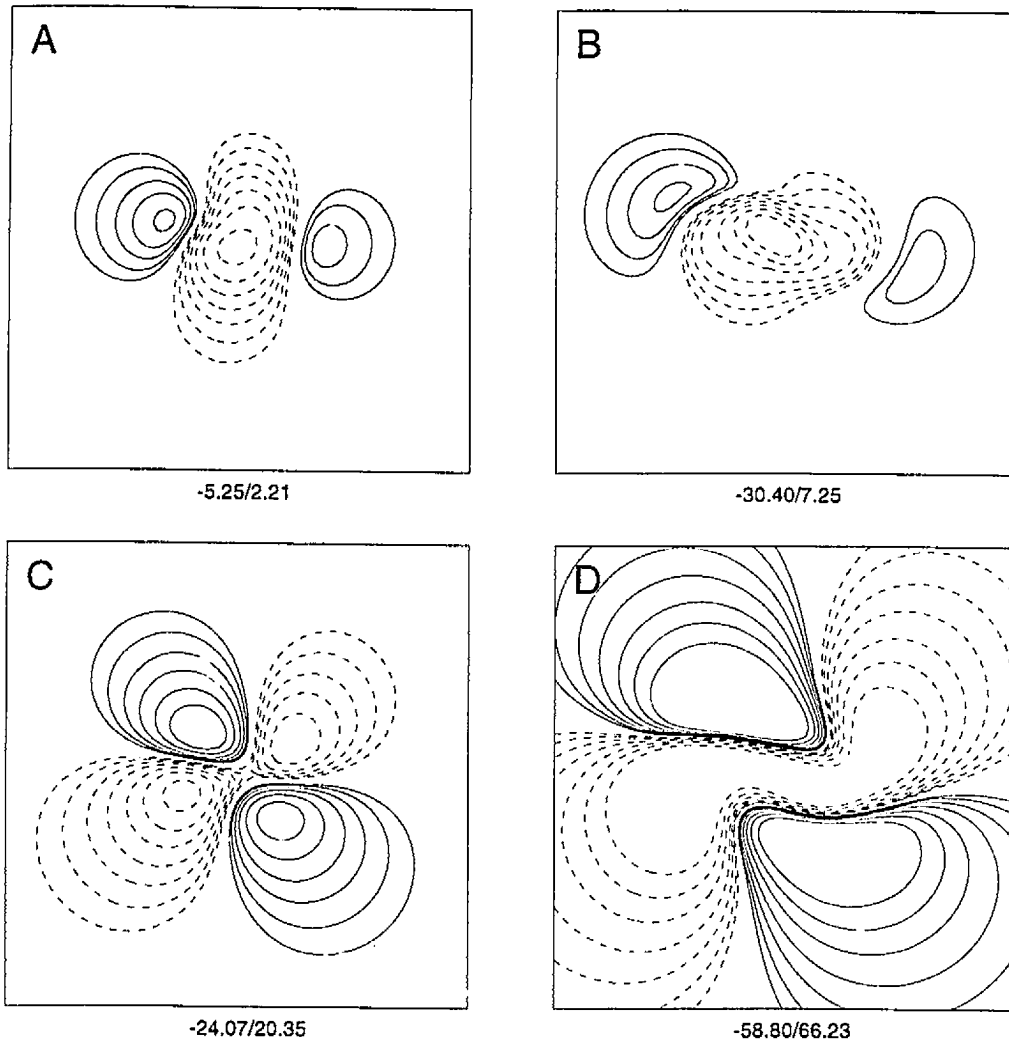


Figure 4.11: Maps of the electric potentials and magnetic field for intramural pacing in a slab with tipping of fibers out of planes parallel to the epicardium. The electric potentials were simulated at 9 ms (A) and 18 ms (B), and the magnetic field was simulated at 9 ms (C) and 18 ms (D), after the onset of activation. Compare with control maps in Figs. 4.9A and 4.9B. The areas of positive potentials have maxima of unequal amplitude, with the minimum progressively shifting toward the stronger of the maxima (on the left). See the legends of Figs. 4.5 and 4.6 for details of the layout.

potentials and magnetic field at 9 ms and at 18 ms after intramural pacing in the modified slab model. Tipping fibers out of planes causes an asymmetry of the positive potential areas (maxima of unequal amplitude) and a slight distortion of the negative region, with the minimum progressively shifting toward the stronger of the maxima (to the left of the central minimum). As in simulations performed in the slab model with no tipping, the axis joining the two maxima is approximately aligned with the fiber direction in the pacing plane at 9 ms after the onset of activation (Fig. 4.11A). At 18 ms after the onset of activation (Fig. 4.11B), positive areas undergo expansion-rotation, with the overall rotation of the axis joining the maxima in a CW direction. Tipping fibers out of the plane also produces asymmetrical pattern in magnetic field maps (Figs. 4.11C and 4.11D).

The results for potential maps in a slab in which fibers were tipped out of the plane parallel to the epicardial surface agree with the experimental results of Taccardi et al. [376] and the simulation study of Henriquez et al. [144]. No experimental or simulation results for the magnetic field of a slab with imbricating fibers are available yet.

4.2.6 Effect of subepicardial necrosis on the electric potentials and magnetic field

Figs. 4.12A and 4.12B show maps of the electric potentials and magnetic field at 9 ms after epicardial pacing for the case in which the axis joining the pacing site and the center of the simulated subepicardial necrosis is approximately parallel to the epicardial fiber direction. Comparison with control maps (produced by the same slab with no simulated necrosis) in Figs. 4.5 and 4.6 shows that necrosis causes a

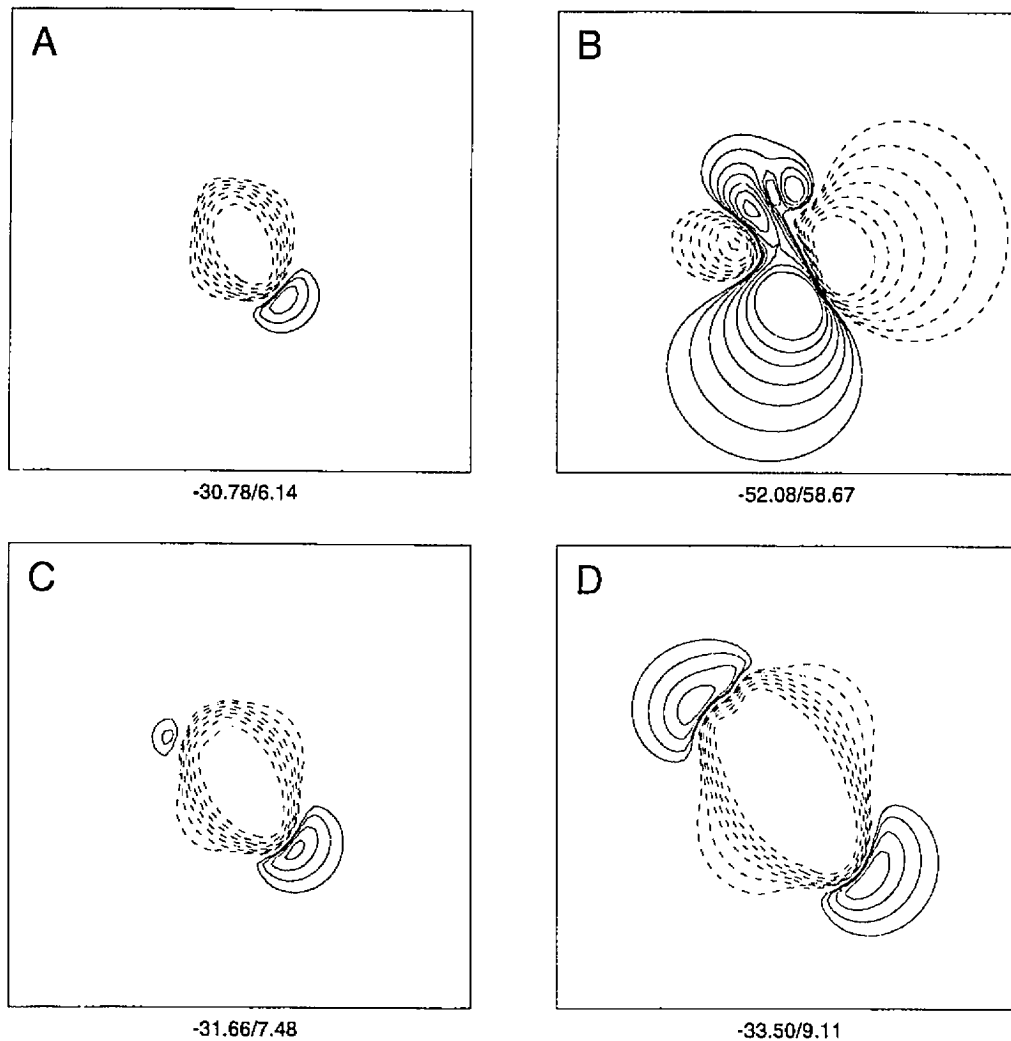


Figure 4.12: Maps of the electric potentials and magnetic field simulated for epicardial pacing in a slab with subepicardial necrosis. The electric potentials were simulated at 9 ms (A), 12 ms (C), and 18 ms (D) after the onset of activation, and the magnetic field was simulated at 9 ms after the onset of activation. Compare with control maps in Figs. 4.5A and 4.6A. The potential maximum is absent at 9 ms after the onset of activation; it reappears at 12 ms after the onset in a position shifted CCW relative to that for the control activation sequence. See the legends of Figs. 4.5 and 4.6 for details of the layout.

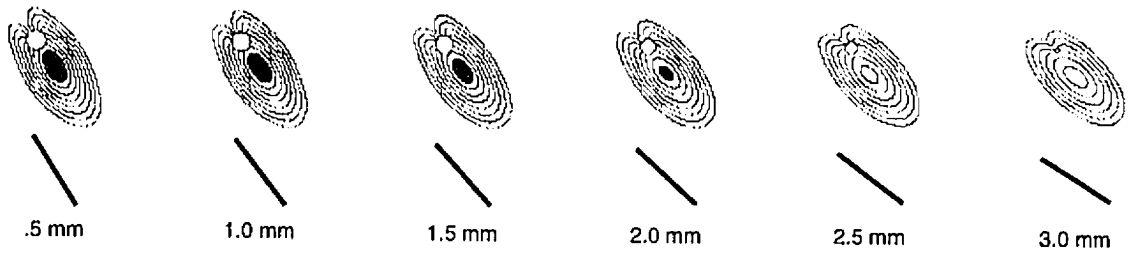


Figure 4.13: Isochronal maps of the activation sequence simulated for epicardial pacing in a slab with subepicardial necrosis. The activation wavefront is transiently distorted by the presence of the necrosis. See the legend of Fig. 4.2 for details of the layout.

complete disappearance of one positive area in the electric potential pattern and marked changes in the magnetic field pattern. These changes are due to a distorted activation sequence (Fig. 4.13).

Later in the sequence, the potential maximum reappears (Fig. 4.12C), however, its position is shifted CCW by approximately 10° (at 12 ms after the onset of activation) from that of the control activation sequence. The patterns of both the electric potentials (Fig. 4.12D) and the magnetic field (not shown) are restored to the control patterns at around 18 ms after the onset of activation, when the wavefront has already passed the necrotic region (Fig. 4.13). However, the maximum remains shifted CCW, and the small indent in the negative isopotential lines (Fig. 4.12D) reveals a concavity in the recovering leading edge of the wavefront. When the axis joining the pacing site and the necrotic region is perpendicular to the epicardial fiber direction, there is no loss of positive potentials or shift in the position of the maximum. The only effect of the simulated necrosis on the electric potential map is a hardly discernible indent in the negative isopotential lines along the minor axis of the ellipse (not shown).

The results for electric potentials on the epicardial surface of the slab with simulated subepicardial necrosis are in agreement with the experiments of Watabe et al. [399], who studied canine ventricular activation in the presence of necrosis created by the injection of a lugol solution. Currently, no corresponding measurements of the magnetic field are available. Barach and Wikswo [19] found a somewhat similar distortion of the magnetic field pattern in a recent simulation study, but that study was performed under different conditions (they modeled cellular uncoupling by increasing the intracellular resistivity eightfold in a 2-D anisotropic sheet of myocardial tissue).

4.3 Realistic ventricular myocardium

After initial tests in the slab model, we investigated epicardial potential distributions (EPDs) created by epicardial, intramural, and endocardial ectopic stimulation in an anatomically accurate model of the ventricles. The specific purpose of these simulations, which are described in this section, was to test how the features that had been observed in the idealized slab model are modified by the realistic structure of the human ventricular myocardium.

4.3.1 Methodology

The realistic model of the human ventricular myocardium described in Chapters 2 and 3 was used to simulate ectopic activation sequences. Infinite medium potentials (see Appendix B) were calculated at 561 field points arranged on a regular grid comprising 33×17 points with a 2-mm spacing and located 0.5 mm above the epicardial surface. (As described in Chapter 5, a larger grid of 33×25 points was used on the LV free wall.) Two different placements of the electrode array were considered: one over

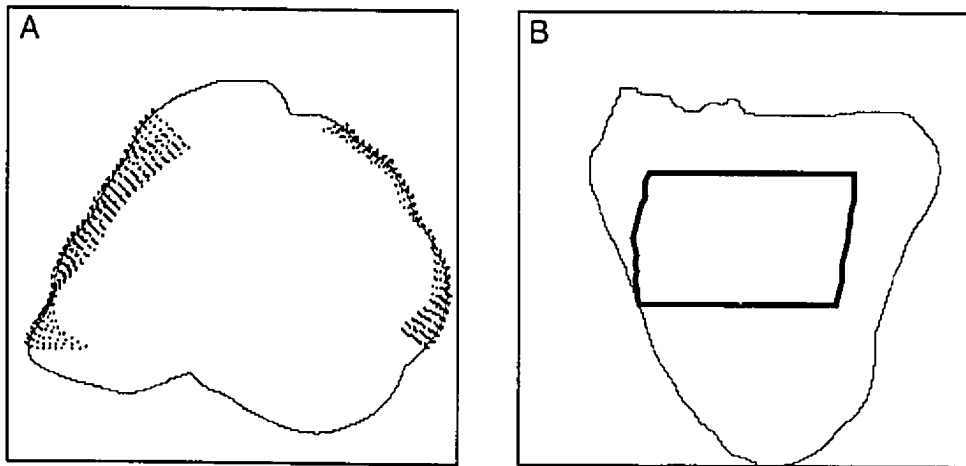


Figure 4.14: Position of 561-electrode arrays covering the RV and LV free wall of the model of the human ventricular myocardium, shown in the apical view (A) and in the left lateral view (B). Both arrays cover an area of 64×32 mm on the epicardial surface, and in both the lower border is 39 mm above the LV apex.

the RV free wall and one over the LV free wall (Fig. 4.14). EPDs were displayed as viewed from the outside, with the posterior border on the right for the LV grid, the anterior border on the right for the RV grid, the apical border below and the basal border above. The epicardial area covered by the grids corresponds to the area experimentally explored by Taccardi et al. [376].

The ectopic activation sequence was initiated at 16 sets of initial sites of activation in the RV free wall and 19 sets of initial sites of activation in the LV free wall. Each set consisted of sites located at distances 0.5 mm along the piecewise linear path μ (defined in Chapter 2) along the vectors normal to the local tangential planes between the endocardium and epicardium. Such an assignment of the intramural pacing sites is advantageous because it allows an imaginary plunge-electrode assembly to follow the curvature of the myocardial wall. In addition, it exactly specifies the distance of the pacing site from the epicardial surface. For each initial site of activation (at

total of 664 sites), EPDs were calculated every 2 ms within 16 ms after the onset of activation. (In Chapter 5, we chose a smaller subset of pacing sites for which to calculate EPDs for up to 60 ms after the onset of activation.)

The effect of nontransmural necrosis on EPDs during the initial phase (this chapter) and later phases (Chapter 5) of the ectopic sequence was also studied. The necroses had a radius of 3–4 mm and were placed subepicardially and subendocardially in the RV free wall, and subepicardially, intramurally, and subendocardially in the LV free wall.

4.3.2 Epicardial potential distributions for epicardial, intramural, and endocardial pacing

Epicardial pacing. Like the simulations in the slab model of myocardial tissue, simulations that were performed in the realistic ventricular model yielded EPDs that included an elongated negative area above the underlying pacing site and two adjacent positive regions, all approximately aligned with the local direction of fibers. As an example, Fig. 4.15 shows EPDs at 10 ms after the onset of activation for four cases of ectopic stimulation on the RV and LV epicardial surfaces; the major axis of the elliptical negative lines and the axis joining the maxima reflect the local fiber direction over the epicardial surface. Closer examination reveals that the axis joining the two maxima is shifted by 5° to 15° (the mean shift is $9.6^\circ \pm 2.4^\circ$ for all epicardial pacing sites) from the local fiber direction at 10 ms after the onset of activation. Although the major axis of the elliptical negative isopotential lines appears to be generally closer to the fiber direction, its orientation cannot be defined with better accuracy than 5° – 10° . These results agree with the results of experimental studies by Taccardi

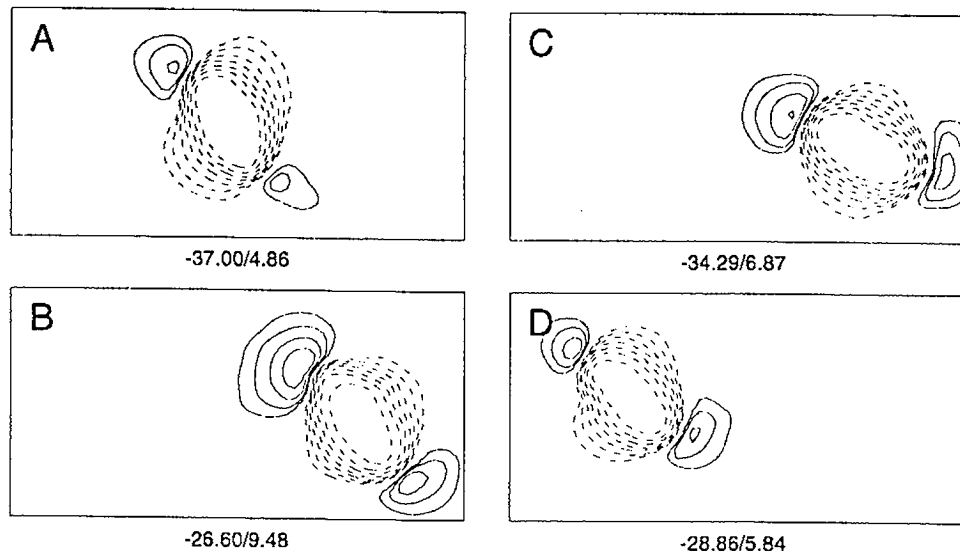


Figure 4.15: EPDs calculated at 10 ms after the onset of activation for epicardial pacing. Panels A and B show distributions on the LV epicardium, and panels C and D on the RV epicardium. In all distributions, the major axis of the ellipse formed by the inner negative isopotential lines and the axis joining the maxima follow the local fiber direction over the epicardial surface. See the legend of Fig. 4.5 for details of the layout.

et al. [376] and Watabe et al. [399], who proposed that the epicardial fiber direction may be determined accurately enough by systematic epicardial pacing.

Intramural pacing. Figs. 4.16 and 4.17 depict EPDs on the epicardial surface at 10 ms after the onset of activation initiated by two sets of pacing sites along the same local piecewise-linear path μ in the RV and LV free walls, respectively. The local thickness of the RV free wall is 5 mm, with the fibers rotating linearly from -44° (epicardium) to 32° (endocardium), and the compacta is in direct contact with the RV cavity. The local thickness of the LV free wall is 10.5 mm: 8.5 mm are occupied by the compacta with the fibers rotating from -47° (epicardium) to 49° (endocardium); the other 2 mm are occupied by the trabeculata, with a fiber direction of 79° .

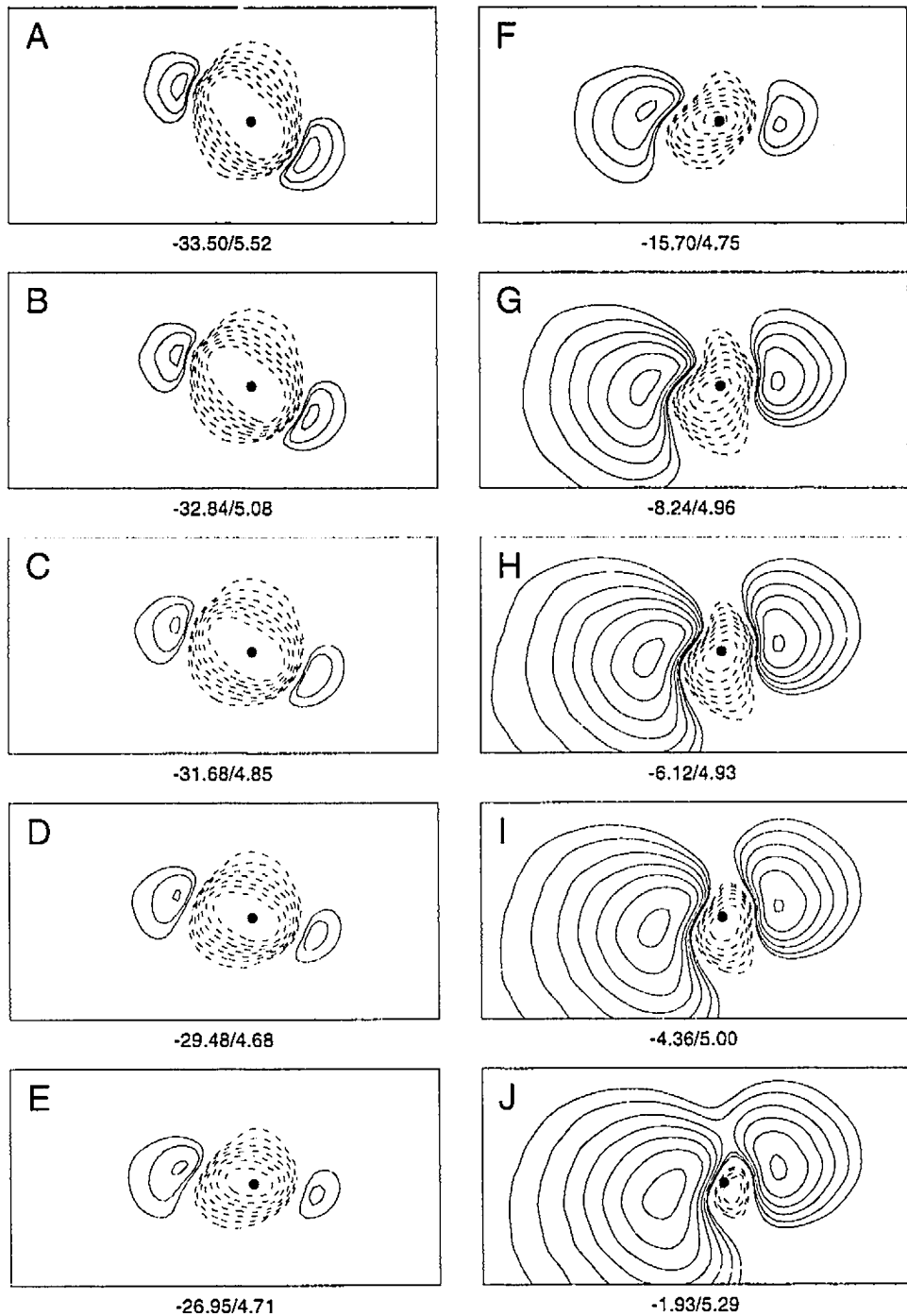


Figure 4.16: EPDs calculated at 10 ms after the onset of activation for pacing sites in the RV free wall. Stimuli were delivered at pacing sites positioned at 0.5-mm increments along the local path μ progressing from the epicardium (panel A) to the endocardium (panel J); the epicardial projection of each pacing site is indicated by the filled circle. The local thickness of the RV free wall is 5 mm. The axis joining the maxima rotates CCW with increasing pacing depths. See the legend of Fig. 4.5 for details of the layout.

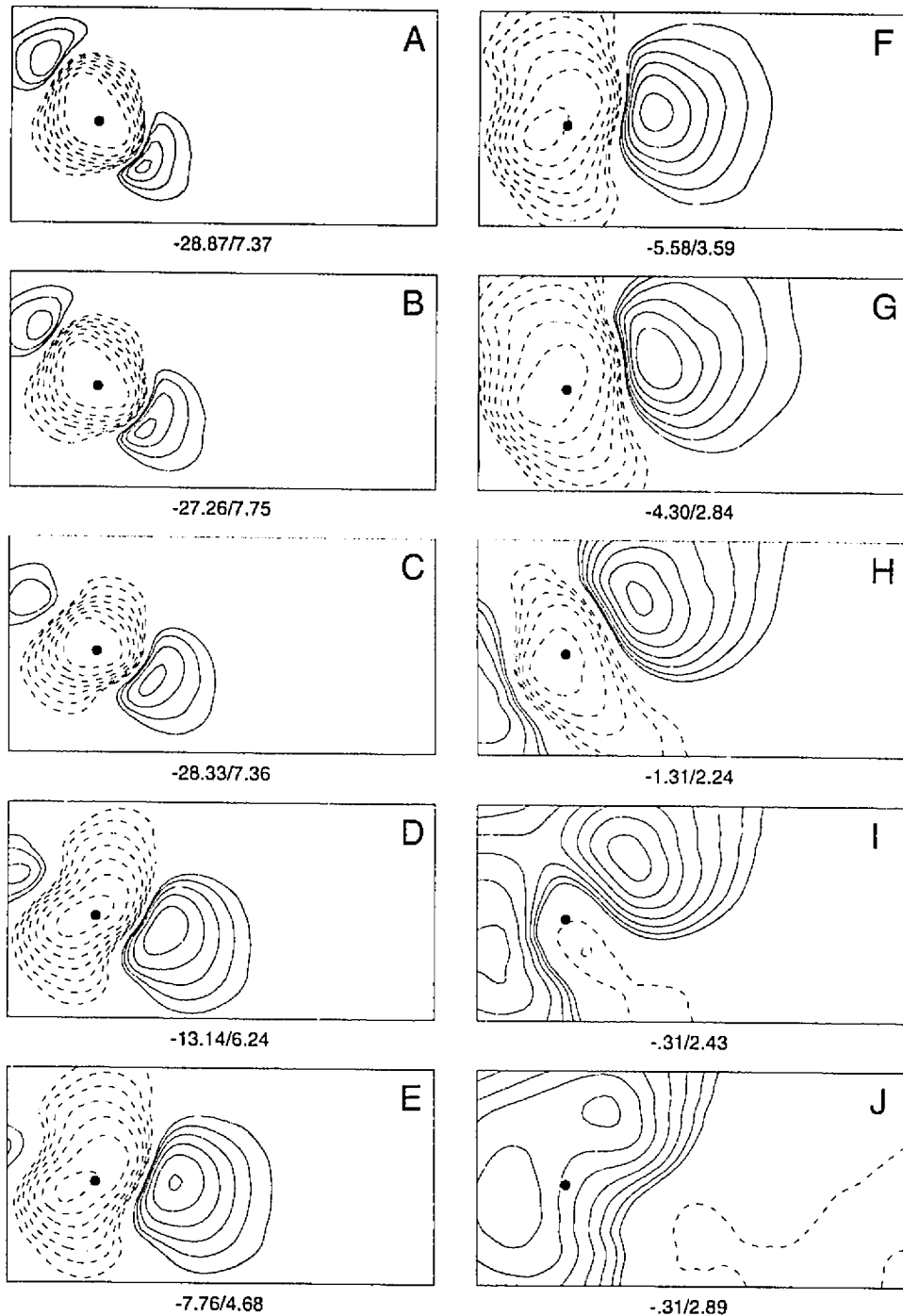


Figure 4.17: EPDs calculated at 10 ms after the onset of activation for pacing sites in the LV free wall. Stimuli were delivered at pacing sites positioned at 1-mm increments along the local path μ progressing from the epicardium (panel A) to the endocardium (panel J); the epicardial projection of each pacing site is indicated by the filled circle. The local thickness of the LV free wall is 10.5 mm. The axis joining the maxima rotates CCW with increasing pacing depths. See the legend of Fig. 4.5 for details of the layout.

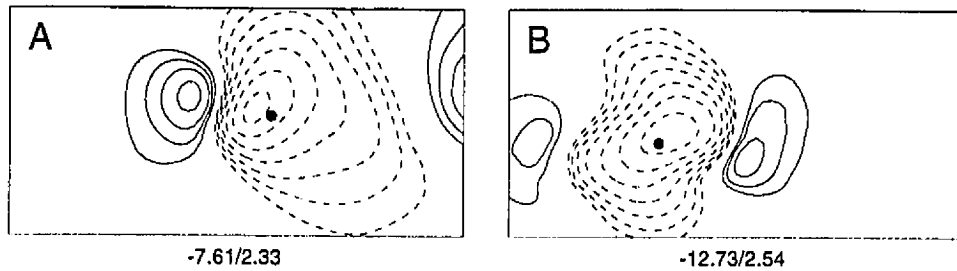


Figure 4.18: EPDs calculated at 14 ms after the onset of activation for intramural pacing at 10 mm (A) or 6 mm (B) below the epicardial surface in a LV free wall whose local thickness is 21 mm (A) or 12 mm (B). In panel A, the left maximum is larger and closer to the central minimum, while the right maximum moves away from the area explored; in panel B, the right maximum is larger and closer to the central minimum. See the legend of Fig. 4.5 for details of the layout.

The patterns of EPDs for intramural pacing in both the RV and the LV (Figs. 4.16 and 4.17) were in agreement with patterns observed in the slab model. The major axis of the negative isopotential lines was approximately perpendicular to the local fiber direction at the site of pacing, and the positive regions rotated CCW as the pacing depth increased, following the transmural CCW rotation of fibers from the epicardium to the endocardium. An interesting feature of the patterns in Fig. 4.16 is that the distance between the maxima does not increase with the pacing depth, most likely because this particular segment of the RV free wall is relatively thin. (The same feature was found in EPDs for other sets of pacing sites in the RV free wall with comparable local wall thickness.) In the LV, for sites at which the local thickness of the ventricular wall exceeded 8 mm, the distance between the extrema consistently increased with the pacing depth (Fig. 4.17), a relationship that held for depths down to 2–3 mm from the endocardium. Another important feature of EPDs was that the maxima were unequal in strengths for most of intramural pacing sites. In our simulations, the larger of the two maxima might be on either side of the pacing site

(Fig. 4.18), whereas in the experimental observations made by Taccardi et al. [376] it was always left of the pacing site (viewed from the outside).

Subendocardial and endocardial pacing. Depending on the pacing depth, subendocardial and endocardial pacing initially generated EPDs that had a single oblong positive area, which developed at 2–18 ms after the onset of activation into the usual pattern with two maxima and one minimum.

An EPD calculated at 10 ms after the onset of activation due to an endocardial stimulus (Fig. 4.16J) is similar to that observed for intramural and epicardial pacing, namely, a central negative area is surrounded by a peripheral positive area with two maxima whose joining axis is approximately parallel to the local fiber direction. This pattern can generally be reproduced at this early instant of the activation sequence only for endocardial pacing at those sites in the RV where the free wall is relatively thin (< 5 mm). A different pattern of EPDs (at 10 ms after the onset of activation) is produced for pacing at sites lying subendocardially along the same local piecewise-linear path μ in an 8-mm-thick segment of the RV free wall with 1.5-mm-thick trabeculata (Fig. 4.19); as the pacing site approaches the endocardium, the distance between maxima decreases, until, finally, for endocardial pacing (Fig. 4.19D), a central oblong positive area emerges.

Similarly, for sets of subendocardial pacing sites in the LV free wall (Fig. 4.20), an endocardial stimulus gives rise to EPDs with a large central positive area. However, although one can clearly deduce the local fiber direction from the major axis of the positive area when the local thickness of the ventricular wall is 11 mm and no trabeculata is involved (Fig. 4.20), one cannot do so when the wall has a thickness

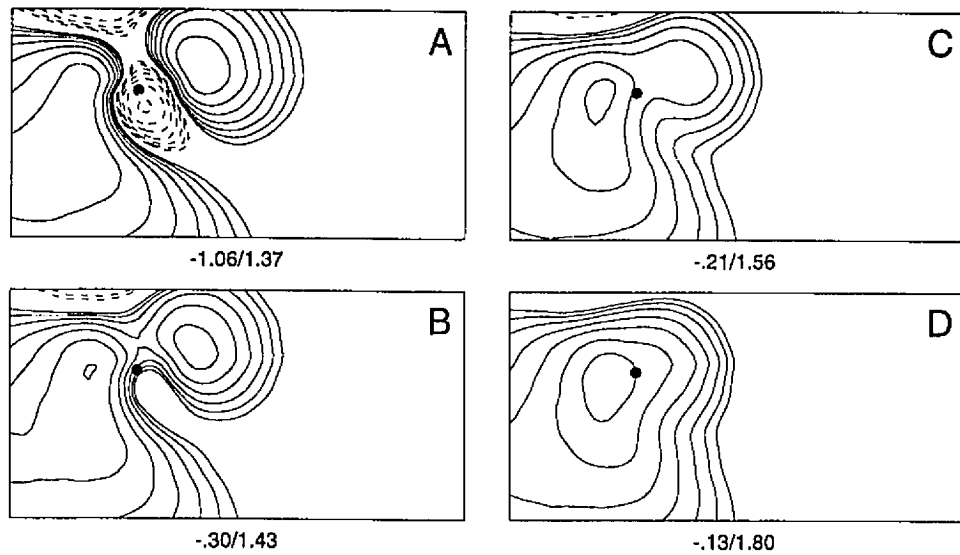


Figure 4.19: EPDs calculated at 10 ms after the onset of activation for subendocardial pacing in the RV free wall. Stimuli were delivered at pacing sites positioned at 0.5-mm increments along the same local path μ , starting 2 mm from the endocardium (A), and progressing toward the endocardium (D). The local thickness of the ventricular wall is 8 mm. See the legend of Fig. 4.5 for details of the layout.

of 12.5 mm with a 2-mm-thick trabeculata, because the positive area has no features that one can correlate with the local fiber direction (Fig. 4.20F).

It thus appears that when the trabeculata is thin, the EPD does not reveal the local fiber direction in the trabeculata itself but in the abutted compacta. When the trabeculata is thicker (> 2 mm), the fiber direction usually cannot be deduced at all from the EPD, which features a large positive area with no clue regarding the underlying anisotropy. On the other hand, our simulations show that EPDs can reveal trabecular fiber orientation when the set of pacing sites is placed along the local path μ in those segments of the LV free wall that include a very thick (> 4 mm) trabeculata close to the base of the papillary muscle. In such a specific case, illustrated in Fig. 4.21, pacing sites in the trabeculata will generate patterns of EPDs similar

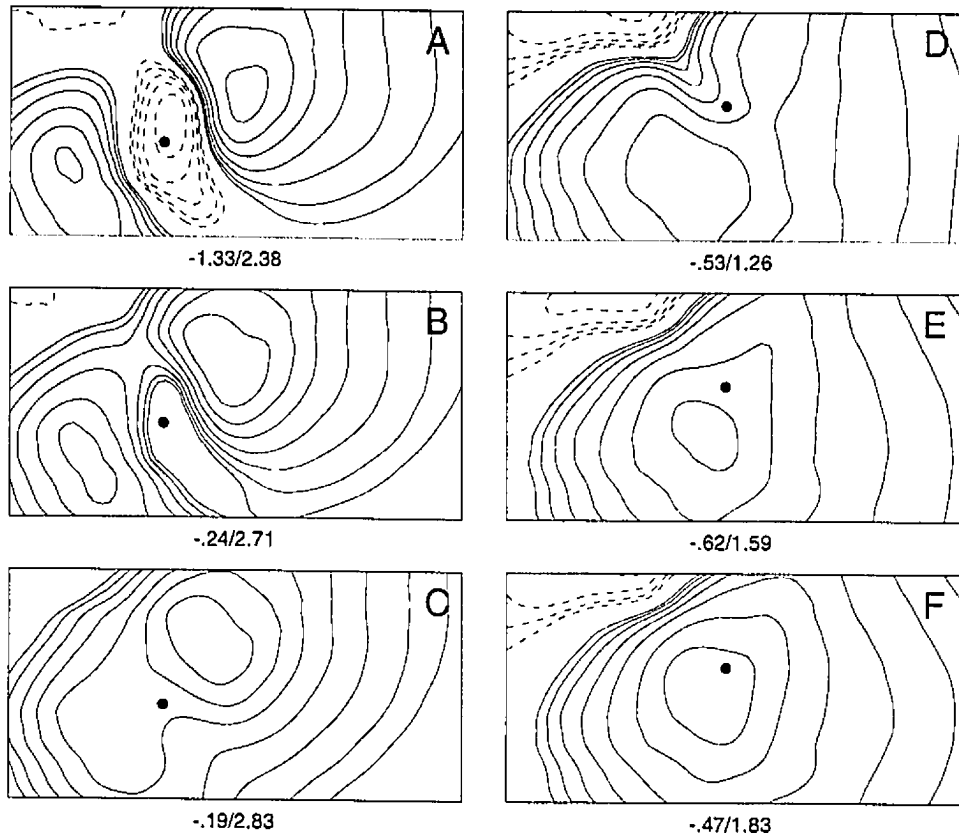


Figure 4.20: EPDs calculated at 10 ms after the onset of subendocardial pacing in the LV free wall for two different cases. Stimuli were delivered at pacing sites positioned at 0.5-mm increments along the same local path μ toward the endocardium, starting 1.5 mm from the endocardium. The local thickness of the ventricular wall is 11 mm in the first case (A through C) and 12.5 mm with a 2-mm-thick trabeculata in the second (D through F). See the legend of Fig. 4.5 for details of the layout.

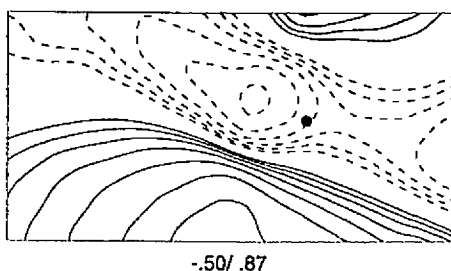


Figure 4.21: EPD calculated at 10 ms after the onset of activation for pacing in the trabeculata of the LV free wall. The stimulus was delivered at a pacing site located deep in the trabeculata (3 mm from the compacta and 4 mm from the LV cavity). The local thickness of the ventricular wall is 23 mm. See the legend of Fig. 4.5 for details of the layout.

to those generated at intramural pacing sites—a central negative area flanked by two positive regions—because the pacing sites are far enough from the endocardium that the wavefront is closed at this early phase of activation, so the normal dipole layer is silent and EPDs are not dominated by the large area of positive potentials.

One generalization that can be made from our series of RV and LV pacing simulations is that the magnitudes of the maxima do not change monotonically as a function of the pacing depth. The maxima first decrease in magnitude with increased pacing depth, but when the pacing site approaches the endocardium (2 to 3 mm distal), the magnitudes of the maxima start increasing again (Figs. 4.16 and 4.17). Such an increase often accompanies the abrupt change in the pattern of EPD for subendocardial pacing sites. The magnitude of the minimum, on the other hand, monotonically decreases with the pacing depth. This is in qualitative—but not in quantitative—agreement with results from the experimental study by Taccardi et al. [376], who observed a more pronounced increase in the amplitude of the positive mound for pacing sites close to the endocardial surface. The discrepancy may exist

because, as noted earlier (Section 4.2), our model tends to underestimate the effect of the isotropic dipoles. This occurs because, although the endocardial surface is in contact with a mass of intracavitary blood *in vivo*, blood masses (which have a high conductivity) were not included as inhomogeneities in our model of the human ventricular myocardium.

Transmural rotation of fibers vs. rotation of potential maxima. Since the fiber direction in the trabeculata is discernible from EPDs only if the trabeculata is very thick, we attempted to correlate only the transmural rotation of the fibers in the compacta with the rotation of the maxima in EPDs.

In the RV, the total rotation of the axis joining the maxima when the pacing site had been moved along the local path μ from the epicardial surface to the endocardial surface of the compacta was found to be $57^\circ \pm 12^\circ$ (mean \pm SD, $n = 16$), and the transmural rotation of the fibers in the compacta was $70^\circ \pm 11^\circ$. In the LV, the total rotation of the maxima was $93^\circ \pm 14^\circ$ ($n = 19$), and the transmural rotation of fibers in the compacta was $103^\circ \pm 11^\circ$. These values compare well with the measurements of Taccardi et al. [376] (who, however, did not distinguish the rotation in the compacta from that in the trabeculata). The difference between the rotation of the maxima and the transmural rotation of fibers is, on average, smaller than that observed for the myocardial slab model, in part because the underlying layer of trabeculata in the realistic ventricular model enhances the rotation of the maxima for pacing sites located on the interface between the compacta and trabeculata.

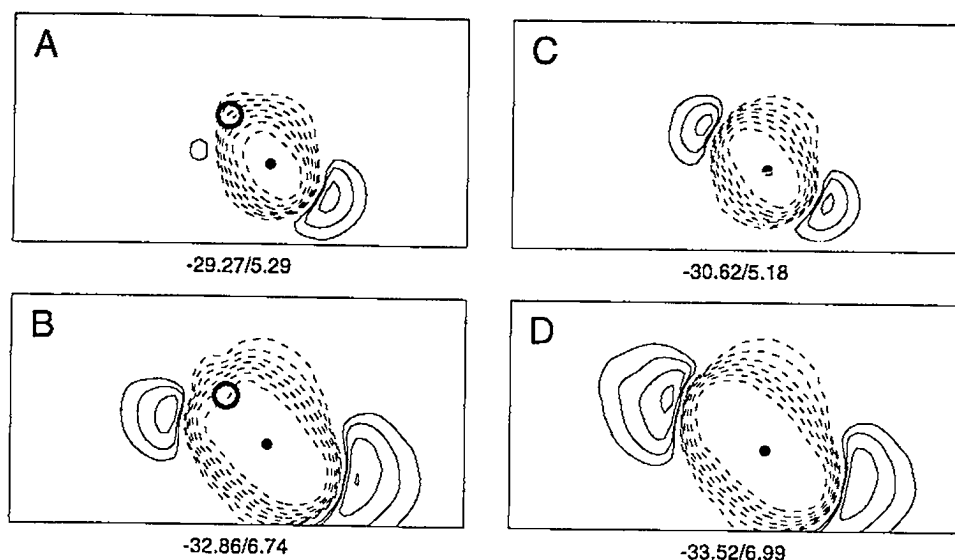


Figure 4.22: EPDs for epicardial pacing in the ventricular model with (A and B) and in the absence of (C and D) nontransmural subepicardial necrosis calculated at 10 ms (top) and 16 ms (bottom) after the onset of activation. The site and extent of necrosis are indicated by an open circle. See the legend of Fig. 4.5 for details of the layout.

4.3.3 Nontransmural necrosis and epicardial potentials

Nontransmural subepicardial necrosis causes a complete loss of one positive area in the EPD when the axis joining the epicardial pacing site and the center of necrosis projected on the epicardial surface is approximately parallel to the fiber direction near the pacing site (not shown). The potential maximum reappears in a position shifted CCW relative to that in the control EPD (Figs. 4.22A and 4.22C). The negative isopotential lines are slightly distorted, thereby reflecting the distortion of the activation wavefront caused by the presence of necrosis. The maximum remains shifted CCW relative to that in the control EPD as the positive areas begin CCW expansion-rotation (Figs. 4.22B and 4.22D). These simulations agree with the experimental findings of Watabe et al. [399].

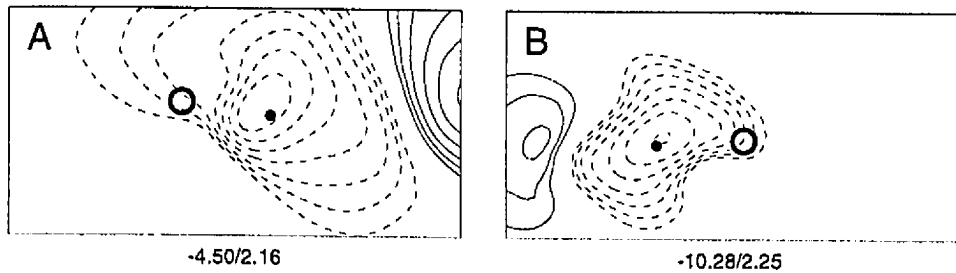


Figure 4.23: EPDs for intramural pacing in the ventricular model with intramural necrosis calculated at 14 ms after the onset of activation at 10 mm (A) and 6 mm (B) below the epicardial surface in a LV free wall whose local thickness is 20 mm (A) or 12 mm (B). For the control EPDs, see Fig. 4.18. The site and extent of necrosis are indicated by an open circle. See the legend of Fig. 4.5 for details of the layout.

Intramural necrosis (i.e., one that does not extend to the surface of the ventricular wall) affects the ectopic sequence initiated intramurally much as subepicardial necrosis does. Because the pattern of EPDs is broader for intramural pacing sites, the loss of positive area—and its concurrent replacement by negative potentials when the activation wavefront is moving into the necrosis—is more clearly visible, as shown in Figs. 4.23A and 4.23B for two different cases (compare with the control EPDs in Figs. 4.18A and 4.18B).

It is interesting that nontransmural subendocardial necrosis affects EPDs resulting from endocardial stimulation only in cases in which the control EPD has the usual pattern of one minimum and two maxima. (This is illustrated in Fig. 4.24, where the necrosis causes the loss of negative area and attenuation of the positive area that is located above the necrosis.) This rather surprising finding, that the negative area is absent compared to the control, may be explained by the fact that subendocardial necrosis diminishes the contribution of the axial dipoles (which generate EPDs with a single minimum and two maxima), thereby enhancing the relative contribution of

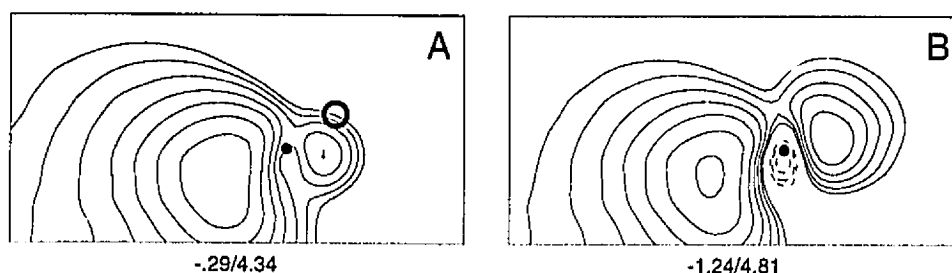


Figure 4.24: EPDs for endocardial pacing in the ventricular model with (A) and in the absence of (B) subendocardial necrosis calculated at 10 ms after the onset of activation. The site and extent of necrosis are indicated by an open circle. See the legend of Fig. 4.5 for details of the layout.

the isotropic dipoles. This explanation is supported by another observation that the necrosis does not affect EPDs with a single positive area (not shown). Since Watabe et al. [399] did not perform intramural and subendocardial pacing, we were not able to validate our simulations.

4.3.4 Comparison of simulations with experimental studies

The simulations of EPDs during the early phase of ectopically initiated ventricular activation have shown that these distributions reveal the local fiber architecture near the pacing site. They can enable one to predict, based on existing knowledge of ventricular structure, the depth of the ectopic site below the epicardial surface, or they can help determine fiber orientation when the depth of stimulation is known. These simulations can be validated only by comparison with EPDs actually recorded under similar conditions [376, 399]. Overall, our results agree—at least in a qualitative sense—with the experimental observations. Further recorded data would be required for a quantitative comparison in terms of relative errors and correlation coefficients.

The only significant qualitative departure of our simulations from the recorded

data is in regard to the pattern of the observed asymmetry of potential maxima. Taccardi et al. [376] reported that for all pacing depths > 6 mm, the two maxima became unequal in strengths, with the weaker of the two being located on the right side of the pacing site (central minimum) when viewed from the outside. In addition, the stronger maximum moved closer to the pacing site while the right maximum moved away from the pacing site and often disappeared. Taccardi et al. [376] tentatively explained this asymmetry by the imbrication angle of the fibers [367]. The imbrication angle is a measure of the fibers' departure from the direction parallel to the epicardium, such that the fiber direction points slightly inward from the epicardium to the endocardium and from left to right when the ventricles are viewed from the outside. Henriquez et al. [144] demonstrated that a 5° tipping of intramural fibers out of the tangential planes in a slab model leads to nonequal amplitudes of positive regions. Our simulations using the slab model with an imbrication angle of 5° were in qualitative agreement with their simulations. However, as we did not implement the imbrication angle in our model of the human ventricular myocardium, we could not test this hypothesis under more realistic conditions.

Chapter 5

Epicardial potentials during later phases of ventricular activation

It follows from the simulations presented in the previous chapter that the expansion-rotation of the two positive areas in EPDs starts at around 10 ms after the onset of the activation sequence. This expansion-rotation progresses CCW when the activation sequence is initiated on the epicardial surface, both CW and CCW when it is initiated intramurally, and CW when it is initiated on the endocardial surface. This phenomenon has been attributed to the intramural rotation of the activation wavefront caused by the ventricular fibrous structure.

In this chapter, we present the results of simulations that were performed in our model of the human ventricular myocardium, and were designed to investigate—by comparison of simulated with measured epicardial potentials [376, 399]—the expansion-rotation of the pattern of potential distributions on the epicardial surface within a 60-ms interval after the onset of activation. However, since it can be expected that from around 40 ms after the onset of activation the Purkinje conduction system may become involved in the spread of activation, we incorporated a simplified model of the distal conduction system into this model of the human ventricular myocardium.

5.1 Model of the ventricular conduction system

The distal conduction system of the ventricles consists mostly of specialized Purkinje cells which form interconnected bundles [382]. Purkinje cells are cylindrical like myocardial cells but have a larger diameter (100 μm). As a result, the propagation of activation is up to three times faster in Purkinje fibers than along myocardial fibers. The Purkinje fibers cover the LV and RV trabeculata in a network-like fashion [379], but they are functionally separated from the myocardium except at discrete points [273, 274, 300, 301, 302, 396] on the trabeculata. It is through these points of junction between the myocardium and Purkinje fibers—so-called insertion sites—that the Purkinje network can activate the myocardium (antegrade conduction) or the myocardium can reactivate the Purkinje network (retrograde conduction).

Although there is a considerable body of evidence about the proximal and central parts of the ventricular conduction system [13, 14, 31, 67, 70, 90, 142, 166, 234, 237, 254, 255, 378, 379, 384, 385, 388, 391] and its distal parts [90, 203, 248, 249, 252, 274, 301, 352, 356, 392], systematic histological-anatomical studies of the distribution of these insertion sites on the surface of the trabeculata have yet to be undertaken. The location of insertion sites is usually inferred from areas of early ventricular activation [329], which can be identified from endocardial electrograms. These measurements are technically very demanding and are often marred by low spatial resolution when carried out in *in situ* hearts [200].

In 1970, Durrer et al. [84] described the intramural activation sequence in seven isolated, perfused human hearts based on measurements of bipolar electrograms from as many as 870 intramural terminals. In spite of the observed variations in the

activation pattern from heart to heart, Durrer and coworkers were able to postulate the following general picture of normal activation. The activation begins almost synchronously (0–2 ms) at three endocardial areas in the LV: 1) an area high on the anterior paraseptal wall just below the attachment of the mitral wall, 2) a central area of the septum, and 3) a posterior paraseptal area about one-third of the distance from the apex to base. Then, 5–10 ms after the onset of activation in the LV endocardium, endocardial RV activation starts at two areas: 1) the attachment of the anterior papillary muscle to the RV free wall and 2) the septal area opposite the anterior papillary muscle.

The epicardial pattern of early activation reflects the endocardial one. The epicardial breakthrough occurs at the anterior RV about 20–25 ms after the onset of activation in the LV endocardium. Then, three early areas of epicardial activation emerge almost simultaneously in the LV at about 30 ms after the onset of activation: 1) an area on the anterior LV close to the atrioventricular sulcus, 2) an anterior LV area halfway from the apex to the base, and 3) a posterior area in the lower middle of the LV. Van Dam [65] studied the sequence of ventricular activation intramurally during complete right bundle branch block (RBBB) and left bundle branch block (LBBB) in two human hearts, and found that the early-activation sites on the endocardium and epicardium in both cases corresponded to the general pattern observed by Durrer et al. [84].

Since the advent of heart transplantation, structurally normal human hearts suitable for experiments have become very scarce, so studies such as those performed by Durrer et al. [84] and van Dam [65] have not been repeated. Their results have

been confirmed, however, indirectly by measurements of electrograms on the epicardial and endocardial surfaces in *in situ* human hearts during surgery. Wyndham et al. [419, 420, 421] carried out epicardial mapping during open-heart surgery in hearts with no conduction defect and in hearts with complete LBBB and left anterior fascicular block. Their results were in general agreement with those by Durrer et al. [84] and van Dam [65]. Cassidy et al. [42] and Vassalo et al. [395] confirmed Durrer's and van Dam's general picture of endocardial activation while performing endocardial catheter mapping in 15 patients with a normal conduction system and in 18 patients with complete LBBB.

Although the general picture of the ventricular activation sequence is reasonably well established, the considerable variability among individual hearts makes it difficult to ascertain its details and thus to organize the experimental evidence into a model of the ventricular conduction system. Two approaches to modeling the distal conduction system of the ventricles have been adopted, their principal difference being the number of insertion sites used. Several attempts to realistically model the ventricular myocardium [4, 8, 24, 265, 305, 344, 345] incorporated only a small number of insertion sites (less than 10); in some cases, these insertion sites were interconnected and linked to the central and proximal parts of the conduction system [189]. Malik et al. [232] used an alternative approach, including approximately 100 insertion sites in their model of the ventricles, and a similar approach was adopted later by Lorange and Gulrajani [218, 219]. Abboud et al. [1] used a fractal-based model of the ventricular conduction system to simulate high-frequency QRS signals. However, experimental studies in canine hearts [273, 274, 300, 301, 302, 396] do not

support the fractal configuration of the ventricular conduction system. Pollard [290], and Pollard and Barr [291] developed an anatomically accurate model of the human ventricular conduction system that included 35 insertion sites. Their model presents an important improvement over the idealized earlier models of the conduction system and significantly enhances the modeling of the normal activation sequence. However, like the conduction model of Malik et al. [232], it was not connected to the myocardium to allow any validation via isochrones or potential distributions produced during the initial phase of intramural activation.

In this study, we incorporated into our model of the human ventricular myocardium an idealized distal conduction system with the specific purpose of simulating the retrograde activation of this system by the myocardium and the antegrade activation of the areas of the myocardium distal to the ectopic activation sites through the Purkinje network. The guiding principle for constructing the ventricular conduction system was that only a few insertion areas (< 10) should be included in the model. Central and proximal parts of the conduction system were not considered at this stage of model development.

5.1.1 Implementation of the conduction system

The insertion sites were chosen in accordance with the experimental work of Durrer et al. [84], van Dam [65], Wyndham et al. [419, 420, 421], Cassidy et al. [42], and Vassalo et al. [395]. These sites were then interconnected by narrow sheets of Purkinje cells. (Experimental studies in dogs [203, 252] showed that the distal Purkinje network can be functionally represented as a sheet.)

In the LV, the insertion sites were located 1) in the high anterior paraseptal

region, 2) in the midseptum and middle anterior paraseptal region, and 3) in the lower posterior paraseptal region. Site 1 was then connected to site 2, and site 2 was connected to site 3; there was no direct connection between sites 3 and 1. The course of the pathways between the insertion sites was first determined on 2-D projections (anterior, posterior, left lateral, and septal) of the LV cavity; these 2-D projections were then used to lay connecting cables on the 3-D surface of the trabeculata. In that way, the distal conduction system followed the anatomical surface of the trabeculata without making any electrical contact with it.

The procedure for constructing the distal RV conduction system was similar to that used in the LV. Insertion sites were selected 1) at the base of the RV anterior papillary muscle, and 2) at the midseptum opposite to the base of the RV anterior papillary muscle, and 3) at the base of the RV posterior papillary muscle (to achieve a better match of the simulated and the observed endocardial activation patterns [65, 84, 395]). Sites 1 and 2 and sites 2 and 3 were interconnected by constructing 2-D sheets between the insertion sites and then projecting them on the surface of the trabeculata.

In the final step of the implementation of the conduction system into the model of the ventricular myocardium, we modified the existing algorithm of propagated activation by introducing an additional mask, whose purpose is to flag the myocardial, insertion-site, and Purkinje cells. The activation is allowed to proceed only from the Purkinje cells to the insertion-site cells and vice versa, and from the insertion-site cells to the myocardial cells and vice versa (thus algorithmically “insulating” Purkinje from myocardial cells). The conduction velocity in the Purkinje network was set at 1.72

m/s.

To validate our model of the distal conduction system, we initiated the normal activation sequence separately in the RV and LV and compared the simulated endocardial and epicardial isochronal maps with recorded ones [42, 65, 84, 395, 419, 420, 421]. Fig. 5.1 shows the isochronal maps on the LV endocardial surface in the left lateral and septal projections for the RBBB activation sequence, and the corresponding epicardial isochronal maps in the anterior and posterior projections are shown in Fig. 5.2. The endocardial activation proceeded rapidly from the sites of early activation, covering in the process the midseptal and midbasal anterior areas, with the left posterolateral basal area activated last. It is interesting to observe that the apex was activated relatively late in the sequence. The earliest epicardial breakthrough was in the LV paraseptal area at 28 ms after the onset of LV endocardial activation and was followed by the breakthroughs in the LV middle anterior paraseptal area and LV midapical posterior paraseptal area. The simulated endocardial and epicardial activation patterns are in agreement with experimental data [42, 84, 419, 420].

Fig. 5.3 shows the isochronal maps on the RV endocardial surface in the septal and right lateral projections for the LBBB-activation sequence, and the corresponding epicardial isochronal maps in the anterior and posterior projections are shown in Fig. 5.4. Endocardial areas in the middle RV septum and middle RV free wall became activated first, with the activation spreading rapidly from those areas in all directions. The last to be activated were the anterior and posterior basal areas. Epicardial breakthrough occurred in the RV anterior paraseptal area (the pretrabecular area) at 12 ms after the onset of RV endocardial activation. The activation wavefront then

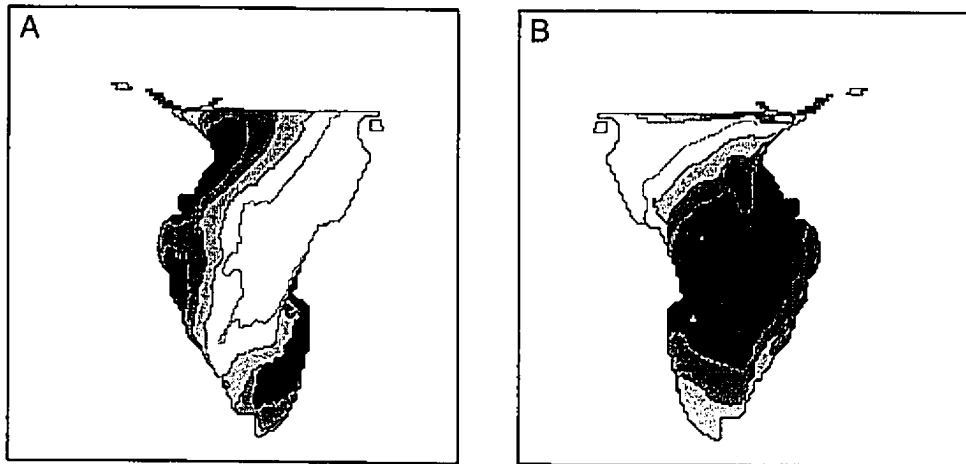


Figure 5.1: Isochronal maps on the LV endocardial surface for the RBBB activation sequence. Isochrones are shown at 8-ms increments (A) in the left lateral projection and (B) in the septal projection.

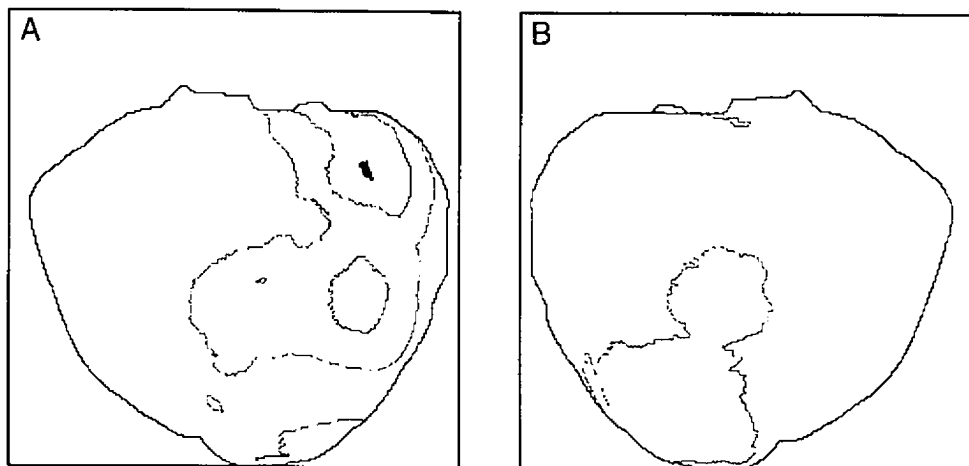


Figure 5.2: Isochronal maps on the epicardial surface for the RBBB activation sequence. The area corresponding to the breakthrough at 28 ms after the onset of LV endocardial activation is shown in black; isochrones are displayed at 8-ms increments starting at 32 ms after the onset of activation (A) in the anterior projection and (B) in the posterior projection.

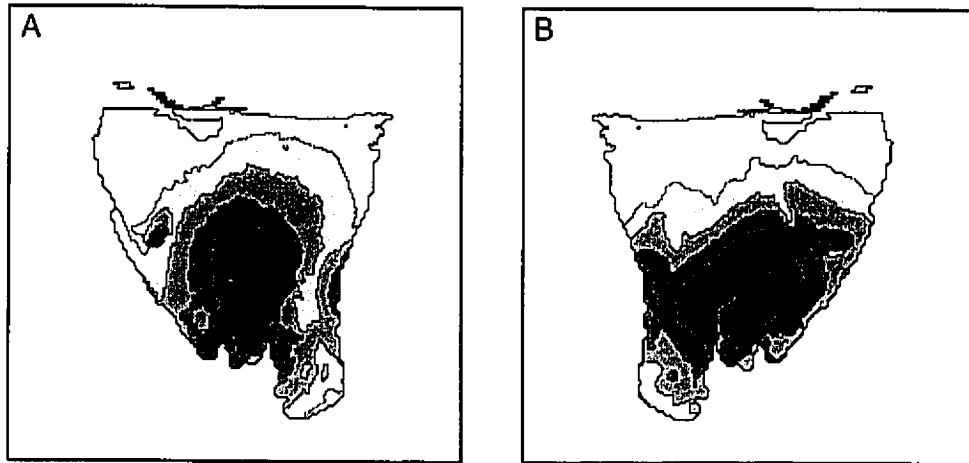


Figure 5.3: Isochronal maps on the RV endocardial surface for the LBBB activation sequence. Isochrones are shown at 8-ms increments (A) in the septal projection and (B) in the right lateral projection.

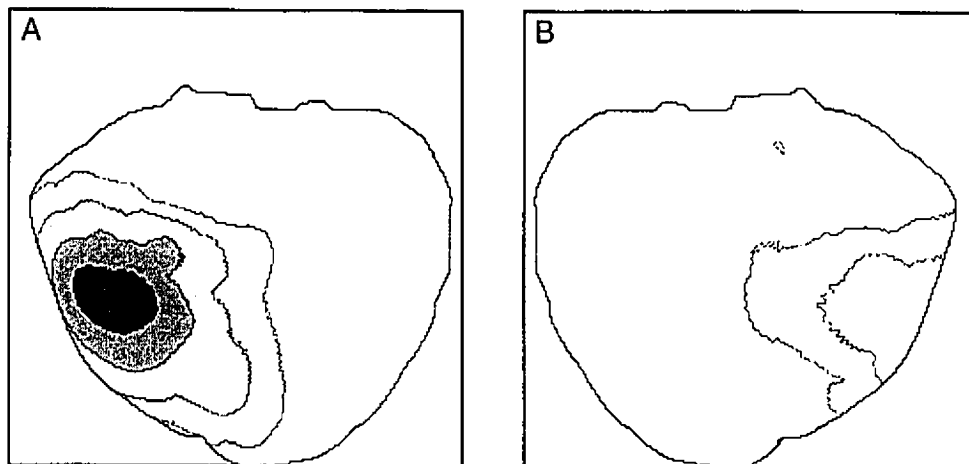


Figure 5.4: Isochronal maps on the epicardial surface for the LBBB activation sequence. The area corresponding to the breakthrough at 12 ms after the onset of RV endocardial activation is shown in black; isochrones are displayed at 8-ms increments starting at 16 ms after the onset of RV activation (A) in the anterior projection and (B) in the posterior projection.

progressed on the anterior and posterior surfaces, merging near the apex. The LV was activated later in the sequence, in a typical V-shaped activation pattern. These simulated patterns closely resemble the experimental observations [65, 395, 419, 420].

5.2 Realistic ventricular myocardium

5.2.1 Epicardial potential distributions for epicardial, intramural, and endocardial pacing

Epicardial pacing. EPDs at different time instants for RV epicardial pacing are shown in Fig. 5.5. The following qualitative features can be deduced from these spatial patterns. The initial elliptically shaped central negative area steadily expands and develops a peanut shape (with a narrowing in its central part). A single minimum, which is located initially in the center of the negative area, divides into two minima that progressively move in opposite directions along the major axis of the oblong negative area. Later, the negative area becomes fragmented, with the central portion less negative than both ends along the major axis. At 40 ms after the onset of activation, the expansion of the negative area becomes more rapid due to the epicardial breakthrough of wavefronts initiated through the insertion sites on the anterior and posterior RV free walls and the subsequent merging of these wavefronts with the original wavefront on the epicardial surface.

The two positive areas initially located along the axis parallel with the epicardial fibers progressively expand CCW, forming a crest-shaped positive ridge on each side of the central, elongated negative region. The expansion is relatively symmetrical. Both initial maxima remain approximately in their former positions along the major axis of the negative region. One or more additional maxima appear in those portions

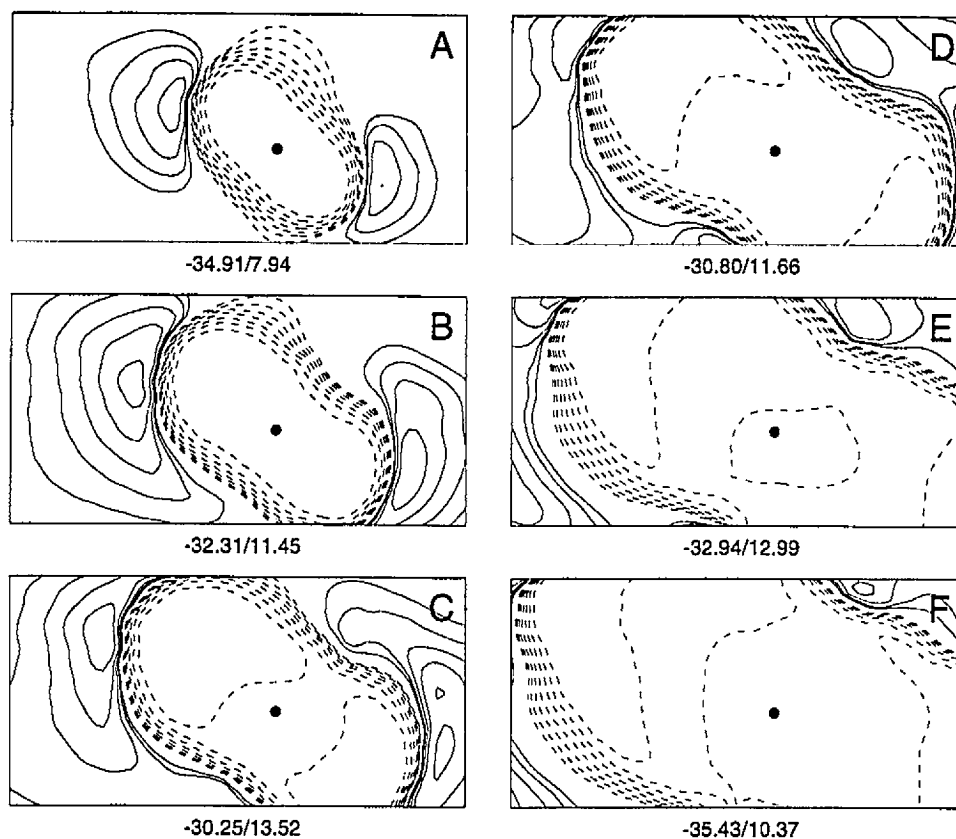


Figure 5.5: EPDs for RV epicardial pacing during the later phases of ventricular activation. The six panels show maps calculated at 18 ms (A), 24 ms (B), 30 ms (C), 36 ms (D), 42 ms (E), and 46 ms (F) after the onset of activation. See the legend of Fig. 4.5 for details of the layout.

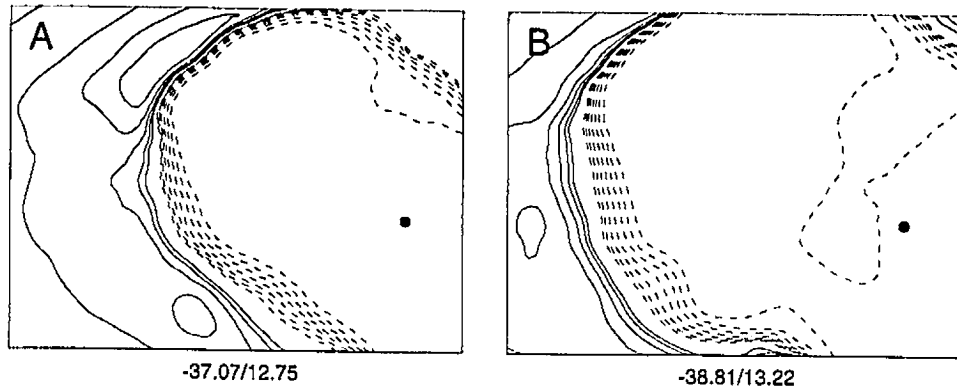


Figure 5.6: EPDs for LV epicardial pacing during the later phases of ventricular activation. The two panels show maps calculated at 44 ms (A) and 54 ms (B) after the onset of activation. See the legend of Fig. 4.5 for details of the layout.

of the expanding positive areas that are shifted CCW with respect to the initial maxima. A semiquantitative index of the amount of rotation of the positive areas (determined, following Watabe et al. [399] and Taccardi et al. [376] as the difference between the angular position of the additional maximum and the initial maximum relative to the pacing site) shows that the left and right positive areas in Fig. 5.5 rotated CCW approximately 90° in 34 ms and 36 ms, respectively, after the onset of activation. For the other RV epicardial pacing sites, the amount of CCW rotation was between 70° and 90° and was completed in 32–38 ms after the onset of activation.

Epicardial pacing in the LV generated EPDs with features similar to those described above. Fig. 5.6 shows potential maps constructed from points on a regular 33×25 grid with 2-mm spacing (with the lower border of the grid 32 mm above the apex). In general, the CCW rotation of the positive areas was between 90° and 120° . However, these values were only estimates, since the potential maxima often moved out of the exploring area (e.g., the maximum is below the lower border of the grid in

Fig. 5.6B).

As shown in Chapter 4, the CCW expansion-rotation of positive areas in EPDs reflects the course of propagated activation. The fastest propagation of the activation wavefront occurs along the subepicardial fibers, and the axis of fastest propagation rotates CCW, lagging behind the transmural fiber rotation, as the wavefront moves through deeper layers of the myocardial wall. Overall, our simulations correspond closely to the data measured by Taccardi et al. [376].

Intramural pacing. For intramural pacing, the negative area is initially stretched perpendicularly to the axis joining the maxima, which coincides with the local fiber direction (Fig. 5.7A). After the epicardial breakthrough, the negative area becomes oblong-shaped, with the major axis intermediate between the fiber direction near the pacing site and the epicardial fiber direction (Fig. 5.7B). This corresponds to the orientation of the major axis of the activation wavefront (see, e.g., Fig. 4.4). In addition, the absolute magnitude of the minimum abruptly increases. Later, the negative area steadily expands, exhibiting features already observed in EPDs for epicardial pacing, e.g., a narrowing in its central part and fragmentation (Figs. 5.7C and 5.7D). In the LV, multiple epicardial breakthroughs are very often reflected in complex patterns of epicardial negative potentials (Fig. 5.8). They may be a consequence of local undulations of the LV geometry. This phenomenon can be understood from the isochronal map (Fig. 5.9) in which the first breakthrough occurs above the pacing site at 16 ms after the onset of activation. This breakthrough is followed by another, at 26 ms after the onset of activation, that is positioned 2.5 cm more anteriorly. Later, the activation wavefronts merge, thereby creating a large negative area.

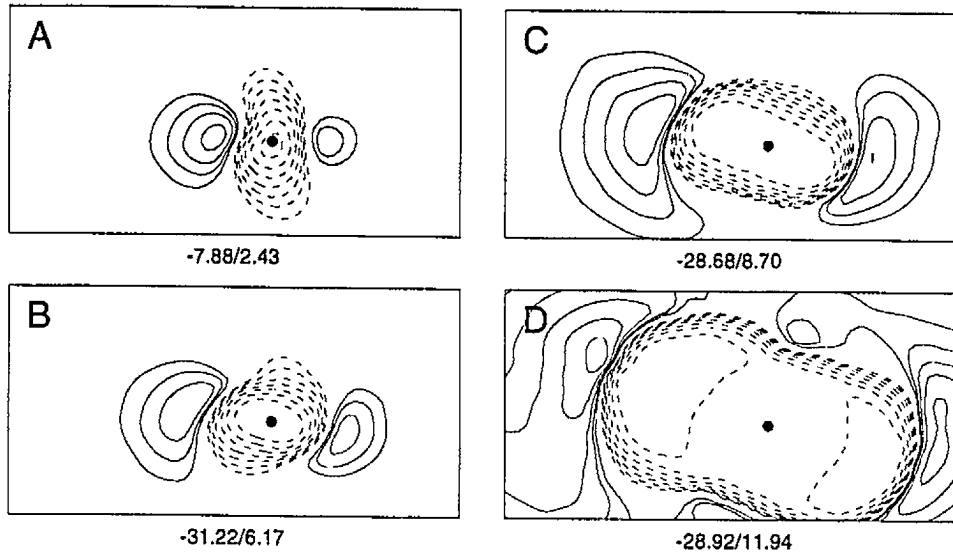


Figure 5.7: EPDs for RV intramural pacing during ventricular activation. The four panels show maps calculated at 6 ms (A), 12 ms (B), 18 ms (C), and 30 ms (D) after the onset of activation. Positive areas expand both CCW and CW. See the legend of Fig. 4.5 for details of the layout.

After the epicardial breakthrough, the two positive areas follow the expansion-rotation both CCW and CW, again becoming crest-shaped. Thus, whereas immediately after the epicardial breakthrough, the maxima rotate CW with respect to their initial position, one or more maxima appear later inside the CCW-expanding area. It is interesting that the pattern of EPDs for intramural pacing appears to be—during the later phases of ventricular activation—very similar to that generated by epicardial pacing, only rotated CCW (compare, e.g., Figs. 5.6B and 5.8D). Another interesting feature is that the EPD immediately after the epicardial breakthrough resembles the initial EPD for epicardial pacing, with the oblong-shaped negative region being flanked by the two maxima. This feature is present even when more than one epicardial breakthrough appears (the maximum at the lower border of map in Fig. 5.8B) or when one of the positive areas moves out of the exploring area during the initial phase

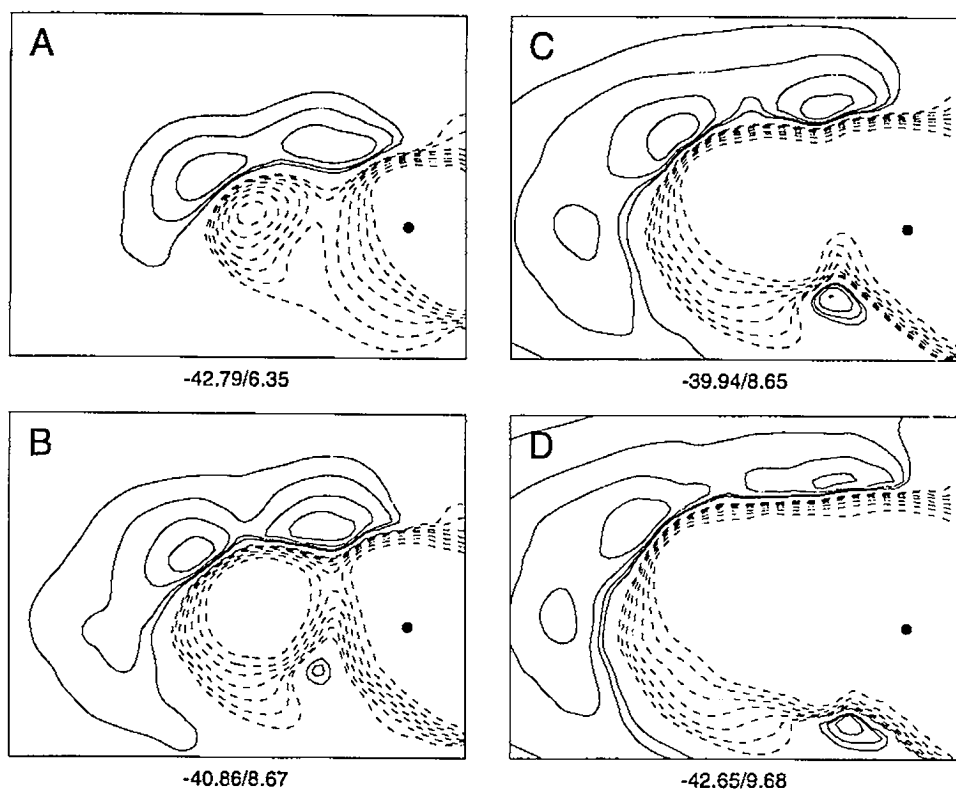


Figure 5.8: EPDs for LV intramural pacing during the later phases of ventricular activation. The four panels show maps calculated at 24 ms (A), 28 ms (B), 34 ms (C), and 38 ms (D) after the onset of activation. See the legend of Fig. 4.5 for details of the layout.

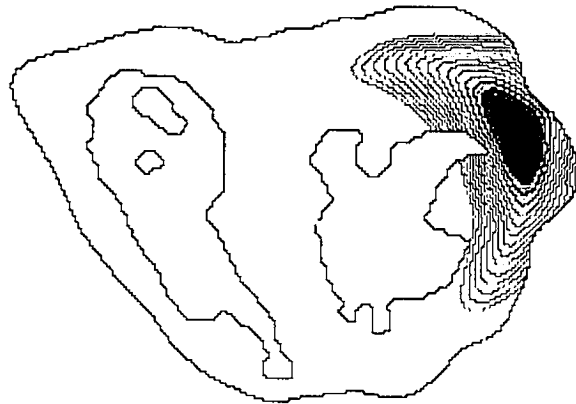


Figure 5.9: Isochronal map calculated for LV intramural pacing. The initial breakthrough occurs above the pacing site and is followed by another breakthrough positioned more anteriorly. The isochrones are displayed at 2-ms increments; the region activated during the first 16 ms is shaded.

of ventricular activation (not shown). As shown by our simulations in Chapter 4, the two maxima are the reflection of those parts of the activation wavefront that move along the epicardial fibers.

Subendocardial pacing. EPDs at different time instants following LV subendocardial pacing are shown in Fig. 5.10. At 16 ms after the onset of activation, the epicardial potentials exhibit a broad positive area overlying the stimulus site, then at 20 ms after the onset of activation, the positive area is invaded by a central negative region, which establishes the usual pattern with two maxima and one minimum. By contrast, Fig. 5.11 shows the positive area becoming separated by the negative region earlier, at 12 ms after the onset of activation, and at variance with the EPD shown in Fig. 5.10, the positive areas undergo pronounced CW rotation even before the epicardial breakthrough.

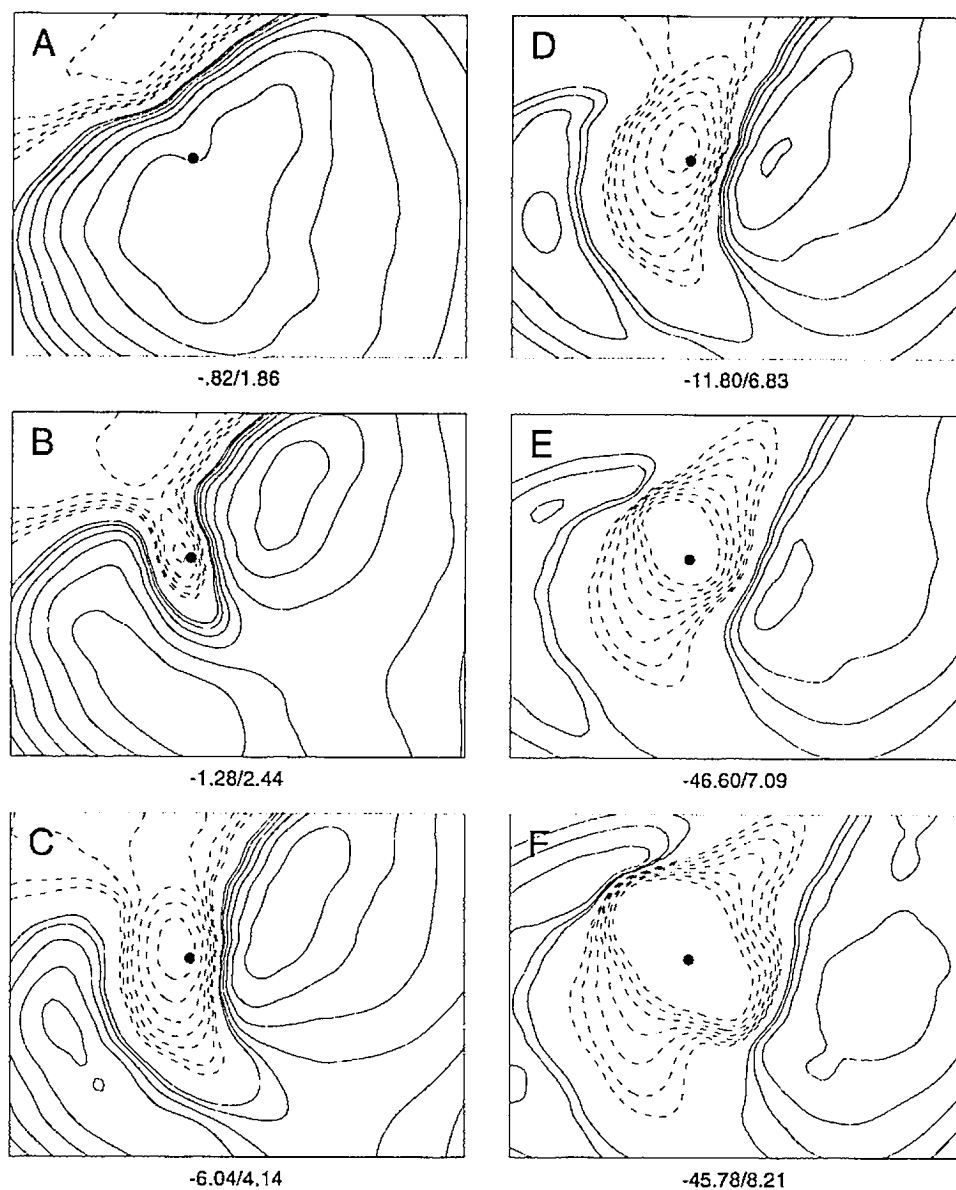


Figure 5.10: EPDs for LV subendocardial pacing during the later phases of ventricular activation in a 12.5-mm-thick wall. The six panels show maps calculated at 16 ms (A), 20 ms (B), 24 ms (C), 28 ms (D), 32 ms (E), and 38 ms (F) after the onset of activation. See the legend of Fig. 4.5 for details of the layout.

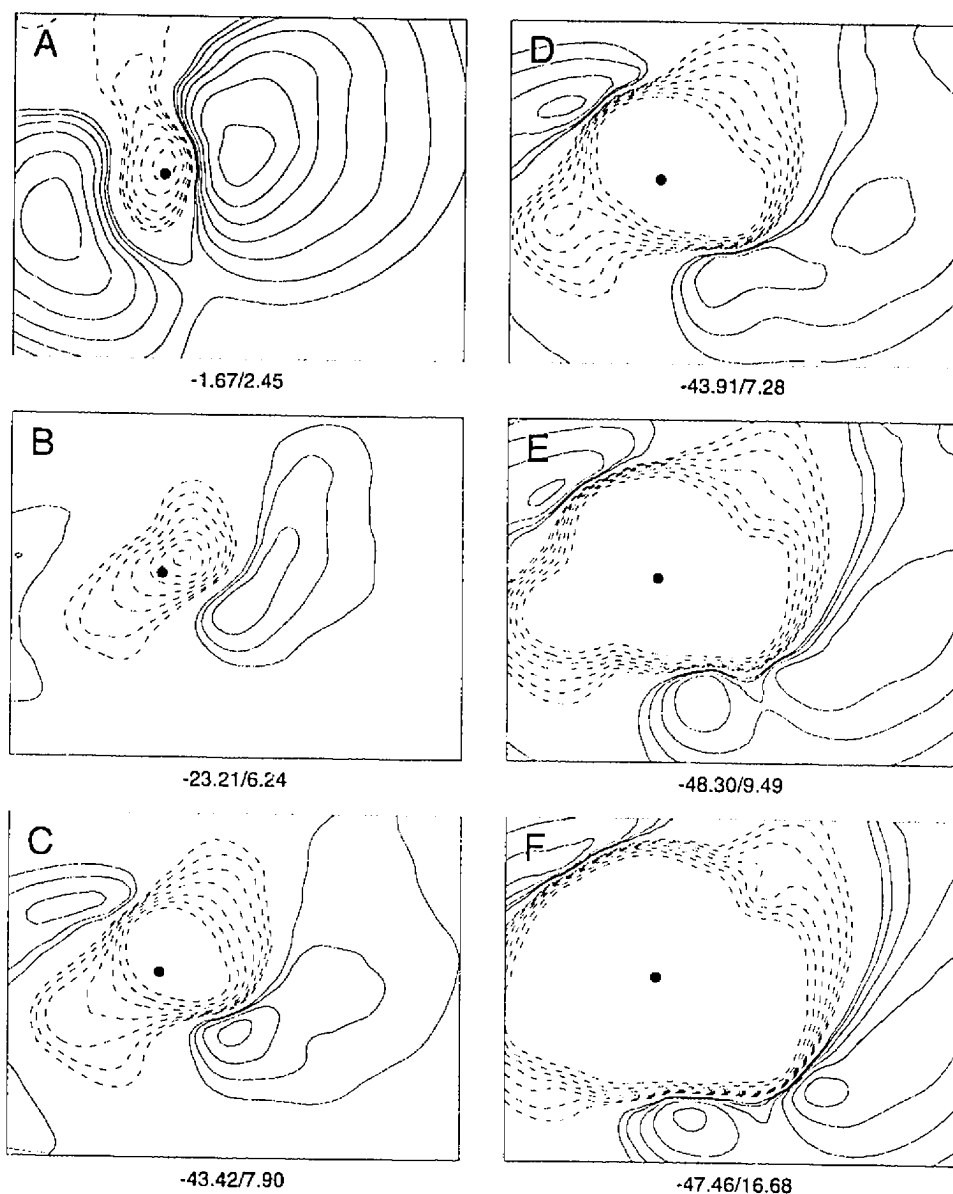


Figure 5.11: EPDs for LV subendocardial pacing during the later phases of ventricular activation in a 9.5-mm-thick wall. The six panels show maps calculated at 12 ms (A), 20 ms (B), 24 ms (C), 30 ms (D), 34 ms (E), and 40 ms (F) after the onset of activation. See the legend of Fig. 4.5 for details of the layout.

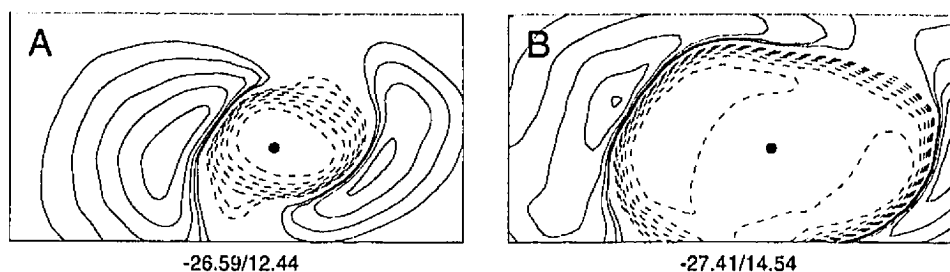


Figure 5.12: EPDs for RV endocardial pacing calculated at 22 ms (A) and 34 ms (B) after the onset of activation. Positive areas expand CW. See the legend of Fig. 4.5 for details of the layout.

In both cases of subendocardial pacing, the negative isopotential lines are stretched in a direction perpendicular to that of the fibers until the epicardial breakthrough occurs and then become oblong-shaped (Figs. 5.10D, 5.11C, and 5.12A). Additional breakthrough appears in Fig. 5.11D. After the epicardial breakthrough, the two positive areas rotate further, predominantly CW, and often fragment (e.g., Fig. 5.11E). The pattern of EPDs for endocardial pacing during the later phases of activation resemble those observed for epicardial and intramural pacing, except that the entire pattern is further rotated CCW (e.g., Fig. 5.12B).

For those endocardial pacing sites located close to the base of the papillary muscle (i.e., where the thickness of the trabeculata abruptly changes), we observed the small amount of the CCW expansion-rotation (not shown), because the wavefront of propagated activation progressed through the compacta toward the epicardial surface (which accounted for the expected CW expansion-rotation), as well as through deeper trabeculata (which caused a small CCW expansion-rotation).

The sequences of EPDs agree in their general features with those measured by Taccardi et al. [376]. However, Taccardi et al. [376] observed the positive potentials

above the pacing site just before the epicardial breakthrough. In our simulations, the area above the pacing site is consistently negative after the changes in potential pattern are completed during the initial phase of ventricular activation.

5.2.2 Effect of intramural and subendocardial necrosis on epicardial potentials

EPDs for RV epicardial pacing with nontransmural subendocardial necrosis and for LV epicardial pacing with intramural necrosis are shown in Figs. 5.13 and 5.14, respectively. In both cases, the left positive area is transiently interrupted by a negative gap, which persists for 4 ms; the pacing site, the epicardial projection of necrosis, and the negative gap are aligned. As the center of the necrotic region was moved deeper into the ventricular wall, the gap in the positive area occurred progressively later. Whether the gap appeared depended on the position of the pacing site; there was no gap unless significant portions of the leading edge of the wavefront, moving along the local fiber direction, collided with the necrosis.

These findings are consistent with our observations made in simulations of the initial phase of ventricular activation (Chapter 4), where we showed a complete transient loss of one of the positive areas when the activation propagated directly into the necrosis. When the pacing was delivered on the epicardial surface and necrosis was positioned intramurally or subendocardially, the wavefront of propagated activation underwent a considerable amount of CCW rotation before it encountered the necrosis, and it was therefore more widespread. For this reason, the CCW expansion-rotation of the potential pattern was interrupted by the presence of the necrosis during the later phases of ventricular activation. Again, our simulated data compare well with

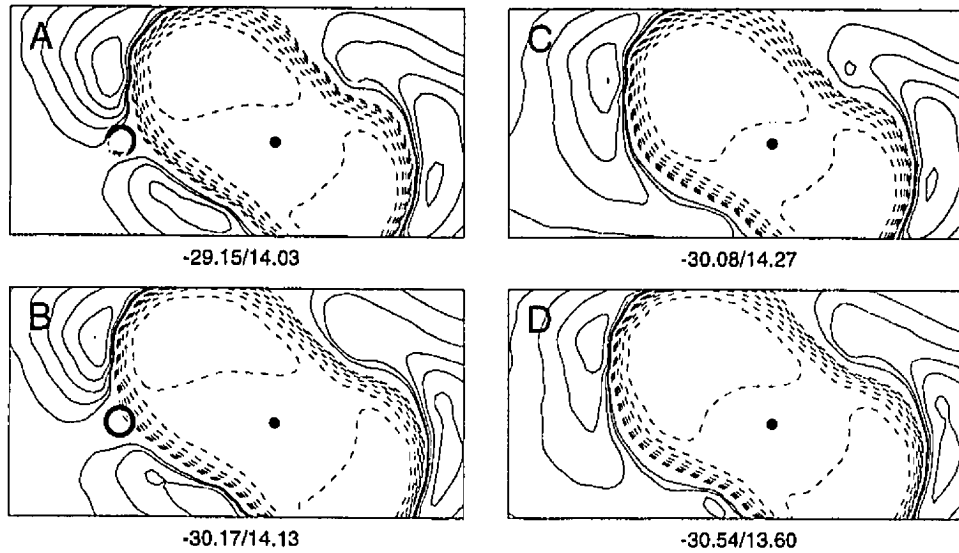


Figure 5.13: EPDs for RV epicardial pacing in the ventricular model with (A and B) and in the absence of (C and D) nontransmural subendocardial necrosis calculated at 28 ms (top) and 32 ms (bottom) after the onset of activation. The site and extent of necrosis are indicated by an open circle. See the legend of Fig. 4.5 for details of the layout.

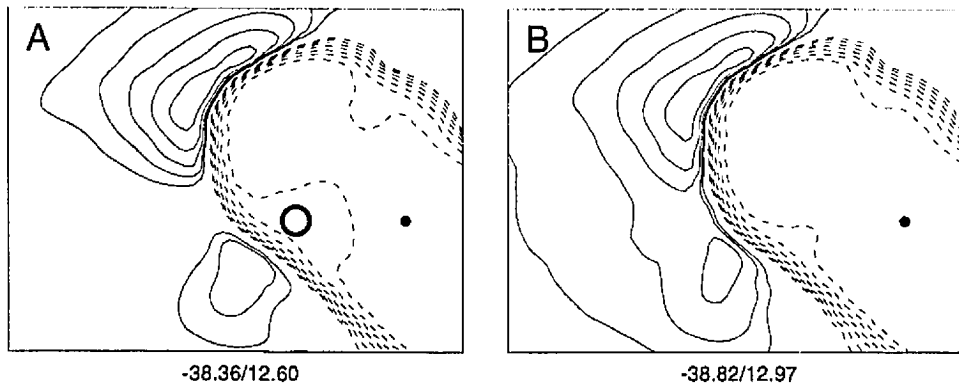


Figure 5.14: EPDs for LV epicardial pacing in the ventricular model with (A) and in the absence of (B) intramural necrosis calculated at 34 ms after the onset of activation. The site and extent of necrosis are indicated by an open circle. See the legend of Fig. 4.5 for details of the layout.

the experimental data [399].

5.3 Discussion

The success of a particular model of the ventricular myocardium depends on how well it approximates measurable manifestations in the vicinity of the cardiac sources. As has been noted by Gulrajani [130], it is considerably easier to predict smoothed-over potential distributions on the torso surface than it is to simulate near-field epicardial potentials. Difficulties in the realistic modeling of the geometry and intramural anisotropic structure of the ventricles have severely limited attempts to adequately simulate potentials on the epicardial surface to date. In the simulations presented in Chapters 4 and 5, we used our model of the human ventricular myocardium to calculate ectopic activation sequences initiated at varying intramural depths in the LV and RV walls, and in the presence of small local necroses. The specific aim of our study was to examine the effects of realistic fibrous structure on the pattern of propagated activation and epicardial potentials. We know of no comparable modeling studies that have been published so far.

Our results were validated by qualitative comparison with published data [376, 399]. To accomplish this task, we used—in accordance with the proposal of Colli Franzone et al. [52]—the following major morphological features of EPDs: 1) the location and magnitude of the potential minimum and the shape of negative isopotential lines, 2) the location, mutual distance, and magnitude of the potential maxima before the epicardial breakthrough, 3) the rotation of maxima before and after the epicardial breakthrough, and 4) the expansion-rotation of the positive areas. In gen-

eral, our simulations showed that a model of the anisotropic myocardium in which the *rotational* fibrous structure is assigned is necessary if the process of propagated activation is to be simulated accurately. To this end, the idealized slab model provides a useful description of major features of EPDs during the initial phase of ventricular activation. These features can be summarized as follows: 1) a pattern with a central minimum and two maxima, with the axis joining these extrema approximately parallel with the fibers near the pacing site, 2) a rotation of the axis joining the maxima in the same direction (CCW) as that of the fibers with increasing pacing depth, accompanied by a deformation of the negative isopotential lines, 3) a change of the pattern for endocardial and subendocardial pacing sites into one with an oblong positive area, and 4) a complete transient loss of one of the positive areas in the presence of localized necrosis.

Simulations with the realistic ventricular model confirmed this picture but also added further details. Firstly, subendocardial and endocardial pacing initially generated EPDs with a single oblong positive area, which later in the sequence developed into the usual pattern with two maxima and one minimum; the time at which the initial evolution was completed was determined by the local properties of the ventricular fibrous structure. Secondly, the local geometry of epicardial surface and convolution of underlying fibers caused the asymmetry of the positive areas in EPDs.

During the later phases of ventricular activation, the idealized slab model is not adequate, because it neglects the curvature and undulations of the epicardial and endocardial surfaces. The major feature of EPDs is the expansion-rotation of the positive areas, which is CCW for epicardial pacing, is both CW and CCW for in-

tramural pacing, and primarily is CW for endocardial pacing. For some endocardial pacing sites—those in the vicinity of parts of the endocardium in which the thickness of the trabeculata abruptly changed (e.g., due to the presence of papillary muscle)—a small amount of CCW expansion-rotation was observed. Intramural and subendocardial necroses brought about a transient gap in the CCW expansion-rotation of positive areas initiated by epicardial stimuli; the gap occurred earlier in the sequence for intramural than for subendocardial necroses. A fragmentation of the positive areas was frequently observed during expansion-rotation, and we attribute this to three factors that affect EPDs by modifying the course of propagated activation to some degree: the interface between the compacta and trabeculata, variable local thickness of the ventricular wall, and local undulations of the trabecular surface. More extensive study based on simpler models would be required to further elucidate these particular effects.

In general, our results are consistent—at least qualitatively—with the experimental descriptions of EPDs [376, 399]. The only significant difference between measured and simulated maps was transient appearance of the positive epicardial potentials above the pacing site observed during experimental endocardial pacing before the epicardial breakthrough. Our simulations consistently predicted negative epicardial potentials, as did an idealized slab model of Colli Franzone and coworkers [52] with and without involvement of the Purkinje network. The reasons for the discrepancy between the simulated and experimental data are unclear.

Our model rests on the assumptions of the equal anisotropy ratio and the oblique dipoles, both of which were discussed in Chapter 3. One can construct more realistic

model, based on the FEM, that would enable calculation of the volume currents in the anisotropic myocardium, as Colli Franzone et al. [52] have already done in an idealized slab model. At present, however, for such a model to have a resolution and intramural anisotropic structure comparable to ours is not feasible.

In our simulations, the inhomogeneity of the intracavitary blood masses was neglected. Although our simulated EPDs qualitatively agree with measured ones, we noted some quantitative differences, which may be the effect of these blood masses. The problem of how the interface between myocardium and blood masses affects the ratio of the isotropic dipole component to axial dipole component has yet to be completely elucidated.

The inclusion of an idealized Purkinje conduction system did not significantly change the observed patterns in the expansion-rotation of positive areas. Its effect was limited to the later phases of ventricular activation and accounted for an accelerated expansion of the central negative area. This effect was sometimes difficult to distinguish from the appearance of additional epicardial breakthroughs, due to the irregular geometry of the epicardial surface. In the study in which Colli Franzone et al. [52] used an idealized slab model, a more pronounced modification of epicardial potential patterns was observed when the simplified Purkinje network was present. However, unlike our model, theirs used a large number of insertion sites distributed on a nearly regular grid covering a relatively small area. In addition, they made no attempt to correlate such a distribution of the Purkinje network with that actually found in the ventricular myocardium. It thus appears that if the Purkinje network is not included into a realistic ventricular model with the utmost care, it may affect

potential distributions in an unrealistic manner.

Our simulation protocol was oriented toward examining EPDs calculated for electrode grids that covered the RV and LV free walls; such a choice was in accordance with published measurement data [376, 399]. We have no reason to think that our results would be qualitatively different had we positioned our grid differently or used a grid that covered the epicardial surface more extensively. Our protocol could be also applied to simulating potentials on the LV or RV endocardial surfaces or as measured by a LV intracavitary probe [187].

Simulations with localized necrotic regions present the first step towards clinically important applications, such as generating diagnostic criteria for myocardial infarctions with various loci. These simulations were relatively easy to perform because the necrotic region had a clear-cut border between the normal and dead myocardial tissue [399]. Actual healed infarctions are much more complex (having a labyrinthine structure), with large intersubject variability; a further complication is the observed cellular uncoupling [75, 172, 191, 304, 418] in the ischemic border zone. The modeling of such a substrate can be undertaken with the tools developed in this study, provided necessary anatomical data are available. The model may then prove valuable for studying the electrophysiological precursors to ventricular tachyarrhythmias. Furthermore, since our model describes both activation and recovery, it can be used to model the ST-segment changes that reflect myocardial ischemia [190].

Chapter 6

Localization of sites of ectopic activation using simulated BSPMs as templates

6.1 Introduction

Body surface potential mapping is the *noninvasive* method for imaging cardiac electric sources. Body surface potential maps (BSPMs), which can be constructed from multiple ECGs recorded simultaneously on the anterior and posterior chest [68, 225, 370, 371], assess the cardiac sources at a greater distance than do direct recordings on the epicardial surface and therefore are affected by the intervening thoracic tissues. Although this considerably restrains spatial resolution of these electrical images of cardiac sources, the cardinal advantage of body surface potential mapping—its noninvasiveness—makes it routinely applicable in the clinical setting [68, 98, 109, 154, 165].

SippensGroenewegen et al. [337] recently demonstrated that BSPMs can overcome the limitations of 12-lead electrocardiography [2, 3, 165, 195, 196] in determining the site of origin of ectopic activity. They were able to differentiate among 38 patterns

of QRS-integral maps that corresponded to distinct endocardial pacing areas in the LV and the RV.

This chapter describes simulations performed with a model of the human ventricular myocardium that were designed to assess the spatial resolution of BSPMs in localizing the site of origin of endocardial ectopic activity. The additional purpose of these simulations was to further validate our model by comparing simulated and measured potential distributions on the body surface. The next section describes general aspects of the methodology used in simulating BSPMs. Section 6.3 describes a method for discriminating—by means of simulated BSPMs—among different preexcitation sites located on the interventricular septum in patients suffering from Wolff-Parkinson-White (WPW) syndrome. Section 6.4 demonstrates how simulated BSPMs can be used to localize the site of origin of idiopathic ventricular tachycardia (VT). Section 6.5 investigates the spatial resolution with which QRS-integral maps reflect the sites of origin of ventricular ectopic activity by means of *systematic* pacing of the LV and RV endocardial surfaces.

6.2 Methodology

We used a boundary element model of the human torso to calculate the extracardiac electric potentials; the construction of this model has been described in detail elsewhere [152, 229]. The results presented in Appendix B demonstrate that thoracic inhomogeneities and alterations in thoracic geometry do not markedly alter the qualitative features of BSPMs. Therefore, the standard homogeneous torso model was used throughout in this study.

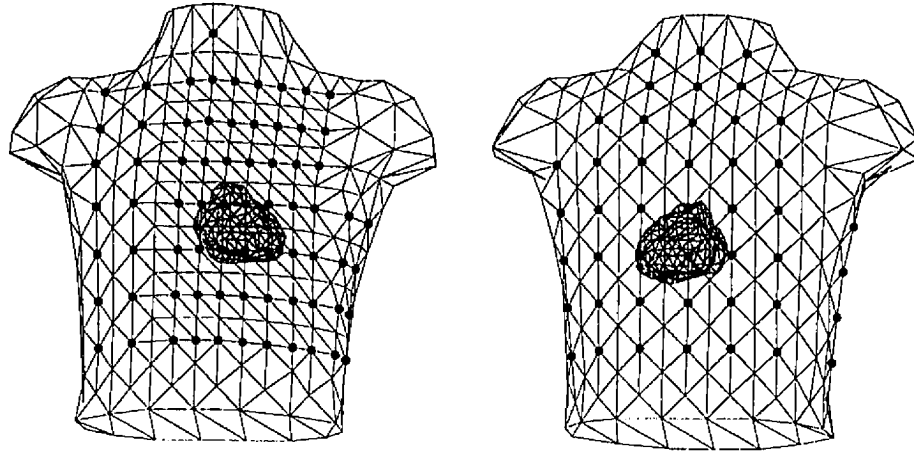


Figure 6.1: The anterior and posterior views of the standard homogeneous torso model comprising the body surface and the epicardial surface. The electrode sites used in our clinical BSPM protocol are shown as filled circles.

The outer boundary of the torso model was tessellated with 700 triangles (defined by 352 nodes), and a same conductivity of 0.2 S/m was assigned to all torso tissues. The set of 117 electrode sites for the BSPM system used at this institution [229, 242], with each site corresponding to a node point, is shown in Fig. 6.1. The discretization of fundamental integral equations was performed in a manner that produced a node-to-node relationship among potentials [164, 330, 430]; thus, forward calculations for any given set of cardiac sources yielded potentials at the measurement sites directly. The model of the human ventricular myocardium was carefully positioned in the torso model to best fit the heart's anatomical location. An additional surface, which represents the epicardium and completely encloses the ventricular model, was added to the torso model (Fig. 6.1). The surface of the epicardium was tessellated with 400 triangles (defined by 202 nodes). Special care was taken that each node was positioned approximately 1 mm above the epicardial surface of the ventricular model.

BSPMs were displayed as isopotential lines on a flattened torso. Epicardial potential maps (EPMs) were displayed in a polar format corresponding to the standard radiological view [7], with the LV apex at the center of the plot and successive layers pulled back and stretched to become concentric rings in the polar projection.

6.3 BSPM localization of septal preexcitation sites in WPW syndrome

Ventricular preexcitation via atrioventricular (A-V) accessory pathways in patients suffering from Wolff-Parkinson-White (WPW) syndrome [106, 108, 427] is a model for focal activation in the structurally normal heart, with the pathological preexcitation activity originating on the epicardial side of the A-V ring. Several investigators have correlated specific patterns of BSPMs with the particular location of any given preexcitation site [29, 69, 123, 169, 182, 424]. They noted that the maximum is relatively stationary during the early phase (up to 40 ms after the onset) of ventricular activation initiated by the preexcitation and is positioned on the left anterior torso for all preexcitation sites. It is thus the position of the minimum (and of the negative area) that identifies a specific preexcitation site. The minimum appears at sites that approximately correspond to the body surface projection of the potential minimum above the given preexcitation site on the A-V ring [250, 348]. For the initial site of ventricular activation occurring at the left anterior the left lateral, the left posterior, the right posterior, the right lateral, and the right anterior aspects of the A-V ring, the body surface minimum migrates along the projection of the A-V ring from the upper right posterior torso to the lower right posterior torso (the left aspect of the A-V ring) and from the lower right anterior torso to the upper right anterior torso (the

right aspect of the A-V ring) [182]. To localize the site of ventricular preexcitation, five general empirical criteria for interpretation of BSPMs were derived by Kamakura et al. [182] and Grogin et al. [128]: 1) the minimum on the right anterior torso corresponds to the preexcitation sites located in the RV; 2) the minimum on the back corresponds to the preexcitation sites in the LV; 3) the region of negative potentials over the entire lower torso corresponds to the posterior sites; 4) the region of positive potentials over the entire lower torso corresponds to the anterior sites; 5) BSPMs corresponding to the lateral (free wall) preexcitation sites in both ventricles are characterized by regions of near-zero potentials on the anterior and posterior torso that run in a nearly vertical direction on the map. This simple interpretation of BSPMs was later substantiated by computer models [217, 257, 402] and successfully employed in a clinical practice to guide catheter ablation of accessory pathways [83, 128].

While earlier studies focused on distinguishing between the adjacent sites positioned around the A-V ring, little attempt has been made to examine the septal preexcitation sites more closely. Epstein et al. [89] and Grogin et al. [128] recently reported difficulty in separating adjacent septal sites.

6.3.1 Results

We simulated a set of BSPMs for 16 preexcitation sites at different regions of the basal septum. For each activation sequence, we calculated BSPMs at 2-ms increments within the first 40 ms after the onset of activation. Fig. 6.2 shows BSPMs calculated at 30 ms after the onset of activation for six septal preexcitation sites: the left posteroparaseptal (LPP), the right posteroparaseptal (RPP), the right intermediate septal (RIS), the right anteroseptal (RAS), the right anteroparaseptal (RAP), and the

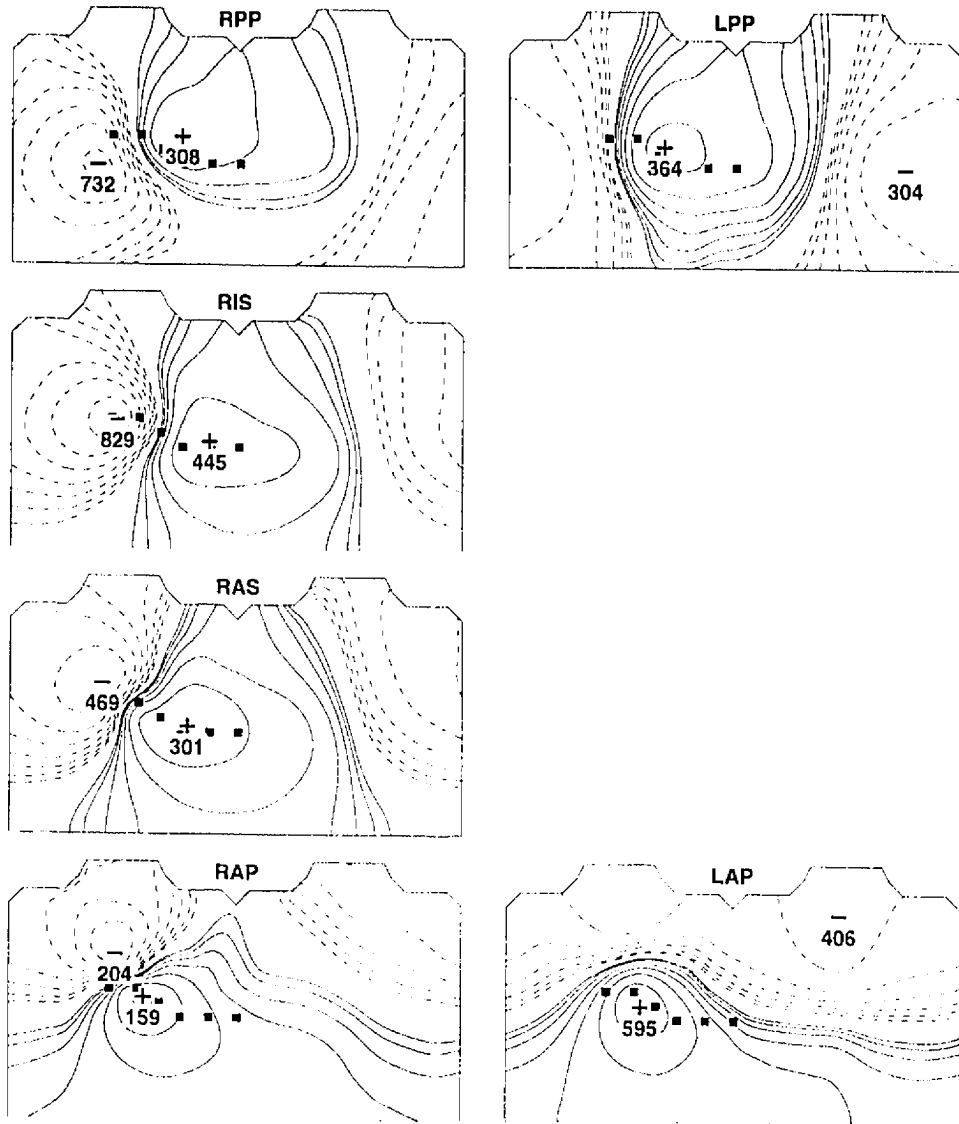


Figure 6.2: BSPMs calculated at 30 ms after the onset of an activation sequence initiated at six septal preexcitation sites. The top border of each map represents the neck and shoulders, and the lower border the waist; the anterior chest is depicted on the left half of the map, with the left midaxillary line at the center of the map. Precordial leads V_1 through V_6 are shown as black squares. The extrema are denoted in μV , and isopotential lines are plotted in logarithmic increments. LPP, left posteroparaseptal; RPP, right posteroparaseptal; RIS, right intermediate septal; RAS, right anteroseptal; RAP, right anteroparaseptal; LAP, left anteroparaseptal.

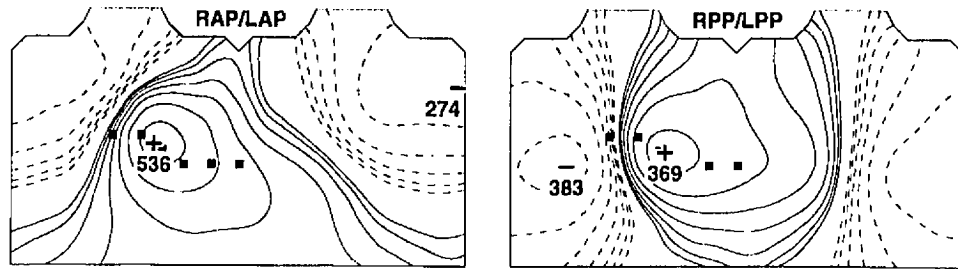


Figure 6.3: BSPMs calculated at 30 ms after the onset of an activation sequence initiated at the anteroseptal and posteroseptal sites. RAP/LAP, the intermediate site between the right anteroparaseptal (RAP) and the left anteroparaseptal (LAP) sites; LPP/RPP, the intermediate site between the left posteroparaseptal (LPP) and the right posteroparaseptal (RPP) sites. See the legend of Fig. 6.2 for details of the layout.

left anteroparaseptal (LAP). Fig. 6.3 shows BSPMs for two additional preexcitation sites: one between the RAP and LAP sites, and the other between the RPP and LPP sites. The changes in BSPMs were assessed for the preexcitation site assuming positions on the basal septum in the following order: 1) from the RPP toward RAP regions, 2) from the RAP toward LAP regions, and 3) from the RPP toward LPP regions.

The preexcitation sites between the RPP and RAP regions. The activation sequence originating at the RPP preexcitation site gives rise to BSPMs in which the minimum is located inferiorly to the maximum and the negative potentials cover the right anterior and right posterior torso. Although this pattern is very similar to that generated by the activation sequence initiated at the right posterior preexcitation site (see, e.g., [257]), the region of near-zero potentials on the posterior torso is more vertical, and the potential values on the right posterior torso are more negative, with a steeper potential gradient in BSPMs corresponding to the RPP preexcitation

site. As the preexcitation site is moved closer to the RIS site, the region of near-zero potentials on the right posterior torso becomes nearly vertical, with positive potentials covering the entire left side of the torso (from shoulders to waist); the position of the minimum rotates CW, thereby becoming located at the same level, or slightly superior to, the maximum. BSPMs generated by the activation sequence originating at the RAS preexcitation site exhibit a simultaneous expansion of the positive area on the lower torso and shrinking of the positive area on the upper torso. For BSPMs corresponding to the RAP preexcitation site, the lower torso becomes completely positive; the position of the minimum and the negative area of the map become rotated further CW, ending up being located superior to the maximum and the positive area and covering almost the entire upper torso.

The progressive changes of the BSPMs described above reflect the course of ventricular activation. The wavefront of propagated activation initiated at the RIS preexcitation site advances symmetrically in the direction of the anterior and posterior septum, thereby creating BSPMs that, consistent with experimental data [89], have a virtually vertical region of near-zero potentials and a horizontal line connecting the extrema. When the preexcitation site is shifted toward either the anterior or posterior septum, the course of the resulting propagated activation sequence becomes asymmetrical (with only one side of the wavefront propagating in the septum). This produces, in turn, a superiorly located minimum in the former case, an inferiorly located minimum in the latter, and in both cases, a more horizontal region of near-zero potentials.

The preexcitation sites between the RAP and LAP regions. Comparison between BSPMs generated by the activation sequences originating at the RAP and LAP preexcitation sites shows changes in the following features: 1) the region of near-zero potentials becomes more horizontal for the LAP site, and 2) the position of the minimum is shifted from the right mid-anterior torso for the RAP site to the posterior neck for the LAP site. The activation sequence initiated at the antero-septal preexcitation site between the RAP and LAP sites gives rise to a BSPM pattern in which the configuration of the region of near-zero potentials is similar to the one corresponding to the RAP preexcitation site but in which the minimum is located on the upper right posterior torso.

The preexcitation sites between the RPP and LPP regions. For the pre-excitation site being shifted from the right-sided septal region toward the left-sided septal region on the posterior side of the epicardium, changes in BSPMs are more subtle than those on the anterior side of the epicardium: 1) the region of near-zero potentials on the anterior and posterior torso becomes more vertical, and 2) the minimum migrates progressively toward the right midaxillary line of the torso and, for the LPP preexcitation site appears on the lower right posterior torso. BSPMs generated by the activation sequence originating at the LPP preexcitation site are similar to those generated by the activation sequence initiated at the left posterior preexcitation site (see, e.g., [257]). However, the region of near-zero potentials on the posterior torso is more vertical in BSPMs corresponding to the LPP site. In addition, the positive potentials extend to the lower left torso in BSPMs corresponding to the LPP preexcitation site.

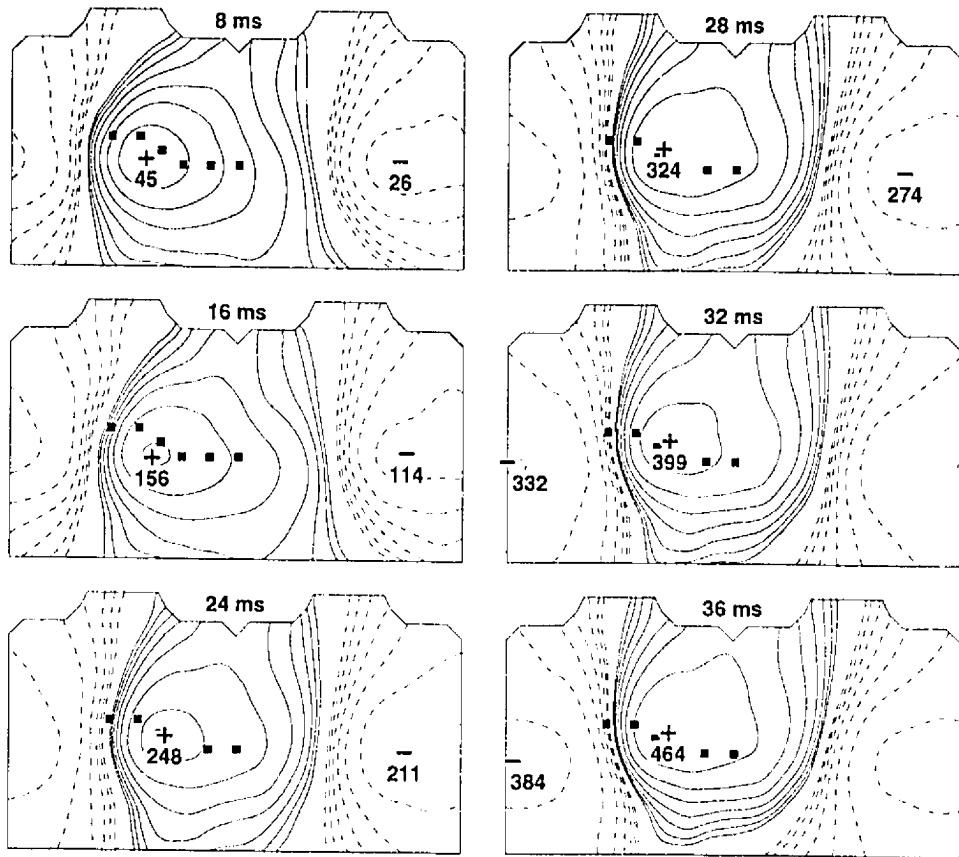


Figure 6.4: BSPMs calculated at six time instants after the onset of an activation sequence initiated at the left posteroparaseptal (LPP) site. See the legend of Fig. 6.2 for details of the layout.

BSPMs corresponding to the septal preexcitation sites are characterized by a relatively stable pattern during the first 40 ms after the onset of activation. The position of the extrema remains stationary in nearly all cases. However, whereas the configuration of the region of near-zero potentials is stable from the very onset of activation for some preexcitation sites, for others it undergoes change during the initial 10 ms after the onset but does not significantly change thereafter. It is also interesting that nearly all BSPMs generated by the activation sequences originating at all septal preexcitation sites other than the LAP site and the site between the RAP and the LAP sites exhibit the LBBB pattern (i.e., the precordial lead V_1 is negative). This implies that a considerable portion of the wavefront of propagated activation spreads from the right side of the septum toward the left side of the septum.

Left-sided posteroparaseptal sites are the exception with respect to the stationarity of the minimum, as shown in Fig. 6.4. For all of those sites, the minimum is initially positioned on the right posterior torso but then progressively migrates toward the torso's right midaxillary line.

6.4 BSPM localization of the site of origin of idiopathic VT

Idiopathic VT [39, 112, 214, 263, 407] is another model of focal activation in the structurally normal heart. It has a relatively well-defined origin, positioned either in the RV outflow tract (RVOT) or in the apical region of the LV endocardium. Because the sites of origin are well separated, a standard 12-lead ECG is usually sufficient for the gross localization of the area of origin of idiopathic VT and may thus be used to supplant BSPMs in guiding radiofrequency (RF) catheter ablation

[40, 45, 192]. SippensGroenewegen et al. [336], Klug et al. [194], and Kamakura [180] demonstrated the ability of BSPMs to accurately localize the site of origin of idiopathic VT. Klug et al. [194] found two different BSPM patterns that did not depend on the clinical presentation of idiopathic VT: 1) the LBBB configuration with the minimum located on the upper anterior torso, corresponding to the origin of VT in the RV outflow tract, and 2) the RBBB configuration with the minimum positioned on the lower anterior torso, corresponding to the origin of VT in the apical region of the LV endocardium. Klug et al. [194] also noted that the LBBB pattern remained stable from the onset throughout the QRS complex, whereas the RBBB pattern exhibited initial instability and evolved—approximately when the activation of the apex had been completed—into a stable pattern.

Simulations of BSPMs corresponding to idiopathic VT have not been attempted before. The additional purpose of the study presented in this section was to validate our ventricular model by initiating ectopic activation in a limited area of the RV and LV endocardium before embarking on the systematic development of the simulated BSPM reference data base for paced activation sequences in human ventricles (Section 6.5).

6.4.1 Results

We simulated BSPMs that correspond to the two distinct anatomical areas—one at the RVOT and the other at the posteroseptal apical area of the LV endocardium—in which ectopic activation originates in patients suffering from idiopathic VT. For each of the eight simulated activation sequences, we calculated, at 4-ms increments, corresponding BSPMs and EPs within the first 120 ms after the onset of activation.

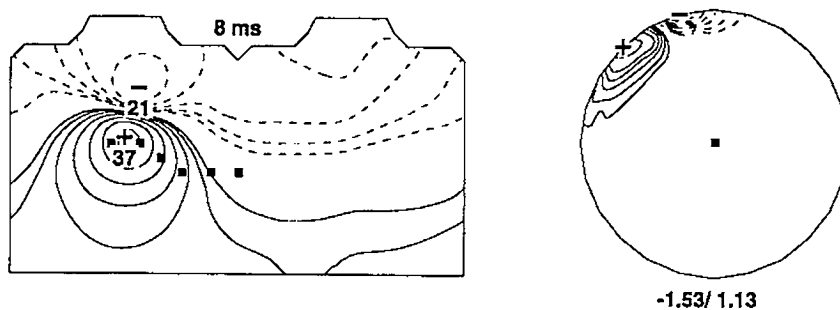


Figure 6.5: BSPM and EPM calculated at 8 ms after the onset of an activation sequence initiated at the right ventricular outflow tract (RVOT). The EPM is displayed with the anterior epicardium at the top and the posterior epicardium on the bottom, the right free wall on the left side, and the left free wall on the right side; the position of the LV apex is shown as the black square. The extrema are denoted in mV below the map, and isopotential lines are plotted in logarithmic increments. For details of the layout of the BSPM, see the legend of Fig. 6.2.

We also calculated QRS-integral maps extending from the onset of activation to the time when activation of the ventricles has been completed.

Idiopathic VT with the origin of activation at the RVOT. Fig. 6.5 shows a BSPM and an EPM calculated at 8 ms after the onset of an activation sequence initiated at the RVOT. The potential minimum, indicating the basal RV breakthrough, is located on the upper anterior torso. This minimum is a reflection of the potential minimum in the EPM at the RV basal anterior site that coincides with the site of early ectopic activation (see Chapters 4 and 5 for details). Fig. 6.6 shows BSPMs for the same case at 12 different time instants. The pattern of the BSPMs evolves slowly from the onset of activation throughout the sequence, and the following general features can be identified: 1) the region of negative potentials covers the upper torso, and the region of positive potentials covers the lower torso (inferior axis), 2) the potential maximum is initially on the left midanterior torso and in the last third of

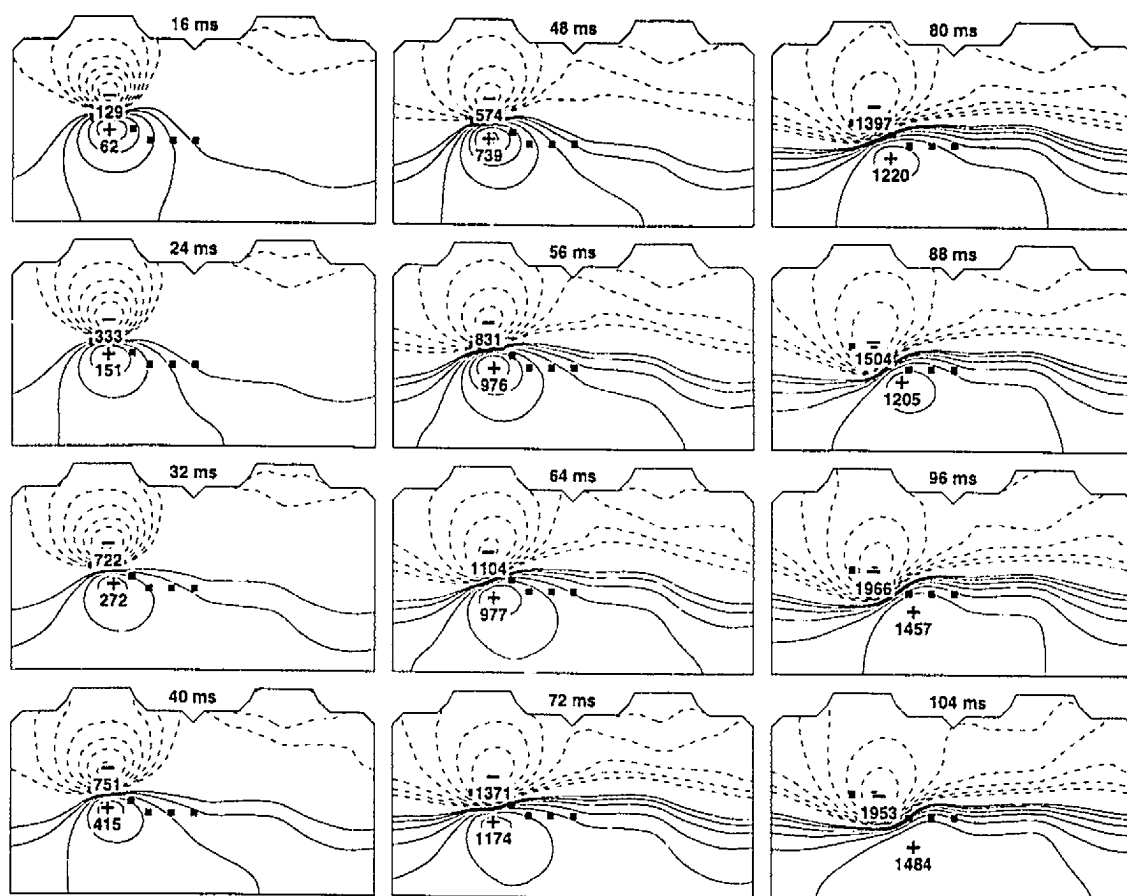


Figure 6.6: BSPMs calculated at 12 time instants after the onset of an activation sequence initiated at the RVOT. See the legend of Fig. 6.2 for details of the layout.

the sequence moves downward and leftward, and 3) the potential minimum is on the upper anterior torso through most of the sequence, subtly moving downward toward the midanterior torso during the final phase of the activation sequence. The location of the minimum and the extent of the negative area indicate the course of the propagated activation from the base toward the apex. The expansion of the positive area and the migration of the maximum reflect the course of propagation from right to left. Simulated BSPMs in Figs. 6.5 and 6.6 correspond very well with an activation sequence measured by Klug et al. [194].

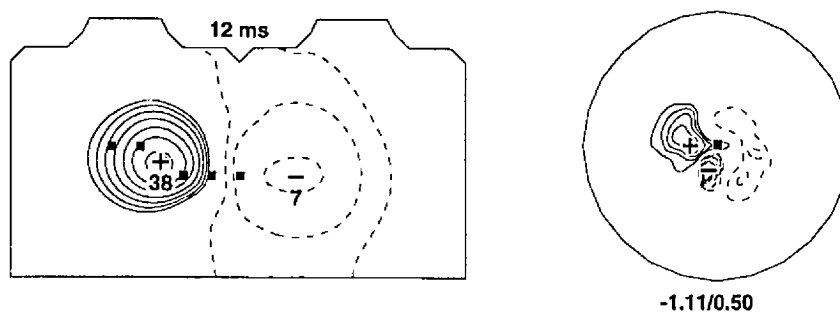


Figure 6.7: BSPM and EPM calculated at 12 ms after the onset of an activation sequence initiated at the posteroseptal apical region of the LV endocardium. See the legends of Fig. 6.2 and 6.5 for details of the layout.

Idiopathic VT with the origin of activation at the LV apical region. Fig. 6.7 shows a BSPM and an EPM calculated at 12 ms after the onset of an activation sequence initiated at the LV posteroseptal apical region, and Fig. 6.8 shows BSPMs at 12 time instants later in the same activation sequence. The position of the potential minimum in the EPM (Fig. 6.7) reveals the apical posteroseptal origin of the activation. Unlike the BSPMs calculated during the activation sequence initiated at the RVOT, these BSPMs—characterized by low-amplitude (< 0.1 mV) potentials—

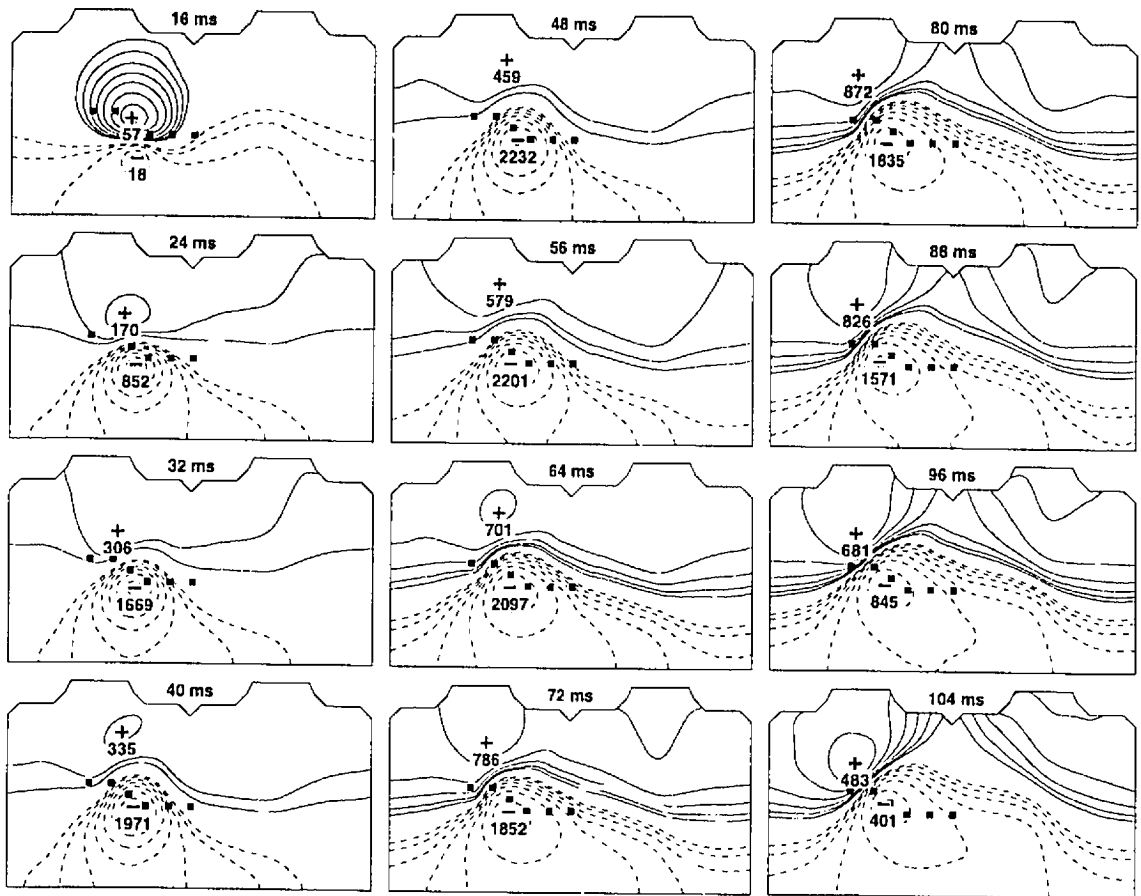


Figure 6.8: BSPMs calculated at 12 time instants after the onset of an activation sequence initiated at the posteroseptal apical region of the LV endocardium. The BSPM pattern stabilizes at 16 ms after the onset of activation and evolves slowly thereafter (compare with Fig. 6.7). See the legend of Fig. 6.2 for details of the layout.

change during the initial phase of this activation sequence. At the approximate time of epicardial breakthrough (at 16 ms after the onset of activation), the BSPMs evolve into a distinct pattern with the following features (Fig. 6.8): 1) the region of positive potentials covers the upper torso, and the region of negative potentials covers the lower torso (superior axis), 2) the potential maximum is on the upper middle of the anterior torso, and 3) the potential minimum is between precordial leads V_3 and V_4 . The location of the minimum and the extent of the negative area reflect the apical breakthrough and subsequent propagation of activation from the apex toward the base. The entire sequence of BSPMs in Fig. 6.8 is nearly a mirror image (obtained by exchanging the regions of negative and positive potentials about the region of near-zero potentials) of the sequence of BSPMs generated by ectopic activation originating at the RVOT (Fig. 6.6). The BSPMs in Fig. 6.8 closely resemble the later phases of an activation sequence measured by Klug et al. [194]. The initial pattern of their BSPMs was, however, different (indicating the inferior axis) from that of our simulated BSPMs (indicating the rightward axis) and also stabilized slightly later (at ≈ 20 ms after the onset of activation) than ours (16 ms).

QRS-integral maps. Fig. 6.9 shows QRS-integral maps for simulated activation sequences initiated at the RVOT and at the posteroseptal apical region of the LV endocardium. In the former case, the pattern of the QRS-integral maps resembles that of instantaneous BSPMs throughout the sequence, while in the latter case, it resembles that of instantaneous BSPMs during the later phases of activation (when the amplitude of the potentials is high). The correlation coefficient between QRS-integral maps corresponding to the sequences initiated at the RVOT and at the LV

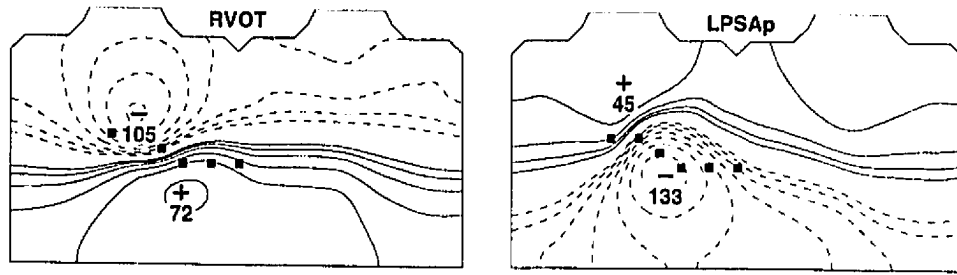


Figure 6.9: QRS-integral maps calculated for activation sequences initiated at the right ventricular outflow tract (RVOT) and at the LV endocardial posteroseptal apical (LPSAp) area. The extrema are denoted in μVs . See the legend of Fig. 6.2 for other details of the layout.

posteroseptal apical region is -0.772 , which provides a quantitative index of the major pattern difference between the ectopic activation sequences initiated at these widely separated sites (RV anterobasal vs. LV posteroapical). Both simulated QRS-integral maps very closely resemble those measured clinically by SippensGroenewegen et al. [336] and Klug et al. [194].

To determine how QRS-integral maps are affected by small alterations in the position of the ectopic activation site within the local endocardial area, we calculated QRS-integral maps for ectopic activation sequences initiated at two additional sites of the RVOT. (One site, RVOA, was positioned 6 mm closer to the apex, and the other site, RVOP, was 13 mm more posterior than the site on the anterior side of the RVOT used to generate the QRS-integral map in Fig. 6.9.) Comparison of the QRS-integral maps corresponding to these slightly shifted initial sites with the map shown in Fig. 6.9 reveals only small changes in the position of the extrema and in the morphology of the region of near-zero values, thereby resulting in high correlation coefficients (0.974 for the more posterior site and 0.977 for the more apical site, with respect to the RVOT reference map). These simulations agree with

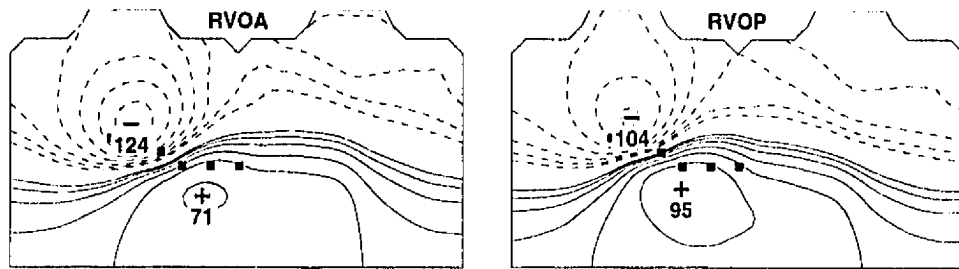


Figure 6.10: QRS-integral maps calculated for activation sequences initiated at two different sites of the RVOT. RVOA, the ectopic activation site is positioned 6 mm closer to the apex than the one in Fig. 6.9; RVOP, the ectopic activation site is positioned 13 mm more posteriorly than the one in Fig. 6.9. See the legends of Figs. 6.2 and 6.9 for details of the layout.

measurements of SippensGroenewegen et al. [339], who noted that pacing in the RVOT and basal anterior RV endocardial region generated QRS-integral maps with very little morphological variation. Similar results (not shown), demonstrating small pattern differences in QRS-integral maps, were also obtained for the apical region of the LV endocardium. This, too, agrees with the data of SippensGroenewegen et al. [339].

6.5 BSPM reference data base for paced activation sequences in human ventricles

The precise localization of the sites of ectopic ventricular activation is a prerequisite for the successful ablative treatment of monomorphic or polymorphic VTs. Endocardial activation sequence mapping during VT that has been induced by a programmed electrical stimulation [405, 406] is a successful and widely accepted method of accurately predicting the arrhythmogenic regions. It can be performed with a catheter in an electrophysiology laboratory (catheter mapping) [140, 175, 176] or in the exposed

heart during surgery (intraoperative mapping) [15, 16, 17, 61, 107, 139, 156, 198, 215, 276]. However, the method has associated risks since it can induce—albeit under clinically controlled conditions—a potentially lethal arrhythmogenic state. Some VTs may not be tolerated hemodynamically, may decay into ventricular fibrillation, or may not be morphologically stable. The utility of intraoperative mapping is additionally constrained by the time and difficulty involved in inducing VT during surgery.

Catheter pace mapping has been proposed [177] as an alternative indirect localization technique. Its utility is based on the assumption that ectopic pacing at the area of origin of VT could reproduce the ECG morphology of spontaneous or induced VT. The pace mapping procedure has usually been guided by means of a 12-lead ECG because Josephson and coworkers [177, 400] had successfully used a 12-lead ECG to show that the morphology of the QRS complex of ventricular ectopic beats reflects the activation sequence and its endocardial area of origin (within a mean area of $\approx 20\text{--}25\text{ cm}^2$). Recently however, SippensGroenewegen et al. [337] demonstrated that localization by means of a standard 12-lead ECG cannot be better than that corresponding to a mean area of $15 \pm 12\text{ cm}^2$. As has been noted already, one can more accurately differentiate ectopic activation sites by inspecting BSPMs.

Early studies by Ushijima et al. [393], Hayashi et al. [141], Kamakura et al. [181], Klersy et al. [193], and Savard et al. [326] were limited because they focused only on specific features (such as a location of minimum with an amplitude more negative than -0.5 mV) of BSPMs at a single time instant. SippensGroenewegen et al. [339] subdivided the LV and RV endocardium into 38 segments (with a mean area resolution

of $3.3 \pm 1.4 \text{ cm}^2$ in the LV, and with a mean area resolution of $6.7 \pm 2.9 \text{ cm}^2$ in the RV), and their aim was to develop a classification based on BSPM recordings that would discriminate among the activation sequences initiated at those segments. Twelve patients with no ventriculographic or 2-D echocardiographic evidence of structural heart disease underwent BSPM recordings during ectopic beats generated by catheter stimulation at endocardial sites corresponding to the selected segments. The study later was expanded to include hearts compromised by a prior anterior or inferior myocardial infarction [340]. They subsequently used patterns derived from QRS-integral maps as templates to supplant the guiding of surgical and catheter ablation [338].

In preliminary work [160, 161], we simulated ectopic activation in the model of the human ventricular myocardium. We initiated the activation sequences at 45 LV and 20 RV endocardial sites and calculated isochronal maps of activation and BSPMs at 60 ms after the onset of activation. The results of our simulations indicated that the BSPM patterns generated by the developed wavefronts were distinctly determined by the initial sites of activation and closely resembled the BSPMs recorded by SipensGroenewegen et al. [339]. Although we have shown in this initial study that, for a limited number of sites at least, QRS-integral distributions can be relatively accurately approximated by the instantaneous distributions at 60 ms after the onset of activation, having arbitrarily chosen one particular time instant limited our study. In this section, we shall advance that preliminary work and calculate QRS-integral maps generated by systematic ectopic pacing in the LV and RV.

6.5.1 Simulated activation sequences

We initiated ectopic activation sequences at 126 LV endocardial pacing sites and 58 RV endocardial pacing sites. Endocardial ectopic pacing sites were in six levels (basal, basal/midbasal, midbasal, middle, midapical, and apical) at 12 equiangular increments (relative to the local geometric center of the ventricular cavity) around the LV and RV endocardium; in the LV, additional endocardial levels (viz., midbasal/middle, middle/midapical, midapical/apical) were also explored. We calculated BSPMs, EPMs and QRS-integral maps corresponding to each ectopic activation sequence according to the protocol described in Section 6.4. In this subsection, the sequences of BSPMs calculated at different time instants will be related to the corresponding isochronal maps and EPMs.

Anterior endocardial pacing in the middle level of the LV. Fig. 6.11 shows the isochronal map calculated for an activation sequence initiated at the anterior endocardial pacing site in the middle level of the LV. As already demonstrated in Chapters 4 and 5, the anisotropy has a pronounced effect on the propagation of activation. The leading edge of the crest-like wavefront, following the principal fiber direction, moves much faster around the LV cavity than across the wall, and it spreads CCW toward the base and CW toward the apex in a characteristic spiral pattern. Epicardial breakthrough occurs at 24 ms after the onset of activation in the anterior area of the LV epicardium.

Fig. 6.12 shows the pattern of BSPMs and EPMs calculated at 12, 36, and 60 ms into the sequence. At 12 ms after the onset of activation, the EPM shows one

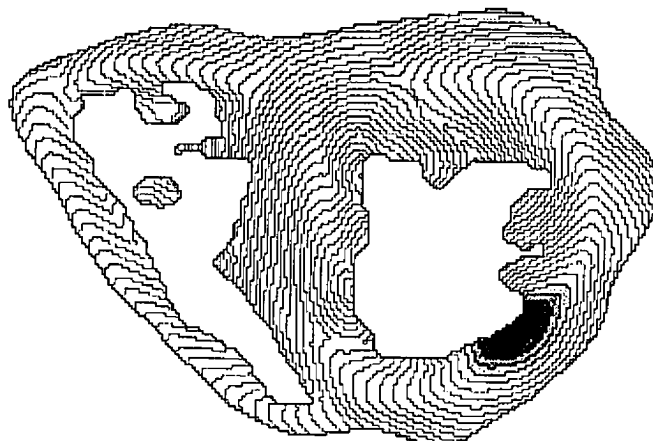


Figure 6.11: Isochronal map calculated for an activation sequence initiated at the anterior endocardial pacing site in the middle level of the LV. Isochrones are shown in an axial cross section taken through the model at 45 mm above the LV apex. See the legend of Fig. 5.9 for details of the layout.

negative area above the endocardial pacing site and the two adjacent positive areas. At 36 ms, after the epicardial breakthrough, the central negative area expands and develops an oblong shape, while the two positive areas expand and rotate CW. At 60 ms, the negative area further expands, covering nearly the entire anterolateral LV epicardium, and both negative and positive areas become fragmented in part due to the involvement of the conduction system.

The sequence of corresponding BSPMs (Figs. 6.12 and 6.13) reflects the activation isochrones and EPMs. The formation of the elliptically shaped central negative area on the epicardium after the epicardial breakthrough is concomitant with the evolution of initially unstable BSPM patterns—characterized by low-amplitude potentials—into a distinct and stable dipolar pattern. When the BSPM pattern stabilizes, the potential minimum is located on the upper middle posterior torso (close to the left

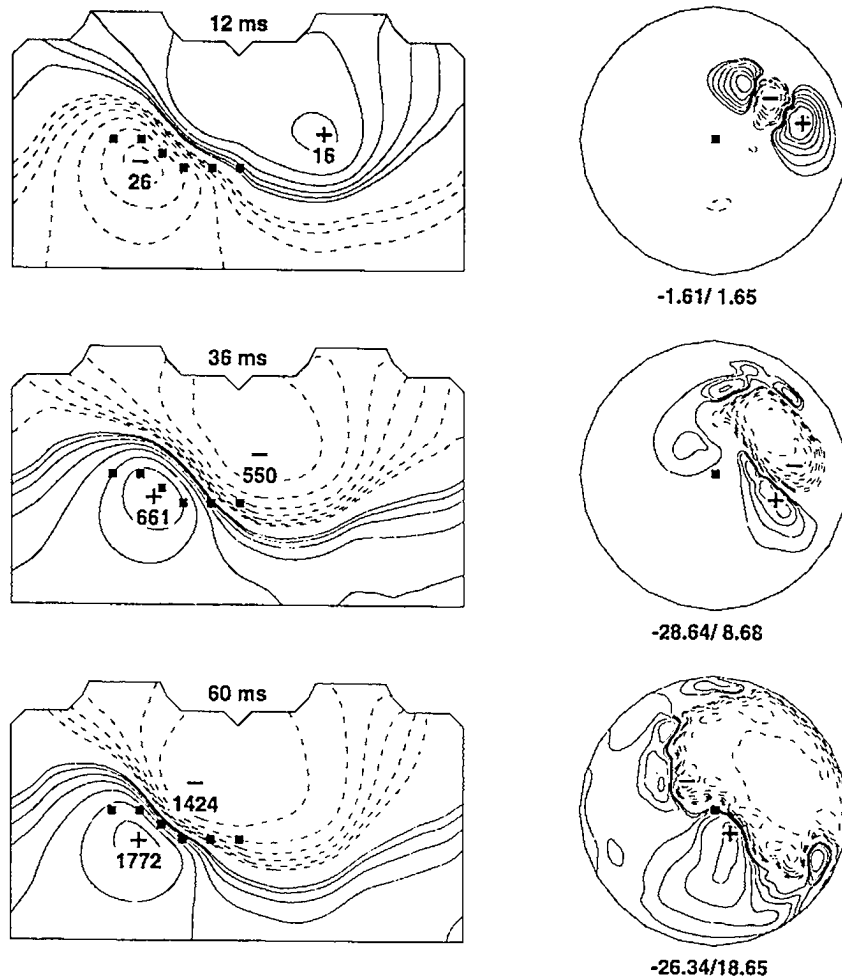


Figure 6.12: BSPMs and EPMs calculated at three time instants after the onset of an activation sequence initiated at the anterior endocardial pacing site in the middle level of the LV. See the legends of Fig. 6.2 and 6.5 for details of the layout.

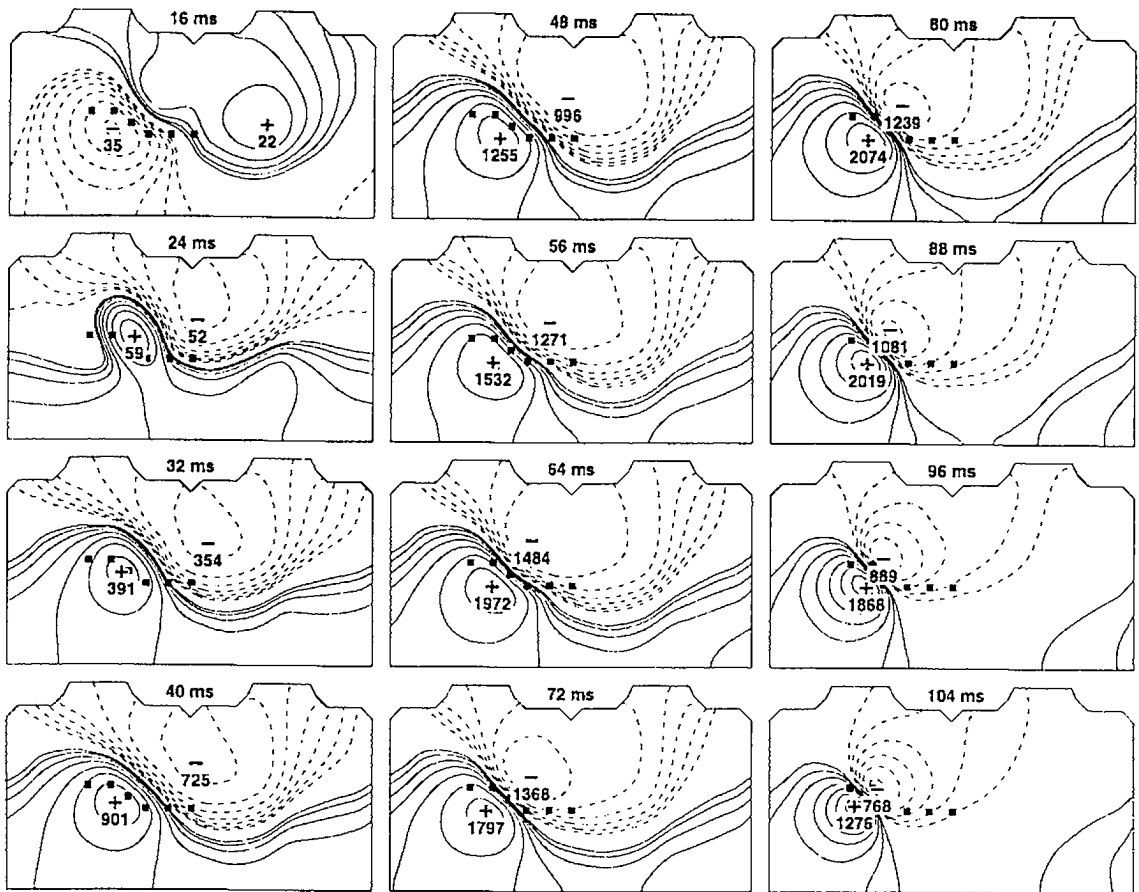


Figure 6.13: BSPMs calculated at 12 time instants after the onset of an activation sequence initiated at the anterior endocardial pacing site in the middle level of the LV. The BSPM pattern stabilizes at 24 ms after the onset of activation, and remains stable thereafter. See the legend of Fig. 6.2 for details of the layout.

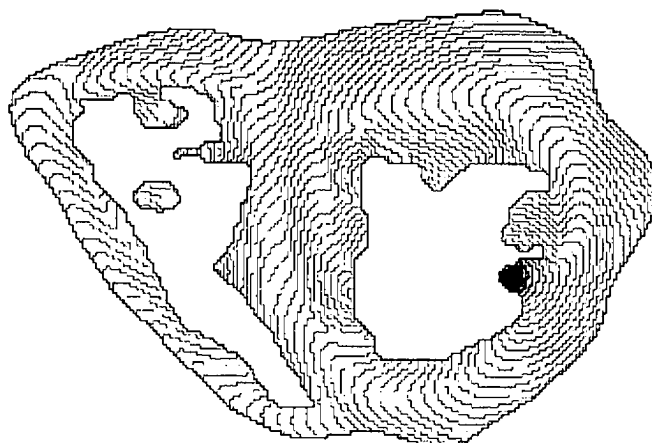


Figure 6.14: Isochronal map calculated for an activation sequence initiated at the anterolateral endocardial pacing site in the middle level of the LV. Isochrones are shown in an axial cross section taken through the model at 45 mm above the LV apex. See the legend of Fig. 5.9 for details of the layout.

midaxillary line), thereby revealing the epicardial breakthrough in the anterior LV free wall. Since the propagated activation progresses from the anterior LV toward the RV, the potential maximum is on the lower middle anterior torso and the region of positive potentials covers the entire lower torso. Some small changes in the BSPM pattern also can be observed after the pattern has stabilized. The area of negative potentials expands toward the sternum of the anterior torso (e.g., at 36 ms after the onset of activation, only V_6 is negative; at 104 ms after the onset of activation, all precordial leads but V_1 are negative), with the minimum concurrently migrating toward the anterior side of the left midaxillary line.

Anterolateral endocardial pacing in the middle level of the LV. Figs. 6.14, 6.15, and 6.16 show the isochronal map, EPM, and BSPMs calculated for an activation sequence initiated at the anterolateral endocardial pacing site in the middle

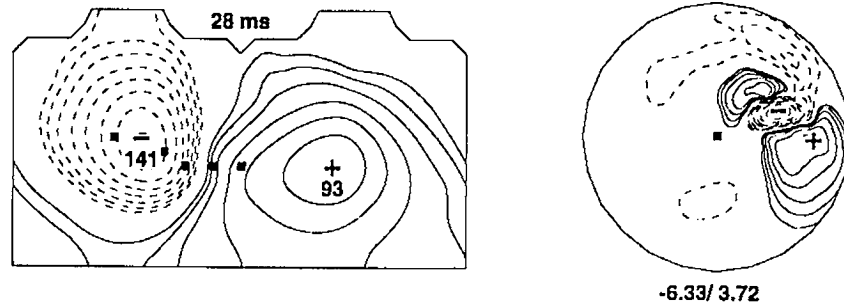


Figure 6.15: BSPM and EPM calculated at 28 ms after the onset of an activation sequence initiated at the anterolateral endocardial pacing site in the middle level of the LV. See the legends of Fig. 6.2 and 6.5 for details of the layout.

level of the LV. (This site is positioned slightly more laterally than the previous one.) While the initial patterns of the EPM and BSPMs are very similar to those observed in the previous case for the anterior endocardial pacing site in the middle level of the LV, the BSPM pattern does not stabilize until 46 ms after the onset of activation. This delay in the evolution of the BSPM pattern occurs because the endocardial pacing is delivered at the portion of the ventricular wall that is covered with thick trabeculata. Such pacing produces an activation wavefront that reaches the epicardial surface later in the activation sequence, as shown by the isochrones in Fig. 6.14. After the epicardial breakthrough, BSPMs with a stable dipolar pattern (Fig. 6.16) feature extrema that are rotated CW compared to those in BSPMs corresponding to the more anterior ectopic activation site shown in Fig. 6.13. In addition, the region of near-zero potentials becomes almost vertical on the posterior and anterior torso.

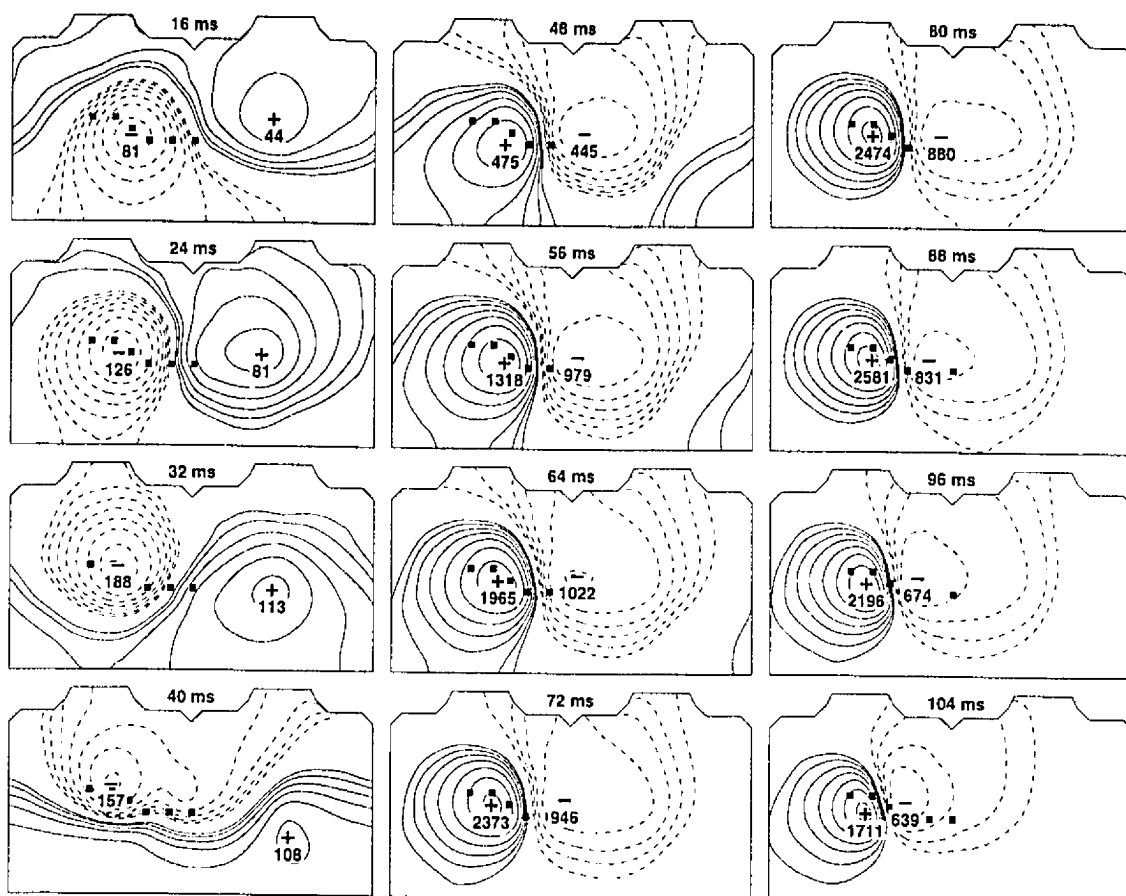


Figure 6.16: BSPMs calculated at 12 time instants after the onset of an activation sequence initiated at the anterolateral endocardial pacing site in the middle level of the LV. The BSPM pattern stabilizes at 46 ms after the onset of activation, and remains stable thereafter. See the legend of Fig. 6.2 for details of the layout.

Apical RV endocardial pacing. Figs. 6.17, 6.18 and 6.19 show isochronal maps, EPMs and BSPMs calculated for an activation sequence initiated near the apex of the RV endocardium. The location of the potential minimum in the EPM at 12 ms after the onset of activation points to ectopic activation initiated near the endocardial apex of the RV. (Compare this with the position of the minimum in EPM shown in Fig. 6.7, which corresponds to ectopic activation initiated in the posteroseptal apical area of the LV.) The region of negative potentials in the EPMs during the more advanced phases of the activation sequence corresponds to the wavefront spreading from the apex toward the base; the propagation is more rapid over the RV than over the LV epicardium. These findings regarding the direction and velocity of propagation are clearly evident in the isochronal map (Fig. 6.17A).

Unlike what occurred in the two LV cases presented above, the BSPM pattern corresponding to RV activation remains relatively stable from the very onset. The region of high-amplitude negative potentials initially covers the precordial area, with the minimum being located near precordial lead V_4 . Later in the sequence, the area of negative potentials covers the entire lower torso, and the area of positive potentials covers the upper torso; the low-amplitude maximum is located on the posterior torso through nearly the entire activation sequence. The sequence of BSPMs in Fig. 6.19 is similar to the one corresponding to idiopathic VT, with the origin at the apical area of the LV endocardium featuring—during the final phase of activation—almost identical morphology (Fig. 6.8). The resemblance of these sequences is due to the proximity of their ectopic activation sites.

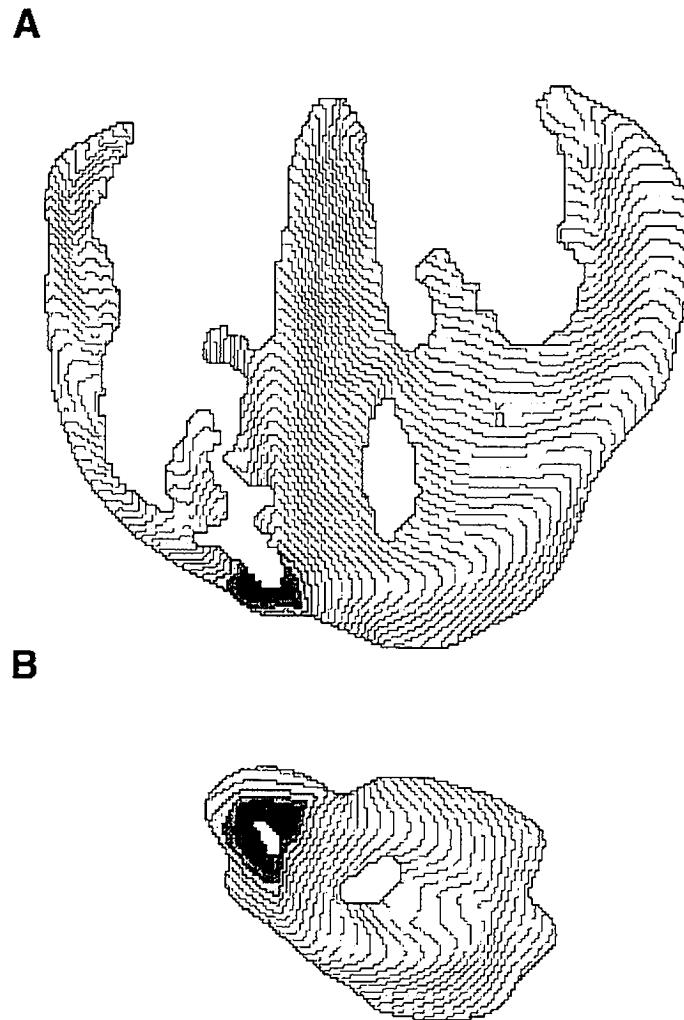


Figure 6.17: Isochronal maps calculated for an activation sequence initiated near the apex of the RV endocardium. The isochrones are shown in coronal cross section taken through the model at 11 mm posterior to the LV apex (A) and in axial cross section taken through the model at 11.5 mm above the LV apex (B). See the legend of Fig. 5.9 for details of the layout.

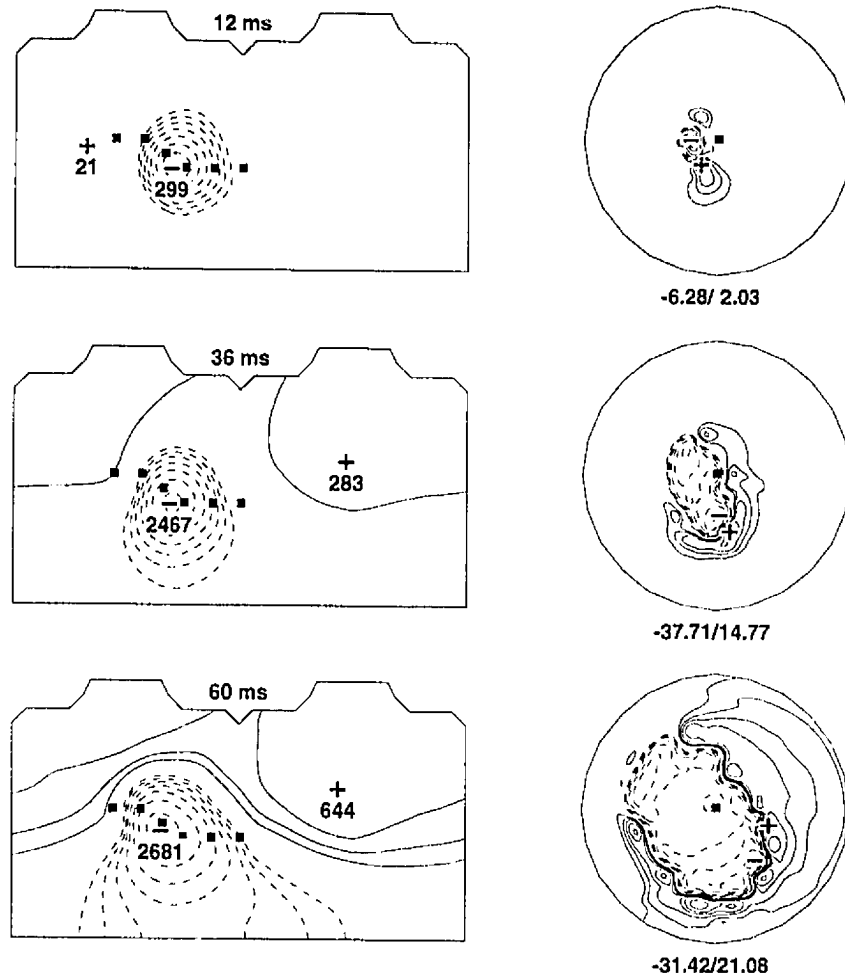


Figure 6.18: BSPMs and EPMs calculated at three time instants after the onset of an activation sequence initiated near the apex of the RV endocardium. See the legends of Fig. 6.2 and 6.5 for details of the layout.

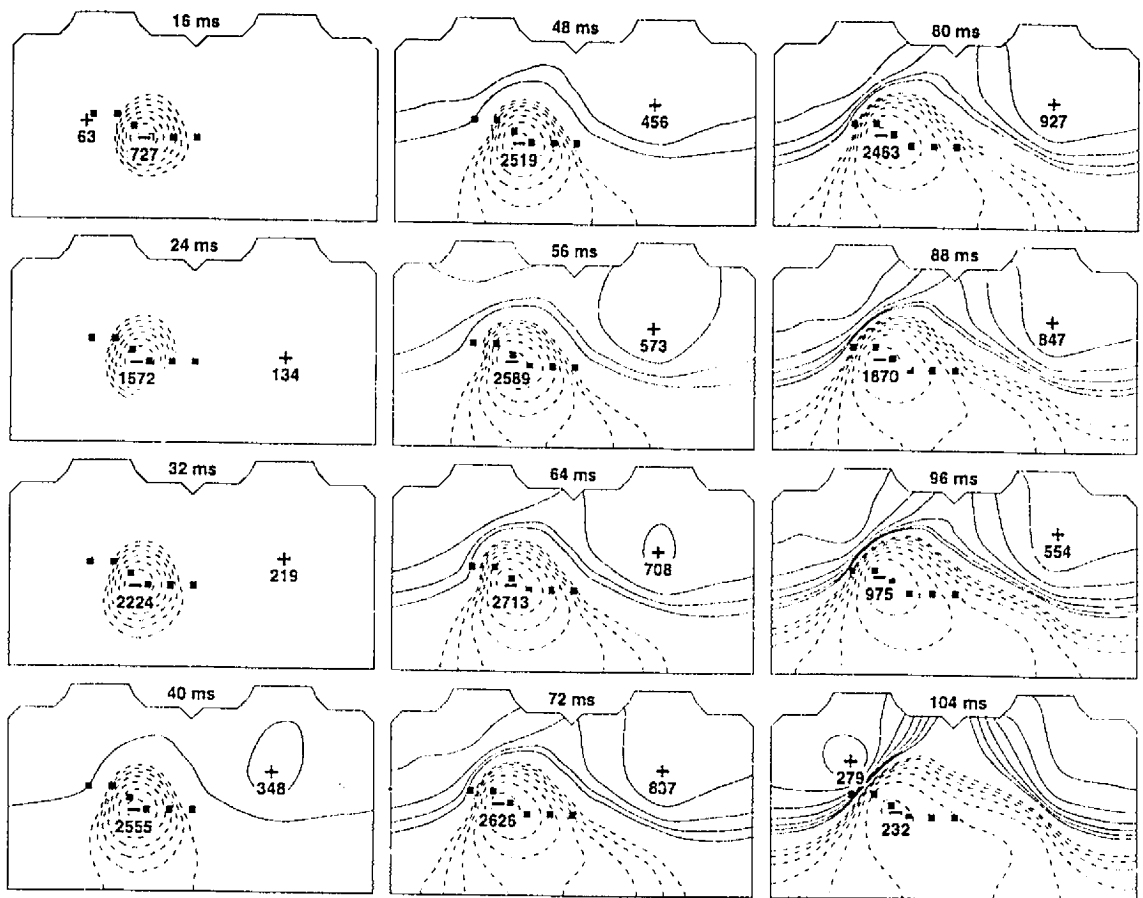


Figure 6.19: BSPMs calculated at 12 time instants after the onset of an activation sequence initiated near the apex of the RV endocardium. The BSPM pattern remains stable throughout the sequence. See the legend of Fig. 6.2 for details of the layout.

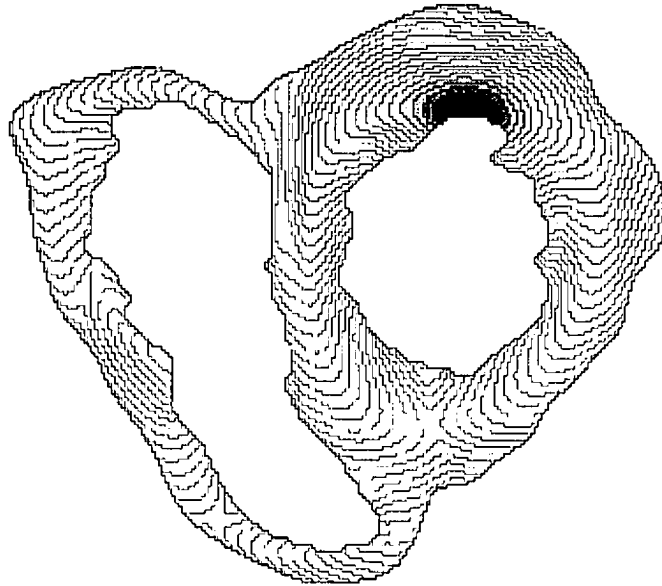


Figure 6.20: Isochronal map calculated for an activation sequence initiated at the posterolateral endocardial pacing site in the basal level of the LV. Isochrones are shown in an axial cross section taken through the model at 70 mm above the LV apex. See the legend of Fig. 5.9 for details of the layout.

Posterolateral endocardial pacing in the basal level of the LV. Figs. 6.20 and 6.21 show the isochronal map, EPs, and BSPMs calculated for an activation sequence initiated at the posterolateral endocardial pacing site in the basal level of the LV. The epicardial breakthrough site at the posterolateral basal LV is reflected in the region of negative potentials located over the lower torso, with the minimum on the lower posterior torso. The basal location of the pacing site determines the principal features of BSPMs, and even though the activation starts at the endocardial, as opposed to the epicardial, site in this case, the BSPMs resemble those corresponding to the left posterior preexcitation site in patients suffering from WPW syndrome [128, 182].

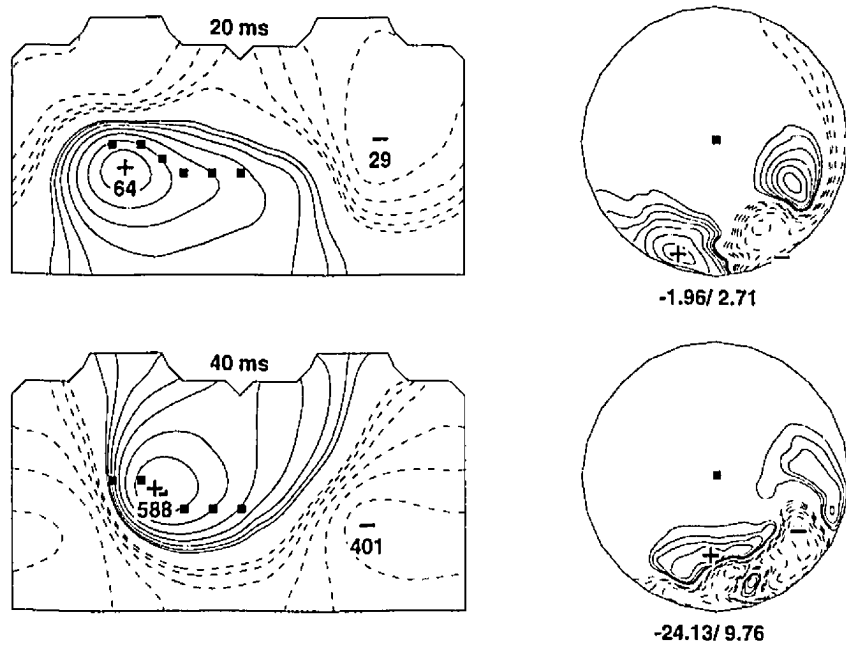


Figure 6.21: BSPMs and EPMs calculated at 20 ms and 40 ms after the onset of an activation sequence initiated at the posterolateral endocardial pacing site in the basal level of the LV. See the legends of Fig. 6.2 and 6.5 for details of the layout.

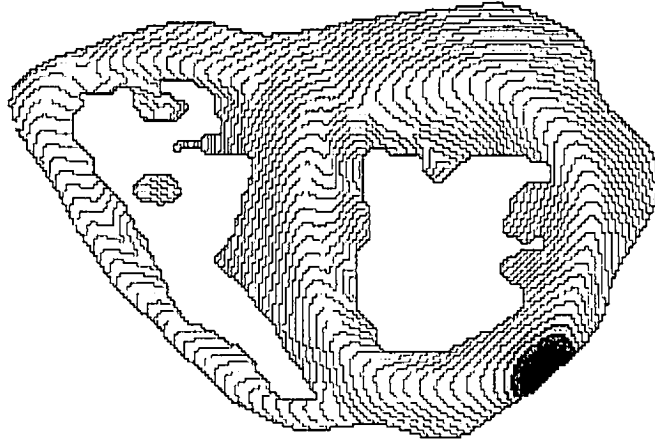


Figure 6.22: Isochronal map calculated for an activation sequence initiated at the anterior epicardial pacing site in the middle level of the LV. The isochrones are shown in an axial cross section taken through the model at 45 mm above the LV apex. Compare with the isochronal map (in Fig. 6.11) generated by the corresponding endocardial pacing. See the legend of Fig. 5.9 for details of the layout.

Comparison of activation sequences for epicardial and endocardial pacing.

To compare the sequences initiated by epicardial stimuli and those initiated by endocardial stimuli, we also simulated sequences of BSPMs starting at a few epicardial pacing sites (three in the LV free wall and one in the RV free wall) for which we have already investigated the corresponding endocardial sites. Figs. 6.22 and 6.23 show the isochronal map and BSPMs calculated for an activation sequence initiated at the anterior epicardial pacing site of the middle level of the LV (for the sequence of BSPMs elicited at the corresponding endocardial pacing site, see Fig. 6.13). The pattern of BSPMs generated by epicardial pacing is stable from the very onset of activation. Comparison with its endocardial counterpart reveals major pattern differences during the initial phase of the activation sequence (with high negative correlation coefficients, e.g., -0.866 at 16 ms after the onset of activation), while during the later phases of

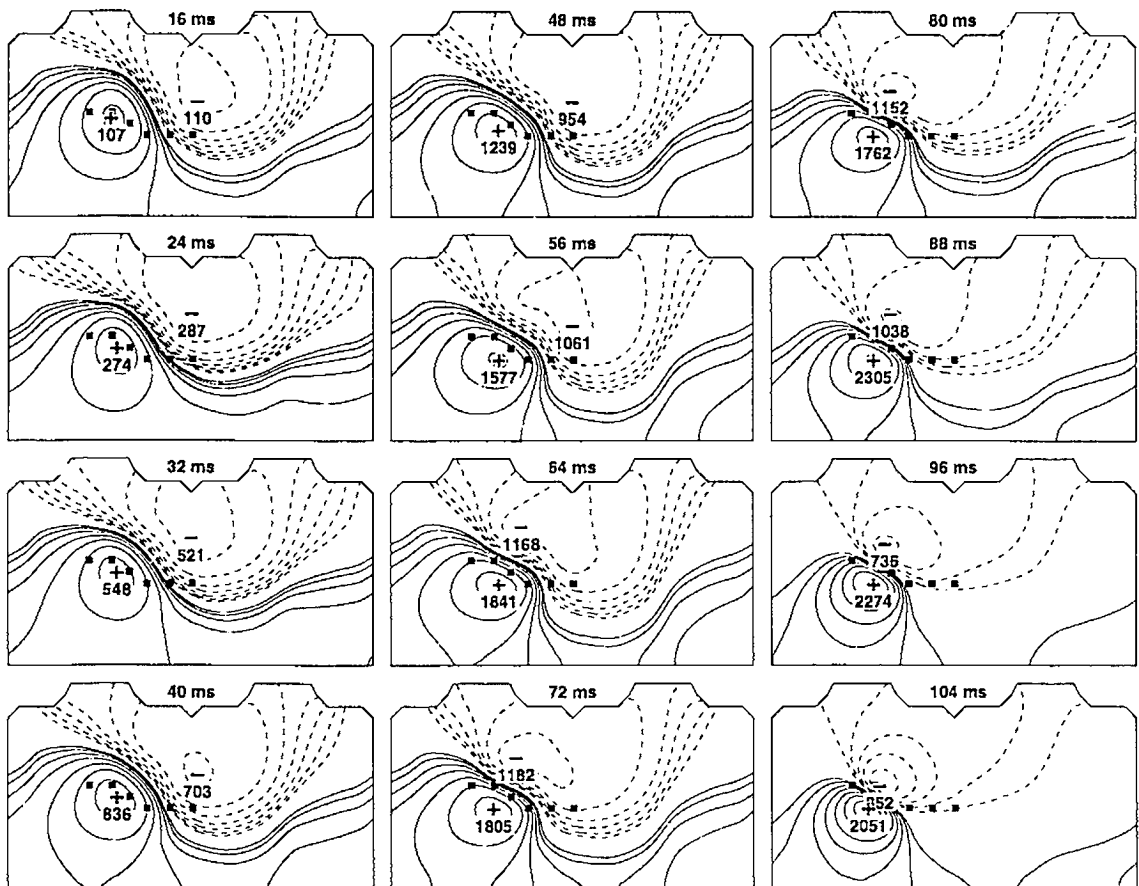


Figure 6.23: BSPMs calculated at 12 different time instants after the onset of an activation sequence initiated at the anterior epicardial pacing site in the middle level of the LV. The BSPM pattern is stable from the very onset of activation. Compare with the sequence (in Fig. 6.13) generated by the corresponding endocardial pacing. See the legend of Fig. 6.2 for details of the layout.

the activation sequence, there are only minor pattern differences between the epicardially and endocardially paced maps (which is indicated by high positive correlation coefficients, e.g., 0.992 at 32 ms or 0.969 at 72 ms after the onset of activation).

The isochronal map in Fig. 6.22 confirms the picture suggested by the sequence of BSPMs. During the initial phase, the activation wavefront moves from the epicardium toward the endocardium in a direction opposite to the one resulting from the activation elicited on the endocardial surface (the isochronal map shown in Fig. 6.11). During the later phases of the activation sequence (i.e., after the endocardially paced wavefront reaches the epicardial surface), the wavefronts in both cases progress in a very similar manner.

6.5.2 Data base of QRS-integral maps

LV endocardial pacing sites. The simulated QRS-integral maps that correspond to the LV endocardial pacing sites are shown in Figs. 6.24–6.29. The QRS-integral maps for the endocardial pacing sites—which were moved in equiangular increments at a given level between the midapical and basal segments of the LV—feature a CCW rotation of the axis joining the extrema as the ectopic pacing site is shifted from the lateral to the anterior, septal, and posterior aspects of the LV endocardium. This rotation of the electrocardiographic axis in the QRS-integral maps corresponding to the adjacent pacing sites on the same level of the LV endocardium is most rapid at the anteroseptal and posteroseptal junctions of the LV. Pacing on both sides of the anteroseptal junction (from the anterior to the septal aspects) generates an almost 90° CCW rotation of the axis, while near the posteroseptal junction (from the septal to the posterior aspects) it results in a nearly 180° CCW rotation of the axis. This ro-

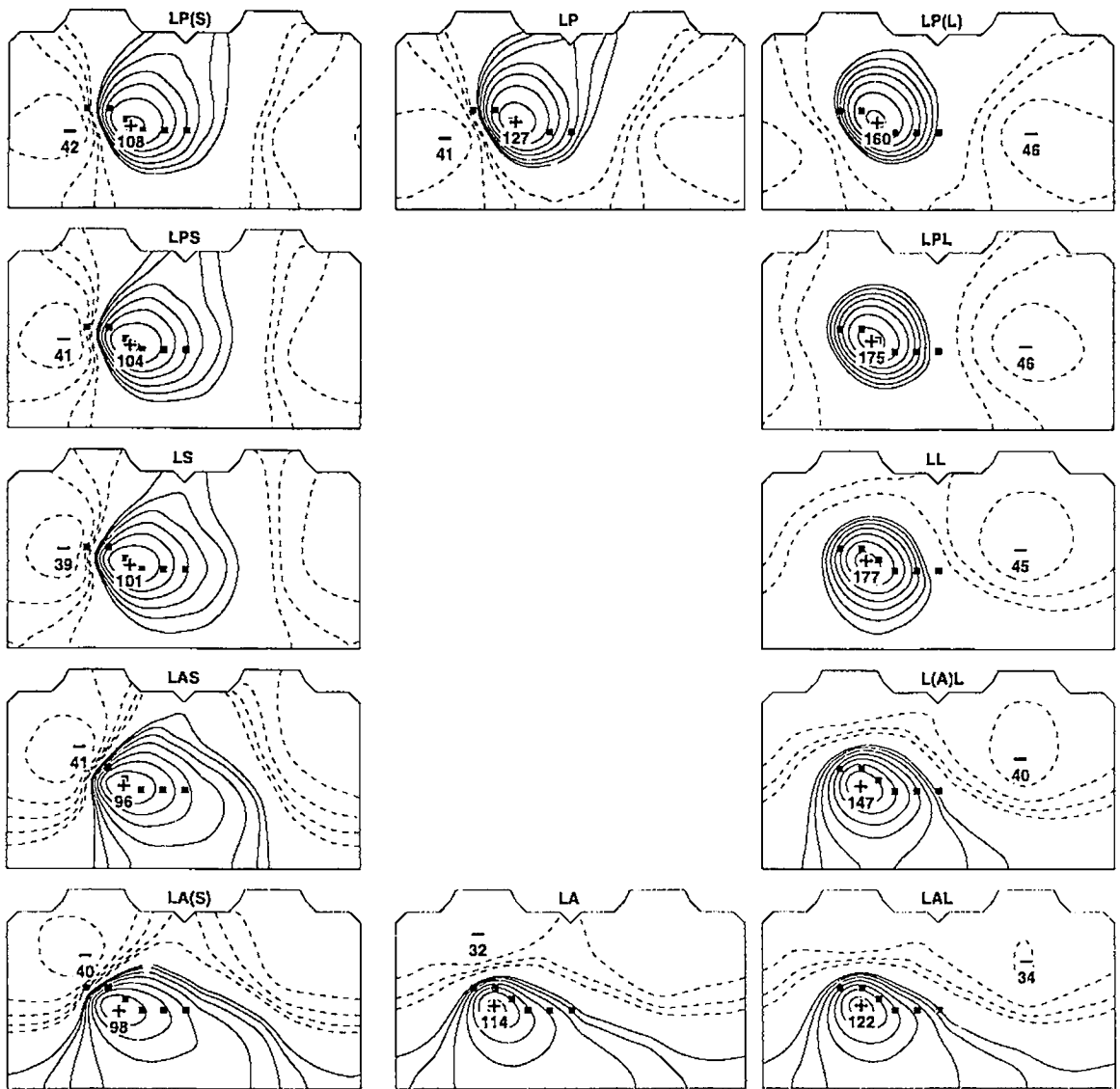


Figure 6.24: QRS-integral maps calculated for activation sequences initiated at 12 endocardial sites in the basal level of the LV. Clockwise (starting with the QRS-integral map at 3 o'clock): LL, left lateral; L(A)L, left lateral/anterolateral; LAL left anterolateral; LA, left anterior; LAS, left anteroseptal; L(A)S, left septal/anteroseptal; LS, left septal; LPS, left posteroseptal; LP(S), left posterior/posteroseptal; LP, left posterior; LP(L), left posterior/posterolateral; LPL, left posterolateral. See the legends of Figs. 6.2 and 6.9 for details of the layout.

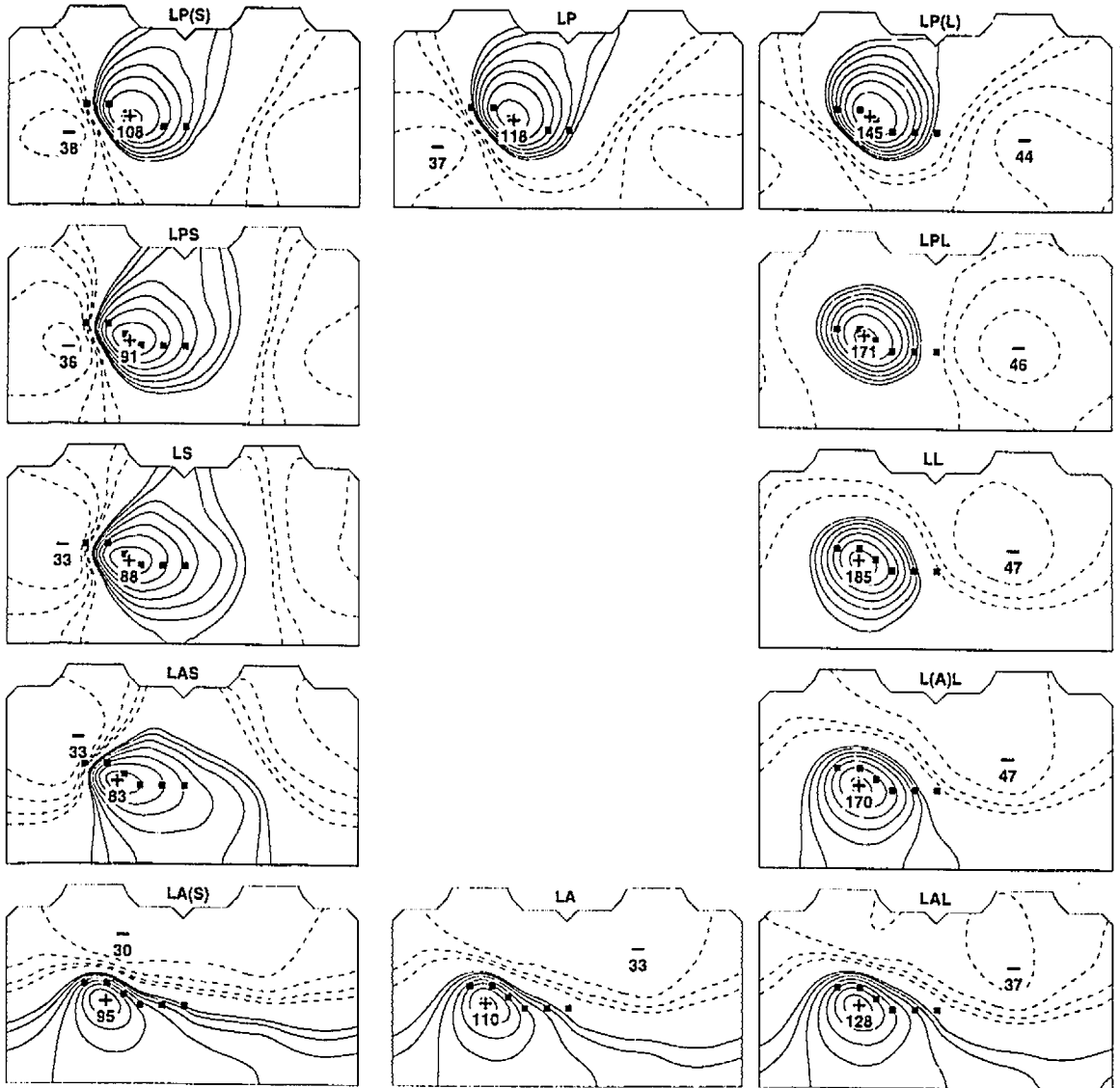


Figure 6.25: QRS-integral maps calculated for activation sequences initiated at 12 endocardial sites in the basal/midbasal level of the LV. See the legends of Figs. 6.2, 6.9, and 6.24 for details of the layout.

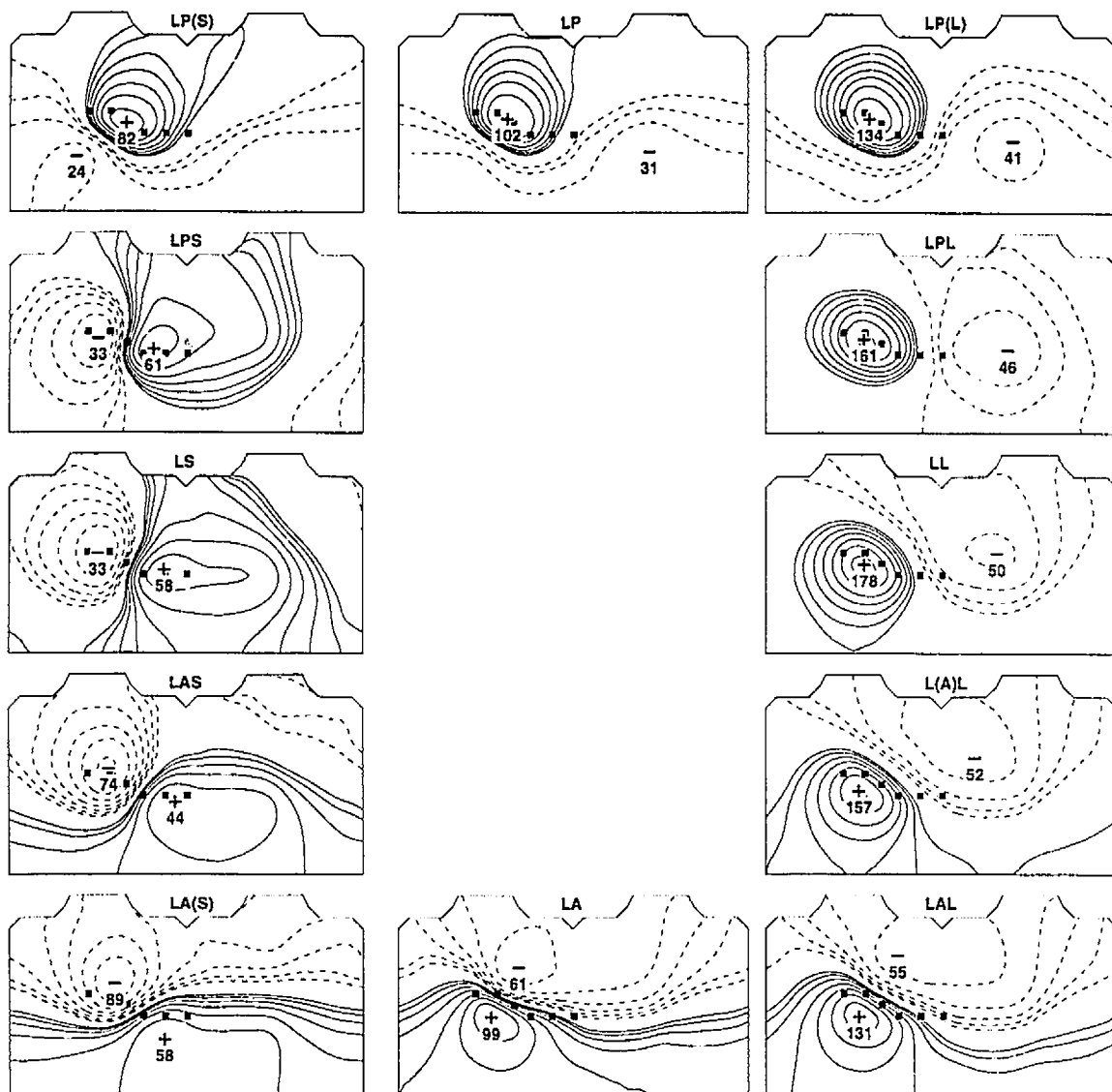


Figure 6.26: QRS-integral maps calculated for activation sequences initiated at 12 endocardial sites in the midbasal level of the LV. See the legends of Figs. 6.2, 6.9, and 6.24 for details of the layout.

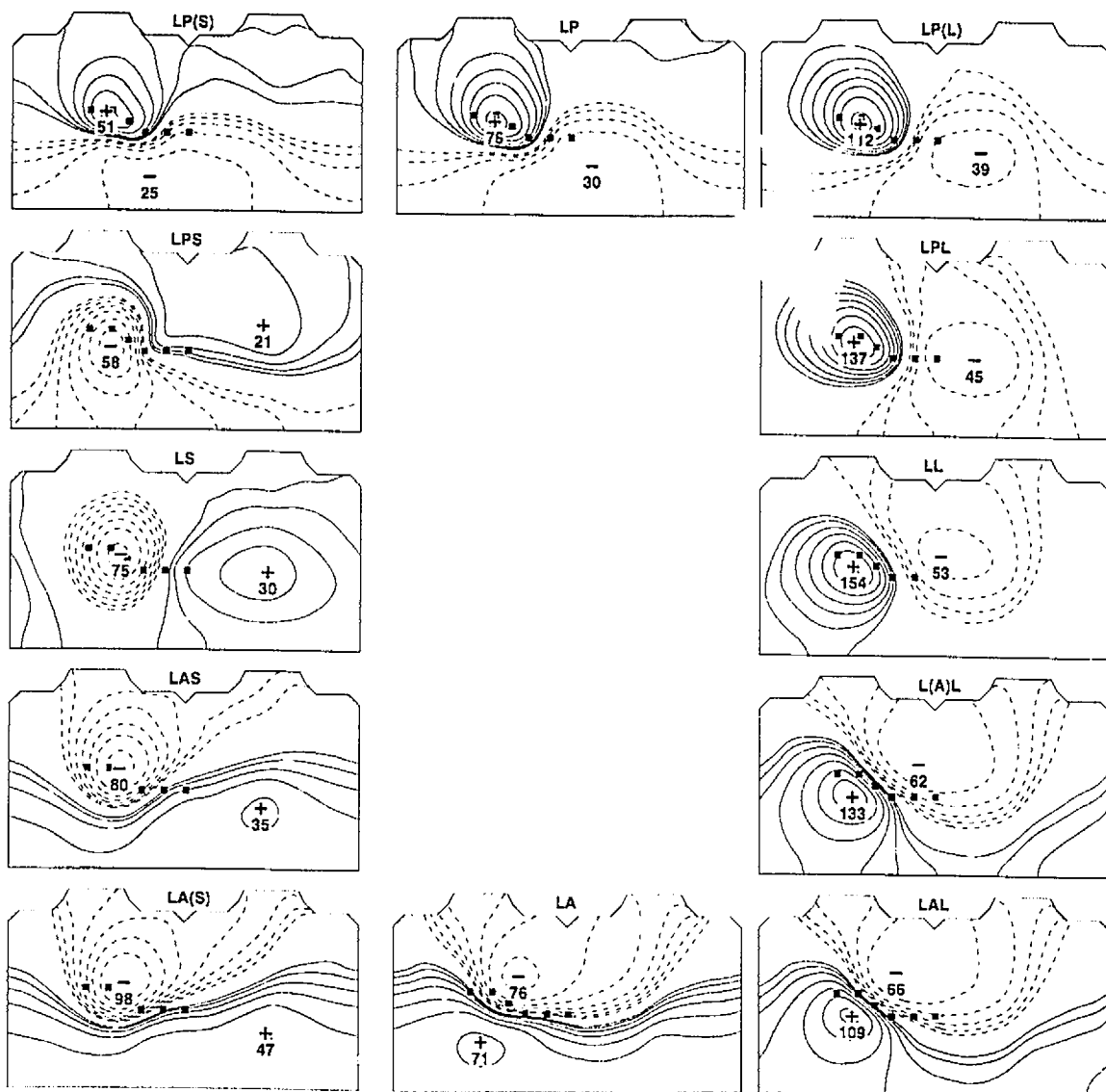


Figure 6.27: QRS-integral maps calculated for activation sequences initiated at 12 endocardial sites in the middle level of the LV. See the legends of Figs. 6.2, 6.9, and 6.24 for details of the layout.

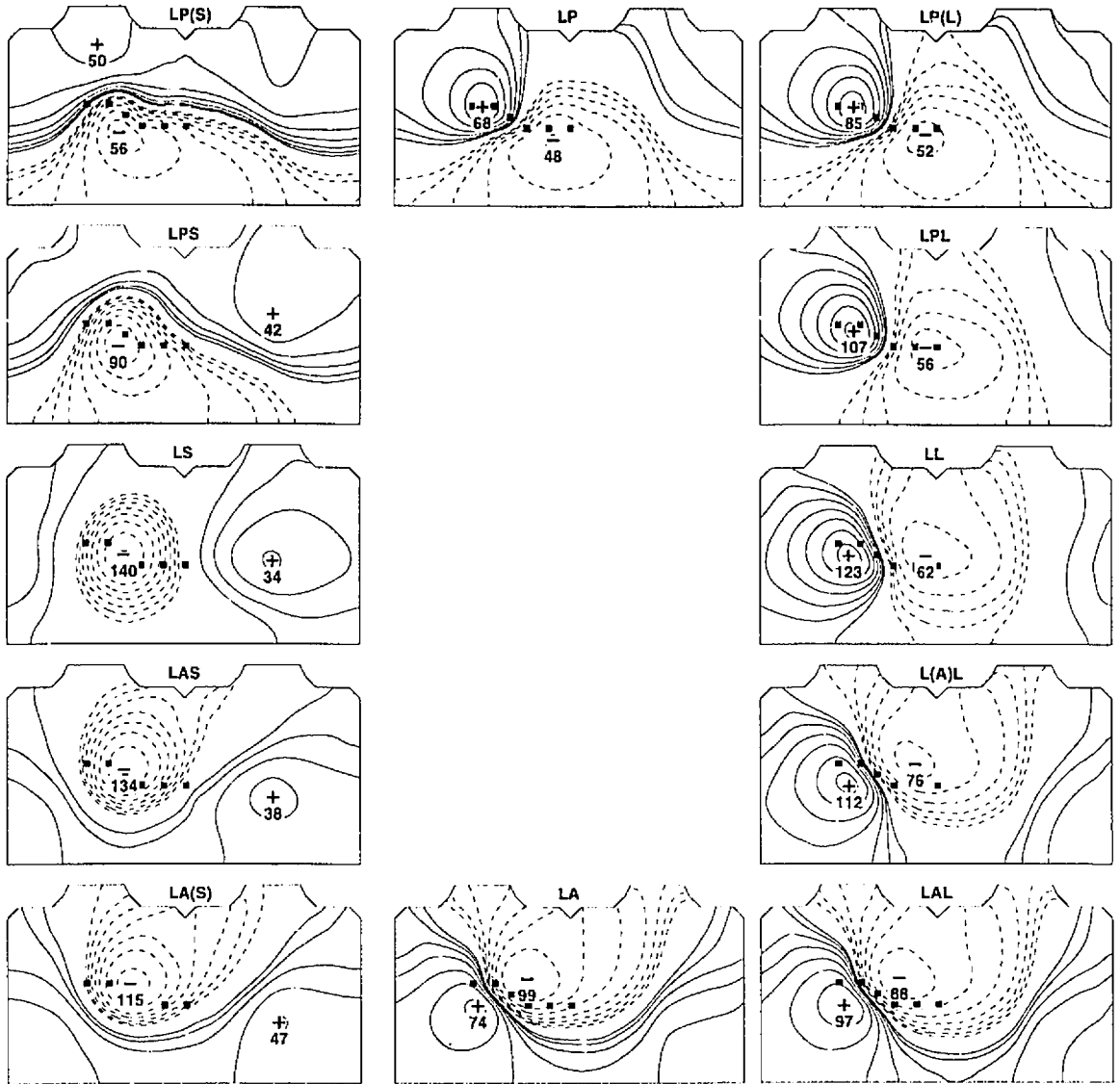


Figure 6.28: QRS-integral maps calculated for activation sequences initiated at 12 endocardial sites in the midapical level of the LV. See the legends of Figs. 6.2, 6.9, and 6.24 for details of the layout.

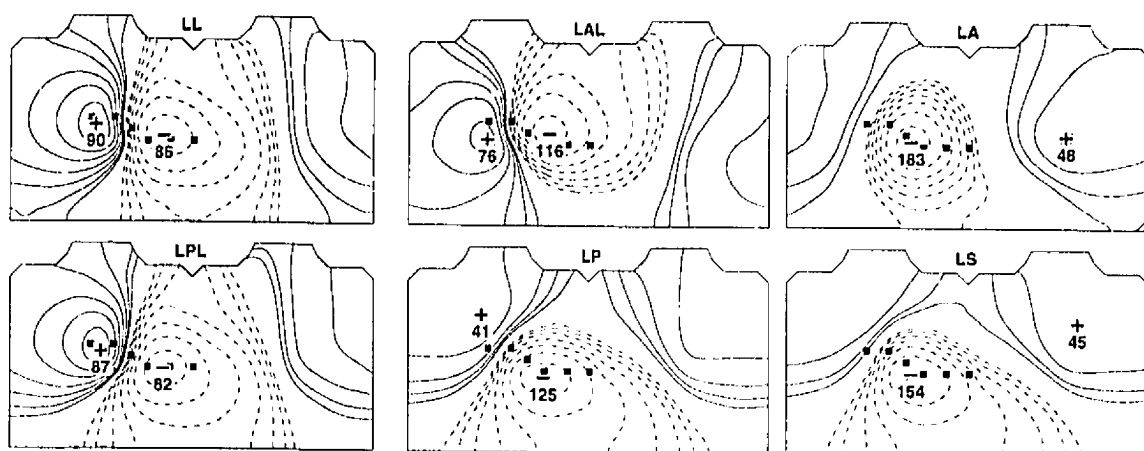


Figure 6.29: QRS-integral maps calculated for activation sequences initiated at 6 endocardial sites in the apical level of the LV. See the legends of Figs. 6.2, 6.9, and 6.24 for details of the layout.

tation of the axis (extrema) is accompanied by progressive changes of the amplitudes of the extrema in the QRS-integral maps, with maps corresponding to the lateral sites being characterized by high-amplitude positive QRS-integral values and those corresponding to the septal sites being characterized by high-amplitude negative values. The exception is the basal level of the LV endocardium, where QRS-integral maps exhibit high-amplitude positive values and low-amplitude negative values for all pacing sites. In general, the amplitudes (in μVs) of the positive QRS-integral values are—for a given aspect of the LV endocardium—larger in the QRS-integral maps that correspond to the basal segment than in those that correspond to the midapical segment; the amplitudes of the negative QRS-integral values show the opposite trend.

In the apical region (Fig. 6.29), the QRS-integral maps are characterized by a region of negative QRS-integral values covering part or all of the precordial area, with

Table 6.1: Correlation Coefficients between QRS-integral Maps for Adjacent and Opposite Pacing Sites Around the LV Endocardium

Level	Adjacent sites	Opposite sites
Basal	0.959 ± 0.023	0.471 ± 0.177
Basal/midbasal	0.931 ± 0.096	0.264 ± 0.253
Midbasal	0.847 ± 0.169	-0.498 ± 0.177
Middle	0.824 ± 0.241	-0.658 ± 0.150
Midapical	0.885 ± 0.106	-0.222 ± 0.100
Apical	0.963 ± 0.021	0.501 ± 0.108

Values are means \pm SD.

the minimum in the lower middle of the anterior torso, close to the precordial lead V_4 . The region of the positive QRS-integral values and the position of the maxima move from the right anterior torso to the right posterior, upper posterior, and upper anterior torso as the pacing site is shifted from the lateral to the anteroseptal and septal aspects of the LV endocardium.

It is interesting that the QRS-integral maps for LV septal pacing sites located between the basal and apical levels and for LV anteroseptal sites between the middle and apical levels feature an LBBB morphology (with a negative precordial lead V_1). As can be expected, the basal QRS-integral maps in Fig. 6.24 resemble the preexcitation BSPMs of patients suffering from WPW syndrome [83, 257] despite the fact that the activation starts at endocardial rather than epicardial sites.

We quantitatively assessed the variability in QRS-integral maps at the same level of the LV endocardium by calculating the correlation coefficients between maps corresponding to adjacent pacing sites, and between maps corresponding to sites on opposite sides of the LV endocardium. The middle and midbasal levels exhibit the

most pronounced variability in the patterns of their QRS-integral maps, i.e., relatively low correlation coefficients, with large standard deviations for the adjacent maps (Table 6.1). The most marked change between adjacent QRS-integral maps was observed for pacing at the middle and midbasal anteroseptal and posteroseptal junctions of the LV, which agrees with qualitative observations (described above) regarding the rotation of the electrocardiographic axis. (For example, the correlation coefficients between LV middle posteroseptal and adjacent LV middle posterior and LV middle septal maps were 0.116 and 0.641, respectively.) By contrast, at the basal level, high positive correlation coefficients with small standard deviations were found for the adjacent maps.

Figs. 6.30 and 6.31 are two examples showing how QRS-integral maps differ between different levels of the anterior and posteroseptal aspects of the LV endocardium. These alterations are clearly seen in changes in the zero-line configuration and the axis joining the extrema. Fig. 6.32 shows QRS-integral maps for the lateral aspect of the LV endocardium where differences among QRS-integral maps are less obvious because the changes in the distance between the extrema are subtler and the shifting of the regions of negative and positive QRS-integral values is relatively small. Quantitative evaluation of pattern variability between QRS-integral maps that correspond to adjacent levels shows more pronounced differences for the posteroseptal (with the average correlation coefficient of 0.874 ± 0.155) than for the anterior (0.966 ± 0.016) or the lateral sites (0.983 ± 0.008). Quantitative assessment of the total difference between maps corresponding to the basal and midapical levels reveals a similarly larger variability in the posteroseptal aspect (resulting in the negative correlation co-

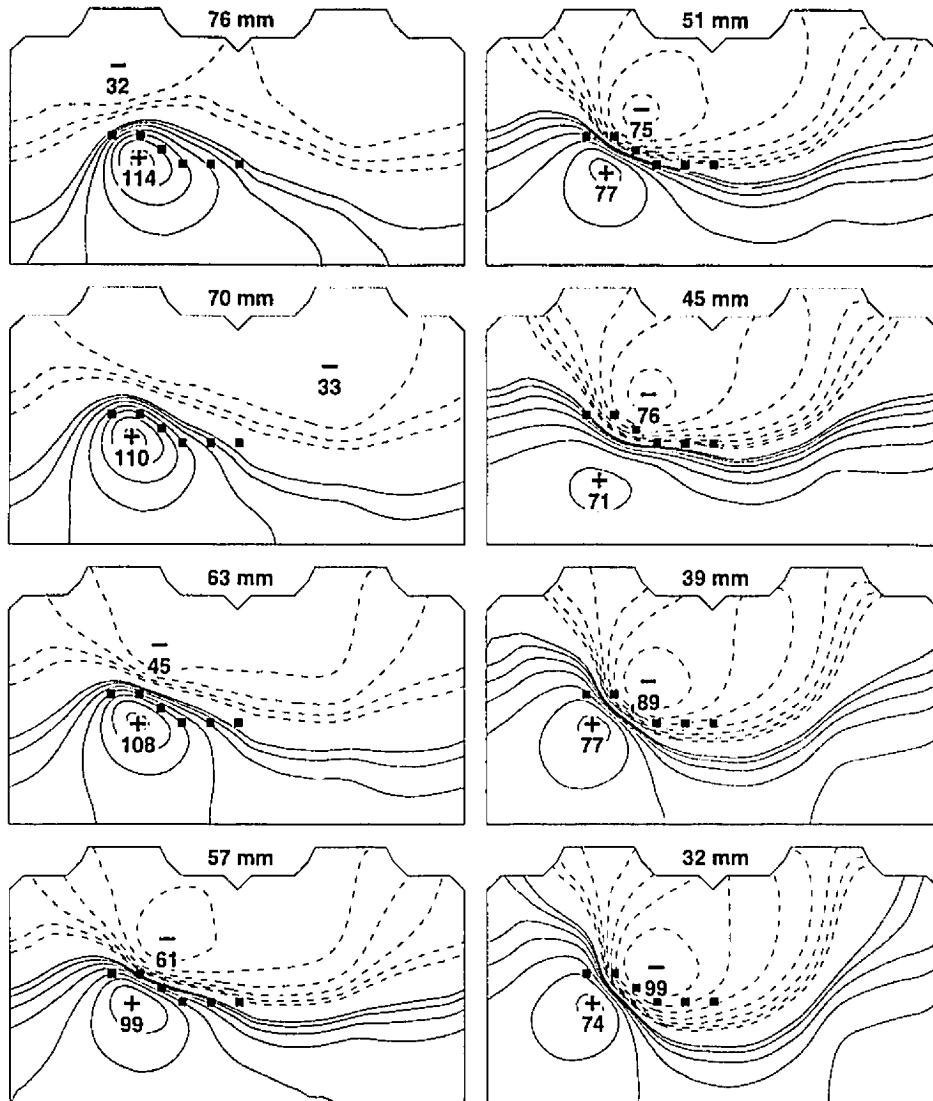


Figure 6.30: QRS-integral maps calculated for activation sequences initiated at 8 levels in the anterior aspect of the LV endocardium. The number above each map corresponds to the height of the pacing site above the LV apex. See the legends of Figs. 6.2 and 6.9 for details of the layout.

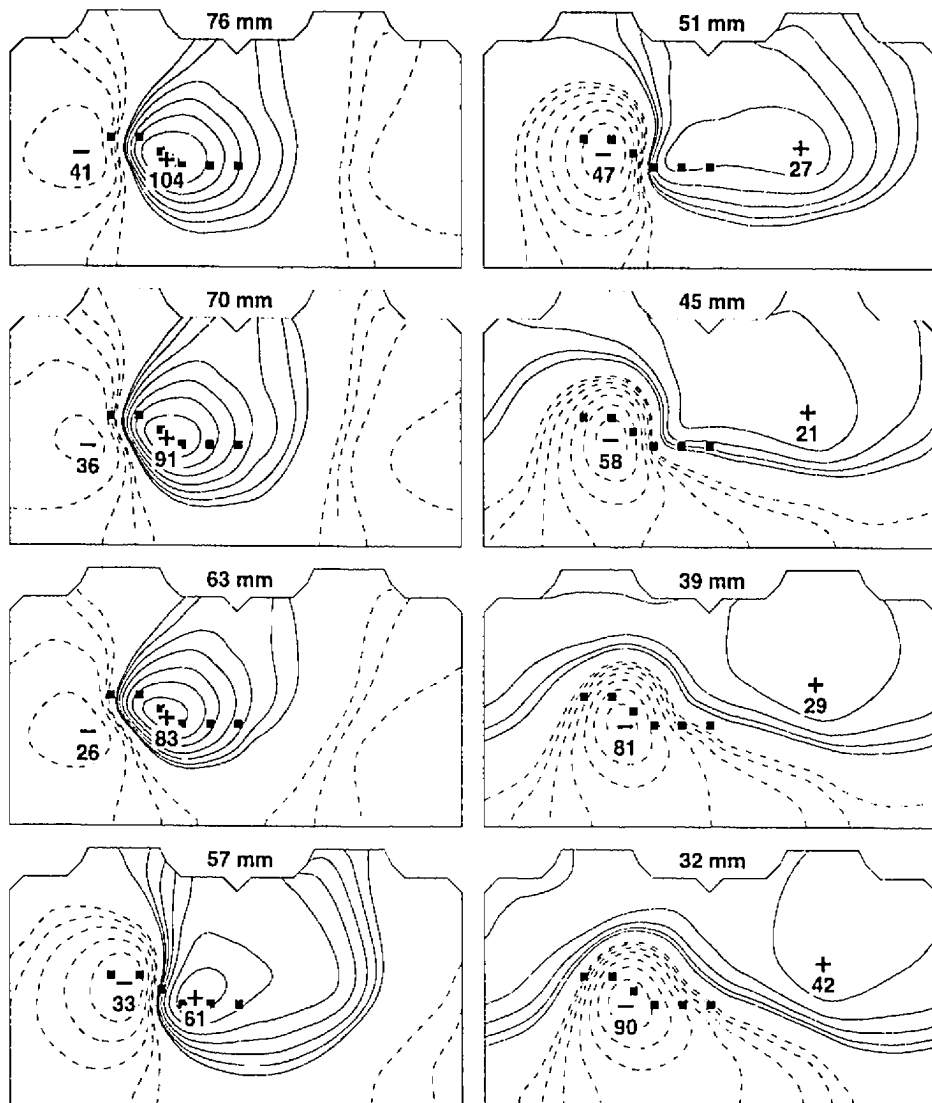


Figure 6.31: QRS-integral maps calculated for activation sequences initiated at 8 levels in the posteroseptal aspect of the LV endocardium. See the legends of Figs. 6.2, 6.9, and 6.30 for details of the layout.

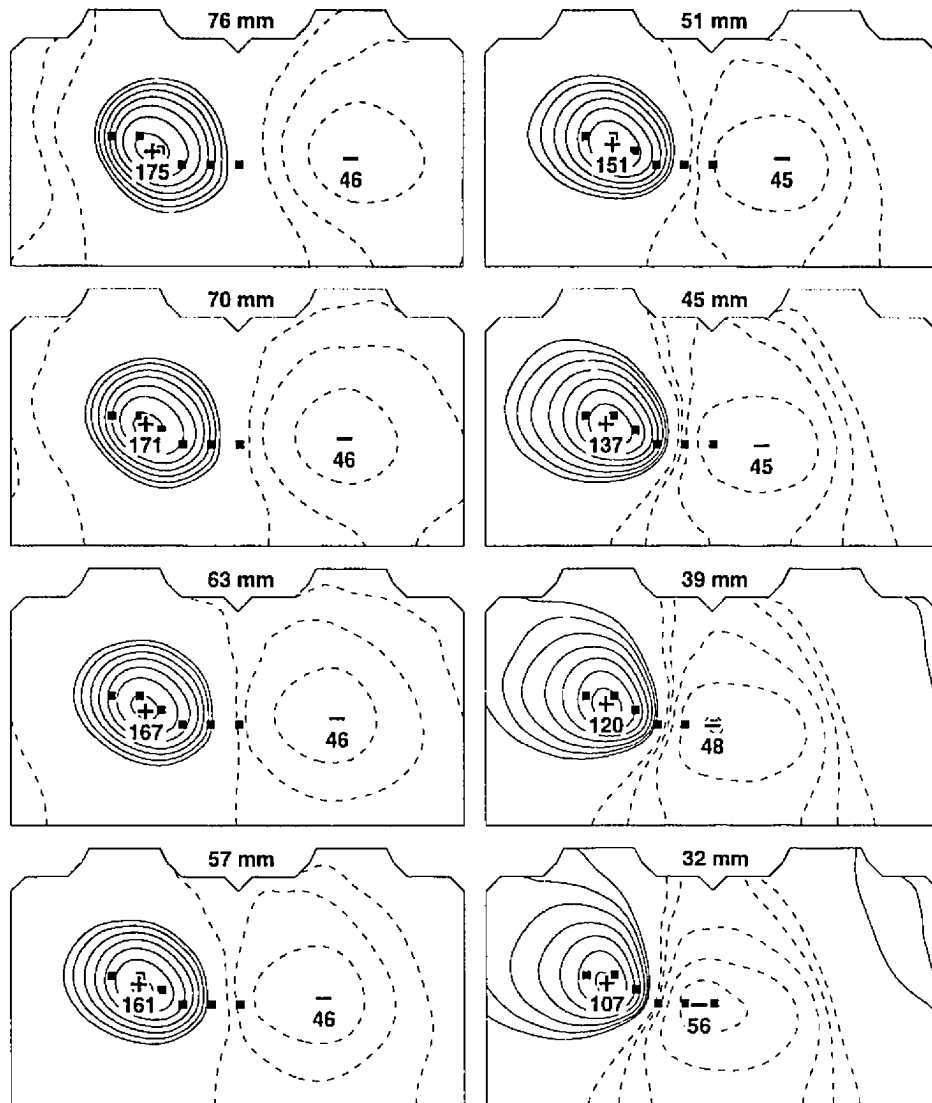


Figure 6.32: QRS-integral maps calculated for activation sequences initiated at 8 levels in the anterior aspect of the LV endocardium. See the legends of Figs. 6.2, 6.9, and 6.30 for details of the layout.

efficients of -0.597) than in the anterior and lateral aspects (exhibiting low positive correlation coefficients of 0.312 and 0.368 , respectively) of the LV endocardium.

RV endocardial pacing sites. The simulated QRS-integral maps for the RV endocardial pacing sites are shown in Figs. 6.33–6.35. All feature a region of high-amplitude negative values on the anterior torso, with a distinct LBBB morphology. The position of the extrema and orientation of their joining axis are affected to a relatively small degree when the pacing site is shifted around the RV endocardium. The configuration of the region of near-zero values appears to be the most potent discriminator between QRS-integral maps.

The similarity among RV QRS-integral maps was reflected in high average positive correlation coefficients between the adjacent maps in the same level (0.947 ± 0.042 for the basal level, 0.919 ± 0.130 for the middle level, and 0.882 ± 0.197 for the midapical level) of the RV endocardium. The most pronounced change between adjacent QRS-integral maps was observed for the RV middle anteroseptal/septal site and the RV midapical anterior/anteroseptal site, which had correlation coefficients of 0.627 and 0.419 , respectively. It is interesting that a marked pattern similarity was found between maps corresponding to distant pacing sites: high positive correlation coefficients were obtained between the RV basal septal site and the RV basal lateral site (0.944), between the RV middle septal site and the RV middle posterolateral site (0.974), and between the RV midapical anteroseptal site and the RV midapical posterolateral site (0.968).

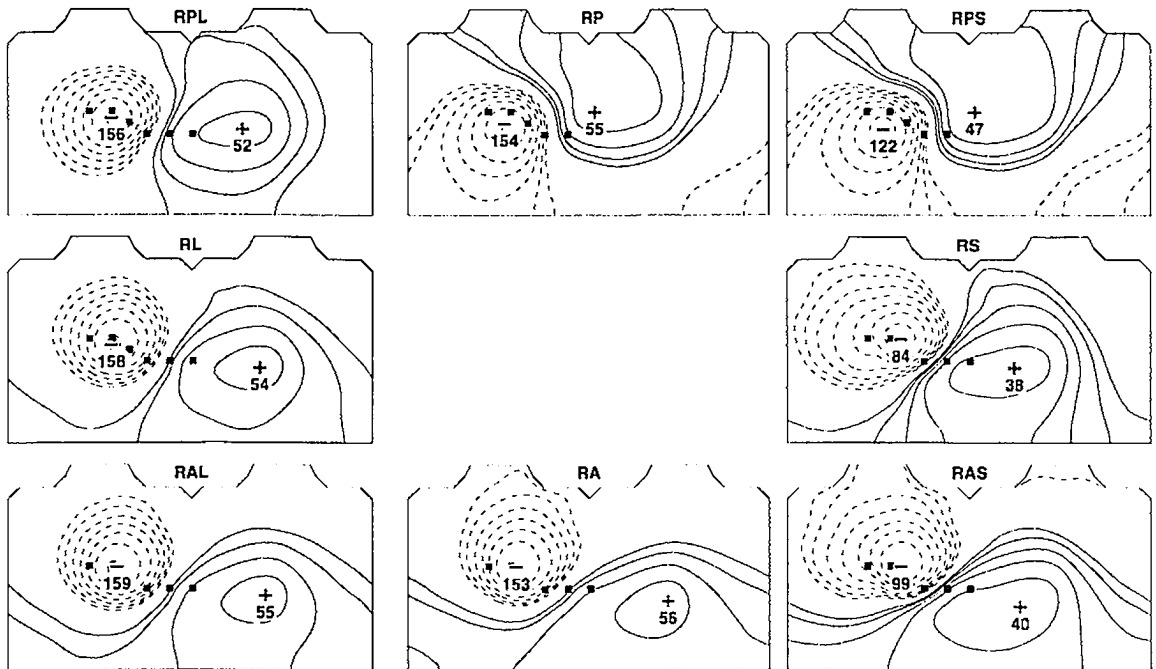


Figure 6.33: QRS-integral maps calculated for activation sequences initiated at 8 endocardial sites in the basal/midbasal level of the RV. Counterclockwise (starting with the QRS-integral map at 9 o'clock): RL, right lateral; RAL right anterolateral; RA, right anterior; RAS, right anteroseptal; RS, right septal; RPS, right posteroseptal; RP, right posterior; RPL, right posterolateral. See the legends of Figs. 6.2 and 6.9 for details of the layout.

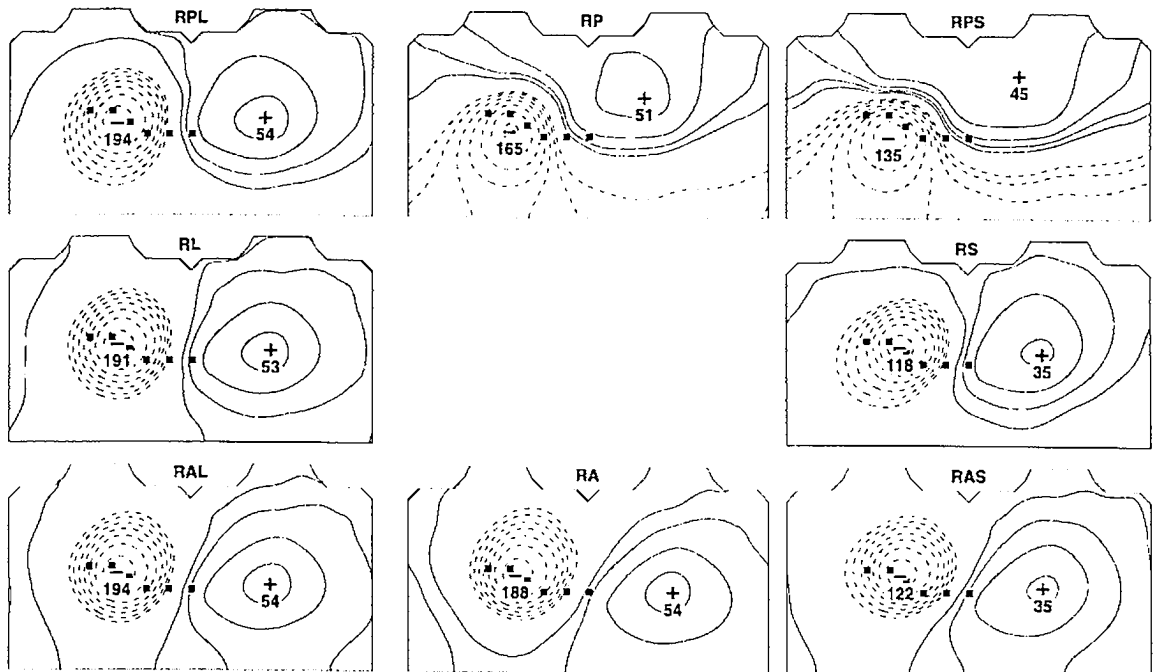


Figure 6.34: QRS-integral maps calculated for activation sequences initiated at 8 endocardial sites in the middle level of the RV. See the legends of Figs. 6.2, 6.9, and 6.33 for details of the layout.

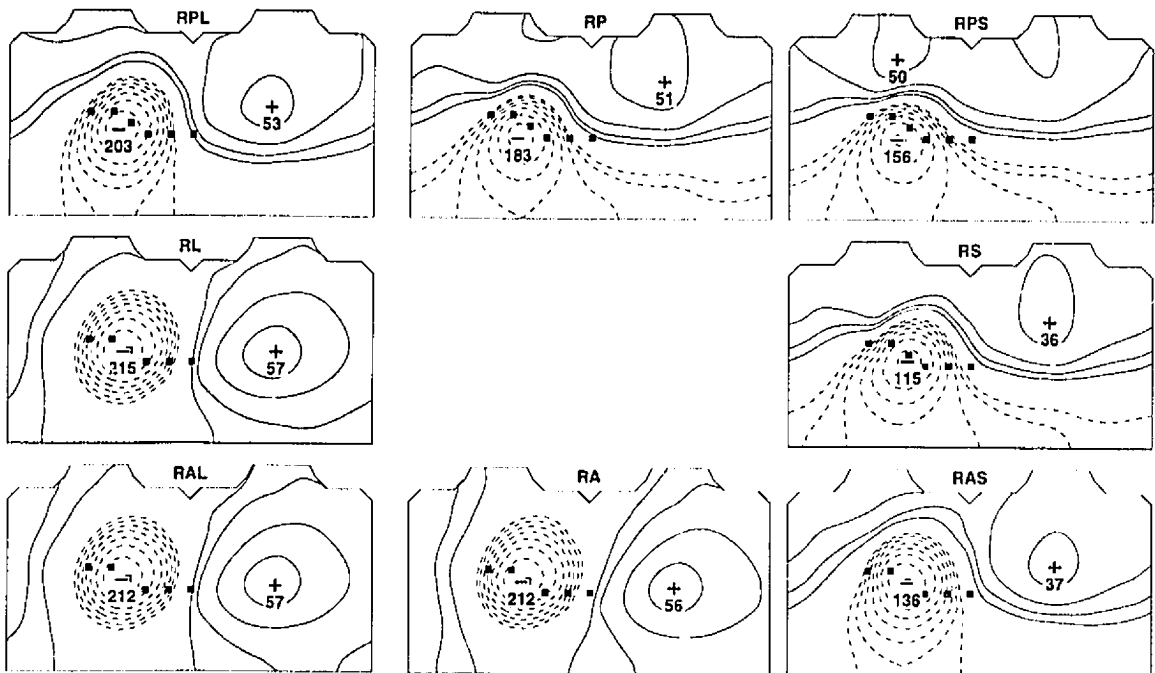


Figure 6.35: QRS-integral maps calculated for activation sequences initiated at 8 endocardial sites in the midapical level of the RV. See the legends of Figs. 6.2, 6.9, and 6.33 for details of the layout.

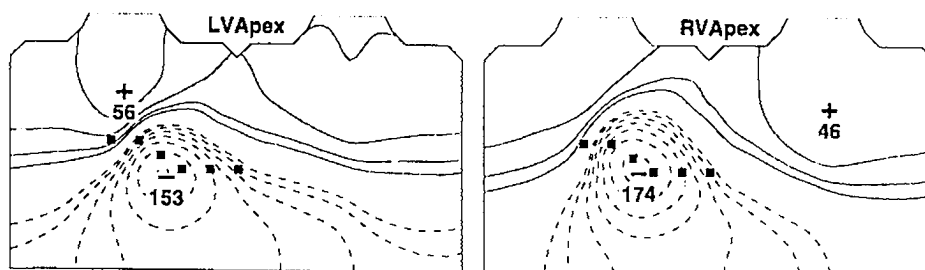


Figure 6.36: QRS-integral maps calculated for activation sequences initiated at endocardial sites near the LV and RV apex. See the legends of Figs. 6.2 and 6.9 for details of the layout.

Comparison between LV and RV endocardial pacing sites. QRS-integral maps generated by endocardial pacing in the lateral, posterior, and anterior aspects of the LV are distinctly different from those generated by endocardial pacing in the same aspects of the RV; the correlation coefficients calculated between these LV and RV maps yield negative or low positive values. By contrast, QRS-integral maps generated by endocardial pacing in the septal aspect of the LV (having an LBBB morphology) resemble some of those generated by endocardial pacing of the RV. We obtained high positive correlation coefficients between the LV and RV QRS-integral maps corresponding to the following segments of the LV and RV endocardium: 1) the LV midapical septal segment and the RV midapical anterior (0.967), the RV midapical lateral (0.971), and the RV midapical anterolateral (0.970) segment, respectively, 2) the LV midbasal anteroseptal segment and the RV midbasal anteroseptal (0.911) segment, 3) the LV middle septal segment and the RV lateral (0.981) segment, 4) the LV middle posteroseptal/septal segment and the RV middle posteroseptal (0.943) segment, and 5) the LV midapical posteroseptal/septal segment and the RV midapical septal (0.963) segment. The distinction between the LV and RV QRS-integral maps

often can be inferred from the amplitude of the minima, but this discriminator has to be applied with care, since the LV and RV QRS-integral sometimes have the minima of similar amplitudes.

QRS-integral maps generated by pacing near the apex of the LV endocardium and the RV endocardium (Fig. 6.36) have a very similar morphology with a high positive correlation (0.936) because of the proximity of the pacing sites. In both cases, maps exhibit a large minimum in the precordial area, but the location of the maxima (on the anterior torso for LV pacing and on the posterior torso for RV pacing) is a discriminating feature.

6.5.3 Correspondence with clinical data

The simulated QRS-integral maps in Figs. 6.24–6.36 were compared visually to the maps recorded during ectopic activation sequences in patients who were suffering from VT but who had no structural heart disease [339]. Our simulations agree with the measured data in the following fundamental morphological aspects of QRS-integral maps:

- the axis joining the extrema rotates CCW when the pacing site is moved around the LV endocardium
- pacing at adjacent LV endocardial sites produces maps with similar morphology, and pacing at distant LV endocardial sites generates maps with markedly different patterns
- pacing close to the anteroseptal and posteroseptal junctions of the LV endocardium produces maps that are markedly different from maps generated by

pacing at the adjacent sites of the junction

- pacing in the RV endocardium generates maps that have relatively small variability, with the most pronounced changes occurring in maps for the anteroseptal segment of the RV endocardium
- pacing at some distant RV endocardial (lateral/posterolateral and septal/antero-septal) sites produces maps with similar morphology
- pacing at some pairs of LV and RV endocardial sites (LV and RV endocardial apex; LV anteroseptal/septal/posteroseptal and RV lateral/anterior/septal/posteroseptal) generates maps with a similar morphology

In general, the simulated dipolar patterns with the characteristic position of the extrema and the zero-line configuration for nearly all pacing sites corresponded well to the measured ones. A small discrepancy between the simulated and measured data was found for pacing sites near the apex of the LV endocardium, where SippensGroenewegen et al. [339] reported QRS-integral maps with negative values near precordial lead V_1 . In our simulations, QRS-integral values near the lead V_1 were located in the positive region, possibly because of a small discrepancy in the position of the heart in the model and in the actual patients. In comparing simulated and measured QRS-integral maps, we could only consider qualitative features due to schematic nature of measured QRS-integral maps in the publication [339]. A more rigorous comparison should use statistical techniques (e.g., calculated correlation coefficients), and this would require access to the measured data.

The relative uniformity of RV QRS-integral maps and the similarity between some LV and RV maps pose a problem for efforts at pattern classification. The amplitude of QRS-integral values is, as noted earlier by SippensGroenewegen et al. [339], often unreliable because it is subject to marked variability during the recording session. It is difficult to adequately address such a problem using simulations as we currently perform them, since the parameters describing the structure of the ventricles and the human body are kept constant in our model.

Simulations are invaluable for exploring those areas of the endocardium (as well as intramural and epicardial sites) which were not probed during the actual recordings. SippensGroenewegen and coworkers [339] had to pool data recorded in eight patients to obtain a relatively good spatial distribution of ectopic pacing sites on the LV endocardial surface, and in six patients for the RV endocardial surface. However, because the procedure is so demanding, some areas (e.g., the LV middle to basal septum, the LV apical lateral area) were not investigated. In addition, it can be expected that the variability in patients' torso geometry, in position of the heart, and in placement of the leads, caused errors to be introduced when the pacing sites and QRS-integral maps collected from different patients were correlated.

Our simulations agree with the data of SippensGroenewegen et al. [339] in that the dipolar potential distributions of QRS-integral maps and the developed activation sequence of BSPMs are distinctly determined by the initial sites of ectopic activation. A discrepancy between the simulated and measured data was observed regarding the initial instability of dipolar patterns. SippensGroenewegen et al. [339] noted that, in two-thirds of all pacing sites, the BSPM patterns remain stable right from the onset

of activation; only in the remaining one-third was the potential distribution subject to initial instability before it evolved at 31 ± 15 ms into the stable dipolar pattern. In our simulations, we observed this initial instability of the BSPM pattern for nearly all pacing sites, and it generally reflected the spread of activation from the endocardium toward the epicardium before the epicardial breakthrough. The small discrepancy between measured and simulated BSPMs may be partly explained by the fact that SippensGroenewegen et al. [339] used a potential amplitude of ± 0.2 mV to mark the onset of activation. In our simulations, we were able to follow the evolution of early BSPM patterns with potentials of much lower amplitude than their threshold dictated by the noise in BSPM recordings.

6.5.4 Protocol for localizing the site of origin of ectopic LV activation using the data base of QRS-integral maps

To gauge the ability of the simulated reference data base of QRS-integral maps to localize the origin of ectopic endocardial activation, we used a subset comprising QRS-integral maps for the LV endocardial sites between the base and midapex shown in Fig. 6.37. (These maps were presented in more detail—with the amplitudes of the extrema—in Figs. 6.24–6.28.) The QRS-integral maps generated by endocardial pacing in those levels of the LV that were not included in this subset were used as the test set. The QRS-integral maps of the test set were correlated with each map of the reference subset, and the correlation coefficients for the given test set map were displayed as correlation maps, with the layout corresponding to the reference subset in Fig. 6.37.

Figs. 6.38 and 6.39 illustrate the protocol for localizing the site of origin of ec-

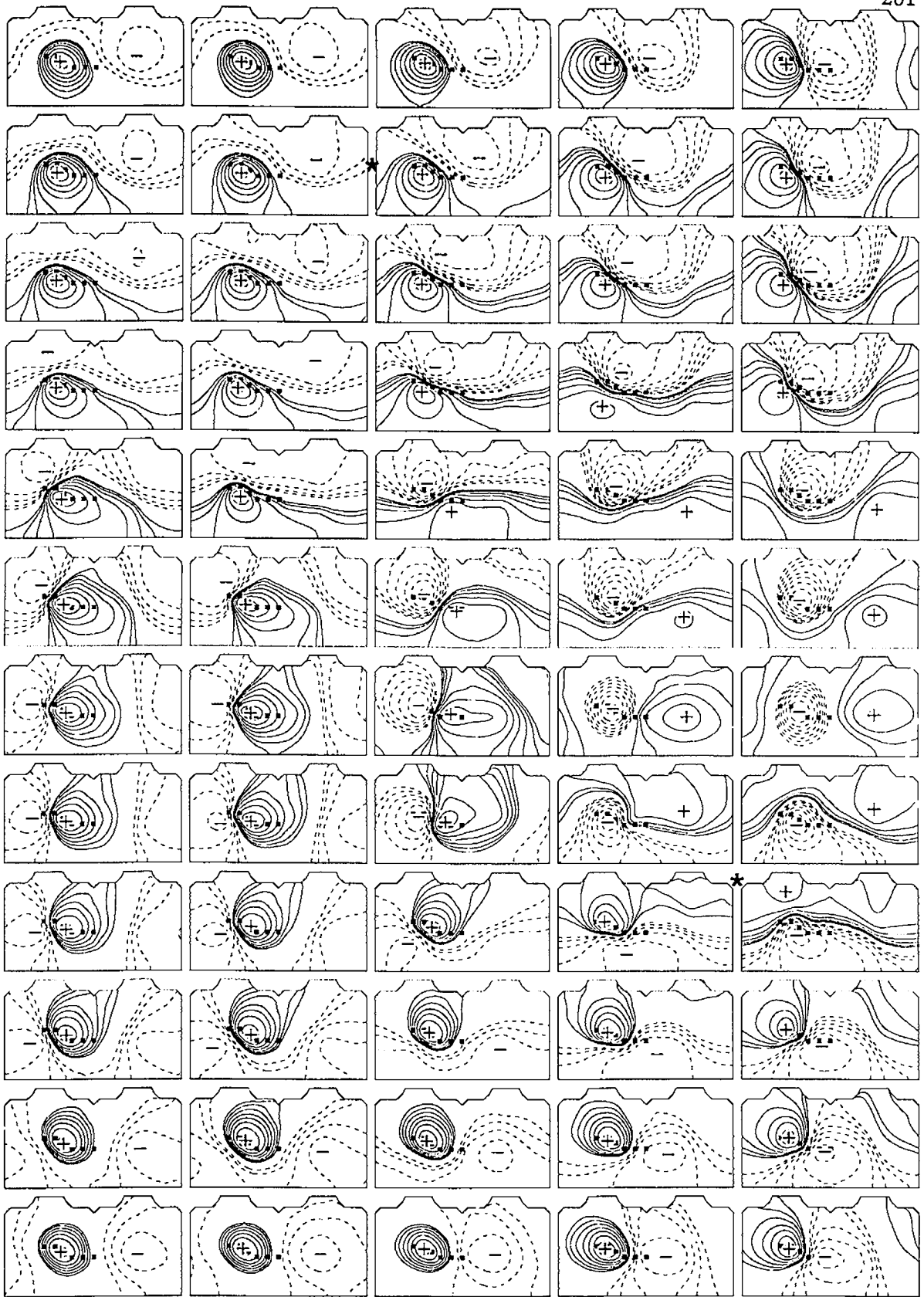


Figure 6.37: QRS-integral maps calculated for activation sequences initiated at endocardial sites between the basal and midapical levels of the LV. As in Figs. 6.24–6.28, each column corresponds to a different level of the LV endocardium and each row to the initial sites positioned circumferentially from the lateral (top row) to the anterior, septal, and posterior aspects of the LV endocardium. Asterisks (*) denote approximate position of QRS-integral maps shown in Figs. 6.38 and 6.39; see Figs. 6.24–6.28 for amplitudes of the extrema, and the legends of Figs. 6.2 and 6.9 for details of the layout of each map.

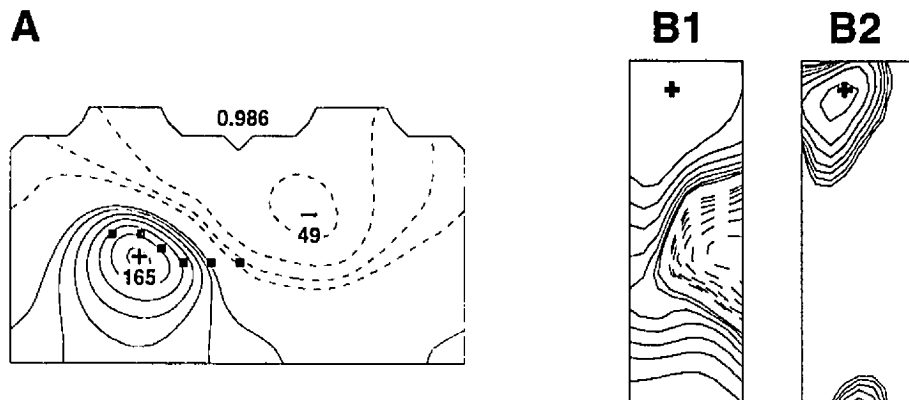


Figure 6.38: QRS-integral map (A) and correlation maps (B1 and B2) calculated for an activation sequence initiated at the lateral/anterolateral endocardial pacing site in the midbasal/basal level of the LV. The correlation maps were constructed by correlating the QRS-integral map in panel A with each map of the reference subset in Fig. 6.37. The layout of the correlation maps corresponds to the layout of the reference subset; the number above the QRS-integral map denotes the highest correlation coefficient, with its position in the correlation maps shown as a cross. In panel B1, all correlation values were used to construct the correlation map; in panel B2, only correlation values above the threshold (chosen at 0.90) were used. Isocorrelation lines are displayed in equal increments; see the legends of Figs. 6.2 and 6.9 for details of the layout of QRS-integral map.

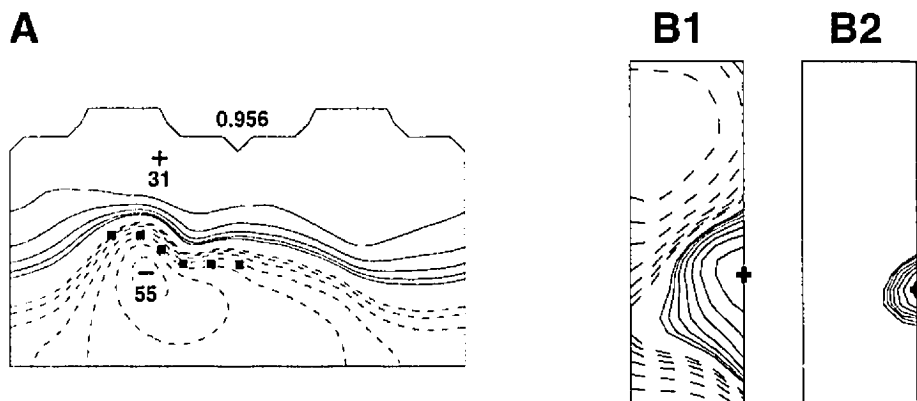


Figure 6.39: QRS-integral map (A) and correlation maps (B1 and B2) calculated for an activation sequence initiated at the posteroseptal/posterior endocardial pacing site in the middle/midapical level of the LV. See the legend of Fig. 6.38 for details of the layout.

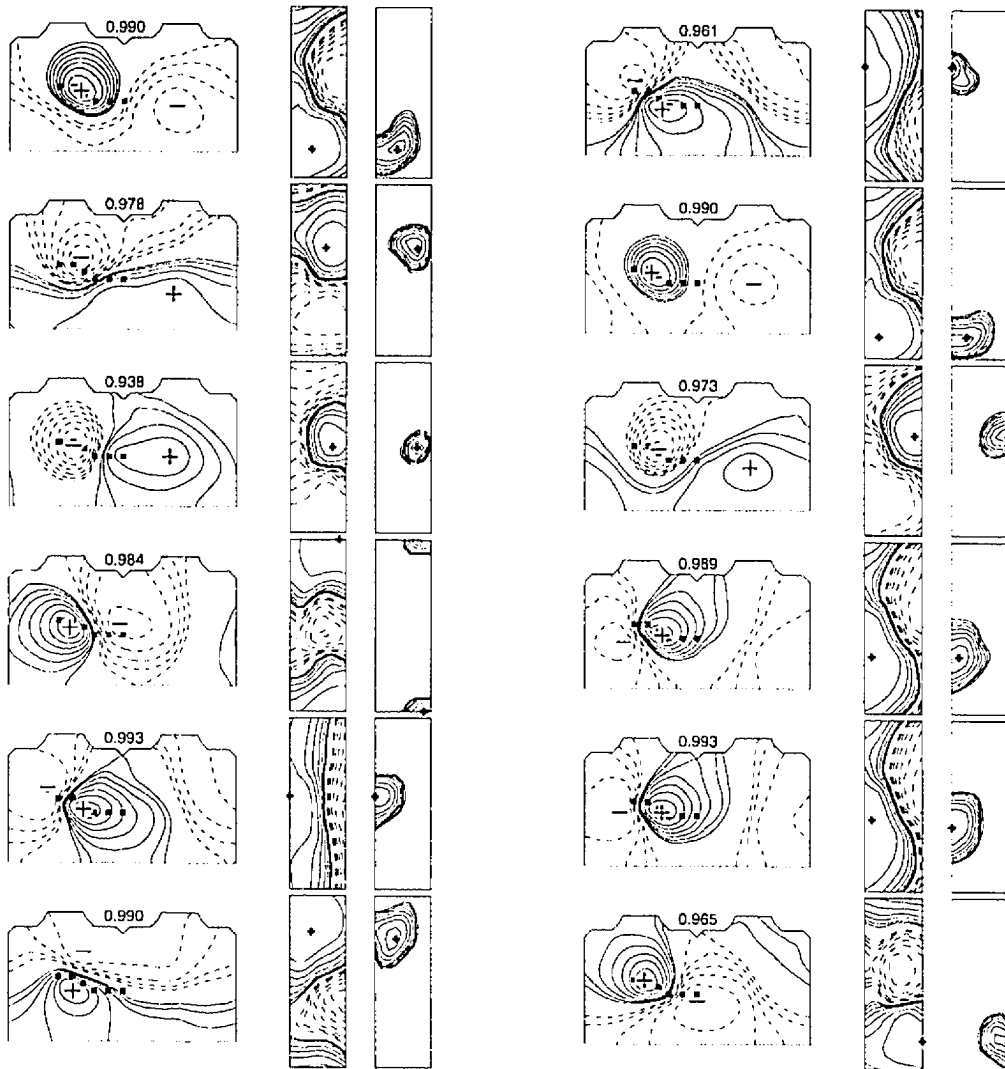


Figure 6.40: QRS-integral maps and correlation maps calculated for activation sequences initiated at 12 endocardial sites in the LV. See the legend of Fig. 6.38 for details of the layout.

topic activation: the former pertains to the activation sequence initiated at the lateral/anterolateral endocardial site in the midbasal/basal level of the LV; the latter to the sequence initiated at the posteroseptal/posterior endocardial site in the middle/midapical level of the LV. It is apparent that in both cases, the position of the maximum in the correlation map (indicating where the highest correlation coefficient is) agrees with the initial site of the test activation sequence. Similar observations were made for 12 other sites of the test activation sequences presented in Fig. 6.40. The correlation maps in Figs. 6.38–6.40 confirm quantitatively that there are major pattern differences between QRS-integral maps corresponding to the distant activation sites (area of negative correlations). On the other hand, any similarity between patterns is localized enough that one can accurately identify the site of origin as an area of high positive correlations. One can improve the accuracy of the protocol that makes use of the correlation maps by precomputing the reference data base with a denser distribution of ectopic pacing sites. However, the resolution limits that uncertainties in catheter positioning and interindividual variability in the position of the heart relative to the electrode locations will impose on this protocol must be determined in a clinical setting.

6.6 Discussion

Any model of the human ventricular myocardium should faithfully reconstruct both electrograms on the epicardial surface and ECGs on the body surface. As we have demonstrated in Chapters 4 and 5, the architecture of the ventricular fibrous structure is the primary factor determining the distribution of epicardial potentials. The

distribution of potentials on the body surface is, moreover, affected by the distance from the cardiac sources to the electrode locations, the position of the heart in the torso, and the torso's boundaries and, hence, is less directly related to the underlying cardiac fibrous structure. This "smoothing" action of the torso produces mostly dipolar potential distributions on the body surface, featuring only a single maximum and a single minimum. The simulations presented in Chapter 6 used a realistic model of the human ventricular myocardium to calculate BSPMs that correspond to the ectopic activation sequences. No modeling studies have yet incorporated such a detailed representation of the ventricular myocardium.

Our results were validated through a qualitative comparison with published data [194, 339]. To make the comparison, we used the major morphological features of BSPMs and QRS-integral maps: 1) the locations and magnitudes of the extrema, 2) the distance between the extrema, and 3) the configuration of the region of near-zero values. By inspecting these specific features of BSPMs, we established criteria for differentiating among septal accessory pathways in patients suffering from WPW syndrome. The criteria developed by our simulations have already proven useful in the clinical setting at this institution. In particular, these criteria have been used to improve the localization of accessory pathways before RF catheter ablation in two important ways: firstly, fewer repeated discharges have been required to ablate the given pathway, which, in turn, decreases the extent of tissue damage; secondly, the duration of the ablative procedure has been shortened, which reduces the risks associated with the procedure, including radiation exposure of both patient and operator.

Based on our simulations, we have developed a clinically applicable protocol for

localizing the origin of idiopathic VT. We first identified two distinct BSPM sequences that correspond to the origin of idiopathic VT at the RVOT (with an LBBB morphology) and at the posteroseptal apical region of the LV (with an RBBB morphology). We found that the LBBB pattern was stable from the onset of ectopic activation, while the RBBB pattern stabilized at the approximate time of epicardial breakthrough. These simulations were relatively easy to perform because both endocardial areas of origin were well defined and well separated. However, SippensGroenewegen et al. [336] recently demonstrated that the origin of polymorphic idiopathic VTs with the LBBB morphology may be located not only at the RVOT but also on the RV midseptum, and Kottkamp et al. [197] observed that idiopathic VTs with the RBBB morphology may actually originate from places in the LV septum that are distributed from the apex to the base.

In our effort to unify and complement currently available clinical data pertaining to the origin of ectopic activation, we *systematically* paced the LV and RV endocardium from sites on a regular endocardial grid in our model of the human ventricular myocardium. The primary objective of these simulations was to further investigate the capabilities of sequential BSPMs and QRS-integral maps in localizing the site of origin of ectopic activation. SippensGroenewegen et al. [339] gathered BSPMs and QRS-integral maps for multiple endocardial pacing sites under clinical conditions. However, they had to resort to intersubject pooling of data to cover the LV and RV endocardium adequately, and this inevitably caused an increase in variability and an overlap between regions with distinct QRS-integral maps. Our modeling approach is well suited for complementing previous clinical findings because it enables pacing of

the LV and RV endocardium at a large number of sites that have an exactly defined location. In conjunction with our proposed protocol, the results of our simulations can provide valuable guidance during the clinical pace mapping.

The correspondence between our simulations and the clinical data of SippensGroenewegen et al. [339] was discussed in detail in Section 6.5.3. In another simulation study, Xu et al. [423] also correlated their simulations with the same set of clinical data and concluded that their simulations agree “very well”. However, closer inspection of their results reveals that they were, in fact, unable to accurately reproduce the observed BSPMs in the lateral, anterior, and septal aspects of the LV endocardium between midbase and midapex. Absent in their simulations is the CCW rotation of the axis joining the extrema, which represents the fundamental feature of BSPMs when the pacing site is moved from the lateral to the anterior, septal, and posterior aspects of the middle LV endocardium. In addition, rather than performing ectopic pacing in a systematic manner, Xu et al. [423] selected the endocardial ectopic sites “iteratively” to obtain the best overall agreement between the simulated and measured BSPMs. Such an approach may cause a biased (too favorable) evaluation of the model’s capabilities. Thus, their study is limited by an inability to reproduce some fundamental qualitative features of measured QRS-integral maps. This may well result from an oversimplified representation of both the ventricular fibrous structure and the process of propagated activation in their model.

Recent clinical results [45, 244, 253, 408] have supported the use of RF ablation as the primary therapy for LV and RV idiopathic VTs. Successful RF ablation requires that the origin of VT be precisely determined. Such a localization of target sites for

ablation can be facilitated by *interactive pace mapping*, i.e., by quantitatively correlating a precomputed reference data base of QRS-integral maps with QRS-integral maps recorded during the pace mapping. Since QRS-integral maps can be obtained from single beats, this technique can enable the localization of the origin of those VTs that cannot be localized by conventional mapping procedures, such as VTs that appear only temporarily and/or are morphologically unstable. Using tools developed in this study, one can systematically compute the simulated data base of QRS-integral maps with a very fine spatial resolution. Such an approach is not possible when one is assembling the data base from clinical BSPM data.

Our simulations confirmed the usefulness of QRS-integral maps that were introduced by this laboratory [155, 242] and later adopted by SippensGroenewegen et al. [338, 339, 340]. QRS-integral maps substantially compress the data pertaining to the entire activation sequence, thus making the classification of the resulting patterns more convenient. In our simulations, the QRS-integral maps generally reflected the developed wavefronts of propagated activation. This is important because QRS-integral maps are therefore not affected by the possible variations caused by initial instability of instantaneous BSPMs (which most likely arises due to the interindividual variability in the anatomy of the trabeculata).

An obvious extension of our study would be to generate a reference data base of QRS-integral maps for the ectopic activation sites located epicardially and intramurally; such a study can be readily undertaken with our model of the human ventricular myocardium. Another area of future work can include simulating activation sequences in a model of ventricles damaged by previous infarction. We have, in fact, already

presented some preliminary results [161]. However, to adequately model the infarcted areas, one must take special care to account for their interindividual variability. As already pointed out in Chapter 5, detailed data regarding the anatomy and histology of infarcted regions would be necessary for adequate modeling of the arrhythmogenic substrate. Our preliminary results showed that one way in which the course of propagated activation is altered depends on whether the infarction is transmural or there is the layer of surviving tissue in the subepicardium or subendocardium. In addition, the size of the infarction is also important.

While our simulations were directed toward localizing the origin of VTs by means of BSPMs in the structurally normal ventricular myocardium, simulations of ventricles damaged by myocardial infarction also have to build on understanding the electrophysiological precursors to VTs [32, 78, 138, 179, 289, 390]. Specifically, the application of RF ablation to patients with structural heart disease (e.g., ischemic cardiomyopathy) and VT is limited because the arrhythmogenic substrate is diffuse (with scarring and fibrosis) and so is difficult to localize and eliminate with the small focal lesions generated by the RF ablative procedure [33, 66]. The surgical ablative procedure, on the other hand, may not require such precise electrocardiographic guiding [76].

Our realistic ventricular model advances the effort to solve the forward problem of electrocardiography, which is the prerequisite for the ultimate goal of clinical electrocardiography—solving the inverse problem of electrocardiography [135]. Even though our model is too complex to be applied to the inverse solution, our results demonstrate that the simple interpretation of the qualitative features of BSPMs and

QRS-integral maps (enhanced by quantitative assessment using correlation coefficients) may be an alternative to localizing ectopic activity by solving the inverse problem. Two approaches to solving the electrocardiographic (and magnetocardiographic) inverse problems are widely used in conjunction with numerical models of the human torso. One involves estimating the single dipole source by means of, e.g., the Levenberg-Marquardt algorithm [266, 297], and the other requires estimating distributed dipolar sources using, e.g., the minimum-norm estimate method [93, 137]. The ability of these methods to accurately localize the site of ectopic activation has frequently been overstated [133, 251, 260, 324, 404]. Recent studies [159, 163, 164] showed that any effort to solve the inverse problem in terms of the single dipole model is susceptible to the variations in patients' geometry and intrathoracic inhomogeneities of conductivity and, thus, may not be appropriate for clinical applications. Distributed dipolar sources are, on the other hand, affected by imposed constraints (such as the position and/or orientation of the current dipoles), which are set *a priori* and may often lack a physiological foundation [188, 259].

While some earlier forward modeling studies reconstructed the potential distributions on the human torso, practically no attempt has been made to reconstruct concurrent epicardial potential distributions. (Recently, Simms and Geselowitz [335] used the isotropic model of cardiac electrical sources developed earlier by Miller and Geselowitz [238] to calculate epicardial electrograms, and a similar approach was also used by Lu and Xia [221].) The analysis of simultaneous sequences of BSPMs and EPMs provides additional information about the electrocardiographic features on the body surface by examining distinct changes (such as the displacement of the mini-

mum) in potential distributions on both surfaces [23]. In addition, sequences identify not only the origin of activation, but also the course of propagated activation [325]. Since *in vivo* experiments cannot be performed simultaneously on the epicardial and body surfaces in humans, our computer model of the human ventricular myocardium can be instrumental in reconstructing the measurable potential distributions both in the vicinity of the cardiac sources and on the body surface. These simulated distributions of electric potential on both surfaces will provide a means for validating the electrocardiographic inverse solution in terms of the epicardial potentials and for deriving meaningful physiologically based constraints for regularizing such solutions [230, 277, 316, 317].

Chapter 7

Conclusions

The aims of this study—to develop a computer model of the human ventricular myocardium and to validate it by comparing simulated isochronal maps, epicardial potential maps, and body surface potential maps with measured ones—have been achieved. Our ventricular model incorporates an anatomically accurate assignment of the fibrous structure and a physiologically accurate description of propagated excitation. These features allowed us to simulate measurable manifestations of propagated activation in the human heart in greater detail than ever before.

Our slab model, which simulates the elementary anatomical structure of the ventricular myocardium with its rotating anisotropy, yielded isochronal maps and maps of the electric potentials and magnetic field during the initial phase of ectopic transmural activation, that satisfactorily reproduced those measured by Taccardi et al. [376], Watabe et al. [399], and Staton et al. [361] in terms of their general morphological features. To achieve even closer agreement with the experimental data of Taccardi et al. [376] and Watabe et al. [399] during the initial and, especially, later phases of ectopic activation, we used a realistic model of the human ventricular myocardium, which successfully reproduced a number of the distinct features of the

epicardial potential distributions.

We used simulated body surface potential maps to develop a clinical protocol for differentiating between the accessory pathways located on the basal septum in patients suffering from Wolff-Parkinson-White syndrome, which will help localize these pathways during RF ablation. Similarly, our simulated body surface potential maps during idiopathic ventricular tachycardia, which match very well the data recorded by SippensGroenewegen et al. [339] and Klug et al. [194], will help enhance the efficacy of the RF ablative treatment of ventricular arrhythmias.

Finally, we generated a reference data base of QRS-integral maps by systematically pacing the LV and RV endocardium. These simulations significantly advance the existing data base, which was collected in a clinical electrophysiology laboratory by means of intersubject pooling [339]. Our data base of simulated QRS-integral distributions on the body surface offers a high-resolution reference frame for localizing distinct endocardial regions. It promises to be a useful tool for enhancing the performance of catheter pace mapping used in combination with body surface potential mapping.

In general, the results presented in this dissertation demonstrate that *an anatomically accurate* model of the human ventricular myocardium is required if one is to accurately predict the potential distributions on both the epicardial surface and the body surface. The primary focus of this particular study was on ectopic activation in structurally normal myocardial tissue or in the presence of localized necroses with clear-cut borders. Further work will be needed to elucidate how ectopic activation is altered by the presence of the more complex arrhythmogenic substrate.

Appendix A

Functions used in simulating propagated excitation

This appendix summarizes functions used in simulating propagated excitation in the anisotropic myocardium.

Function for ionic current $i_{ion}(v_m)$. Presently, only the time-independent K^+ current i_{K1} is considered when the cell is in *the relative refractory state*. The formulation of this current follows the Luo-Rudy ionic model [224].

An AP function. An AP during *the absolute refractory state* is approximated by a function [305]

$$v(t) = v_p + \frac{\ln\{1 - t(1 - e^{-\alpha(v_p - v_{th})})/APD\}}{\alpha}, \quad (\text{A.1})$$

where at the beginning of the plateau phase, $t = 0$, $v_p = 20$ mV, and $\alpha = 0.04$. The action potential duration APD is determined from the recovery time t_r and the restitution curve [212]

$$APD = A - B_1 e^{-t/\tau_1} - B_2 e^{-t/\tau_2} \quad t_r > t_{min} \quad (\text{A.2})$$

where $A = 270$ ms, $B_1 = 2441$ ms, $B_2 = 90.02$ ms, $\tau_1 = 19.6$ ms, $\tau_2 = 200.5$ ms, and $t_{min} = 53.5$ ms.

Finite difference approximation of parabolic partial differential equation.

The transmembrane potential at time $t + \delta t$ (where δt is a time step) is calculated by discretizing Eq. 3.12,

$$v_m(t + \delta t) = v_m(t) + \frac{\delta t}{c_m} \frac{k}{k+1} \nabla \cdot \mathbf{D}_i \nabla v_m(t) - i_{K1}(v_m(t)) + i_{app}. \quad (\text{A.3})$$

The term defining local circuit currents $\nabla \cdot \mathbf{D}_i \nabla v_m(t)$ can be rewritten in the form

$$\begin{aligned} \nabla \cdot \mathbf{D}_i \nabla v_m(t) = & (\sigma_l^i - \sigma_i^i) (\mathbf{a}_1 \mathbf{a}_1^\Gamma \frac{\partial^2 v_m}{\partial x^2} + \mathbf{a}_2 \mathbf{a}_2^\Gamma \frac{\partial^2 v_m}{\partial y^2} + \mathbf{a}_3 \mathbf{a}_3^\Gamma \frac{\partial^2 v_m}{\partial z^2} + 2\mathbf{a}_1 \mathbf{a}_2^\Gamma \frac{\partial^2 v_m}{\partial x \partial y} + \\ & 2\mathbf{a}_2 \mathbf{a}_3^\Gamma \frac{\partial^2 v_m}{\partial y \partial z} + 2\mathbf{a}_1 \mathbf{a}_3^\Gamma \frac{\partial^2 v_m}{\partial x \partial z}) + \sigma_i^i \left(\frac{\partial^2 v_m}{\partial x^2} + \frac{\partial^2 v_m}{\partial y^2} + \frac{\partial^2 v_m}{\partial z^2} \right). \quad (\text{A.4}) \end{aligned}$$

The partial derivatives are discretized using the central difference approximation,

$$\frac{\partial^2 v_m}{\partial x^2} = \frac{1}{d^2} \{v_m(x+d, y, z) - 2v_m(x, y, z) + v_m(x-d, y, z)\} \quad (\text{A.5})$$

$$\frac{\partial^2 v_m}{\partial y^2} = \frac{1}{d^2} \{v_m(x, y+d, z) - 2v_m(x, y, z) + v_m(x, y-d, z)\} \quad (\text{A.6})$$

$$\frac{\partial^2 v_m}{\partial z^2} = \frac{1}{d^2} \{v_m(x, y, z+d) - 2v_m(x, y, z) + v_m(x, y, z-d)\} \quad (\text{A.7})$$

$$\begin{aligned} \frac{\partial^2 v_m}{\partial x \partial y} = & \frac{1}{4d^2} \{v_m(x+d, y+d, z) + v_m(x-d, y-d, z) \\ & - v_m(x+d, y-d, z) - v_m(x-d, y+d, z)\} \quad (\text{A.8}) \end{aligned}$$

$$\begin{aligned} \frac{\partial^2 v_m}{\partial y \partial z} = & \frac{1}{4d^2} \{v_m(x, y+d, z+d) + v_m(x, y-d, z-d) \\ & - v_m(x, y+d, z-d) - v_m(x, y-d, z+d)\} \quad (\text{A.9}) \end{aligned}$$

$$\begin{aligned} \frac{\partial^2 v_m}{\partial x \partial z} = & \frac{1}{4d^2} \{v_m(x+d, y, z+d) + v_m(x-d, y, z-d) \\ & - v_m(x+d, y, z-d) - v_m(x-d, y, z+d)\}, \quad (\text{A.10}) \end{aligned}$$

where d is a spatial step.

Appendix B

Effect of volume conductor boundaries on epicardial and body surface potentials

Before we simulated potential distributions on the epicardial and body surface and compared them with measured data, we estimated how sensitive the forward solution that used primary sources generated by a model of the human ventricular myocardium was to variations in the volume conductor's properties [159, 163, 164, 168, 270, 298]. The answer to this question is important for keeping the calculation of extracardiac potentials reasonably simple. This appendix summarizes the results of our investigations.

Three boundary element models of the human torso were used: the standard male torso model [152, 229] and individualized male and female torso models [162]. All three models (Figs. B.1 and B.2) were represented by an outer boundary, an epicardial boundary and lungs. The outer boundary of the standard torso model was tessellated with 700 triangles (defined by 352 nodes) and the lungs were tessellated with 326 triangles (defined by 157 nodes). The outer boundary of the male torso model was

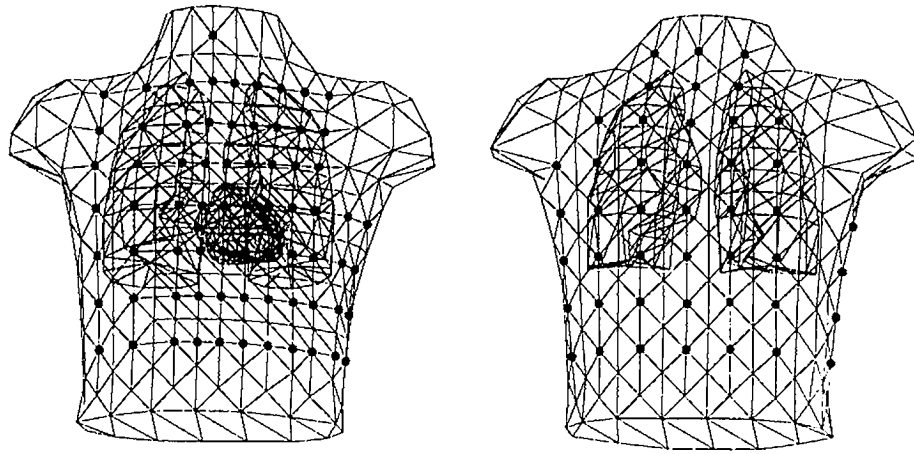


Figure B.1: The anterior and posterior views of the standard torso model with the lead positions displayed. The lungs and epicardial surface are also shown.

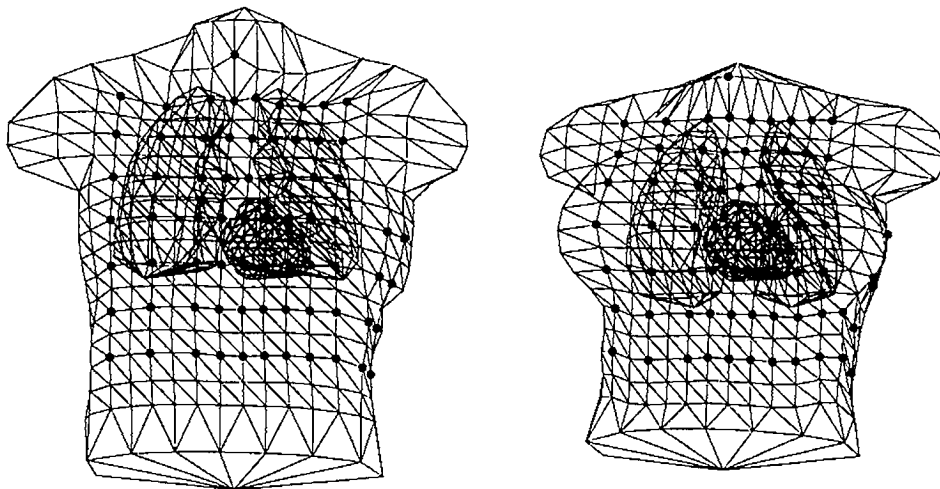


Figure B.2: Individualized male and female torso models constructed using surface harmonic expansion. The anterior lead positions, the lungs, and the epicardial surface are also shown.

approximated by 782 triangles (defined by 393 nodes), and the outer boundary of the female torso model had 762 triangles (defined by 383 nodes). The male and female torso models included lung boundaries tessellated with 456 triangles (defined by 232 nodes) and 432 triangles (defined by 220 nodes), respectively. The conductivity was 0.05 S/m for the lungs and 0.2 S/m for all other torso tissues. In all three models, each of 117 lead positions of the body surface mapping system used at this institution [229, 242] corresponded to a node point. The model of the human ventricular myocardium was appropriately placed in, and the epicardial surface, tessellated with 400 triangles (defined by 202 nodes), was added to each model.

To generate primary sources with which to test the torso models, we initiated ectopic activation in the midapical, middle, and basal levels of the ventricles at 12 sites in the LV endocardium and at 24 sites on both the RV and LV epicardium, using the propagation parameters described in Chapter 4. For the primary sources associated with each activation sequence, we calculated the corresponding potential distributions on the epicardial and body surfaces at 10-ms increments within 40 ms after the onset of activation. The infinite-medium and bounded-medium potentials were calculated for each node of the models, as outlined in Chapter 3. The potential distributions on the epicardial and body surface were displayed as BSPMs and EPMs using the layout described in Chapter 6. (Because the potentials on the surface of each torso models were calculated from primary sources at only 117 torso sites, some of the potential values at 352 nodes of the standard torso model had to be interpolated for the purposes of the display; this was done by means of an algorithm introduced by Oostendorp et al. [267].)

Effect of epicardial boundary on epicardial potential distributions

The first issue investigated was whether the potential distribution predicted by an infinite homogeneous model adequately describes the potential distribution on the insulated epicardium. (In the infinite homogeneous model, only the first term in Eq. 3.26 is used to calculate the potentials at the electrode positions; this model neglects the realistic shape of the boundary surface and assumes that at each electrode location the electric potential is twice the potential in a homogeneous volume conductor of infinite extent [281].) Table B.1 shows the correlation coefficients and relative differences (i.e., normalized rms differences) between potential distributions obtained by the boundary element model of an insulated homogeneous epicardium and those obtained by a model of an infinite homogeneous medium; the results were averaged for each time instant over all 36 stimulation sites. The relative difference between the potential distributions yielded by the two models does not markedly change through the sequence. On the other hand, the potential distributions tend to become slightly less correlated as the activation wavefront spreads through the ventricles.

Fig. B.3 shows pairs of EPMS calculated at 30 ms after the onset of activation for four different ectopic sites, assuming the insulated homogeneous epicardial model and the infinite homogeneous model. Figs. B.3A and B.3B, Figs. B.3C and B.3D, and Figs. B.3E and B.3F, show representative pairs of potential distributions for three cases: for the first pair, the correlation coefficient is 0.979 and the relative difference is 0.38; for the second pair, the corresponding values are 0.967 and 0.37; and for the third pair, the corresponding values are 0.988 and 0.22. Figs. B.3G and B.3H

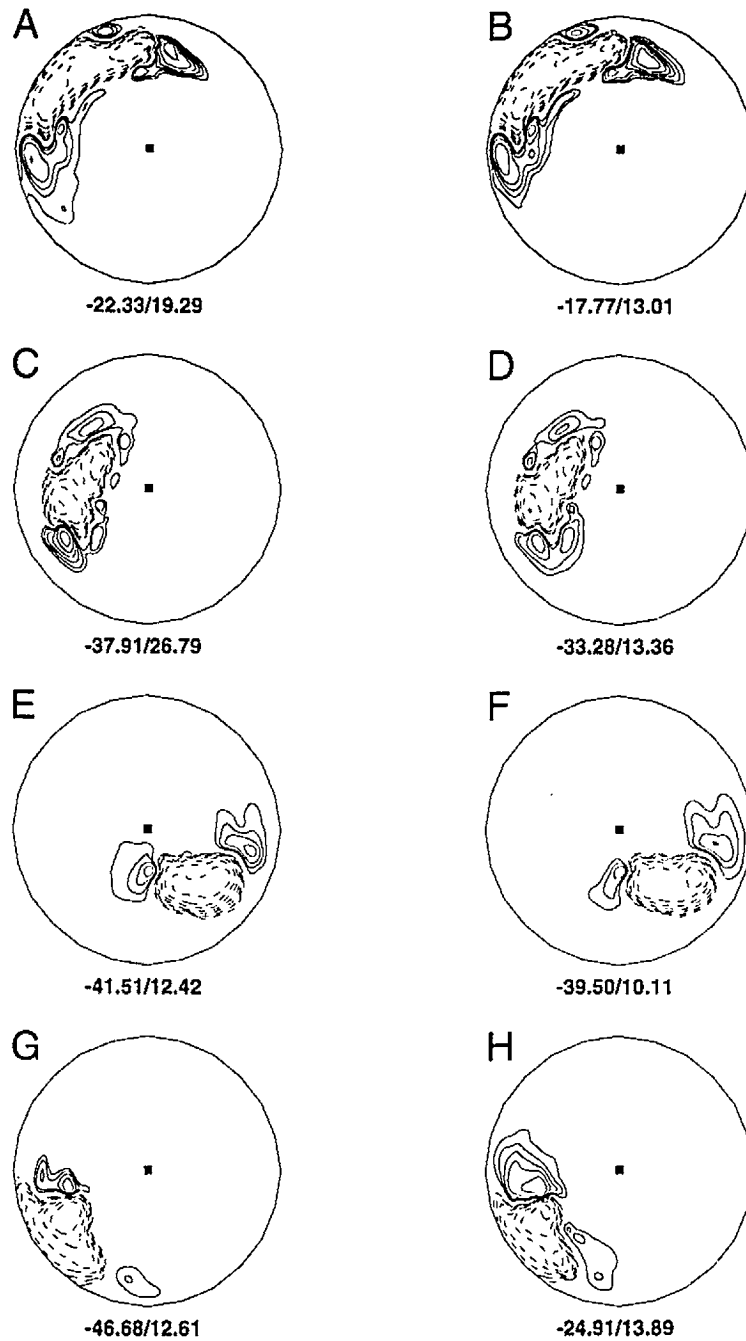


Figure B.3: Epicardial potential maps calculated at 30 ms after the onset of activation for four ectopic sites for the insulated homogeneous epicardial model (A, C, E and G) and the infinite homogeneous model (B, D, F and H). See the legend of Fig. 6.5 for details of the layout.

Table B.1: Effect of Epicardial Boundary on Epicardial Potential Distributions

Time [ms]	Correlation coefficient*	Relative difference*
10	0.989 ± 0.010	0.31 ± 0.25
20	0.982 ± 0.011	0.29 ± 0.12
30	0.979 ± 0.015	0.31 ± 0.14
40	0.973 ± 0.014	0.36 ± 0.11

Values are means \pm SD.

*corresponding values between EPMS obtained with the homogeneous epicardial model and those obtained with the infinite homogeneous model

show the pair of potential distributions with the worst correlation coefficient (0.916) and the worst relative difference (0.92) among all 36 ectopic sites. In general, it was observed that the assumption of an infinite homogeneous medium primarily affects the amplitudes of the extrema (they are lower than in the boundary element model of an insulated epicardium) but has a relatively small effect on the qualitative features of EPMS. Simms and Geselowitz [335] reached a similar conclusion.

Effect of torso boundaries on BSPMs

The next issue addressed was whether a model must include a torso boundary or lungs to adequately represent the patterns of BSPMs. We considered three models: the standard torso model with lungs, the homogeneous standard torso model, and the infinite homogeneous model. The potential distributions on the body surface that were obtained via the standard torso model with lungs were taken as the reference distributions, and potential distributions yielded by the other two models were compared with them. Table B.2 summarizes the results for each of four time instants averaged over all 36 stimulation sites. Inspection of the correlation coefficients and

Table B.2: **Effect of Torso Boundaries on BSPMs**

Time [ms]	Correlation coefficient		Relative difference	
	HT	SI	HT	SI
10	0.990 ± 0.009	0.960 ± 0.015	0.19 ± 0.10	0.39 ± 0.11
20	0.989 ± 0.015	0.960 ± 0.019	0.19 ± 0.10	0.38 ± 0.10
30	0.986 ± 0.017	0.955 ± 0.033	0.19 ± 0.08	0.37 ± 0.10
40	0.990 ± 0.010	0.965 ± 0.021	0.16 ± 0.06	0.34 ± 0.10

Values are means \pm SD.

HT, homogeneous standard torso compared with standard torso with lungs

SI, infinite homogeneous model compared with standard torso with lungs

relative differences reveals that the inclusion of the torso boundary is more important than the inclusion of the lungs as inhomogeneities. This agrees with observations made earlier by other investigators for a single dipole source model [164, 298].

The BSPMs presented in Fig. B.4 for two different cases of ectopic activation sequence illustrate the quantitative results. Excluding the lungs as inhomogeneities causes only subtle changes in the position of the extrema and in the morphology of the region of near-zero potentials (the correlation coefficient is 0.995 and the relative difference is 0.19 for the case presented in Fig. B.4A; the corresponding values are 0.975 and 0.25 for the case presented in Fig. B.4B). By contrast, however, excluding the torso boundaries causes more pronounced changes in the region of near-zero potentials, although the position of the extrema in this particular example is not significantly affected (the correlation coefficient is 0.925 and the relative difference is 0.38 for the case shown in Fig. B.4A; the corresponding values are 0.920 and 0.52 for the case shown in Fig. B.4B).

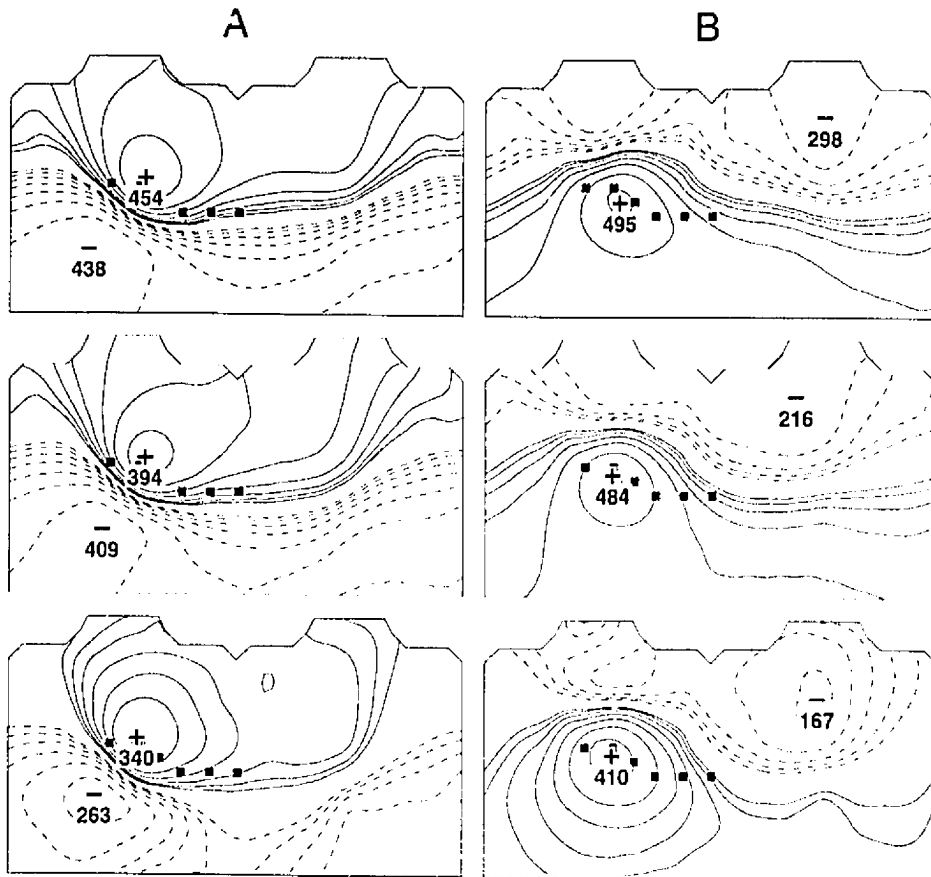


Figure B.4: BSPMs calculated at 30 ms after the onset of ectopic activation initiated at two sites (A and B) when using the standard torso model with lungs (top row), the homogeneous standard torso model (middle row), and the infinite homogeneous model (bottom row). See the legend of Fig. 6.2 for details of the layout.

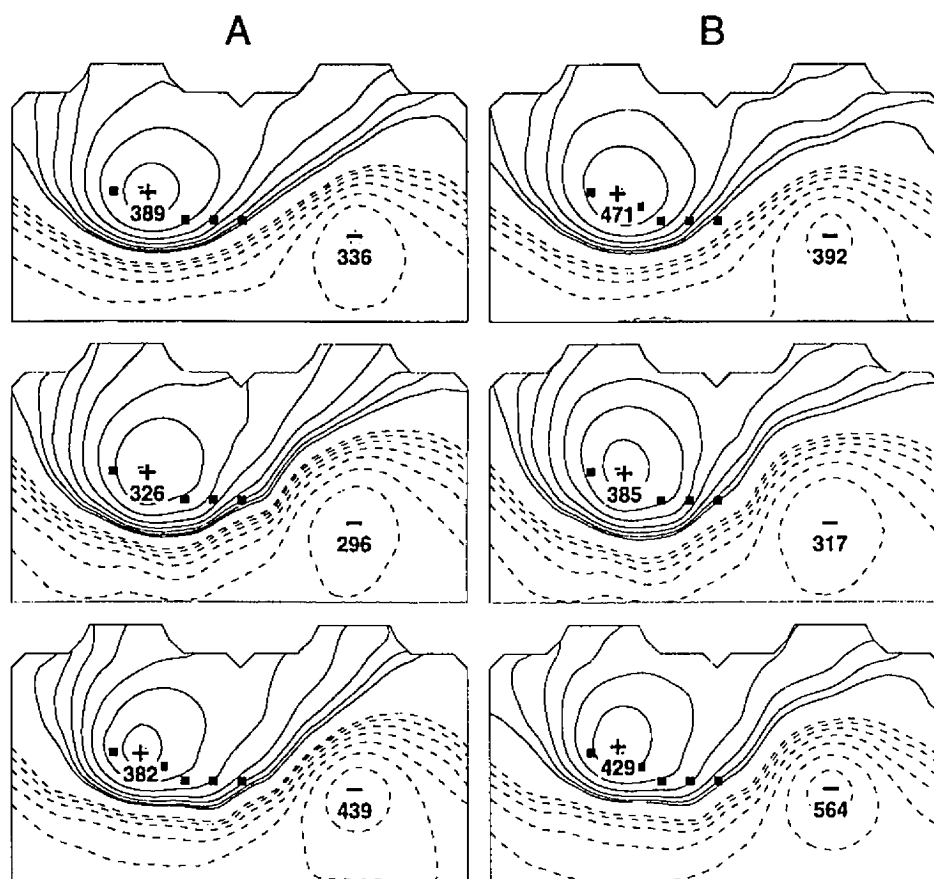


Figure B.5: BSPMs calculated at 30 ms after the onset of ectopic activation when using different homogeneous torso models (A) and when using different torso models with lungs (B). Top row, the standard torso model; middle row, individualized male torso model; bottom row, individualized female torso model. See legend of Fig. 6.2 for details of the layout.

Table B.3: **Effect of Individualized Torso Boundaries on BSPMs**

Time [ms]	HMale	HFemale	LMale	LFemale
10	0.991 ± 0.005	0.978 ± 0.009	0.985 ± 0.010	0.967 ± 0.016
20	0.991 ± 0.004	0.978 ± 0.008	0.986 ± 0.008	0.965 ± 0.023
30	0.991 ± 0.004	0.978 ± 0.008	0.984 ± 0.010	0.967 ± 0.013
40	0.991 ± 0.004	0.980 ± 0.006	0.987 ± 0.006	0.971 ± 0.010

Values are means \pm SD.

HMale, homogeneous individualized male torso correlated with homogeneous standard torso

HFemale, homogeneous individualized female torso correlated with homogeneous standard torso

LMale, individualized male torso with lungs correlated with the standard torso with lungs

LFemale, individualized female torso with lungs correlated with the standard torso with lungs

Effect of individualized torso boundaries on BSPMs

Another issue addressed was whether individualized torso boundaries are a prerequisite for obtaining accurate BSPMs. We used the standard torso model and the individualized male and female torso models, either assuming that the torso includes inhomogeneities or assuming that the torso tissues are homogeneous. (The BSPMs obtained by the standard models with and without lungs were taken as the reference distributions.) Table B.3 summarizes the average correlation coefficients and relative differences over 36 ectopic sites for each of four time instants for the male and female torso models. A comparison of the data in Tables B.2 and B.3 reveals that the effect on BSPMs of excluding the lungs in the standard torso model is quantitatively comparable to the effect of “tailoring” the torso boundaries in the torso male model. By contrast, the effect of the tailored boundaries in the female torso model on BSPMs is much more pronounced than that of excluding the lungs in the standard torso model.

Fig. B.5 illustrates the qualitative differences among the BSPMs yielded by the various torso models. The correlation coefficient between the BSPM obtained with the homogeneous male torso model and that obtained with the homogeneous standard torso model is 0.991, the correlation coefficient between the BSPM obtained with the homogeneous female torso model and that obtained with the homogeneous standard torso model is 0.978, the correlation coefficient between the BSPM obtained with the male torso model with lungs and that obtained with the standard torso model with lungs is 0.990, and the correlation coefficient between the BSPM obtained with the female torso model with lungs and that obtained with the standard torso model with lungs is 0.965. It is evident that the major morphological features of the BSPMs remain unaltered by the choice of torso model.

Discussion

This auxiliary study showed that the infinite homogeneous model is adequate for capturing the qualitative features of epicardial potential distributions generated via a model of the human ventricular myocardium. The important practical implication of this conclusion is that it simplifies the calculation of epicardial potential distributions, since the epicardial surface need not be retessellated each time the size or placement of the epicardial measurement grid is changed. This study also showed that the tailoring of the torso models influences BSPMs more than do inhomogeneities, such as the lungs. However, these effects do not markedly alter the qualitative features of the BSPMs. This resistance of the qualitative features in BSPMs to variability in the shape and size of patients was also observed in recordings of SippensGroenewegen et al. [339]. The homogeneous torso assumption, therefore, appears to be justified when

one is calculating the standard, generic potential distributions on the body surface rather than those pertaining to a particular individual.

Appendix C

Localization of the site of origin of idiopathic VT by magnetic field mapping

Magnetic field mapping [369] is another noninvasive method for imaging cardiac electric sources and one that complements body surface potential mapping. In this appendix, we describe simulations of the magnetic field for activation sequences from initial activation sites in idiopathic VT. We calculated magnetic field normal to the chest at 225 points (a regular 15×15 grid with 2-cm spacing) in the plane that is parallel to the anatomical frontal plane of the torso and is situated 2 cm above the anterior chest (Fig. C.1). Magnetic field maps (MFMs) were calculated at 4-ms increments during the first 120 ms of the activation sequence initiated at the RVOT and the posteroseptal apical area of the LV endocardium. QRS-integral maps were also calculated from these instantaneous MFMs.

Results

Idiopathic VT with the origin of activation at the RVOT. Fig. C.2 shows MFMs calculated at 13 time instants after the onset of an activation sequence initiated

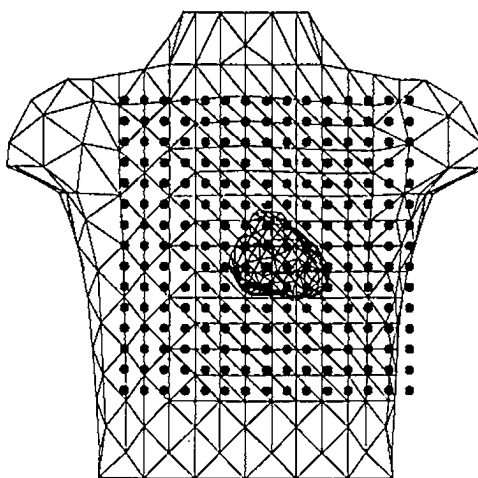


Figure C.1: The anterior view of the standard torso model with epicardial surface. The magnetic field component normal to the chest was simulated at 225 points on a 15×15 grid with 2-cm spacing and situated 2 cm in front of the anterior chest.

at the RVOT. The pattern of these MFMs, like that of BSPMs (shown in Fig. 6.6) for the same initial site of activation, evolves slowly from the onset of activation throughout the sequence and has the following general features: 1) the positive region of the magnetic field (i.e., field vectors pointing from the anterior to the posterior torso) covers the right anterior torso, and the negative region of the magnetic field (i.e., field vectors pointing from the posterior to the anterior torso) covers the left anterior torso, 2) the axis joining the extrema is initially almost horizontal and at the level of the upper midanterior torso, but moves downward and leftward in the last third of the sequence, and 3) the region of near-zero magnetic field is nearly vertical through most of the sequence. Comparison with BSPMs on the anterior torso in Fig. 6.6 reveals that the morphological features of the MFMs are rotated by about 90° .

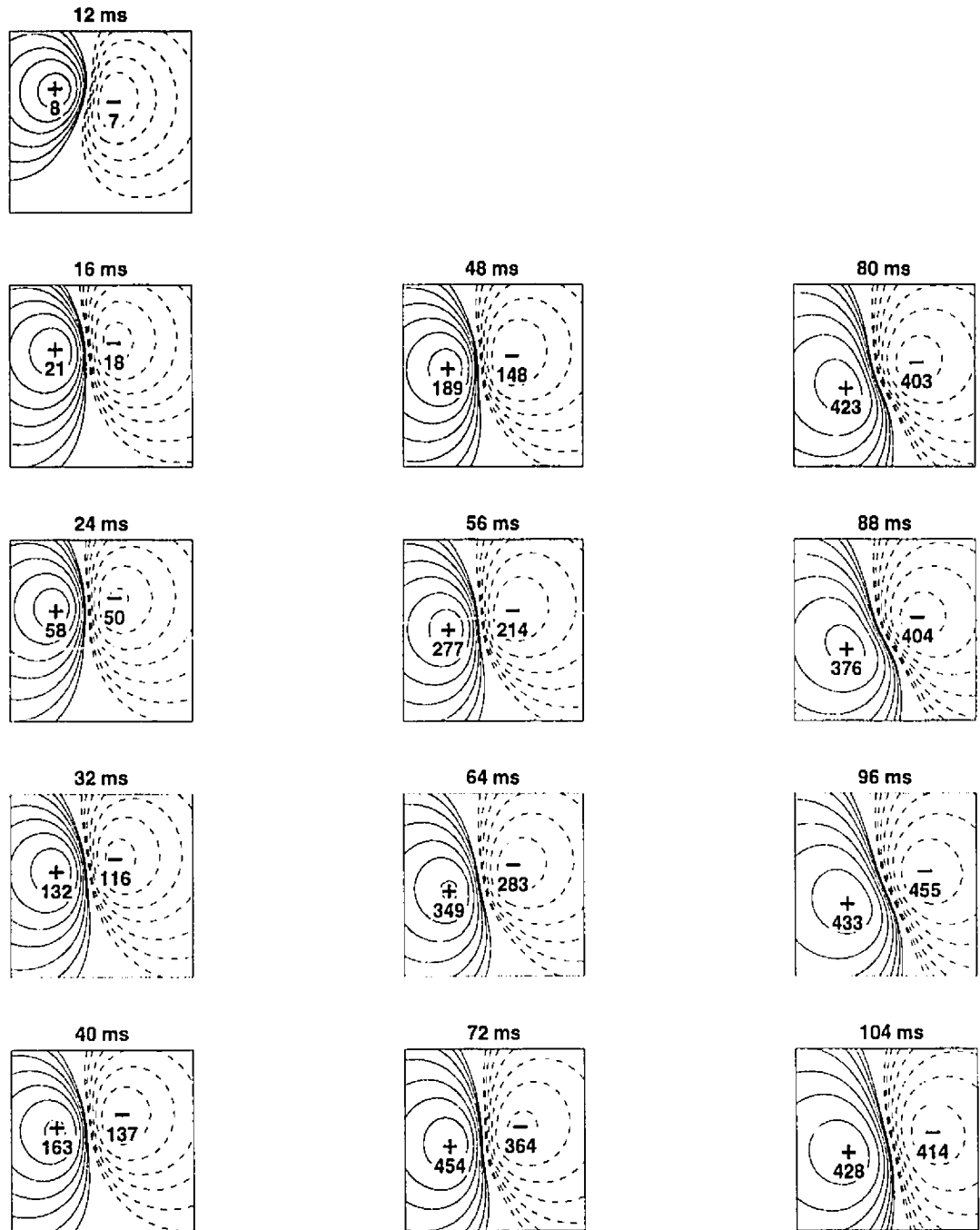


Figure C.2: MFMs calculated at 13 time instants after the onset of an activation sequence initiated at the RVOT. The extrema are denoted in 10^{-10} T, and isofield lines are plotted for equal intervals, with solid contours representing the magnetic field from the anterior to the posterior torso.

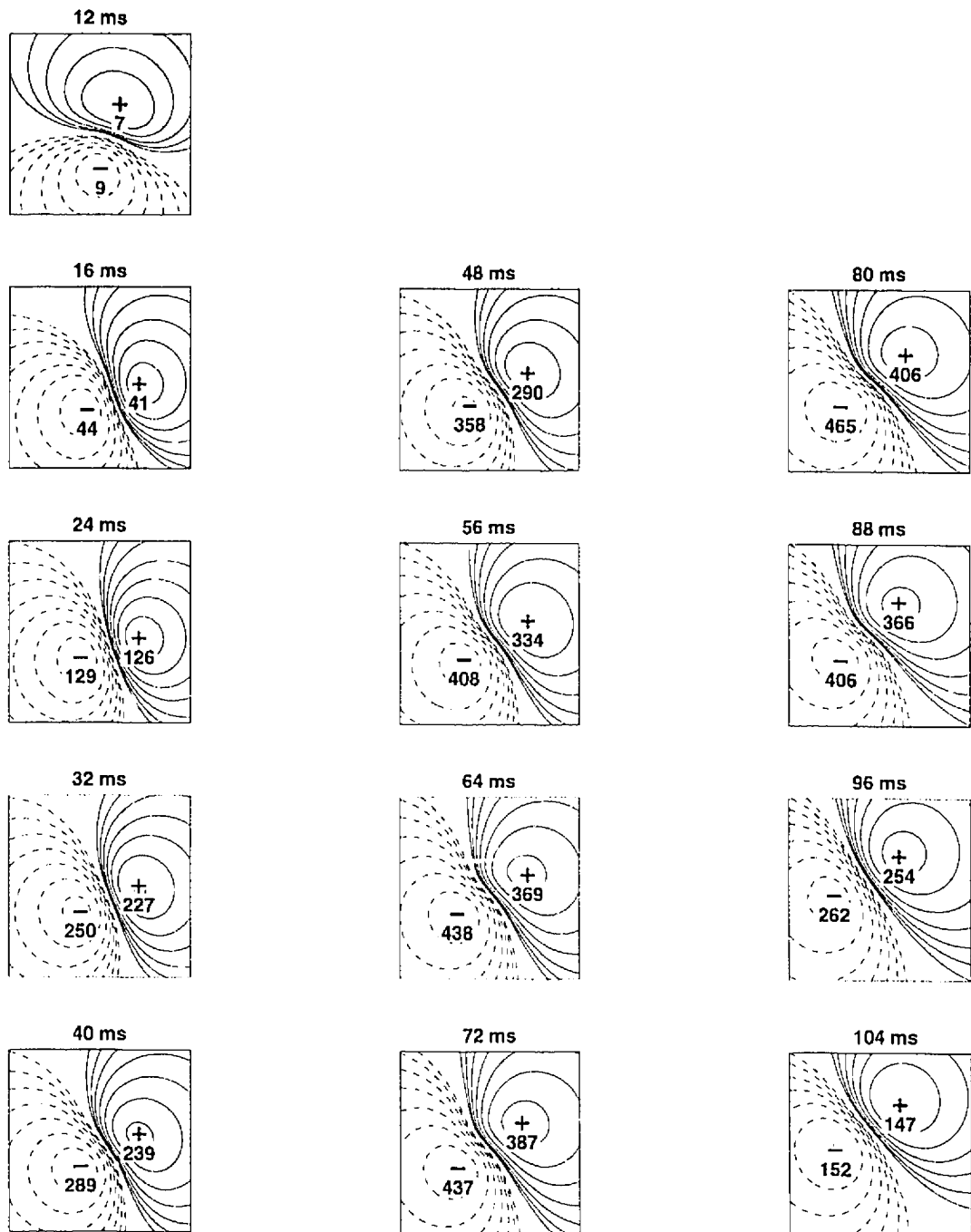


Figure C.3: MFMs calculated at 13 time instants after the onset of an activation sequence initiated at the posteroseptal apical area of the LV endocardium. See the legend of Fig. C.2 for details of the layout.

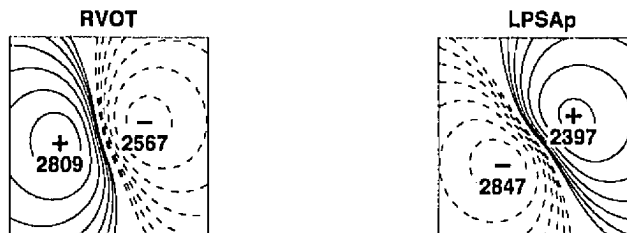


Figure C.4: QRS-integral maps calculated from instantaneous MFMs for activation sequences initiated at the RV outflow tract (RVOT) and at the LV endocardial posteroseptal apical (LPSAp) area. The extrema are denoted in 10^{-12} Ts. See the legend of Fig. C.2 for details of the layout.

Idiopathic VT with the origin of activation at the LV apical area. Fig. C.3 shows MFMs calculated at 13 time instants after the onset of an activation sequence initiated at the posteroseptal apical area of the LV endocardium. The pattern of the MFMs changes during the initial phase of this activation sequence and later in the sequence evolves into a distinct pattern with the positive region of the magnetic field over the left anterior torso and the negative region of the magnetic field over the right anterior torso. The entire sequence of MFMs in Fig. C.3 is nearly a mirror image of the sequence of MFMs generated by the activation originating at the RVOT (Fig. C.2). Again, the morphological features of the MFMs are rotated by about 90° relative to those found in BSPMs (Fig. 6.8). However, unlike BSPMs, which feature a dipolar distribution with markedly unequal extrema, the MFMs have a dipolar distribution with extrema of similar amplitudes.

QRS-integral maps. Fig. C.4 shows QRS-integral maps for simulated activation sequences initiated at the RVOT and at the posteroseptal apical area of the LV endocardium, as calculated from MFMs. Comparison of QRS-integral maps for these

widely separated sites reveals major pattern differences (with a high negative correlation coefficient of -0.944).

Discussion

The results in this appendix demonstrate that our model of the human ventricular myocardium can also be used for simulating the magnetic field above the chest. No MFMs recorded in patients suffering from idiopathic VT that would enable us to validate our simulations have as yet been published. We have shown that the patterns of MFMs undergo sequential changes similar to those of BSPMs on the anterior torso; in general, the morphological features of MFMs are rotated by about 90° relative to those found in BSPMs on the anterior torso.

The advantage of magnetic field mapping is that it can be performed faster than body surface potential mapping (provided the necessary multichannel equipment is available in the clinical setting); its major drawbacks are the high costs and the requirement of a specially designed magnetically shielded room. Future research should determine whether MFMs contain any diagnostically valuable information that is not available in BSPMs [271, 383].

Bibliography

- [1] S. Abboud, O. Berenfeld, and D. Sadeh. Simulation of high-resolution QRS complex using a ventricular model with a fractal conduction system. *Circ Res*, 68:1751–1760, 1991.
- [2] J.A. Abildskov, M.S. Burgess, R.L. Lux, and R.F. Wyatt. Experimental evidence for regional cardiac influence in body surface isopotential maps of dogs. *Circ Res*, 38:386–391, 1976.
- [3] J.A. Abildskov and L.S. Green. The recognition of arrhythmia vulnerability by body surface electrocardiographic mapping. *Circulation*, 75(Suppl III):III-79–III-83, 1987.
- [4] D. Adam. Propagation of depolarization and repolarization processes in the myocardium: An anisotropic model. *IEEE Trans Biomed Eng*, BME-38:133–141, 1991.
- [5] D. Adam, O. Hareuveni, and S. Sideman. Semiautomated border tracking of cine echocardiographic ventricular images. *IEEE Trans Med Imag*, 6:266–272, 1987.
- [6] D. Adam, D. Hekstra, and S. Sideman. 3-Dimensional anisotropic model of myocardial electrical propagation. In K.L. Ripley, editor, *Computers in Cardiology*, pages 405–408. IEEE Computer Society Press, Washington, D.C., 1985.
- [7] AHA/ACC Recommendation on Tomographic Imaging. Standardization of cardiac tomographic imaging: An ACC/AHA policy statement. *J Am Coll Cardiol*, 20:255–256, 1992.
- [8] M. Aoki, Y. Okamoto, T. Musha, and K. Haruni. Three-dimensional simulation of the ventricular depolarization and repolarization processes and body surface potentials: Normal heart and bundle branch block. *IEEE Trans Biomed Eng*, BME-34:454–462, 1987.
- [9] G. Arisi, E. Macchi, S. Baruffi, S. Spaggiari, and B. Taccardi. Potential fields on the ventricular surface of the exposed dog heart during normal excitation. *Circ Res*, 52:706–715, 1983.

- [10] G. Arisi, D. Stilli, S. Spaggiari, S. Baruffi, E. Musso, E. Macchi, and B. Taccardi. Potential distribution on the dog's ventricular surface as revealed by 1912 epicardial leads. In P.W. Macfarlane, editor, *Progress in Electrocardiology*, pages 59–63. Pitman Medical, Tunbridge Wells, Kent, 1979.
- [11] J.A. Armour and W.C. Randall. Structural basis for cardiac function. *Am J Physiol*, 218:1517–1523, 1970.
- [12] A.C. Arntzenius, J.J. Schipperheyn, P.H. Huisman, H.E. Kulbertus, H.J. Ritsema van Eck, K.L. Simoons, and R.V.H. Vinke. Model studies on activation of the heart. *Eur J Cardiol*, 8:261–270, 1978.
- [13] R.D. Baerg and D.L. Bassett. Permanent gross demonstration of the conduction tissue in the dog heart with palladium iodide. *Anat Rec*, 146:313–317, 1963.
- [14] J.A. Baird and J.S. Robb. The study, reconstruction and gross dissection of the A-V conducting system in the dog heart. *Anat Rec*, 108:747–763, 1950.
- [15] J.M.T. de Bakker, F.J.L. van Capelle, and M.J. Janse. Endocardial mapping by inflatable balloon technique. In S. Sideman and R. Beyar, editors, *Imaging, Measurements and Analysis of the Heart*, pages 337–350. Hemisphere Publishing, Washington, DC, 1991.
- [16] J.M.T. de Bakker, F.J.L. van Capelle, M.J. Janse, A.A.M. Wilde, R. Coronel, A.E. Becker, K.P. Dingemans, N.M. van Hemel, and R.N.W. Hauer. Reentry as a cause of ventricular tachycardia in patients with chronic ischemic heart disease: Electrophysiologic and anatomic correlation. *Circulation*, 77:589–606, 1988.
- [17] J.M.T. de Bakker, M.J. Janse, F.J.L. van Capelle, and D. Durrer. Endocardial mapping by simultaneous recording of endocardial electrograms during cardiac surgery for ventricular aneurysm. *J Am Coll Cardiol*, 2:947–953, 1983.
- [18] J.P. Barach. A simulation of cardiac action currents having curl. *IEEE Trans Biomed Eng*, BME-40:49–58, 1993.
- [19] J.P. Barach and J.P. Wikswo, Jr. Magnetic field from simulated cardiac action currents. *IEEE Trans Biomed Eng*, BME-41:969–974, 1994.
- [20] A.C.L. Barnard, I.M. Duck, M.S. Lynn, and W.P. Timlake. The application of electromagnetic theory in electrocardiology. II. Numerical solution of the integral equations. *Biophys J*, 7:463–490, 1967.
- [21] R.C. Barr, T.C. Pilkington, J.P. Boineau, and M.S. Spach. Determining surface potentials from current dipoles, with application to electrocardiography. *IEEE Trans Biomed Eng*, BME-13:88–92, 1966.
- [22] R.C. Barr and R. Plonsey. Propagation of excitation in idealized anisotropic two-dimensional tissue. *Biophys J*, 45:1191–1202, 1984.

- [23] R.C. Barr and M. S. Spach. Inverse calculation of QRS-T epicardial potentials from body surface potential distributions for normal and ectopic beats in the intact dog. *Circ Res*, 42:661–675, 1978.
- [24] E. Barta, D. Adam, E. Salant, and S. Sideman. 3-D ventricular myocardial electrical excitation: A minimal orthogonal pathways model. *Ann Biomed Eng*, 15:443–456, 1987.
- [25] S. Baruffi, S. Spaggiari, G. Arisi, A. Malanca, E. Macchi, and B. Taccardi. The effect of myocardial anisotropy on epicardial potential distributions in the dog heart *in situ*. In K. Yamada, K. Harumi, and T. Musha, editors, *Advances in Body Surface Potential Mapping*, pages 151–155. University of Nagoya Press, Tokyo, 1983.
- [26] S. Baruffi, S. Spaggiari, D. Stilli, E. Musso, and B. Taccardi. The importance of fiber orientation in determining features of cardiac electric field. In Z. Antaloczy, editor, *Modern Electrocardiology*, pages 89–92. Excerpta Medica, Amsterdam, 1978.
- [27] G.K. Batchelor. *An Introduction to Fluid Dynamics*. Cambridge University Press, Cambridge, 1983.
- [28] G.W. Beeler and H. Reuter. Reconstruction of the action potential of ventricular myocardial fibers. *J Physiol (Lond)*, 268:177–210, 1977.
- [29] D.W. Benson, Jr., R. Sterba, J.J. Gallagher, A. Walston II, and M.S. Spach. Localization of the site of ventricular preexcitation with body surface maps in patients with Wolff-Parkinson-White syndrome. *Circulation*, 65:1259–1268, 1982.
- [30] P.M. Berry. Space harmonics of the oblate spheroid. *Ann NY Acad Sci*, 65:1126–1134, 1956.
- [31] D.M. Blair and F. Davies. Observations on the conducting system of the heart. *J Anat (Lond)*, 69:303–325, 1935.
- [32] J.P. Boineau, R.B. Schuessler, S.B. Eisenberg, J.S. Tweddell, A. Harada, C.K. Rokkas, and J.L. Cox. Potential distribution mapping of ventricular tachycardia. In M. Shenasa, M. Borggreffe, and G. Breithardt, editors, *Cardiac Mapping*, pages 85–107. Futura Publishing, Mount Kisco, NY, 1993.
- [33] M. Borggreffe, X. Chen, G. Hindricks, W. Haverkamp, S. Willems, H. Kottkamp, B. Rotman, A. Martinez-Rubio, M. Shenasa, M. Block, and G. Breithardt. Catheter ablation of ventricular tachycardia in patients with coronary heart disease. In D.P. Zipes and J. Jalife, editors, *Cardiac Electrophysiology: From Cell to Bedside*, pages 1502–1517. W.B. Saunders Company, Philadelphia, 1995.
- [34] C.A. Brebbia, J.C.F. Telles, and L.C. Wrobel. *Boundary Element Techniques: Theory and Applications in Engineering*. Springer-Verlag, Berlin, 1984.

- [35] G. Breithardt, M. Shenasa, M. Biermann, M. Borggrefe, W. Haverkamp, G. Hindricks, B. Vogt, and L. Reinhardt. Precision and reproducibility of isochronal electrical cardiac mapping. In M. Shenasa, M. Borggrefe, and G. Breithardt, editors, *Cardiac Mapping*, pages 35–59. Futura Publishing, Mount Kisco, NY, 1993.
- [36] D.A. Brody. A theoretical analysis of intracavitary blood mass influence on the heart-lead relationship. *Circ Res*, 4:731–738, 1956.
- [37] D.A. Brody, F.H. Terry, and E. Ideker. Eccentric dipole in a spherical medium: Generalized expression for surface potentials. *IEEE Trans Biomed Eng*, 20:141–143, 1973.
- [38] M.J. Burgess, B.M. Steinhaus, K.W. Spitzer, and P.R. Ershler. Nonuniform epicardial activation and repolarization properties of the *in vivo* canine pulmonary conus. *Circ Res*, 62:233–246, 1988.
- [39] A.E. Buxton, H.L. Waxman, F.E. Marchlinski, M.B. Simson, D. Cassidy, and M.E. Josephson. Right ventricular tachycardia: Clinical and electrophysiologic characteristics. *Circulation*, 68:917–927, 1983.
- [40] H. Calkins, S.J. Kalbfleisch, R. El-Atassi, J.J. Langberg, and F. Morady. Relation between efficacy of radiofrequency catheter ablation and site of origin of idiopathic ventricular tachycardia. *Am J Cardiol*, 71:827–833, 1993.
- [41] F.J.L. van Capelle and D. Durrer. Computer simulation of arrhythmias in a network of coupled excitable elements. *Circ Res*, 47:454–466, 1980.
- [42] D.M. Cassidy, J.A. Vassallo, F.E. Marchlinski, A.E. Buxton, W.J. Untereker, and M.E. Josephson. Endocardial mapping in humans in sinus rhythm with normal left ventricles: Activation patterns and characteristics of electrograms. *Circulation*, 70:37–42, 1984.
- [43] S.Y. Chen, W.C. Lin, C.C. Liang, and C.T. Chen. Improvement on dynamic elastic interpolation technique for reconstructing 3-D objects from serial cross sections. *IEEE Trans Med Imag*, 9:71–83, 1990.
- [44] L. Clerc. Directional differences of impulse spread in trabecular muscle from mammalian heart. *J Physiol (Lond)*, 255:335–346, 1976.
- [45] D.L. Coggins, R.J. Lee, J. Sweeney, W.W. Chein, G. Van Hare, L. Epstein, R. Gonzales, J.C. Griffin, M.D. Lesh, and M.M. Scheinman. Radiofrequency catheter ablation as a cure for idiopathic tachycardia of both left and right origin. *J Am Coll Cardiol*, 23:1333–1341, 1994.
- [46] J.D. Cole. *Perturbation Methods in Applied Mathematics*. Blaisdel, Waltham, MA, 1968.
- [47] K.W. Cole. *Membranes, Ions, and Impulses*. University of California Press, Berkeley, 1968.

- [48] P. Colli Franzone and L. Guerri. Models of the spreading of excitation in myocardial tissue. *CRC Crit Rev Biomed Eng*, 20:211-253, 1992.
- [49] P. Colli Franzone and L. Guerri. Spreading of excitation in 3-D models of the anisotropic cardiac tissue. I. Validation of the eikonal model. *Math Biosci*, 113:145-209, 1993.
- [50] P. Colli Franzone, L. Guerri, and E. Magenes. Oblique double layer potentials for the direct and inverse problems of electrocardiology. *Math Biosci*, 68:23-55, 1984.
- [51] P. Colli Franzone, L. Guerri, and S. Rovida. Wavefront propagation in an activation model of the anisotropic cardiac tissue: Asymptotic analysis and numerical simulations. *J Math Biol*, 28:121-176, 1990.
- [52] P. Colli Franzone, L. Guerri, and B. Taccardi. Potential distributions generated by point stimulation in a myocardial volume: Simulation studies in a model of anisotropic ventricular muscle. *J Cardiovasc Physiol*, 4:438-458, 1993.
- [53] P. Colli Franzone, L. Guerri, and B. Taccardi. Spread of excitation in a myocardial volume: Simulation studies in a model of anisotropic ventricular muscle activated by point stimulation. *J Cardiovasc Physiol*, 4:144-160, 1993.
- [54] P. Colli Franzone, L. Guerri, B. Taccardi, and C. Viganotti. Finite element approximation of regularized solution of the inverse potential problem of electrocardiography and application to experimental data. *Calcolo*, 22:91-186, 1985.
- [55] P. Colli Franzone, L. Guerri, and S. Tentoni. Mathematical modelling of the excitation process in myocardial tissue: Influence of fiber rotation on wavefront propagation and potential field. *Math Biosci*, 101:155-235, 1990.
- [56] P. Colli Franzone, L. Guerri, S. Tentoni, C. Viganotti, S. Spaggiari, and B. Taccardi. A numerical procedure for solving the inverse problem of electrocardiography: Analysis of the time-space accuracy from *in vitro* experimental data. *Math Biosci*, 77:353-396, 1985.
- [57] P. Colli Franzone, L. Guerri, and C. Viganotti. Oblique dipole layer potentials applied to electrocardiology. *J Math Biol*, 17:93-124, 1983.
- [58] P. Colli Franzone, L. Guerri, C. Viganotti, E. Macchi, S. Baruffi, S. Spaggiari, and B. Taccardi. Potential fields generated by oblique dipole layers modeling excitation wavefronts in the anisotropic myocardium: Comparison with potential fields elicited by paced dog hearts in a volume conductor. *Circ Res*, 51:330-346, 1982.
- [59] L.V. Corbin II and A.M. Scher. The canine heart as an electrocardiographic generator: Dependence on cardiac cell orientation. *Circ Res*, 41:58-67, 1977.

- [60] M. Courtemanche, W. Skaggs, and A. Winfree. Stable three dimensional action potential circulation in the Fitzhugh-Nagumo model. *Physica D*, 41:173–182, 1990.
- [61] J.L. Cox. Patient selection criteria and results of surgery for refractory ischemic ventricular tachycardia. *Circulation*, 79(Suppl I):I-163–I-177, 1989.
- [62] L.L. Creswell, S.G. Wyers, J.S. Pirolo, W.H. Perman, M.W. Vannier, and M.K. Pasque. Mathematical modeling of the heart using magnetic resonance imaging. *IEEE Trans Med Imag*, 11:581–589, 1992.
- [63] B.N. Cuffin and D. Cohen. Magnetic fields of a dipole in special volume conductor shapes. *IEEE Trans Biomed Eng*, BME-24:372–381, 1977.
- [64] B.N. Cuffin and D.B. Geselowitz. Studies of the electrocardiogram using realistic cardiac and torso models. *IEEE Trans Biomed Eng*, BME-24:242–252, 1977.
- [65] R.Th. van Dam. Ventricular activation in human and canine bundle branch block. In H.J.J. Wellens, K.I. Lie, and M.J. Janse, editors, *The Conduction System of the Heart: Structure, Function and Clinical Implications*, pages 377–392. Lea & Febiger, Philadelphia, 1976.
- [66] E. Daoud and F. Morady. Catheter ablation of ventricular tachycardia. *Curr Opinion Cardiol*, 10:21–25, 1995.
- [67] M.J. Davies, R.H. Anderson, and A.E. Becker. *The Conduction System of the Heart*. Butterworth, London, 1983.
- [68] L. De Ambroggi, E. Musso, and B. Taccardi. Body-surface mapping. In P.W. Macfarlane and T.D.V. Lawrie, editors, *Comprehensive Electrocardiology*, pages 1015–1049. Pergamon Press, New York, 1989.
- [69] L. De Ambroggi, B. Taccardi, and E. Macchi. Body-surface maps of heart potentials: Tentative localization of pre-excited areas in forty-two Wolff-Parkinson-White patients. *Circulation*, 54:251–263, 1976.
- [70] J.C. Demoulin and H.E. Kulbertus. Histopathological examination of the concept of left hemiblock. *Br Heart J*, 34:807–814, 1972.
- [71] P.J. Diaz, Y. Rudy, and R. Plonsey. A model study of the effect of intercalated discs on discontinuous propagation in cardiac muscle. *Adv Exp Biol Med*, 161:79–89, 1982.
- [72] P.J. Diaz, Y. Rudy, and R. Plonsey. The intercalated discs as a cause for discontinuous propagation in cardiac muscle: A theoretical simulation. *Ann Biomed Eng*, 11:177–190, 1983.
- [73] J.M. Dieudonne. The left ventricle as confocal prolate spheroids. *Bull Math Biophys*, 31:433–439, 1969.

- [74] D. DiFrancesco and D. Noble. A model of cardiac electrical activity incorporating ionic pumps and concentration changes. *Phil Trans R Soc Lond B*, 307:353–398, 1985.
- [75] S.M. Dillon, M.A. Allesie, P.C. Ursell, and A.L. Wit. Influence of anisotropic tissue structure on reentrant circuit in the epicardial border zone of subacute canine infarcts. *Circ Res*, 63:182–206, 1988.
- [76] J.P. DiMarco and D.E. Haines. Surgery for ventricular tachycardia: Is mapping necessary? In M. Shenasa, M. Borggrefe, and G. Breithardt, editors, *Cardiac Mapping*, pages 525–531. Futura Publishing, Mount Kisco, NY, 1993.
- [77] E. Downar, L. Harris, L.L. Mickleborough, N. Shaikh, and I.D. Parson. Endocardial mapping of ventricular tachycardia in the intact human ventricle: Evidence of reentrant mechanism. *J Am Coll Cardiol*, 11:783–791, 1988.
- [78] E. Downar, S. Masse, T.C.K. Chen, L. Mickleborough, and E. Sevaptisidis. An approach to three-dimensional mapping of clinical ventricular arrhythmias. In M. Shenasa, M. Borggrefe, and G. Breithardt, editors, *Cardiac Mapping*, pages 515–522. Futura Publishing, Mount Kisco, NY, 1993.
- [79] M.H. Draper and M. Mya-Tu. A comparison of the conduction velocity in cardiac tissues of various mammals. *Q J Exp Physiol*, 44:91–109, 1959.
- [80] J.-P. Drouhard and F.A. Roberge. A simulation of repolarization events of the cardiac Purkinje fiber action potential. *IEEE Trans Biomed Eng*, BME-29:481–493, 1982.
- [81] J.-P. Drouhard and F.A. Roberge. A simulation study of the ventricular myocardial action potential. *IEEE Trans Biomed Eng*, BME-29:494–502, 1982.
- [82] J.-P. Drouhard and F.A. Roberge. Revised formulation of the Hodgkin-Huxley representation of the Na^+ current in cardiac cells. *Comp Biomed Res*, 20:333–350, 1987.
- [83] M. Dubuc, R. Nadeau, G. Tremblay, T. Kus, F. Molin, and P. Savard. Pace mapping using body surface potential maps to guide catheter ablation of accessory pathways in patients with Wolff-Parkinson-White syndrome. *Circulation*, 87:135–143, 1993.
- [84] D. Durrer, R.Th. van Dam, G.E. Freud, M.J. Janse, F. L. Meijler, and R. C. Arzbaeher. Total excitation of the isolated human heart. *Circulation*, 41:899–912, 1970.
- [85] L. Ebihara and E.A. Johnson. Fast sodium current in cardiac muscle. *Biophys J*, 32:779–790, 1980.
- [86] W.J. Eifler, E. Macchi, H.J. Ritsema van Eck, B.M. Horacek, and P.M. Rautaharju. Mechanism of generation of body surface electrocardiographic P-waves in normal, middle, and lower sinus rhythms. *Circ Res*, 48:168–182, 1981.

- [87] W. Einthoven. Über die Richtung und die Manifeste Grösse der Potentialschwankungen im menschlichen Herzen und über des Einfluss der Herzlage auf die Form des Elektrokardiogramms. *Pflügers Arch*, 150:275–315, 1913.
- [88] V. Elharrar and B. Surawicz. Cycle length effect on restitution of action potential duration in dog cardiac fibers. *Am J Physiol*, 244:H782–H792, 1983.
- [89] A.E. Epstein, J.K. Kirklin, W.L. Holman, V.J. Plumb, and G.K. Kay. Intermediate septal accessory pathways: Electrocardiographic characteristics, electrophysiologic observations and their surgical implications. *J Am Coll Cardiol*, 17:1570–1578, 1991.
- [90] W.G. Esmond, G.A. Moulton, R.A. Cowley, S. Attar, and E. Blair. Peripheral ramification of the cardiac conducting system. *Circulation*, 28:732–738, 1963.
- [91] T.L. Faber, E.M. Stokely, R.M. Peshock, and J.R. Corbett. A model-based four-dimensional left ventricular surface detector. *IEEE Trans Med Imag*, 10:321–329, 1991.
- [92] A.S. Ferguson and G. Stroink. The potential generated by current sources located in an insulated rectangular volume conductor. *J Appl Phys*, 76:7671–7676, 1994.
- [93] A.S. Ferguson, D. Vardy, R. Hren, and G. Stroink. A regularized minimum norm method for calculating distributions of source currents on epicardial surfaces. In L. Deecke, C. Baumgartner, G. Stroink, and S.J. Williamson, editors, *Biomagnetism: Fundamental Research and Clinical Applications*, pages 676–679. Elsevier, Amsterdam, 1995.
- [94] A.S. Ferguson, X. Zhang, and G. Stroink. A complete linear discretization for calculating the magnetic field using the boundary element method. *IEEE Trans Biomed Eng*, BME-41:455–459, 1994.
- [95] P.C. Fife. *Mathematical Aspects of Reacting and Diffusing Systems*.
- [96] L.K. Flanigan. *A Cellular Model of Electrical Conduction in the Mammalian Atrioventricular Node*. PhD thesis, University of Michigan, Ann Arbor, MI, 1965.
- [97] L.K. Flanigan and H.H. Swain. Computer simulation of AV nodal conduction. *Univ Mich Med Center J*, 33:234–241, 1967.
- [98] N.C. Flowers and L.G. Horan. Body surface potential mapping. In D.P. Zipes and J. Jalife, editors, *Cardiac Electrophysiology: From Cell to Bedside*, pages 1049–1067. W.B. Saunders Company, Philadelphia, 1995.
- [99] C.C. Fox and G.M. Hutchins. The architecture of the human ventricular myocardium. *Johns Hopkins Med J*, 130:289–299, 1972.

- [100] J. Foy, Jr. *A Computer Simulation of Impulse Conduction in Cardiac Muscle*. PhD thesis, University of Michigan, Ann Arbor, MI, 1974.
- [101] H.A. Fozzard and M.F. Arnsdorf. Cardiac electrophysiology. In H.A. Fozzard, E. Huber, R.B. Jennings, A.M. Katz, and H.E. Morgan, editors, *The Heart and Cardiovascular System: Scientific Foundations*, pages 63–99. Raven Press, New York, 1991.
- [102] E. Frank. Electric potential produced by two point current sources in a homogeneous conducting sphere. *J Appl Phys*, 23:1225–1228, 1952.
- [103] E. Frank. A comparative analysis of the eccentric double-layer representation of the human heart. *Am Heart J*, 46:364, 1953.
- [104] M.R. Franz, J. Schaefer, M. Schottler, W.A. Seed, and M.I. Noble. Electrical and mechanical restitution of the human heart at different rates of stimulation. *Circ Res*, 53:815–822, 1983.
- [105] D.W. Frazier, W. Krassowska, P.S. Chen, P.D. Wolf, N.D. Danieleley, W.M. Smith, and R.E. Ideker. Transmural activations and stimulus potentials in three-dimensional anisotropic canine myocardium. *Circ Res*, 63:135–146, 1988.
- [106] J.J. Gallagher, M. Gilbert, R.H. Svenson, W.C. Sealy, J. Kasell, and A.G. Wallace. Wolff-Parkinson-White syndrome: The problem, evaluation, and surgical correction. *Circulation*, 5:767–785, 1975.
- [107] J.J. Gallagher, J.H. Kasell, J.L. Cox, W.M. Smith, R.E. Ideker, and W.M. Smith. Techniques of intraoperative electrophysiologic mapping. *Am J Cardiol*, 49:221–40, 1982.
- [108] J.J. Gallagher, L.C. Pritchett, W.C. Sealy, J. Kasell, and A.G. Wallace. The pre-excitation syndromes. *Prog Cardiovasc Dis*, 20:285–327, 1978.
- [109] M.J. Gardner, T.J. Montague, C.S. Armstrong, B.M. Horáček, and E.R. Smith. Vulnerability to ventricular arrhythmia: Assessment by mapping of body surface potential. *Circulation*, 73:684–692, 1986.
- [110] E.A. Geiser, S.M. Lupkiewicz, L.G. Christie, M. Ariet, D.A. Conetta, and C.R. Conti. A framework for three-dimensional time-varying reconstruction of the human left ventricle: Sources of error and estimation of their magnitude. *Comput Biomed Res*, 13:225–241, 1980.
- [111] H.L. Gelernter and J.C. Swihart. A mathematical-physical model of the genesis of the electrocardiogram. *Biophys J*, 4:285–301, 1964.
- [112] L.D. German, D.L. Packer, G.H. Bardy, and J.J. Gallagher. Ventricular tachycardia induced by atrial stimulation in patients without symptomatic cardiac disease. *Am J Cardiol*, 52:1202–1210, 1983.

- [113] B. Geršak, R. Trobec, T. Gabrijelčič, and B. Slivnik. The model of topical heart cooling during induced hypothermic cardiac arrest in open heart surgery. In A. Murray and R. Arzbaeher, editors, *Computers in Cardiology*, pages 597–600. IEEE Computer Society Press, Los Alamitos, CA, 1995.
- [114] D.B. Geselowitz. Dipole theory in electrocardiography. *Am J Cardiol*, 14:301–306, 1964.
- [115] D.B. Geselowitz. On bioelectric potentials in an inhomogeneous volume conductor. *Biophys J*, 7:1–11, 1967.
- [116] D.B. Geselowitz. On the magnetic field generated outside an inhomogeneous volume conductor by internal current sources. *IEEE Trans Mag*, MAG-6:346–347, 1970.
- [117] D.B. Geselowitz. Computer simulation of the human magnetocardiogram. *IEEE Trans Mag*, MAG-16:812–817, 1980.
- [118] D.B. Geselowitz. Theory and simulation of the electrocardiogram. In P.W. Macfarlane and T.D.V. Lawrie, editors, *Comprehensive Electrocardiology*, pages 181–195. Pergamon Press, New York, 1989.
- [119] D.B. Geselowitz, R.C. Barr, M.S. Spach, and W.T. Miller III. The impact of adjacent isotropic fluids on electrograms from anisotropic cardiac muscle: A modeling study. *Circ Res*, 51:602–613, 1982.
- [120] D.B. Geselowitz and W.T. Miller III. A bidomain model for anisotropic cardiac muscle. *Ann Biomed Eng*, 11:191–206, 1983.
- [121] D.B. Geselowitz and O.H. Schmitt. Electrocardiography. In H.P. Schwan, editor, *Biological Engineering*, pages 333–390. McGraw-Hill, New York, 1969.
- [122] D.B. Geselowitz, S. Smith, K. Mowrey, and E.J. Berbari. Model studies of extracellular electrograms arising from an excitation wave propagating in a thin layer. *IEEE Trans Biomed Eng*, BME-38:526–530, 1991.
- [123] C. Giorgi, R. Nadeau, P. Savard, M. Shenasa, P. Pagé, and R. Cardinal. Body surface isopotential mapping of the entire QRST complex in the Wolff-Parkinson-White syndrome: Correlation with the location of the accessory pathway. *Am Heart J*, 121:1445–1453, 1991.
- [124] A.L. Goldberger and E. Goldberger. *Clinical Electrocardiography: A Simplified Approach*. C.V. Mosby, Toronto, 1994.
- [125] P. Gould, D. Ghista, L. Brombolich, and I. Mirsky. *In vivo* stresses in the human left ventricular wall: Analysis accounting for the irregular 3-dimensional geometry and comparison with idealised geometry analysis. *J Biomech*, 5:521–539, 1972.

- [126] L.S. Green, B. Taccardi, P.R. Ershler, and R.L. Lux. Epicardial potential mapping: Effects of conducting media on isopotential and isochrone distributions. *Circulation*, 84:2513–2521, 1991.
- [127] R.A. Greenbaum, S. Yen Ho, D.G. Gibson, A.E. Becker, and R.H. Anderson. Left ventricular fibre architecture in man. *Br Heart J*, 45:248–263, 1981.
- [128] H.R. Grogan, M.L. Stanley, S.J. Eisenberg, B.M. Horáček, and M.D. Lesh. Body surface mapping for localization of accessory pathways in WPW syndrome. In A. Murray and R. Arzbaeher, editors, *Computers in Cardiology*, pages 255–258. IEEE Computer Society Press, Los Alamitos, CA, 1992.
- [129] F. Grynszpan and D.B. Geselowitz. Model studies of the magnetocardiogram. *Biophys J*, 13:911–924, 1973.
- [130] R.M. Gulrajani. Models of the electrical activity of the heart and the computer simulation of the electrocardiogram. *CRC Crit Rev Biomed Eng*, 16:1–66, 1988.
- [131] R.M. Gulrajani and M. Lorange. Simulation of myocardial anisotropy effects on the ECG. In *Proceedings of the 8th Annual Conference of the IEEE EMBS*, pages 358–360. IEEE, New York, 1986.
- [132] R.M. Gulrajani and G.E. Mailloux. A simulation study of the effects of torso inhomogeneities on electrocardiographic potentials, using realistic heart and torso models. *Circ Res*, 52:45–56, 1983.
- [133] R.M. Gulrajani, H. Pham-Huy, R.A. Nadeau, P. Savard, J. de Guise, R.E. Primeau, and F.A. Roberge. Application of the single moving dipole inverse solution to the study of the Wolff-Parkinson-White syndrome in man. *J Electrocardiol*, 17:271–287, 1984.
- [134] R.M. Gulrajani, F.A. Roberge, and G.E. Mailloux. The forward problem of electrocardiography. In P.W. Macfarlane and T.D.V. Lawrie, editors, *Comprehensive Electrocardiology*, pages 197–236. Pergamon Press, New York, 1989.
- [135] R.M. Gulrajani, F.A. Roberge, and P. Savard. The inverse problem of electrocardiography. In P.W. Macfarlane and T.D.V. Lawrie, editors, *Comprehensive Electrocardiology*, pages 237–288. Pergamon Press, New York, 1989.
- [136] F.O. Hadlock. A shortest path algorithm for gridgraphs. *Networks*, 7:323–334, 1977.
- [137] M.S. Hämäläinen and R.J. Ilmoniemi. Interpreting magnetic fields of the brain: Minimum norm estimates. *Med Biol Eng Comp*, 32:35–42, 1994.
- [138] A. Harada, H.J. D’Agostino, Jr., R.B. Schuessler, J.P. Boineau, and J.L. Cox. Potential distribution mapping: New method for precise localization of intramural septal origin of ventricular tachycardia. *Circulation*, 78(Suppl III):III-137–III-147, 1988.

- [139] L. Harris, E. Downar, L.L. Mickleborough, N. Shaikh, and I.D. Parson. Activation sequence of ventricular tachycardia: Endocardial and epicardial mapping studies in the human ventricle. *J Am Coll Cardiol*, 10:1040–1047, 1987.
- [140] R.N.W. Hauer, M.T. de Zwart, J.M.T. de Bakker, J.F. Hitchcock, O.C.K.M. Penn, M. Nijsen-Karelse, and E.O. Robles de Medina. Endocardial catheter mapping: Wire skeleton technique for representation of computed arrhythmogenic sites compared with intraoperative mapping. *Circulation*, 74:1346–1354, 1986.
- [141] H. Hayashi, S. Watabe, K. Takami, S. Yabe, H. Uematsu, M. Mizutani, and H. Saito. Sites of origin of ventricular premature beats in patients with and without cardiovascular disease evaluated by body surface mapping. *J Electrocardiol*, 21:137–146, 1988.
- [142] H.H. Hecht, C.E. Kossman, R.W. Childers, R. Langendorf, M. Lev, K.M. Rosen, R.D. Pruitt, R.C. Truex, H.N. Uhley, and T.B. Watt, Jr. Atrioventricular conduction: Revised nomenclature and concepts. *Am J Cardiol*, 31:232–244, 1973.
- [143] C.S. Henriquez. Simulating the electrical behavior of cardiac tissue using the bidomain model. *CRC Crit Rev Biomed Eng*, 21:1–77, 1993.
- [144] C.S. Henriquez, A.L. Muzikant, and C.K. Smoak. Anisotropy, fiber curvature and bath loading effects on activation in thin and thick cardiac tissue preparations: Simulations in a three-dimensional bidomain model. *J Cardiovasc Electrophysiol*, 7:424–444, 1996.
- [145] C.S. Henriquez and R. Plonsey. Simulation of propagation along a bundle of cardiac tissue. I. Mathematical formulation. *IEEE Trans Biomed Eng*, BME-37:850–860, 1990.
- [146] C.S. Henriquez and R. Plonsey. Simulation of propagation along a bundle of cardiac tissue. II. Results of simulation. *IEEE Trans Biomed Eng*, BME-37:861–875, 1990.
- [147] C.S. Henriquez, N. Trayanova, and R. Plonsey. Potential and current distributions in a cylindrical bundle of cardiac tissue. *Biophys J*, 53:907–918, 1988.
- [148] C.S. Henriquez, N. Trayanova, and R. Plonsey. A planar slab model for cardiac tissue. *Ann Biomed Eng*, 18:367–376, 1990.
- [149] A. Heringa and D.F. Stegeman. Comments on “potentials produced by arbitrary current sources in an infinite- and finite-length circular conducting cylinder. *IEEE Trans Biomed Eng*, 34:73–74, 1987.
- [150] A.L. Hodgkin and W.A. Rushton. The electrical constants of crustacean nerve fiber. *Proc R Soc Lond (Biol)*, 133:444–479, 1946.

- [151] B.M. Horáček. Digital model for studies in magnetocardiography. *IEEE Trans Mag*, MAG-9:440–444, 1973.
- [152] B.M. Horáček. Numerical model of an inhomogeneous human torso. *Adv Cardiol*, 10:51–57, 1974.
- [153] B.M. Horáček. Lead theory. In P.W. Macfarlane and T.D.V. Lawrie, editors, *Comprehensive Electrocardiology*, pages 291–314. Pergamon Press, New York, 1989.
- [154] B.M. Horáček, T.J. Montague, M.J. Gardner, and E.R. Smith. Arrhythmogenic conditions. In D.M. Mirvis, editor, *Body Surface Electrocardiographic Mapping*, pages 167–189. Kluwer Academic Publishers, Boston, MA, 1988.
- [155] B.M. Horáček, E.R. Smith, D.A. Cameron, H. Gewirtz, and P.M. Rautaharju. Iso-integral analysis of body-surface potential maps. In P.W. Macfarlane, editor, *Progress in Electrocardiology*, pages 22–27. Pitman Medical, Kent, 1979.
- [156] L.N. Horowitz, M.E. Josephson, and A.H. Harken. Epicardial and endocardial activation during sustained ventricular tachycardia in man. *Circulation*, 61:1227–1338, 1980.
- [157] W. Hort. Untersuchungen über die Muskelfaserdehnung und das Gefüge des Myokards in der rechten Herzkammerwand des Meerschweinchens. *Virchows Arch*, 329:694–731, 1957.
- [158] R.G. Hoyt, J.L. Cohen, and J.E. Saffitz. Distribution and three-dimensional structure of intercellular junctions in canine myocardium. *Circ Res*, 64:563–574, 1989.
- [159] R. Hren. *The Effect of Inhomogeneities on Electrocardiographic and Magneto-cardiographic Inverse Solutions: Application in the Localization of Ventricular Pre-excitation Sites*. Master's thesis, Dalhousie University, Halifax, NS, 1993.
- [160] R. Hren, J. Nenonen, P. MacInnis, and B.M. Horáček. Simulated activation from endocardial pacing sites in an anisotropic model of human ventricles. In A. van Oosterom, T.F. Oostendorp, and G.J.H. Uijen, editors, *Building Bridges in Electrocardiology*, pages 156–157. University Press Nijmegen, Nijmegen, 1995.
- [161] R. Hren, J. Nenonen, P. MacInnis, and B.M. Horáček. Simulated body-surface potential maps for paced activation sequences in human ventricles. In A. Murray and R. Arzbaecher, editors, *Computers in Cardiology*, pages 95–98. IEEE Computer Society Press, Los Alamitos, CA, 1995.
- [162] R. Hren and G. Stroink. Application of surface harmonic expansions for modeling the human torso. *IEEE Trans Biomed Eng*, BME-42:521–524, 1995.

- [163] R. Hren, X. Zhang, and G. Stroink. The effect of conductivity inhomogeneities on the body-surface potential and magnetic field inverse solutions. In L. Deecke, C. Baumgartner, G. Stroink, and S.J. Williamson, editors, *Biomagnetism: Fundamental Research and Clinical Applications*, pages 680–683. Elsevier, Amsterdam, 1995.
- [164] R. Hren, X. Zhang, and G. Stroink. Comparison between electrocardiographic and magnetocardiographic inverse solutions using the boundary element method. *Med Biol Eng Comp*, 34:110–114, 1996.
- [165] C.L. Hubley-Kozey, L.B. Mitchell, M.J. Gardner, J.W. Warren, C.J. Penney, E.R. Smith, and B.M. Horáček. Spatial features in body-surface potential maps can identify patients with a history of sustained ventricular tachycardia. *Circulation*, 92:1825–1838, 1995.
- [166] R.E. Hudson. The human conducting system and its examination. *J Clin Path*, 16:492–498, 1967.
- [167] T. Hughes. *The Finite Element Method: Linear Static and Dynamic Finite Element Analysis*. Prentice-Hall, Englewood Cliffs, NJ.
- [168] G.J. Huiskamp and A. van Oosterom. Tailored versus realistic geometry in the inverse problem of electrocardiography. *IEEE Trans Biomed Eng*, 36:827–835, 1989.
- [169] T. Iwa and T. Magara. Correlation between localization of accessory conduction pathway and body surface maps in the Wolff-Parkinson-White syndrome. *Jpn Circ J*, 45:1192–1198, 1981.
- [170] J.J.B. Jack, D. Noble, and R.W. Tsien. *Electric Current Flow in Excitable Cells*. Clarendon Press, Oxford, 1983.
- [171] J.S. Janicki, K.T. Weber, R.F. Gochman, S. Shroff, and F.J. Geheb. Three-dimensional myocardial and ventricular shape: A surface representation. *Am J Physiol*, 241:H1–H11, 1981.
- [172] M.J. Janse and A.L. Wit. Electrophysiological mechanisms of ventricular arrhythmias resulting from myocardial ischemia and infarction. *Physiol Rev*, 69:1049–1152, 1989.
- [173] R.F. Janz and A.F. Grimm. Finite-element model for the mechanical behavior of the left ventricle. *Circ Res*, 30:244–252, 1972.
- [174] C.R. Johnson, R.S. MacLeod, and P.R. Ershler. A computer model for the study of electrical current flow in the human thorax. *Comput Biol Med*, 22:305–323, 1992.
- [175] M.E. Josephson, L.N. Horowitz, A. Farshidi, J.F. Spear, J.A. Kastor, and E.N. Moore. Recurrent sustained ventricular tachycardia: 2. Endocardial mapping. *Circulation*, 57:440–7, 1978.

- [176] M.E. Josephson, L.N. Horowitz, S.R. Spielman, H.L. Waxman, and A.M. Greenspan. Role of catheter mapping in the preoperative evaluation of ventricular tachycardia. *Am J Cardiol*, 49:207–20, 1982.
- [177] M.E. Josephson, H.L. Waxman, M.E. Cain, M.J. Gardner, and A.E. Buxton. Ventricular activation during ventricular endocardial pacing. II. Role of pace-mapping to localize origin of ventricular tachycardia. *Am J Cardiol*, 50:11–22, 1982.
- [178] W. Kaltenbrunner, R. Cardinal, M. Dubuc, M. Shenasa, R. Nadeau, G. Tremblay, M. Vermeulen, P. Savard, and P.L. Pagé. Epicardial and endocardial mapping of ventricular tachycardia in patients with myocardial infarction. Is the origin of the tachycardia always subendocardially localized? *Circulation*, 84:1058–1071, 1991.
- [179] W. Kaltenbrunner, F. Veit, S. Winter, K. Frohner, A. Podczeck, F. Freihoff, K. Steinbach, R. Cardinal, P. Pagé, M. Shenasa, G. Tremblay, P. Savard, and R. Nadeau. Epicardial and left ventricular endocardial activation mapping of septal tachycardia in patients after myocardial infarction: is estimation of the depth of origin feasible? In M. Shenasa, M. Borggreffe, and G. Breithardt, editors, *Cardiac Mapping*, pages 467–494. Futura Publishing, Mount Kisco, NY, 1993.
- [180] S. Kamakura. Localization of the origin of idiopathic right ventricular tachycardia by body surface mapping [in Japanese]. *Nippon-Rinsho*, 53:151–160, 1995.
- [181] S. Kamakura, N. Aihara, M. Matsuhisa, T. Ohe, and K. Shimomura. The role of initial minimum potentials on body surface maps in localizing the earliest endocardial site of ectopic ventricular excitation (abstract). *Circulation*, 74(Suppl II):II–138, 1986.
- [182] S. Kamakura, K. Shimomura, T. Ohe, M. Matsuhisa, and H. Toyoshima. The role of initial minimum potentials on body surface maps in predicting the site of accessory pathways in patients with Wolff-Parkinson-White syndrome. *Circulation*, 74:89–96, 1986.
- [183] J.P. Keener. *Principles of Applied Mathematics: Transformation and Approximation*. Addison-Wesley, Reading, MA, 1988.
- [184] J.P. Keener. An eikonal-curvature equation for action potential propagation in myocardium. *J Math Biol*, 29:629–651, 1991.
- [185] J.P. Keener and A.V. Panfilov. Three-dimensional propagation in the heart: The effects of geometry and fiber orientation on propagation in myocardium. In D.P. Zipes and J. Jalife, editors, *Cardiac Electrophysiology: From Cell to Bedside*, pages 335–347. W.B. Saunders Company, Philadelphia, 1995.
- [186] O.D. Kellogg. *Potential Theory*. Springer-Verlag, Berlin, 1929.

- [187] D.S. Khoury, B. Taccardi, R.L. Lux, P.R. Ershler, and Y. Rudy. Reconstruction of endocardial potentials and activation sequences from intracavitary probe measurements: Localization of pacing sites and effects of myocardial structure. *Circulation*, 91:845–863, 1995.
- [188] R. Killmann, G.G. Jaros, P. Wach, R. Graumann, W. Moshage, W. Renhardt, and R.H. Fleischmann. Localization of myocardial-ischemia from the magneto-cardiogram using current-density reconstruction method: Computer simulation study. *Med Biol Eng Comp*, 33:643–651, 1995.
- [189] R. Killmann, P. Wach, and F. Dienstl. Three-dimensional computer model of the entire human heart for simulation of reentry and tachycardia: Gap phenomenon and Wolff-Parkinson-White syndrome. *Basic Res Cardiol*, 86:485–501, 1991.
- [190] A.G. Kléber, M.J. Janse, F.J.L. van Capelle, and D. Durrer. Mechanism and time course of S-T and T-Q segment changes during acute regional myocardial ischemia in the pig heart determined by extracellular and intracellular recordings. *Circ Res*, 42:603–613, 1978.
- [191] A.G. Kléber, C.B. Riegger, and M.J. Janse. Electrical uncoupling and increase of extracellular resistance after induction of ischemia in isolated, arterially perfused rabbit papillary muscle. *Circ Res*, 61:271–279, 1987.
- [192] L.S. Klein, H.T. Shih, F.K. Hackett, W.M. Miles, and D.P. Zipes. Radiofrequency catheter ablation of ventricular tachycardia in patients without structural heart disease. *Circulation*, 85:1666–1674, 1992.
- [193] C. Klersy, M. Vigano, L. Martinelli, M. Chimienti, and J.A. Salerno. Body surface map and location of origin of ventricular tachycardia. Comparison with epicardial map. In R.T. van Dam and A. van Oosterom, editors, *Electrocardiographic Body Surface Mapping*, pages 105–108. Martinus Nijhoff, Boston, MA, 1986.
- [194] D. Klug, A. Ferracci, F. Molin, M. Dubuc, P. Savard, T. Kus, F. Hélie, R. Cardinal, and R. Nadeau. Body surface potential distributions during idiopathic ventricular tachycardia. *Circulation*, 91:2002–2009, 1995.
- [195] F. Kornreich and P.M. Rautaharju. The missing waveform and diagnostic information in the standard 12 lead electrocardiogram. *J Electrocardiol*, 14:341–350, 1981.
- [196] F. Kornreich, P.M. Rautaharju, J. Warren, T.J. Montague, and B.M. Horáček. Identification of best electrocardiographic leads for diagnosing myocardial infarction by statistical analysis of body surface potential maps. *Am J Cardiol*, 56:852–856, 1985.

- [197] H. Kottkamp, X. Chen, G. Hindricks, S. Willems, W. Haverkamp, T. Wichter, G. Breithardt, and M. Borggrefe. Idiopathic left ventricular tachycardia: New insights into electrophysiological characteristics and radiofrequency catheter ablation. *PACE*, 18:1285–1297, 1995.
- [198] J. Krafchek, G.M. Lawrie, R. Roberts, S.A. Magro, and C.R.C. Wyndham. Surgical ablation of ventricular tachycardia: Improved results with a map-directed regional approach. *Circulation*, 73:1239–47, 1986.
- [199] W. Krassowska and J.C. Neu. Effective boundary conditions for syncytial tissue. *IEEE Trans Biomed Eng*, BME-40:143–150, 1993.
- [200] J. Kupersmith. Electrophysiologic mapping during open heart surgery. *Prog Cardiovasc Dis*, 19:167–202, 1976.
- [201] P. Lambin and J. Troquet. Complete calculation of the electric potential produced by a pair of current source and sink energizing a circular finite-length cylinder. *J Appl Phys*, 54:4174–4184, 1983.
- [202] P.-S. Laplace. *Traité de mécanique céleste. Théorie de l'action capillaire (Supplément au livre X)*. Coarcien, Paris, 1806.
- [203] R. Lazzara, B.K. Yeh, and P. Samet. Functional anatomy of the canine left bundle branch. *Am J Cardiol*, 33:623–632, 1974.
- [204] R.S. Ledley. *Use of Computers in Biology and Medicine*. McGraw-Hill, New York, 1965.
- [205] I.J. LeGrice, B.H. Smaill, L.Z. Chai, S.G. Edgar, J.B. Gavin, and P.J. Hunter. Laminar structure of the heart: Ventricular myocyte arrangement and connective tissue architecture in the dog. *Am J Physiol*, 269:H571–H582, 1995.
- [206] L.J. Leon. *A Model of Excitation and Recovery in the Anisotropic Myocardium*. PhD thesis, Dalhousie University, Halifax, NS, 1987.
- [207] L.J. Leon and B.M. Horáček. Computer model of excitation and recovery in the anisotropic myocardium. I. Rectangular and cubic arrays of excitable elements. *J Electrocardiol*, 24:1–15, 1991.
- [208] L.J. Leon and B.M. Horáček. Computer model of excitation and recovery in the anisotropic myocardium. II. Excitation in the simplified left ventricle. *J Electrocardiol*, 24:17–31, 1991.
- [209] L.J. Leon and B.M. Horáček. Computer model of excitation and recovery in the anisotropic myocardium. III. Arrhythmogenic conditions in the simplified left ventricle. *J Electrocardiol*, 24:33–41, 1991.
- [210] L.J. Leon and F.A. Roberge. Directional characteristics of action potential propagation in cardiac muscle. A model study. *Circ Res*, 69:378–395, 1991.

- [211] L.J. Leon and F.A. Roberge. Structural complexity effects on transverse propagation in a two-dimensional model of myocardium. *IEEE Trans Biomed Eng*, 38:997–1009, 1991.
- [212] T.J. Lewis and M.R. Guevara. Chaotic dynamics in an ionic model of the propagated cardiac action potential. *J Theor Biol*, 146:407–432, 1990.
- [213] P. Lilly, J. Jenkins, and P. Bourdillon. Automatic contour definition on left ventriculograms by image evidence and a multiple template-based model. *IEEE Trans Med Imag*, 8:173–185, 1989.
- [214] F.C. Lin, C.D. Finely, S.H. Rahimtoola, and D. Wu. Idiopathic paroxysmal ventricular tachycardia with a QRS pattern of right bundle branch block and left axis deviation: A unique clinical entity with specific properties. *Am J Cardiol*, 52:95–103, 1983.
- [215] L. Littmann, R.H. Svenson, J.J. Gallagher, J.G. Selle, S.H. Zimmern, J.M. Fedor, and P.G. Colavita. Functional role of the epicardium in postinfarction ventricular tachycardia: Observations derived from computerized epicardial activation mapping, entrainment, and epicardial laser photoablation. *Circulation*, 83:1577–1591, 1991.
- [216] G.C.-C. Lo and D.M. Monro. Simulation of electric fields in human thorax. *Adv Cardiol*, 21:55–58, 1977.
- [217] M. Lorange and R. M. Gulrajani. Computer simulation of the Wolff-Parkinson-White preexcitation syndrome with a modified Miller-Geselowitz heart model. *IEEE Trans Biomed Eng*, BME-33:862–873, 1986.
- [218] M. Lorange and R.M. Gulrajani. A computer heart model incorporating anisotropic propagation. I. Model construction and simulation of normal activation. *J Electrocardiol*, 26:245–261, 1993.
- [219] M. Lorange, R.M. Gulrajani, R.A. Nadeau, and I. Préda. A computer heart model incorporating anisotropic propagation. II. Simulations of conduction block. *J Electrocardiol*, 26:263–277, 1993.
- [220] R. Lower. *Tractatus de Corde*. J Allestry, London, 1669.
- [221] W.X. Lu and L. Xia. Computer-simulation of epicardial potentials using a heart-torso model with realistic geometry. *IEEE Trans Biomed Eng*, BME-43:211–217, 1996.
- [222] K.F.W. Ludwig. Über den Bau und die Bewegungen der Herzventrikel. *Z Rationelle Med*, 7:189–220, 1849.
- [223] C.-H. Luo and Y. Rudy. A model of the ventricular cardiac action potential: Depolarization, repolarization and their interaction. *Circ Res*, 68:1501–1526, 1991.

- [224] C.-H. Luo and Y. Rudy. A dynamic model of the cardiac ventricular action potential. I. Simulations of ionic currents and concentration changes. *Circ Res*, 74:1071–1096, 1994.
- [225] R.L. Lux. Mapping techniques. In P.W. Macfarlane and T.D.V. Lawrie, editors, *Comprehensive Electrocardiology*, pages 1001–1014. Pergamon Press, New York, 1989.
- [226] M.S. Lynn and W.P. Timlake. The use of multiple deflations in the numerical solution of singular systems of equations, with applications to potential theory. *SIAM J Numer Ana.*, 5:303–322, 1968.
- [227] E. Macchi. *Digital-computer Simulation of the Atrial Electrical Excitation Cycle in Man*. PhD thesis, Dalhousie University, Halifax, NS, 1973.
- [228] E. Macchi, G. Arisi, and B. Taccardi. Identification of ectopic ventricular foci by means of intracavitary potential mapping: A proposed method. *Acta Cardiol*, 47:421–433, 1992.
- [229] R.S. MacLeod. *Percutaneous Transluminal Coronary Angioplasty as a Model of Cardiac Ischemia: Clinical and Modelling Studies*. PhD thesis, Dalhousie University, Halifax, NS, 1990.
- [230] R.S. MacLeod, M.J. Gardner, R.M. Miller, and B.M. Horáček. Application of an electrocardiographic inverse solution to localize ischemia during coronary angioplasty. *J Cardiovasc Electrophysiol*, 6:2–18, 1995.
- [231] T.M. MacRobert. *Spherical Harmonics: An Elementary Treatise on Harmonic Functions with Applications*. Pergamon Press, Oxford, 1967.
- [232] M. Malik, T. Cochrane, and A.J. Camm. Computer simulation of the cardiac conduction system. *Comp Biomed Res*, 16:454–468, 1983.
- [233] D.W. Marquardt. An algorithm for least-squares estimation of nonlinear parameters. *J SIAM*, 11:431–441, 1963.
- [234] G.K. Massing and T.N. James. Anatomical configuration of the His bundle and bundle branches in the human heart. *Circulation*, 53:609–621, 1976.
- [235] M. McLean, M.A. Ross, and J. Prothero. Three-dimensional reconstruction of the myofiber pattern in the fetal and neonatal mouse heart. *Anat Rec*, 224:392–406, 1989.
- [236] D.D. McPherson, D.J. Skorton, S. Koiyalam, L. Petree, M.P. Noel, P. Kieso, R.E. Kerber, S.M. Collins, and K.B. Chandran. Finite element analysis of myocardial diastolic function using three-dimensional echocardiographic reconstructions: Application of a new method for study of acute ischemia in dogs. *Circ Res*, 60:674–682, 1987.

- [237] F.L. Meijler and M. Janse. Morphology and electrophysiology of the mammalian atrioventricular node. *Physiol Rev*, 68:608–647, 1988.
- [238] W.T. Miller III and D.B. Geselowitz. Simulation studies of the electrocardiogram. I. The normal heart. *Circ Res*, 43:301–315, 1978.
- [239] W.T. Miller III and D.B. Geselowitz. Simulation studies of the electrocardiogram. II. Ischemia and infarction. *Circ Res*, 43:316–323, 1978.
- [240] I. Mirsky. Effects of anisotropy and inhomogeneity on left ventricular stresses in the intact heart. *Bull Math Biophys*, 32:197–213, 1973.
- [241] G.K. Moe, W.C. Rheinboldt, and J.A. Abildskov. A computer model of atrial fibrillation. *Am Heart J*, 67:200–220, 1964.
- [242] T.J. Montague, E.R. Smith, D.A. Cameron, P.M. Rautaharju, G.A. Klassen, C.S. Flemington, and B.M. Horáček. Isointegral analysis of body surface maps: Surface distribution and temporal variability in normal subjects. *Circulation*, 63:1166–1172, 1981.
- [243] T. Moriarty. The law of Laplace, its limitations as a relation for diastolic pressure, volume, or wall stress of the left ventricle. *Circ Res*, 46:321–331, 1980.
- [244] J. Mukai, H. Nakagawa, K. Nagata, S. Marakawa, W. Shimizu, Y. Tsuchioka, M. Okamoto, H. Masura, and G. Kajiyama. Long-term results of catheter ablation for idiopathic ventricular tachycardia originated from the right ventricular outflow tract. *Jpn Circ J*, 57:960–968, 1993.
- [245] A.L. Muler and V.S. Markin. Electrical properties of anisotropic nerve-muscle syncytia. III. Steady form of the excitation front. *Biofizika*, 22:671–675, 1977.
- [246] J.C. de Munck. The potential distribution in a layered anisotropic spheroidal volume conductor. *J Appl Phys*, 64:464–470, 1988.
- [247] J.C. de Munck. A linear discretization of the volume conductor boundary integral equation using analytically integrated elements. *IEEE Trans Biomed Eng*, BME-39:986–990, 1992.
- [248] R.J. Myerburg, J. Gelband, and A. Castellanos. Electrophysiology of endocardial intraventricular conduction: The role and function of the specialized conducting system. In H.J. Wellens, K.I. Lie, and M.J. Janse, editors, *The Conduction System of the Heart*, pages 336–359. Lea & Febiger, Philadelphia, 1976.
- [249] R.J. Myerburg, K. Nilsson, A. Castellanos, R. Lazzara, B. Befeler, and H. Gelband. The intraventricular conducting system and patterns of endocardial excitation. *Adv Cardiol*, 14:2–14, 1975.

- [250] R. Nadeau, P. Savard, C. Giorgi, M. Dubuc, G. Tremblay, V. Shahidi, M. Shenasa, R. Cardinal, and P. Pagé. Clinical application of body surface potential mapping in the Wolff-Parkinson-White syndrome. In M. Shenasa, M. Borggreffe, and G. Breithardt, editors, *Cardiac Mapping*, pages 313–323. Futura Publishing, Mount Kisco, NY, 1993.
- [251] R.A. Nadeau, P. Savard, G. Faugère, M. Shenasa, P. Pagé, R.M. Gulrajani, R.A. Guardo, and R. Cardinal. Localization of pre-excitation sites in the Wolff-Parkinson-White syndrome by body surface potential mapping and a single moving dipole representation. In R.Th. van Dam and A. van Oosterom, editors, *Electrocardiographic Body Surface Mapping*, pages 95–98. Martinus Nijhoff, Dordrecht, 1986.
- [252] K. Nagao, J. Toyama, I. Kodama, and K. Yamada. Role of the conduction system in the endocardial excitation spread in the right ventricle. *Am J Cardiol*, 48:864–870, 1981.
- [253] H. Nakagawa, K.J. Beckman, J.H. McClelland, X. Wang, M. Arruda, I. Santoro, H.A. Hazlitt, I. Abdalla, A. Singh, H. Gossinger, R. Sweidan, K. Hirao, L. Widman, J.V. Pitha, R. Lazzara, and W.M. Jackman. Radiofrequency catheter ablation of idiopathic left ventricular tachycardia guided by a purkinje potential. *Circulation*, 88:2607–2617, 1993.
- [254] Y. Nakaya and T. Hiraga. Reassessment of the subdivision block of the left bundle branch. *Jpn Circ J*, 45:503–516, 1981.
- [255] Y. Nakaya, H. Inoue, Y. Hiasa, T. Niki, and H. Mori. Functional importance of the left septal Purkinje network in the left ventricular conduction system. *Jpn Heart J*, 22:363–376, 1981.
- [256] J. Nenonen. *Biomagnetic Functional Localization*. PhD thesis, Helsinki University of Technology, Otaniemi, 1992.
- [257] J. Nenonen, J.A. Edens, L.J. Leon, and B.M. Horáček. Computer model of propagated excitation in the anisotropic human heart. II. Simulation of extracardiac fields. In *Computers in Cardiology*, pages 217–220. IEEE Computer Society Press, Los Alamitos, CA, 1991.
- [258] J. Nenonen, J.A. Edens, L.J. Leon, and B.M. Horáček. Computer model of propagated excitation in the anisotropic human heart. I. Implementation and algorithms. In *Computers in Cardiology*, pages 545–548. IEEE Computer Society Press, Los Alamitos, CA, 1991.
- [259] J. Nenonen, M.S. Hämäläinen, and R.J. Ilmoniemi. Minimum-norm estimate in a boundary-element torso model. *Med Biol Eng Comp*, 32:43–48, 1994.
- [260] J. Nenonen, C. Purcell, B.M. Horáček, G. Stroink, and T. Katila. Magneto-cardiographic functional localization using a current dipole in a realistic torso. *IEEE Trans Biomed Eng*, BME-38:658–664, 1991.

- [261] P.M.F. Nielsen. *The Anatomy of the Heart: A Finite Element Model*. PhD thesis, University of Auckland, Auckland, 1987.
- [262] P.M.F. Nielsen, I.J. LeGrice, B.H. Smaill, and P.J. Hunter. Mathematical model of geometry and fibrous structure of the heart. *Am J Physiol*, 260:H1365–H1378, 1991.
- [263] T. Ohe, K. Shimomura, N. Aihara, S. Kamakura, M. Matsuhisa, I. Sato, H. Nakagawa, and A. Shimizu. Idiopathic sustained left ventricular tachycardia: Clinical and electrophysiologic characteristics. *Circulation*, 77:560–568, 1988. [Published erratum appears in *Circulation*, 78:A5, 1988].
- [264] R.H. Okada. Potentials produced by eccentric current dipole in a finite length circular conducting cylinder. *IRE Trans Med Electron*, PGME 7:14–19, 1956.
- [265] M. Okajima, T. Fujino, T. Kobayashi, and K. Yamada. Computer simulation of the propagation process in excitation of the ventricles. *Circ Res*, 23:203–211, 1968.
- [266] T.F. Oostendorp and A. van Oosterom. Source parameter estimation in inhomogeneous volume conductors of arbitrary shape. *IEEE Trans Biomed Eng*, BME-36:382–391, 1989.
- [267] T.F. Oostendorp, A. van Oosterom, and G. Huiskamp. Interpolation on a triangulated 3D surface. *J Comp Phys*, 80:331–343, 1989.
- [268] A. van Oosterom. Triangulating the human torso. *Comput J*, 21:253–258, 1978.
- [269] A. van Oosterom. Cell models: Macroscopic source description. In P.W. Macfarlane and T.D.V. Lawrie, editors, *Comprehensive Electrocardiology*, pages 155–179. Pergamon Press, New York, 1989.
- [270] A. van Oosterom and G.J. Huiskamp. The effect of torso inhomogeneities on body surface potentials quantified using “tailored” geometry. *J Electrocardiol*, 22:53–72, 1989.
- [271] A. van Oosterom, T.F. Oostendorp, G.J. Huiskamp, and H.J.M. ter Brake. The magnetocardiogram as derived from electrocardiographic data. *Circ Res*, 67:1503–1509, 1990.
- [272] A. van Oosterom and R.Th. van Dam. Potential distribution in the left ventricular wall during depolarization. *Adv Cardiol*, 16:27–31, 1976.
- [273] E.D. Overholt and R.W. Joyner. Electrical coupling in the distal cardiac conduction system (abstract). *Pediat Cardiol*, 5:253, 1984.
- [274] E.D. Overholt, R.W. Joyner, RD Veenstra, DA rawling, and R. Weidmann. Unidirectional block between Purkinje and ventricular layers of papillary muscles. *Am J Physiol*, 247:H584–H595, 1984.

- [275] E. Page. Cardiac gap junctions. In H.A. Fozzard, E. Huber, R.B. Jennings, A.M. Katz, and H.E. Morgan, editors, *The Heart and Cardiovascular System: Scientific Foundations*, pages 1003–1048. Raven Press, New York, 1991.
- [276] P.L. Pagé, R. Cardinal, M. Shenasa, W. Kaltenbrunner, R. Cossette, and R. Nadeau. Surgical treatment of ventricular tachycardia: Regional cryoablation guided by computerized epicardial and endocardial mapping. *Circulation*, 80(Suppl I):i-124-I-134, 1989.
- [277] C.J. Penney, L.M. Title, S.E. Iles, J.C. Clements, M.J. Gardner, and B.M. Horáček. Comparison of 'electrophysiologic imaging' and radionuclide imaging in quantification of controlled cardiac ischemia. In A. Murray and R. Arzbaeher, editors, *Computers in Cardiology*, pages 79–82. IEEE Computer Society Press, Los Alamitos, CA, 1995.
- [278] K.P. Philip, E.L. Dove, D.D. McPherson, N.L. Gotteiner, M.J. Vonesh, W. Stanford, J.E. Reed, J.A. Rumberger, and K.B. Chandran. Automatic detection of myocardial contours in cine-computed tomographic images. *IEEE Trans Med Imag*, 13:241–253, 1994.
- [279] T.C. Pilkington, M.N. Morrow, and P.C. Stanley. A comparison of finite element and integral equation formulations for the calculation of electrocardiographic potentials. *IEEE Trans Biomed Eng*, BME-32:166–173, 1985.
- [280] T.C. Pilkington, M.N. Morrow, and P.C. Stanley. A comparison of finite element and integral equation formulations for the calculation of electrocardiographic potentials. II. *IEEE Trans Biomed Eng*, BME-34:258–260, 1987.
- [281] R. Plonsey. *Bioelectric Phenomena*. McGraw-Hill, New York, 1969.
- [282] R. Plonsey. The nature of sources of bioelectric and biomagnetic fields. *Biophys J*, 39:309–312, 1982.
- [283] R. Plonsey. The use of a bidomain model for the study of excitable media. In H.G. Othmer, editor, *Some Mathematical Questions in Biology*, pages 123–149. A.M.S., Providence, RI, 1989.
- [284] R. Plonsey and R.C. Barr. Current flow patterns in two-dimensional anisotropic bisyncytia with normal and extreme conductivities. *Biophys J*, 45:557–571, 1984.
- [285] R. Plonsey and R.C. Barr. A critique of impedance measurements in cardiac tissue. *Ann Biomed Eng*, 14:307–329, 1986.
- [286] R. Plonsey and R.C. Barr. Effect of microscopic and macroscopic discontinuities on the response of cardiac tissue to defibrillating currents. *Med Biol Eng Comput*, 24:130–136, 1986.
- [287] R. Plonsey and D. Heppner. Considerations of quasistationarity in electrophysiological systems. *Bull Math Biophys*, 29:657–664, 1967.

- [288] R. Plonsey and Y. Rudy. Electrocardiogram sources in a two-dimensional anisotropic activation model. *Med Biol Eng Comp*, 18:87–94, 1980.
- [289] S.M. Pogwizd and P.B. Corr. Multiple mechanisms underlying ventricular tachycardia in the human heart after infarction. In M. Shenasa, M. Borggrefe, and G. Breithardt, editors, *Cardiac Mapping*, pages 495–506. Futura Publishing, Mount Kisco, NY, 1993.
- [290] A.E. Pollard. *An Anatomically Based Computer Model for a Study of the Electrical Activity in the Human Ventricular Conduction System*. PhD thesis, Duke University, Durham, 1988.
- [291] A.E. Pollard and R.C. Barr. The construction of an anatomically based model of the human ventricular conduction system. *IEEE Trans Biomed Eng*, 37:1173–1185, 1990.
- [292] A.E. Pollard, M.J. Burgess, and K.W. Spitzer. Computer simulations of three-dimensional propagation in ventricular myocardium: Effects of intramural fiber rotation and inhomogeneous conductivity on epicardial activation. *Circ Res*, 72:744–756, 1993.
- [293] W.H. Press, B.P. Flannery, S.A. Teukolsky, and W.T. Vetterling. *Numerical Recipes: The Art of Scientific Computing*. Cambridge University Press, Cambridge, 1992.
- [294] R.D. Pruitt. Doublets, dipoles and the negativity hypothesis: A historical note on W.H. Craigs and his relationship with F.N. Wilson and Thomas Lewis. *Johns Hopkins Med J*, 138:279–288, 1976.
- [295] A. Pullan. A high-order finite-element/boundary-element torso model. *IEEE Trans Biomed Eng*, BME-43:292–298, 1996.
- [296] C.J. Purcell. *A Comparison of Electric and Magnetic Body Surface Mapping Using Single Moving Dipole Inverse Solutions*. PhD thesis, Dalhousie University, Halifax, NS, 1988.
- [297] C.J. Purcell and G. Stroink. Moving dipole inverse solutions using realistic torso models. *IEEE Trans Biomed Eng*, BME-38:82–84, 1991.
- [298] C.J. Purcell, G. Stroink, and B.M. Horáček. Effect of torso boundaries on electric potential and magnetic field of a dipole. *IEEE Trans Biomed Eng*, BME-35:671–677, 1988.
- [299] W.L. Quan and Y. Rudy. Unidirectional block and reentry of cardiac excitation: A model study. *Circ Res*, 66:367–382, 1990.
- [300] D.A. Rawling and R.W. Joyner. Canine subendocardial Purkinje-ventricular muscle junctional sites are anatomically fixed (abstract). *Circulation*, 72(Suppl IV):IV–237, 1985.

- [301] D.A. Rawling and R.W. Joyner. Characteristics of junctional regions between Purkinje and ventricular muscle-cells of canine ventricular subendocardium. *Circ Res*, 60:585-585, 1987.
- [302] D.A. Rawling, R.W. Joyner, and E.D. Overholt. Variations in the function electrical coupling between the subendocardial Purkinje and ventricular layers of the canine left ventricle. *Circ Res*, 57:252-261, 1985.
- [303] T.G. Reese, R.M. Weisskoff, and R.N. Smith and. Imaging myocardial fiber architecture *in vivo* with magnetic resonance. *Magn Res Med*, 34:786-791, 1995.
- [304] M. Restivo, W.B. Gough, and N. El-Sherif. Ventricular arrhythmias in the sub-acute myocardial infarction period: High-resolution activation and refractory patterns of reentrant arrhythmias. *Circ Res*, 66:1310-1327, 1989.
- [305] H.J. Ritsema van Eck. *Digital Computer Simulation of Cardiac Excitation and Repolarization in Man*. PhD thesis, Dalhousie University, Halifax, NS, 1972.
- [306] F.A. Roberge, A. Vinet, and B. Victorri. Reconstruction of propagated electrical activity with a two dimensional model of anisotropic heart muscle. *Circ Res*, 58:461-475, 1986.
- [307] D.E. Roberts, L.T. Hersh, and A.M. Scher. Influence of cardiac fiber orientation on wavefront voltage, conduction velocity and tissue resistivity in the dog. *Circ Res*, 44:701-712, 1979.
- [308] D.E. Roberts and A.M. Scher. Effect of tissue anisotropy on extracellular potential fields in canine myocardium *in situ*. *Circ Res*, 50:342-351, 1982.
- [309] M.A. Ross and D.D. Streeter, Jr. Nonuniform subendocardial fiber orientation in the normal macaque left ventricle. *Eur J Cardiol*, 3:229-247, 1975.
- [310] B.J. Roth. The electrical potential produced by a strand of cardiac muscle: A bidomain analysis. *Ann Biomed Eng*, 16:609-637, 1988.
- [311] B.J. Roth. Action potential propagation in a thick strand of cardiac muscle. *Circ Res*, 68:162-173, 1991.
- [312] B.J. Roth. A comparison of two boundary conditions used with the bidomain model of cardiac tissue. *Ann Biomed Eng*, 19:669-678, 1991.
- [313] B.J. Roth, W. Guo, and J.P. Wikswo, Jr. The effect of spiral anisotropy on the electrical potential and the magnetic field at the apex of the heart. *Math Biosci*, 88:191-221, 1988.
- [314] B.J. Roth and J.P. Wikswo Jr. A bidomain model for the extracellular potential and magnetic field of cardiac tissue. *IEEE Trans Biomed Eng*, BME-33:467-469, 1986.

- [315] B.J. Roth and J.P. Wikswo, Jr. Electrically silent magnetic fields. *Biophys J*, 5:739-745, 1986.
- [316] Y. Rudy and B.J. Messinger-Rapport. The inverse problem in electrocardiography: Solutions in terms of epicardial potentials. *CRC Crit Rev Biomed Eng*, 16:215-268, 1988.
- [317] Y. Rudy and H.S. Oster. The electrocardiographic inverse problem. *CRC Crit Rev Biomed Eng*, 20:25-46, 1992.
- [318] Y. Rudy and R. Plonsey. The eccentric spheres model as the basis for a study of the role of geometry and inhomogeneities in electrocardiography. *IEEE Trans Biomed Eng*, BME-26:392-399, 1979.
- [319] Y. Rudy and W.L. Quan. A model study of the effects of the discrete cellular structure on electric propagation in cardiac tissue. *Circ Res*, 61:815-823, 1987.
- [320] Y. Rudy and W.L. Quan. Propagation delays across cardiac gap junctions and their reflection in extracellular potentials: A simulation study. *J Cardiovasc Electrophysiol*, 2:299-315, 1991.
- [321] S. Rush. On the independence of magnetic and electric body surface recordings. *IEEE Trans Biomed Eng*, BME-22:157-167, 1975.
- [322] T. Sano, N. Takayama, and T. Shimamoto. Directional difference of conduction velocity in the cardiac ventricular syncytium studies by microelectrodes. *Circ Res*, 7:262-267, 1959.
- [323] J. Sarvas. Basic mathematical and electromagnetic concepts of the biomagnetic inverse problems. *Phys Med Biol*, 32:11-22, 1987.
- [324] P. Savard, A. Ackaoui, R.M. Gulrajani, R. Nadeau, F.A. Roberge, R. Guardo, and B. Dubé. Localization of cardiac ectopic activity in man by a single moving dipole. Comparison of different computation techniques. *J Electrocardiol*, 18:211-222, 1985.
- [325] P. Savard, R. Nadeau, M. Shenasa, P. Pagé, W. Kaltenbrunner, and R. Cardinal. Thoracic and epicardial potential distributions during induced ventricular tachycardia in patients with prior myocardial infarction. In M. Shenasa, M. Borggrefe, and G. Breithardt, editors, *Cardiac Mapping*, pages 335-345. Futura Publishing, Mount Kisco, NY, 1993.
- [326] P. Savard, M. Shenasa, P. Pagé, R. Cardinal, D. Derome, and R. Nadeau. Body surface potential mapping of induced ventricular tachycardia in man: Electrocardiographic and surgical correlations (abstract). *Circulation*, 76(Suppl IV):IV-438, 1987.

- [327] B.E.H. Saxberg and R.J. Cohen. Cellular automata models of cardiac conduction. In L. Glass, P. Hunter, and A. McCulloch, editors, *Theory of Heart: Biomechanics, Biophysics, and Nonlinear Dynamics of Cardiac Function*, pages 437–476. Springer Verlag, New York, 1991.
- [328] B.E.H. Saxberg, M.P. Grumbach, and R.J. Cohen. A time dependent anatomically detailed model of cardiac conduction. In K.L. Ripley, editor, *Computers in Cardiology*, pages 401–404. IEEE Computer Society Press, Washington, D.C., 1985.
- [329] A.M. Scher and M.S. Spach. Cardiac depolarization and repolarization and the electrocardiogram. In R.M. Berne, N. Sperelakis, and S.R. Geiger, editors, *Handbook of Physiology—Section 2: The Cardiovascular System*, pages 357–392. Am Physiol Soc, Bethesda, MD, 1979.
- [330] H.A. Schlitt, L. Heller, R. Aaron, E. Best, and D.M. Ranken. Evaluation of boundary element methods for the EEG forward problem: Effect of linear interpolation. *IEEE Trans Biomed Eng*, BME-42:52–58, 1995.
- [331] O.H. Schmitt. Biological information processing using the concept of interpenetrating domains. In K.N. Leibovic, editor, *Information Processing in the Nervous System*, pages 325–331. Springer Verlag, New York, 1969.
- [332] N.G. Sepulveda and J.P. Wikswo, Jr. Electric and magnetic fields from two-dimensional anisotropic bisyncytia. *Biophys J*, 5:557–568, 1987.
- [333] A.V. Shahidi, P. Savard, and R. Nadeau. Forward and inverse problems of electrocardiography: Modeling and recovery of epicardial potentials in humans. *IEEE Trans Biomed Eng*, BME-41:249–256, 1994.
- [334] P. Silvester and P. Tymchyshyn. Finite-element modelling of the inhomogeneous thorax. *Adv Cardiol*, 10:46–50, 1974.
- [335] H.D. Simms, Jr. and D.B. Geselowitz. Computation of heart surface potentials using the surface source model. *J Cardiovasc Electrophysiol*, 6:522–531, 1995.
- [336] A. SippensGroenewegen, R.N.W. Hauer, N.M. van Hemel, J.H. Kingma, J.M.T. de Bakker, M.J. Janse, and E.O. Robles de Medina. Design and clinical application of a body surface mapping reference data base for detailed localization of ventricular tachycardia foci in patients without structural cardiac disease. In M. Shenasa, M. Borggreffe, and G. Breithardt, editors, *Cardiac Mapping*, pages 347–363. Futura Publishing, Mount Kisco, NY, 1993.
- [337] A. SippensGroenewegen, H. Spekhorst, N.M. van Hemel, J.H. Kingma, R.N.W. Hauer, J.M.T. de Bakker, C.A. Grimbergen, M.J. Janse, and A.J. Dunning. Localization of the site of origin of postinfarction ventricular tachycardia by endocardial pace mapping: Body surface mapping compared with the 12-lead electrocardiogram. *Circulation*, 88:2290–2306, 1993.

- [338] A. SippensGroenewegen, H. Spekhorst, N.M. van Hemel, J.H. Kingma, R.N.W. Hauer, J.M.T. de Bakker, C.A. Grimbergen, M.J. Janse, and A.J. Dunning. Value of body surface mapping in localizing the site of origin of ventricular tachycardia in patients with previous myocardial infarction. *J Am Coll Cardiol*, 24:1708–1724, 1994.
- [339] A. SippensGroenewegen, H. Spekhorst, N.M. van Hemel, J.H. Kingma, R.N.W. Hauer, M.J. Janse, and A.J. Dunning. Body surface mapping of ectopic left and right ventricular activation: QRS spectrum in patients without structural heart disease. *Circulation*, 82:879–896, 1990.
- [340] A. SippensGroenewegen, H. Spekhorst, N.M. van Hemel, J.H. Kingma, R.N.W. Hauer, M.J. Janse, and A.J. Dunning. Body surface mapping of ectopic left ventricular activation: QRS spectrum in patients with prior myocardial infarction. *Circ Res*, 71:1361–1378, 1992.
- [341] W.P. Smythe. *Static and Dynamic Electricity*. McGraw-Hill, New York, 1938.
- [342] J. Sobotta and H. Becher. *Atlas der Anatomie des Menschen*. Urban & Schwarzenberg, Baltimore, MD, 1990.
- [343] F. Solina and R. Bajesy. Recovery of parametric models from range images: The case for superquadrics with global deformations. *IEEE Trans Patt Anal Mach Intell*, 12:131–146, 1990.
- [344] J.C. Solomon and R.H. Selvester. Myocardial activation sequence simulation. In I. Hoffman, editor, *Vectorcardiography 2*, pages 175–182. North-Holland Publishing Co., Amsterdam, 1971.
- [345] J.C. Solomon and R.H. Selvester. Simulation of measured activation sequence in the human heart. *Am Heart J*, 85:518–524, 1973.
- [346] J.R. Sommer and R.B. Jennings. Ultrastructure of cardiac muscle. In H.A. Fozzard, E. Huber, R.B. Jennings, A.M. Katz, and H.E. Morgan, editors, *The Heart and Cardiovascular System: Scientific Foundations*, pages 3–50. Raven Press, New York, 1991.
- [347] M.S. Spach. The discontinuous nature of electrical propagation in cardiac muscle. *Ann Biomed Eng*, 11:207–261, 1983.
- [348] M.S. Spach, R.C. Barr, and C.F. Lanning. Experimental basis for QRS and T wave potentials in the WPW syndrome: The relation of epicardial to body surface potential distributions in the intact chimpanzee. *Circ Res*, 42:103–118, 1978.
- [349] M.S. Spach and P.C. Dolber. Discontinuous propagation and nonuniform anisotropy: A basis for micro-reentry in human cardiac muscle (abstract). *Circulation*, 70(Suppl II):II-345, 1984.

- [350] M.S. Spach and J.F. Heidlage. A multidimensional model of cellular effects on the spread of electrotonic currents and on propagating action potentials. *Ann Biomed Eng*, 20:141–169, 1992.
- [351] M.S. Spach and J.F. Heidlage. The stochastic nature of cardiac propagation at a microscopic level: Electrical description of myocardial architecture and its application to conduction. *Circ Res*, 76:366–380, 1995.
- [352] M.S. Spach, S. Huang, and C.R. Ayers. Electrical and anatomical study of the Purkinje system of the canine heart. *Am Heart J*, 65:664–673, 1963.
- [353] M.S. Spach and J.M. Kootsey. The nature of electrical propagation in cardiac muscle. *Am J Physiol*, 244:H3–H22, 1983.
- [354] M.S. Spach, W.T. Miller III, D.B. Geselowitz, R.C. Barr, J.M. Kootsey, and E.A. Johnson. The discontinuous nature of propagation in normal canine cardiac muscle. Evidence for recurrent discontinuities of intracellular resistance that affects membrane currents. *Circ Res*, 48:39–54, 1981.
- [355] M.S. Spach, W.T. Miller III, E. Miller-Jones, R.B. Warren, and R.C. Barr. Extracellular potentials related to intracellular action potentials during impulse conduction in anisotropic canine cardiac muscle. *Circ Res*, 45:188–204, 1979.
- [356] M.S. Spach, H. Shao-Nan, S.I. Armstrong, and R.V. Canent. Demonstration of the peripheral conduction system in human hearts. *Circulation*, 28:333–338, 1963.
- [357] S. Spaggiari, S. Baruffi, G. Arisi, E. Macchi, and B. Taccardi. Effect of intramural fiber direction on epicardial isochrone and potential maps (abstract). *Circulation*, 76(Suppl II):II-961, 1987.
- [358] L.H. Staib and J.S. Duncan. Boundary finding with parametrically deformable models. *IEEE Trans Patt Anal Mach Intell*, 14:1061–1075, 1992.
- [359] P.C. Stanley and T.C. Pilkington. The combination method: a numerical technique for electrocardiographic calculations. *IEEE Trans Biomed Eng*, BME-36:456–461, 1989.
- [360] P.C. Stanley, T.C. Pilkington, and M.N. Morrow. The effects of thoracic inhomogeneities on the relationship between epicardial and torso potentials. *IEEE Trans Biomed Eng*, BME-33:273–284, 1986.
- [361] D.J. Staton, R.N. Friedman, and J.P. Wikswo Jr. High resolution SQUID imaging of octupolar currents in anisotropic cardiac tissue. *IEEE Trans Appl Supercond*, 3:1934–1936, 1993.
- [362] W.J. Sternberg and T.L. Smith. *The Theory of Potential and Spherical Harmonics*. Toronto University Press, Toronto, 1948.
- [363] J.A. Stratton. *Electromagnetic Theory*. McGraw-Hill, New York, 1941.

- [364] D.D. Streeter, Jr. Gross morphology and fiber geometry of the heart. In R.M. Berne, N. Sperelakis, and S.R. Geiger, editors, *Handbook of Physiology-Section 2: The Cardiovascular System*, pages 61–112. Am Physiol Soc, Bethesda, MD, 1979.
- [365] D.D. Streeter, Jr. and D.L. Bassett. An engineering analysis of myocardial fiber orientation in pig's left ventricle in systole. *Anat Rec*, 155:503–511, 1966.
- [366] D.D. Streeter, Jr. and W.T. Hanna. Engineering mechanics for successive states in canine left ventricular myocardium: I. Cavity and wall geometry. *Circ Res*, 33:639–655, 1973.
- [367] D.D. Streeter, Jr., W.E. Powers, M.A. Ross, and F. Torrent-Guasp. Three-dimensional fiber orientation in the mammalian left ventricular wall. In J. Baan, A. Noordergraaf, and J. Raines, editors, *Cardiovascular System Dynamics*, pages 73–84. MIT Press, Cambridge, MA, 1978.
- [368] D.D. Streeter, Jr., M.M. Spotnitz, D.P. Patel, J. Ross, Jr., and E.H. Sonnenblick. Fiber orientation in the canine left ventricle during diastole and systole. *Circ Res*, 24:339–347, 1969.
- [369] G. Stroink. Cardiomagnetic imaging. In B.L. Zaret, L. Kaufman, A.S. Berson, and R.A. Dunn, editors, *Frontiers in Cardiovascular Imaging*, pages 161–177. Raven Press, New York, 1993.
- [370] B. Taccardi. Distribution of heart potentials on the thoracic surface of normal human subjects. *Circ Res*, 1:341–351, 1963.
- [371] B. Taccardi, L. De Ambroggi, and C. Viganotti. Body-surface mapping of heart potentials. In C.V. Nelson and D.B. Geselowitz, editors, *The Theoretical Basis of Electrocardiology*, pages 436–466. Clarendon Press, Oxford, 1976.
- [372] B. Taccardi, G. Arisi, E. Macchi, S. Spaggiari, and S. Baruffi. A new intracavitary probe for detecting the site of origin of ectopic ventricular beats during one cardiac cycle. *Circulation*, 75:272–281, 1987.
- [373] B. Taccardi, R.L. Lux, and P. Ershler. Intramural spread of excitation wavefronts and associated potential fields. In Z. Antaloczy, I. Preda, and E. Kekes, editors, *Advances in Electrocardiography*, pages 61–62. Excerpta Medica, Amsterdam, 1990.
- [374] B. Taccardi, R.L. Lux, P.R. Ershler, R.S. MacLeod, and Y. Vyhmeister. Effect of myocardial fiber direction on 3-D shape of excitation wavefronts and associated potential distributions in ventricular walls (abstract). *Circulation*, 86(Suppl I):I-752, 1992.
- [375] B. Taccardi, R.L. Lux, P.R. Ershler, R.S. MacLeod, C. Zabawa, and Y. Vyhmeister. Potential distributions and excitation time maps recorded with high spatial resolution from the entire ventricular surface of exposed dog hearts. In

- A. Murray and R. Arzbaecher, editors, *Computers in Cardiology*, pages 1-4. IEEE Computer Society Press, Los Alamitos, CA, 1992.
- [376] B. Taccardi, E. Macchi, R.L. Lux, P.E. Ershler, S. Spaggiari, S. Baruffi, and Y. Vyhmeister. Effect of myocardial fiber direction on epicardial potentials. *Circulation*, 90:3076-3090, 1994.
- [377] B. Taccardi, S. Watabe, P.R. Ershler, R.L. Lux, and E. Macchi. A method for separating the axial and transverse contribution of excitation wavefronts to the cardiac electric fields (abstract). *Circulation*, 78(Suppl II):II-412, 1988.
- [378] T. Tamiya, T. Yamashiro, T. Matsumoto, S. Ogoshi, and H. Seguchi. A histological study of surgical landmarks for the specialized A-V conduction system with particular reference to the papillary muscles. *Ann Thorac Surg*, 40:599-613, 1985.
- [379] S. Tawara. *Das Reizleitungssystem des Säugetierherzens. Eine anatomisch-histologische Studie über das Atrioventrikularbündel und die Purkinjeschen Fäden*. Gustav Fischer Verlag, Jena, 1906.
- [380] N.V. Thakor and L.N. Eisenman. Three-dimensional computer model of the heart: Fibrillation induced by extrastimulation. *Comp Biomed Res*, 22:532-545, 1989.
- [381] C.E. Thomas. The muscular architecture of the ventricles of hog and dog hearts. *Am J Anat*, 101:17-57, 1957.
- [382] L.-E. Thornell and A. Eriksson. Filament system in the Purkinje fibers of the heart. *Am J Physiol*, 241:H291-H305, 1981.
- [383] L. Thrans, M. Burghoff, K. Brockmeier, and L. Schmitz. Vortex current detected by magnetocardiogram. In C. Aine, E. Flynn, Y. Okada, G. Stroink, S. Swithenby, and C. Wood, editors, *Biomag 96: Advances in Biomagnetism*. Springer Verlag, Berlin. [To be published].
- [384] J.L. Titus. Normal anatomy of the human cardiac conduction system. *Mayo Clinic Proc*, 48:24-30, 1973.
- [385] J.L. Titus, G.W. Daugherty, and J.E. Edwards. Anatomy of the normal human atrioventricular conduction system. *Am J Anat*, 113:407-415, 1963.
- [386] T. Toffoli and N. Margolus. *Cellular Automata Machines*. MIT Press, Cambridge, MA, 1987.
- [387] N. Trayanova and T.P. Pilkington. A bidomain model with periodic intracellular junctions: A one-dimensional analysis. *IEEE Trans Biomed Eng*, 40:424-433, 1993.
- [388] R.C. Truex. Comparative morphology of the conduction system. *Annals NY Acad Sci*, 127:19-33, 1965.

- [389] L. Tung. *A Bidomain Model for Describing Ischemic Myocardial DC Potentials*. PhD thesis, Massachusetts Institute of Technology, Cambridge, MA, 1978.
- [390] J.S. Tweddell, B.H. Branham, A. Harada, C.M. Stone C.K. Rokkas, R.B. Schuessler, J.P. Boineau, and J.L. Cox. Potential mapping in septal tachycardia: Evaluation of a new intraoperative mapping technique. *Circulation*, 80(Suppl 1):I-97-I-108, 1989.
- [391] H.N. Uhley and L. Rivkin. Visualization of the left branch of the human atrioventricular bundle. *Circulation*, 20:419-421, 1959.
- [392] H.N. Uhley and L. Rivkin. Peripheral distribution of the canine A-V conducting system: Observations on gross morphology. *Am J Cardiol*, 5:688-691, 1960.
- [393] S. Ushijima, T. Iwa, and T. Magara. Diagnosis of the site of origin of ventricular tachycardia by body surface mapping. In P d'Alche, editor, *Advances in Electrocardiology*, pages 89-91. Centre de Publications de l'Université de Caen, Caen, 1985.
- [394] C.R. Vander Ark and E.W. Reynolds. An experimental study of propagated electrical activity in the canine heart. *Circ Res*, 26:451-460, 1970.
- [395] J.A. Vassalo, D.M. Cassidy, F.E. Marchlinski, A.E. Buxton, H.L. Waxman, J.U. Doherty, and M.E. Josephson. Endocardial activation of the left bundle branch block. *Circulation*, 69:914-923, 1984.
- [396] R. D. Veenstra, R. W. Joyner, and D. A. Rawling. Purkinje and ventricular activation sequences of canine papillary muscle: Effects of quinidine and calcium on the Purkinje-ventricular conduction delay. *Circ Res*, 54:500-515, 1984.
- [397] P. Wach, R. Killmann, F. Dienstl, and C. Eichinger. A computer model of human ventricular myocardium for simulation of ECG, MCG and activation sequence including reentry rhythms. *Basic Res Cardiol*, 84:404-413, 1989.
- [398] J.R. Wait. The potential of two current point sources in a homogeneous conducting prolate spheroid. *J Appl Phys*, 24:496-497, 1953.
- [399] S. Watabe, B. Taccardi, R.L. Lux, and P.E. Ershler. Effect of nontransmural necrosis on epicardial potential fields: Correlation with fiber direction. *Circulation*, 82:2115-2127, 1994.
- [400] H L. Waxman and M.E. Josephson. Ventricular activation during ventricular endocardial pacing. I. Electrocardiographic patterns related to the site of pacing. *Am J Cardiol*, 50:1-10, 1982.
- [401] D. Wei, O. Okazaki, K. Harumi, E. Harasawa, and H. Hosaka. Comparative simulation of excitation and body surface electrocardiogram with isotropic and anisotropic computer heart models. *IEEE Trans Biomed Eng*, 42:343-357, 1995.

- [402] D. Wei, G. Yamada, T. Musha, H. Tsunakawa, T. Tsutsumi, and K. Harumi. Computer simulation of supraventricular tachycardia with the Wolff-Parkinson-White syndrome using three-dimensional heart models. *J Electrocardiol*, 23:261–273, 1990.
- [403] S. Weidmann. Electrical constants of trabecular muscle from mammalian heart. *J Physiol (Lond)*, 210:1041–54, 1970.
- [404] P. Weismüller, K. Abraham-Fuchs, S. Schneider, P. Richter, M. Kochs, and V. Hombach. Magnetocardiographic non-invasive localization of accessory pathways in the Wolff-Parkinson-White syndrome by a multichannel system. *Eur Heart J*, 13:616–622, 1992.
- [405] H.J.J. Wellens, D.R. Durrer, and K.I. Lie. Observations on mechanisms of ventricular tachycardia in man. *Circulation*, 54:237–244, 1976.
- [406] H.J.J. Wellens, K.I. Lie, and D. Durrer. Further observations on ventricular tachycardia as studied by electrical stimulation of the heart. Chronic recurrent ventricular tachycardia and ventricular tachycardia during acute myocardial infarction. *Circulation*, 49:647–653, 1974.
- [407] H.J.J. Wellens, L.-M. Rodriguez, and J.L. Smets. Ventricular tachycardia in structurally normal hearts. In D.P. Zipes and J. Jalife, editors, *Cardiac Electrophysiology: From Cell to Bedside*, pages 780–788. W.B. Saunders Company, Philadelphia, 1995.
- [408] M.S. Wen, S.J. Yehand, C.C. Wang, F.C. Lin, I.C. Chen, and D. Wu. Radiofrequency ablation therapy in idiopathic left ventricular tachycardia with no obvious structural heart disease. *Circulation*, 89:1690–1696, 1994.
- [409] N. Wiener and A. Rosenbluth. The mathematical formulation of the problem of conduction of impulses in a network of connected excitable elements, specifically in cardiac muscle. *Arch Inst Cardiol Mexico*, 16:205–265, 1946.
- [410] J.P. Wikswo, Jr. Theoretical aspects of the ECG-MCG relationship. In S.A. Williamson, G.L. Romani, L. Kaufman, and I. Modena, editors, *Biomagnetism: An Interdisciplinary Approach*, pages 311–326. Plenum Publishing Corp., New York, 1983.
- [411] J.P. Wikswo, Jr. and J.P. Barach. Possible sources of new information in the magnetocardiogram. *J Theor Biol*, 95:721–729, 1982.
- [412] J.P. Wikswo, Jr., T.A. Wisialowski, W.A. Altemeier, J.R. Balsler, H.A. Kopelman, and D.M. Roden. Virtual cathode effects during stimulation of cardiac muscle: Two-dimensional *in vivo* experiments. *Circ Res*, 68:513–530, 1991.
- [413] F.N. Wilson and R.H. Bayley. The electric field of an eccentric dipole in a homogeneous spherical conducting medium. *Circulation*, 1:84–92, 1950.

- [414] F.N. Wilson, A.G. Macleod, and P.S. Barker. The distribution of the action currents produced by heart muscle and other excitable tissues immersed in extensive conducting media. *J Gen Physiol*, 16:423-456, 1933.
- [415] F.N. Wilson, A.G. Macleod, and P.S. Barker. *The Distribution of the Currents of Action and of Injury Displayed by Heart Muscle and Other Excitable Tissues*. University of Michigan Press, Ann Arbor, MI, 1933.
- [416] S. Wolfram. Universality and complexity in cellular automata. *Physica D*, 10:1-35, 1984.
- [417] A.Y.K. Wong and P. Rautaharju. Stress distribution within the left ventricular wall approximated as a thick ellipsoidal shell. *Am Heart J*, 75:649-662, 1969.
- [418] J. Wu, J. McHowat, J.E. Saffitz, K.A. Yamada, and P.B. Corr. Inhibition of gap junctional conductance by long-chain acylcarnitines and their preferential accumulation in junctional sarcolemma during hypoxia. *Circ Res*, 72:879-889, 1993.
- [419] C.R. Wyndham, M.K. Meeran, T. Smith, R.M. Engelman, S. Levitsky, and K.M. Rosen. Epicardial activation in human left anterior fascicular block. *Am J Cardiol*, 44:638-644, 1979.
- [420] C.R. Wyndham, M.K. Meeran, T. Smith, A. Saxena, R.M. Engelman, S. Levitsky, and J.P. Roos. Epicardial activation of the intact human heart without conduction defect. *Circulation*, 59:161-168, 1979.
- [421] C.R. Wyndham, T. Smith, M.K. Meeran, R. Mammaua, S. Levitsky, and K.M. Rosen. Epicardial activation in patients with left bundle branch block. *Circulation*, 61:696-703, 1980.
- [422] S.B. Xu and W.X. Lu. Surface reconstruction of 3-D objects in computerized tomography. *Comput Vision Graphics Image Process*, 44:270-278, 1988.
- [423] Z. Xu, R.M. Gulrajani, F. Molin, M. Lorange, B. Dubé, P. Savard, and R.A. Nadeau. A computer heart model incorporating anisotropic propagation. III. Simulation of ectopic beats. *J Electrocardiol*, 29:73-90, 1996.
- [424] K. Yamada, J. Toyama, M. Wada, S. Sugiyama, J. Sugenooya, H. Toyoshima, Y. Mizuno, I. Sotobata, T. Kobayashi, and M. Okajima. Body surface isopotential mapping in Wolff-Parkinson-White syndrome: Non-invasive methods to determine the localization of the accessory atrioventricular pathway. *Am Heart J*, 90:721-734, 1975.
- [425] Y. Yamashita and D.B. Geselowitz. Source-field relationships for cardiac generators on the heart surface based on their transfer coefficients. *IEEE Trans Biomed Eng*, BME-32:964-970, 1985.

- [426] Y. Yamashita and T. Takahashi. Use of the finite element method to determine epicardial from body surface potentials under a realistic torso model. *IEEE Trans Biomed Eng*, BME-31:611–621, 1984.
- [427] R. Yee, G.J. Klein, and G.M. Guiraudon. The Wolff-Parkinson-White syndrome. In D.P. Zipes and J. Jalife, editors, *Cardiac Electrophysiology: From Cell to Bedside*, pages 1049–1067. W.B. Saunders Company, Philadelphia, 1995.
- [428] A.L. Yettram and C.A. Vinson. Geometric modeling of the human left ventricle. *J Biomech Eng*, 101:221–223, 1979.
- [429] F.C. Yin, S. Zeger, R. Strumpf, L. Demer, P. Chew, and W.L. Maugham. Assessment of regional ventricular mechanics. In C. Taylor, E. Hinton, D.R. Owen, and E. Onate, editors, *Numerical Methods for Nonlinear Problems*, pages 513–524. Pincridge Press, Swansea, 1984.
- [430] X. Zhang and G. Stroink. A node-based boundary element method to calculate the continuous variation of cardiac potentials over a closed surface. In *Proceedings of the 14th Annual International Conference IEEE EMBS*, pages 1770–1771. IEEE EMBS, Paris, 1992.
- [431] H. Zhou and A. van Oosterom. Application of the boundary element method to the solution of anisotropic electromagnetic problems. *Med Biol Eng Comp*, 32:399–405, 1994.
- [432] O.C. Zienkiewicz and K. Morgan. *The Finite Elements and Approximation*. Wiley, New York, 1982.